INAUGURAL-DISSERTATION

zur

Erlangung der Doktorwürde

der

Naturwissenschaftlich-Mathematischen

Gesamtfakultät

der

Ruprecht-Karls-Universität

Heidelberg

vorgelegt von

Dipl.-Phys. Thorsten Naab

aus Mainz

Tag der mündlichen Prüfung: 20. Dezember 2000

Struktur und Dynamik wechselwirkender Galaxien

Dissertation
submitted to the
Combined Faculties for the Natural Sciences and for Mathematics
of the Rupertus Carola University of
Heidelberg, Germany
for the degree of
Doctor of Natural Sciences

Structure and Dynamics of Interacting Galaxies

presented by
Diplom-Physicist: Thorsten Naab
born in: Mainz

Heidelberg, 20.12.2000

Referees: Priv.-Doz. Dr. Andreas Burkert
            Prof. Dr. Immo Appenzeller

Struktur und Dynamik wechselwirkender Galaxien

Die "Merger Hypothese" sieht den Ursprung von elliptischen Galaxien in Verschmelzungen von Spiralgalaxien. Um diese Hypothese zu testen, wurden stoßfreie Simulationen von verschmelzenden Scheibengalaxien mit unterschiedlichen Massenverhältnissen und relativen Orientierungen durchgeführt. Alle Verschmelzungsprodukte wurden bezüglich ihrer photometrischen und kinematischen Eigenschaften untersucht. Es wurden Untersuchungsmethoden entwickelt, die einen direkten Vergleich mit beobachteten elliptischen Galaxien erlauben. Simulierte Verschmelzungen von Galaxien gleicher Masse resultieren in triaxialen Endprodukten mit einem $r^{1/4}$ Flächendichteprofil. Sie rotieren langsam, sind dispersionsgestützt, zeigen signifikante Rotation entlang der kleinen Halbachse und haben vornehmlich kastenförmige (boxy) Isophoten. Endprodukte von Verschmelzungen mit Massenverhältnissen von 3:1 und 4:1 sind hauptsächlich oblat, rotieren schnell mit wenig Rotation entlang der kleinen Halbachse und haben scheibenförmige (disky) Isophoten. Alle Eigenschaften stimmen sehr gut mit den Beobachtungen von massiven elliptischen Galaxien überein. Projektionseffekte führen zu einer großen Streuung der Ergebnisse, in Übereinstimmung mit den Beobachtungen, ohne die fundamentalen Unterschiede zwischen 1:1 und 3:1 Verschmelzungen aufzuheben. Der Einfluß der Bahngeometrie auf die resultierenden Ergebnisse wird diskutiert. Die Geschwindigkeitsverteilungen entlang der Sichtlinie für die simulierten Galaxien stimmt im allgemeinen nicht mit den Beobachtungen überein. Eine zusätzliche, künstlich eingefügte, ausgedehnte stellare Scheibenkomponente mit mindestens 15% der gesamten stellaren Masse kann eine Übereinstimmung mit den Beobachtungen herstellen. Daher muss eine Gaskomponente mit einer signifikanten Masse in den Vorgängergalaxien vorhanden gewesen sein, um die Entstehung von elliptischen Galaxien durch Verschmelzungen von Spiralgalaxien zu erklären.

Structure and Dynamics of Interacting Galaxies

According to the "merger hypothesis", elliptical galaxies form by mergers of spiral galaxies. To test this hypothesis, simulations of collisionless mergers between disk galaxies with different mass ratios and orbital geometries were performed. Every merger remnant was investigated with respect to its photometric and kinematic properties. The methods used to determine the characteristic properties were developed to resemble the methods used by observational astronomers. Therefore a self-consistent comparison between simulated data and observations was possible. 1:1 merger remnants are triaxial, rotate slowly, are supported by anisotropic velocity dispersions, have significant minor-axis rotation and show predominantly boxy iosphotes in good agreement with observations of bright, boxy, giant elliptical galaxies. 3:1 and 4:1 remnants are oblate isoptropic, fast rotators, show a small amount of minor-axis rotation and have disky isophotes in perfect agreement with observations of faint, disky, giant elliptical galaxies. 2:1 remnants show intermediate properties. Projection effects lead to a large spread in the data in good agreement with observations. They do not change the fundamental differences between 1:1 and 3:1 merger remnants. The effect of the merger geometry on the properties of the remnants is discussed. The shape of the LOSVD of the simulated remnants does in general not agree with observations. An additional stellar disk component with 15% of the total stellar mass and a scale length of the order of the effective radius, artificially added to the merger remnants, can solve this problem. The results lead to the conclusion that collisionless merging of disk galaxies cannot explain the formation of observed elliptical galaxies. The progenitor galaxies must have contained a significant amount of gas.

meiner Familie

Contents

I

Chapter 1

Introduction

Toomre & Toomre (1972) invented the idea that dynamically hot elliptical galaxies could originate from mergers of dynamically cold disk galaxies. This "merger hypothesis" has become one of the most popular formation scenarios for elliptical galaxies. Therefore the study of nearby interacting systems – if they evolve into elliptical galaxies at all – will help to illuminate the important mechanisms responsible for the observed properties of elliptical galaxies in general. In the local universe there are several candidates for merging gas rich disk galaxies using which the hypothesis can be tested. The "Antennae" galaxies (NGC 4038/39) are the classic example of a nearby system composed of two overlapping late-type spiral galaxies in an early phase of a merger. The long extended tails most likely have a tidal origin and are characteristic for gravitationally interacting spiral galaxies. The merger of the Antennae galaxies is accompanied by several bursts of star formation in the two nuclei and the surrounding spiral arms. The most intense burst, however, takes place in an off-nucleus region where the two galaxy disks overlap (Figure 1.1; Mirabel et al., 1998). Here the most massive star clusters in the Antennae form. They are not visible at optical wavelengths since this region is heavily obscured by dust. However, most of the energy from this region is emitted by dust which is heated by an intense starburst within giant molecular clouds. This emission can only be measured at infrared wavelengths. In addition, exploding supernovae in starburst regions heat the surrounding gas very effectively. These hot gas bubbles are emitting at X-ray wavelengths (see Figure 1.1).

The Antennae galaxies, at a distance of 20 Mpc, have a total infrared luminosity of $L_{ir} \approx 10^{11} L_{\odot}$ which is about five times its luminosity at optical wavelengths. Therefore the Antennae galaxies belong to the class of luminous infrared galaxies (LIRGs). At luminosities $L_{bol} \geq 10^{11}$, LIRGs become the dominant population of galaxies in the local universe (see Sanders & Mirabel, 1996). They emit more energy in the infrared $(5 - 500\mu m)$ than at all other wavelengths combined. At luminosities of $L_{ir} \geq 10^{12} L_{\odot}$ (ultra luminous infrared galaxies = ULIRGs) all sources are very gas and dust-rich interacting systems. A small percentage $(\approx 7\%)$ of ULIRGs can be considered to be fully relaxed systems with no signs of interaction, $\approx 22\%$ already completed the merger process and show no second nucleus, and $\approx 50\%$ of ULIRGs are still interacting, since both nuclei can be identified on the images (Rigopoulou et al., 1999). Clearly, the ULIRGs in the local neighborhood can not explain the formation of elliptical galaxies with an age of $5 - 10$ Gyrs or more. However, Hibbard & Vacca (1997) have shown that ULIRGs are the best local analogues of disturbed high redshift galaxies observed
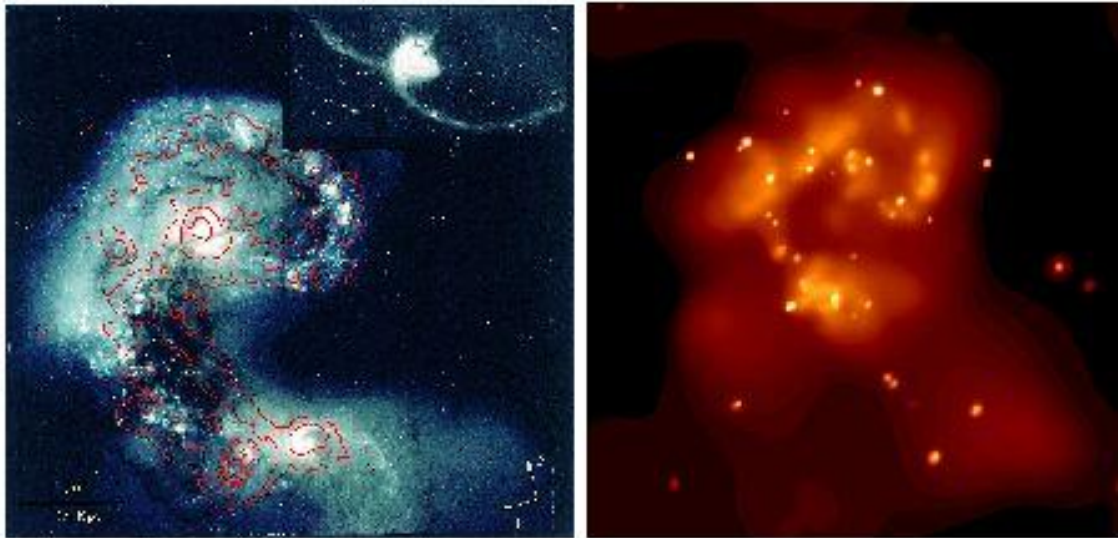
Figure 1.1: Different views of the Antennae galaxies. *Left*: The visible image in the upper right shows the extended tidal tails, typical for interacting galaxies. The central region as seen by HST (Hubble Space Telescope) exhibits bright spots of newly born stars and the two distinct nuclei. The infrared emission measured by ISO (Infrared Space Observatory) is indicated by the contour lines. The strongest emission comes from an obscured interarm region connecting the two nuclei (Mirabel et al., 1998). *Right*: The X-ray view of the Antennae galaxies measured by Chandra (Fabbiano et al., 2000, Astronomy Picture of the Day (APOD), August 18). Single point sources (black hole candidates and neutron stars) are surrounded by X-ray emitting gas heated by supernova explosions.

in the HDF or other deep fields with respect to their morphology, star formation rate, and spectral energy distribution. ULIRGs are therefore good candidates to represent a primary state in the formation of elliptical galaxy cores.

The question whether gas rich mergers evolve into systems that resemble present day elliptical galaxies is still not fully explored. The "Toomre Sequence" (Toomre, 1977; see also Toomre & Toomre, 1972) of the 11 foremost examples of ongoing mergers of late-type spiral galaxies selected from the New General Catalouge (NGC) provides considerable insight into the merger process. The optically selected sequence represents the proposed stages of merging disk galaxies. Early-stage mergers have well separated but distorted disk components (Antennae, Arp 295, NGC 4676, and others). Intermediate-stage mergers exhibit distinct nuclei in a common envelope of luminous material with clear signs of interaction as extended tidal tails (e.g. NGC 520). Late-stage mergers consist of a dynamically relaxed central part with tidal appendages emanating from a single nucleus (e.g. NGC 3921, NGC 7252, Arp 220; Figure 1.2; see Hibbard & van Gorkom, 1996).

A recent study of 3 late-stage mergers has shown that the luminosity profile in the case of NGC 3921 and NGC 7252 (see Figure 1.2) will evolve to an $r^{1/4}$ law, which is typical for
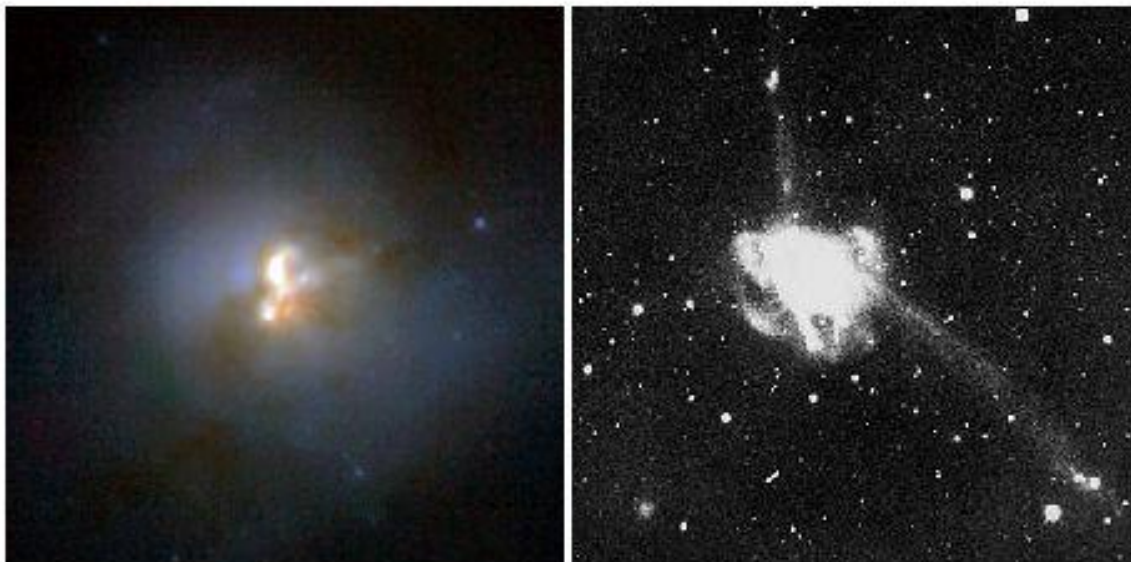
Figure 1.2: Late-stage mergers in the local universe. *Left*: Arp 200, the most luminous galaxy in the local universe (Thompson et al., 1997, APOD, June, 17). *Right*: NGC 7252.

elliptical galaxies. However, Arp 220 (Figure 1.2), which is the most luminous galaxy in the local universe and belongs to the class of ULIRGs, shows an excess of light in the central part. This excess of light is not a common feature among elliptical galaxies. It is found only in some cores of ellipticals. However, different processes like powerful expanding super-winds or massive starbursts with an IMF that is biased towards massive stars can lead to reduced central stellar densities when Arp 220 evolves with time. Observed physical processes taking place in interacting galaxies in the local universe are dominated by gas dynamics and star formation. The role of stellar dynamics, however, is difficult to estimate.

Dynamical modeling has demonstrated that large scale interactions are efficient means of driving central inflows of gas and therefore can trigger nuclear starbursts or AGNs as energy sources for the enormous infrared emission seen in ULIRGs (see e.g. Barnes & Hernquist, 1996). However, the detailed processes leading to a starburst are not well understood. Up to now, numerical simulations which include stellar dynamics, gas dynamics, star formation and its feedback were not able to reproduce all the observed features (Mihos & Hernquist, 1996; Barnes & Hernquist, 1996; see Hibbard & Yun, 1999). In particular, there are several questions that have to be addressed in detail. How much gas in total is needed to get the high densities observed in centers of elliptical galaxies? What is the influence of gas on the global dynamics of merger remnants? When, where, and how does the gas transform into stars? Where does the hot X-ray emitting gas, observed in massive giant elliptical galaxies, come from? Does gas accrete onto a central black hole? How does the existence of a black hole influence the dynamics of the remnant? What is the influence of magnetic fields? However, all these questions involve complicated physical processes that are either poorly understood theoretically – such as star formation in molecular clouds – or involve complicated physics and are very difficult to implement numerically, like magnetic fields or relativistic hydrodynamics.

There exists a lot of detailed information about central and global photometry, global kinematical properties and spatially resolved local kinematics of giant elliptical galaxies. This data can be compared with dynamical models of interacting galaxies. It is remarkable that even collisionless dynamical models which only involve gravitation have only been investigated to a small extent. In particular, it is not clear in how far collisionless mergers succeed or fail to explain the formation of elliptical galaxies by collisionless mergers of disk galaxies.

In this thesis we focus on the properties of purely collisionless merger models and compare them self-consistently with most of the available data of giant elliptical galaxies. We can thus test whether the merger scenario for collisionless mergers is successful. The investigations provide fundamental insights into the dominant processes controlling the structure and kinematics of interacting galaxies. Addressing several topics (like line-of sight velocity dispersions) in detail and focusing on the related basic questions, we build a fundamental basis for future investigations in the field of interacting galaxies.

The thesis is structured as follows. We review the most important observations of elliptical galaxies in general and the observational methods relevant for the investigations here in detail. This is accompanied by an overview of the numerical work published up until the time of the beginning of our investigations (Chapter 2.1). In Chapter 3 we discuss the numerical models, the simulation methods, and our merger survey. The results concerning the global structure of simulated remnants are given in Chapter 4, the results of our detailed investigation of the line-of-sight velocity distributions are given in Chapter 5 together with a dynamical model to explain the discrepancies in relation to observations. In Chapter 6 and 7 we conclude and give an outlook on future work.

Chapter 2

Elliptical galaxies

In this chapter we give an overview of the status regarding observations of elliptical galaxies and the numerical work done so far to understand their formation by merging of disk galaxies. We describe in great detail observational and numerical methods and results that are relevant for the investigations in this thesis. For aspects which are briefly discussed, we refer to a list of literature.

2.1 Observations of elliptical galaxies

In the traditional view, galaxies have been classified by their appearance on images. The most widely used classification scheme is the one invented by Hubble in the year 1936 in his book *The Realm of the Nebulae* (Hubble, 1936).
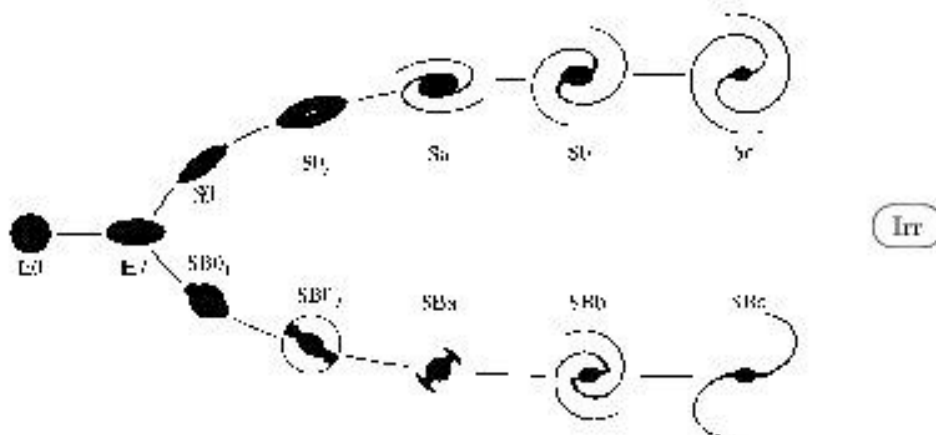

Figure 2.1: Classification of galaxies after E. P. Hubble

His tuning-fork diagram (Figure 2.1) suggested that galaxies evolve from the right hand side — the so called late-type galaxies which are spiral galaxies — to the left hand side, the region of elliptical galaxies. Elliptical galaxies have long been thought to be spheroidal dynamically relaxed stellar systems. They were believed to follow a universal surface brightness distribution (de Vaucouleurs, 1948), the so called de Vaucouleurs $r^{1/4}$-law

$$I(r) \quad = \quad I_e 10^{-3.33[(r/r_{\text{eff}})^{1/4}-1]} \tag{2.1}$$

5

$$= \; I_e \exp(-7.67[(r/r_{\text{eff}})^{1/4} - 1]). \tag{2.2}$$

The scale length r_{eff} is the effective radius and the factor 3.33 in equation (2.1) is chosen such that half of the total light of the galaxy is emitted inside r_{eff} assuming spherical symmetry for the galaxy image. I_e is the surface brightness at $r = r_{\text{eff}}$ (see Binney & Merrifield, 1998). The only parameter used for the classification of elliptical galaxies was their ellipticity. They can appear nearly round or have a rather elongated shape. The type of the elliptical is denoted by En where n is the ratio of the major and minor axis of the galaxy, a/b, by $n = (10 \times (1 - (b/a))$. The types range from nearly round E0 galaxies to elongated E6 ellipticals. No observed elliptical galaxy appears to be more elongated than E7. The flattening was believed to be caused by simple rotation.

It had also been recognized relatively early that most elliptical galaxies and S0s are found in galaxy clusters (e.g. Hubble & Humason, 1931). This suggests that the galaxy environment plays an important role for the morphological evolution of galaxies. Indeed Oemler (1974) found that regularly shaped and probably dynamically relaxed clusters contain more ellipticals (up to 40%) than unrelaxed clusters with a disturbed morphology (around 15%). Later on, Melnick & Sargent (1977) found a relation between the morphological type of individual galaxies and the distance from the cluster center: a morphology-radius relation. Nearly all elliptical and lenticular galaxies in regular clusters are concentrated in the cores of clusters while most of the spirals lie at larger distances from the cluster center. Detailed observations by Dressler (1980) suggest a well-defined relationship between the local density in clusters and the galaxy type, the morphology-density relation (see also Whitmore & Gilmore, 1991). Here the number of ellipticals increases with increasing local galaxy density whereas the number of spirals decreases. Postman & Geller (1984) extended the study of the morphology-density relation to poorer groups of galaxies and defined a single morphology-density relation which is valid over six orders of magnitude in density. It is still a matter of debate whether the morphology-radius relationship results from the morphology-density relation or vice versa. Whitmore et al. (1993) argue on the basis of Dressler's data that the distance of a galaxy from the cluster center is the more fundamental factor in determining the morphology of a galaxy. This is supported by the study of Sanroma & Salvador-Sole (1990) who showed that the radial variations in cluster properties are preserved if one smoothes out the substructure of a cluster. From all these investigations it is not clear whether the complex processes that dictate the morphology of early type galaxies are related to the properties of their immediate surroundings (local density) or their broader environment.

Starting with the advent of modern CCD cameras, detailed isophotal analysis of massive elliptical galaxies has become possible. It has been shown by several authors that the isophotes of elliptical galaxies deviate from perfect elliptical shapes and that their deviations correlate with fundamental physical parameters of the galaxies (Section 2.2). Furthermore, HST observations (see Faber et al., 1997) opened a window to the centers of ellipticals, revealing core properties that also correlate with isophotal deviations and other global parameters. It actually turned out that the deviation from isophotal shape could be a more fundamental parameter for the classification of ellipticals than their apparent ellipticity (Kormendy & Bender, 1996).

In the following two sections we review results from kinematical and photometric measure-

ments of giant elliptical galaxies. The cited literature contains relevant information related to this topic but it does not provide a complete overview of the properties of elliptical galaxies.
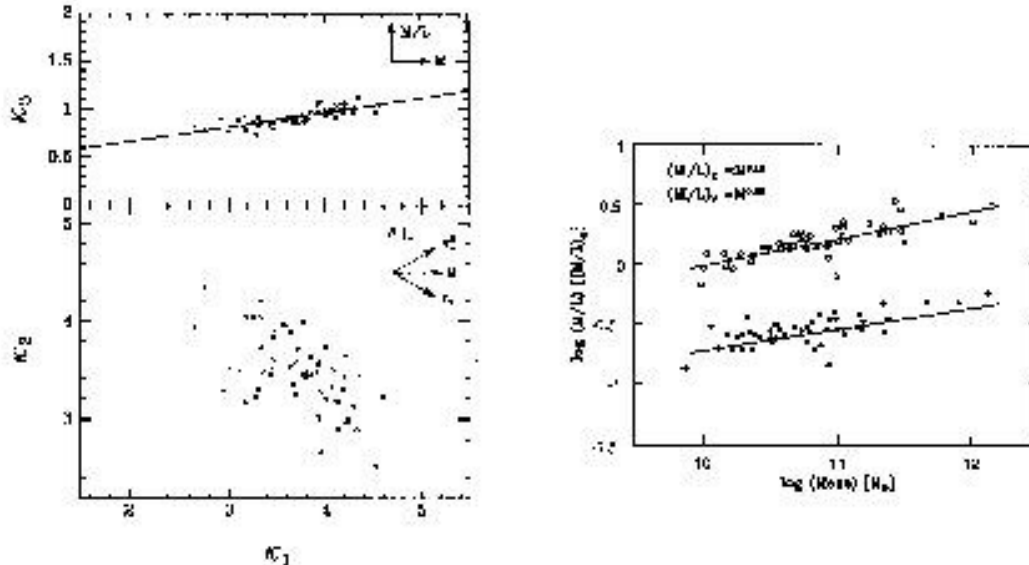

Figure 2.2: *Left*: The Fundamental Plane at visible wavelengths for Virgo and Coma ellipticals (Bender et al., 1992). *Right*: Tilt of the optical $(M/L))_V \propto M^{0.23}$ and near-infrared $(M/L))_K \propto M^{0.18}$ FP for Coma ellipticals (Mobasher et al., 1999).

For example, elliptical galaxies follow the Fundamental Plane (FP), a two-dimensional manifold in the three dimensional parameter space of the global parameters which are effective radius $r_{\rm eff}$, mean effective surface brightness $< \Sigma >_{\rm eff}$, and central velocity dispersion σ_0 (Djorgovski & Davis, 1987; Dressler et al., 1987; Kelson et al., 1997). Bender et al. (1992) used the following coordinate system to represent the Fundamental Plane:

$$\kappa_1 \equiv (\log \sigma_0^2 + \log r_{\rm eff})/\sqrt{s}, \qquad (2.3)$$

$$\kappa_2 \equiv (\log \sigma_0^2 + 2\log \Sigma_{\rm eff} - \log r_{\rm eff})/\sqrt{3}, \qquad (2.4)$$

$$\kappa_3 \equiv (\log \sigma_0^2 - \log \Sigma_{\rm eff} - \log r_{\rm eff})/\sqrt{6}. \qquad (2.5)$$

If we define the luminosity L and the mass M of a galaxy as $L = c_1 \Sigma_{\rm eff} r_{\rm eff}^2$ and $M = c_2 \sigma_0^2 r_{\rm eff}$ and c_1 and c_2 are structure constants, the effective radius can be written as $r_{\rm eff} = (c_1/c_2)(M/L)^{-1} \sigma_0^2 \Sigma_{\rm eff}^{-1}$. Then κ_1 is proportional to $\log(M)$, κ_3 is proportional to $\log(M/L)$, and κ_2 is proportional to $\log(M/L)\Sigma_{\rm eff}^3$. Therefore a possible way to represent the FP edge on is plotting κ_3 versus κ_1 which is M/L versus M. The tilt of the FP in visible wavelengths is 0.23 (see Figure 2.2). The FP seems to be independent of the environment (Jorgensen et al., 1996) and does in general also exist for S0s and dwarf ellipticals (Nieto et al., 1990; Bender et al., 1992; Saglia et al., 1993a). In addition to the optical, a FP can also be found in the infrared, however with a slightly different slope (Figure 2.2; Mobasher et al., 1999), and probably in the X-ray (Fukugita & Peebles, 1999). The biparametric nature of elliptical galaxies most probably is a consequence of the virial theorem and the fact that ellipticals have an almost homologous structure with a small and continuous variation of the mass-to-light ratios at a given luminosity (Bender et al., 1992; Pahre et al., 1998).

2.2   Correlations with isophotal shapes of elliptical galaxies

At the end of the 1980s it was shown that a large fraction of ellipticals exhibit small deviations from purely elliptical isophotes (Lauer, 1985; Carter, 1987; Jedrzejewski, 1987; Jedrzejewski et al., 1987; Bender et al., 1987; Bender, 1988b; Nieto et al., 1991b; Poulain et al., 1992; Nieto et al., 1994; see Kormendy & Djorgovski, 1989 for a review). The deviations can be measured by expanding the radial deviations $\Delta r_i = r(t_i) - r_E(t_i)$ between the radius of an isophote $r(t_i)$ and the best fitting elliptical isophote $r_E(t_i)$ in a Fourier series. Here the t_i are the equidistant polar angles from the origin to N isophote points. With $\Delta r_i = \Delta r(t_i)$, $r_i = r(t_i)$ and $r_{i,E} = r_E(t_i)$ the expansion becomes

$$\Delta r_i = r_i - r_{i,E} = \sum_{j=0}^{N-1} a_j \cos\left(\frac{2\pi i j}{N}\right) + b_j \sin\left(\frac{2\pi i j}{N}\right). \tag{2.6}$$

Coefficients with $j \leq 2$ characterize the position of the fitted ellipse relative to the measured isophote: a_0 and a_2 are the deviations from the long and short axis, a_1 and b_1 are the zero-point-offsets of the axes. The angle between the semi-major axis of the fitted ellipse with respect to the long axis of the isophotes is measured by b_2. All these coefficients are minimized by iteratively determining the best fitting ellipse. Coefficients with $j \geq 3$ describe deviations from the elliptical shape. In nearly all elliptical galaxies with significant deviations from perfectly elliptical isophotes, the fourth-order cosine coefficient a_4 dominates the Fourier spectrum. Figure 2.3 shows the effect of a non-zero a_4-coefficient. A positive value of a_4 corresponds to an elongated, pointed or disk-like shape (hereafter called *disky*) while a negative value of a_4 corresponds to an isophote with a box-like shape (hereafter called *boxy*). To get a scale free parameter for the isophotal shape it is convenient to measure isophote shapes by $a4 = a_4/a$ where a is the semi-major axis length of the best fitting elliptical isophote.
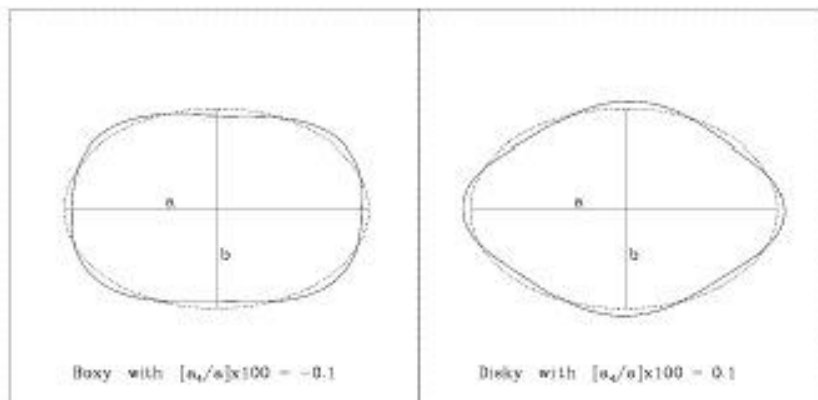

Figure 2.3: Illustration of a boxy ($a4 \times 100 = -0.1$) and a disky ($a4 \times 100 = -0.1$) isophotal shape compared to the corresponding ellipse (dashed). a and b is the long and short axis, respectively.

The first systematic investigation of a magnitude limited sample (brighter than $B_T = 12.4$ mag) of Northern bright elliptical galaxies was carried out by Bender et al. (1988) and Bender

et al. (1989). In order to assign a typical value $a4_{\text{eff}}$ to every elliptical galaxy indicating the characteristic isophotal shape around its half-light radius r_{eff}, the a_4/a values were averaged between r_s (seeing radius) and $1.5r_{\text{eff}}$ and multiplied by 100. They found that $\approx 1/3$ of all ellipticals show boxy isophotes, $\approx 1/3$ disky isophotes, and $\approx 1/3$ irregular isophotes where no characteristic $a4$-coefficient can be derived (Bender et al., 1989). Reasons for irregular isophotes can be a radial change from disky to boxy isophotes inside r_{eff}. This indicates a complicated internal structure, like tidal extensions (Nieto & Bender, 1989), non-axisymmetric, irregular deviations dominated by odd Fourier-coefficients or large-scale dust lanes (Moellenhoff et al., 1992) that prevent a reliable measurement.

To correlate the isophotal shapes of elliptical galaxies with other characteristic properties, Bender et al. (1988) defined a characteristic ellipticity ϵ_{eff} which is the maximum along the major axis or, in case of a continuous increase in ellipticity, the value at r_{eff}. The rotational support of a galaxy can be measured by the ratio of major-axis rotation v_{maj} at one effective radius and the central velocity dispersion σ_0, defined as the mean velocity dispersion between the center and $0.5r_{\text{eff}}$. Theoretical predictions for an oblate, isotropic body that is flattened by rotation lead to

$$(v_{\text{maj}}/\sigma_0)_{\text{theo}} = \sqrt{\epsilon/(1-\epsilon)}. \tag{2.7}$$

This formula is an approximation to the original formula derived by Binney (1978). Following Kormendy (1982) and Davies et al. (1983) one can then parametrize the amount of anisotropic velocity dispersions in elliptical galaxies by the anisotropy parameter $(v_{\text{maj}}/\sigma_0)^*$, defined as the ratio of the observed values for $(v_{\text{maj}}/\sigma_0)_{\text{obs}}$ and the theoretical expectation derived from the measured ellipticity ϵ_{obs} adopting equation (2.7):

$$(v_{\text{maj}}/\sigma_0)^* = \frac{(v_{\text{maj}}/\sigma_0)_{\text{obs}}}{(v_{\text{maj}}/\sigma_0)_{\text{theo}}} = \frac{(v_{\text{maj}}/\sigma_0)_{\text{obs}}}{\sqrt{\epsilon_{\text{obs}}/(1-\epsilon_{\text{obs}})}}. \tag{2.8}$$

An edge on, rotationally flattened stellar system with constant ellipticity will have a value of $(v_m/\sigma_0)^* = 1$. An inclination of the equatorial plane of the galaxy will cause $(v_m/\sigma_0)^* > 1$ (Binney et al., 1982). Since observed ellipticals do not show constant ellipticity along the major axis it can be assumed that $(v_m/\sigma_0)^* \leq 0.7$ indicates anisotropies in the velocity dispersions (Bender, 1988b). In addition to rotation along the major-axis, the amount of rotation along the minor axis can be parametrized by $\mu = (v_{\text{min}}/\sqrt{v_{\text{maj}}^2 + v_{\text{min}}^2})$ (Binney, 1985). Minor-axis rotation, in addition to isophotal twist, would then serve as a test for the triaxiality of the stellar body. Bender et al. (1988) investigated isophotal twist for elliptical galaxies and found that apparently round ellipticals show significantly larger twists than elongated galaxies (Figure 2.4). Nieto et al. (1992) conclude that a large number of ellipticals are intrinsically triaxial and contain bar-like structures in their centers.

Figure 2.5 shows the correlations between the isophotal shapes of elliptical galaxies and the discussed kinematical parameters. Along the major axis, the mean fractional radial departures from ellipses $a4_{\text{eff}}$ typically lie in the range of $-2 \leq a4_{\text{eff}} \leq 4$. Galaxies with higher values are generally classified as S0s. The distribution of $a4_{\text{eff}}$ versus ϵ_{eff} shows a characteristic V-shaped figure. Round ellipticals have smaller deviations from pure ellipses than more flattened ellipticals (Bender et al., 1989, Figure 2.5). Elongated ellipticals with $\epsilon \approx 0.4$ are
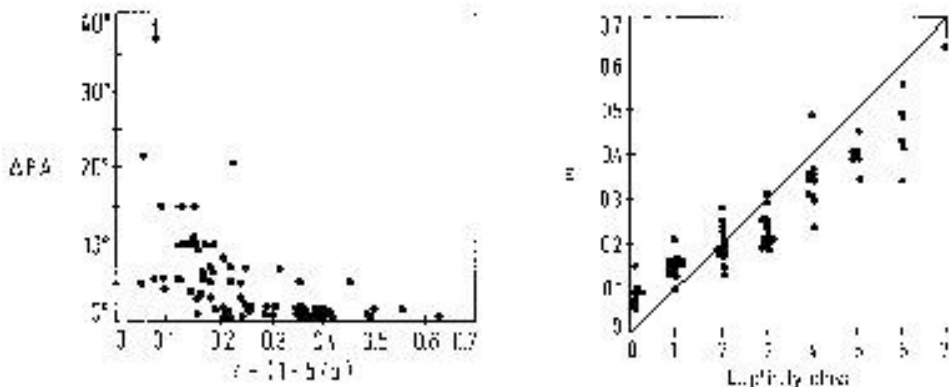
Figure 2.4: *Left*: Isophotal twists between the innermost isophote not affected by seeing and 1.5 r_{eff} as a function of ellipticity. *Right*: Ellipticities as a function of the ellipticity class according to RSA (A Revised Shapley-Ames Catalouge of Bright Galaxies, Sandage & Tamman (1981)). The discrepancy is due to the fact that the ellipticity classes were derived at larger radii than the ellipticities. The plots are reproduced from Bender et al. (1988).

either boxy or disky, while those with $\epsilon > 0.4$ are mostly disky.

Disky ellipticals follow the theoretical predictions for oblate isotropic rotators and almost all show $(v_{\text{maj}}/\sigma_0)^* > 0.7$ $(\log(v_{\text{maj}}/\sigma_0)^* > -0.15)$. They are therefore assumed to be flattened by rotation. In addition, they show only a small amount of minor-axis rotation. The disky appearance is supposed to be caused by embedded weak stellar disks (Carter, 1987; Nieto et al., 1988; Scorza & Bender, 1995; Scorza & Bender, 1990; Rix & White, 1990; Rix & White, 1992; Scorza et al., 1998) which could contribute up to 30% to the total light in the galaxy. Therefore, the disk-to-bulge ratios of disky elliptical galaxies overlap with those of S0-galaxies (Rix & White, 1990; Kormendy & Bender, 1996; Bender & Saglia, 1999).

The kinematics of boxy ellipticals is generally more complex than that of disky ellipticals. Rotation is less important here (top right panel in Figure 2.5). Although they show a variety of $(v_{\text{maj}}/\sigma)^*$ values, they include all of the galaxies with negligible rotation and are flattened due to velocity anisotropy $(v_{\text{maj}}/\sigma)^* < 0.7$. They are also notable for showing significant minor-axis rotation (lower right panel of Figure 2.5; Wagner et al., 1988; Franx et al., 1989). This leads to the conclusion that the stellar body of a typical boxy elliptical galaxy is triaxial. Occasionally, massive boxy ellipticals have kinematically distinct cores (Franx & Illingworth, 1988; Jedrzejewski & Schechter, 1988; Bender, 1988a; Franx et al., 1989; Forbes et al., 1994; Forbes et al., 1995; Forbes et al., 1996; Koprolin & Zeilinger, 2000). These cores inhibit flattened, rapidly rotating disk- or torus-like components dominating the light in the central few hundred parsecs of the galaxy (Bender, 1990a; Rix & White, 1992; Mehlert et al., 1998), but they contribute only a few percent to the total light of the galaxy. The fact that these cores are metal-enhanced shows that gas must have played an important role during the formation of the central regions (Bender & Surma, 1992; Davies et al., 1993; Bender, 1996; Davies, 1996).

As pointed out by Bender et al. (1989), the deviations from ellipses correlate with the blue luminosities L_B of ellipticals in the sense that galaxies with $\log L_{B,solar} \geq 11.1$ (corresponding to masses $\geq 10^{12} M_\odot$, see Figure 2.6 (f)) exhibit nearly elliptical or boxy isophotes (Figure
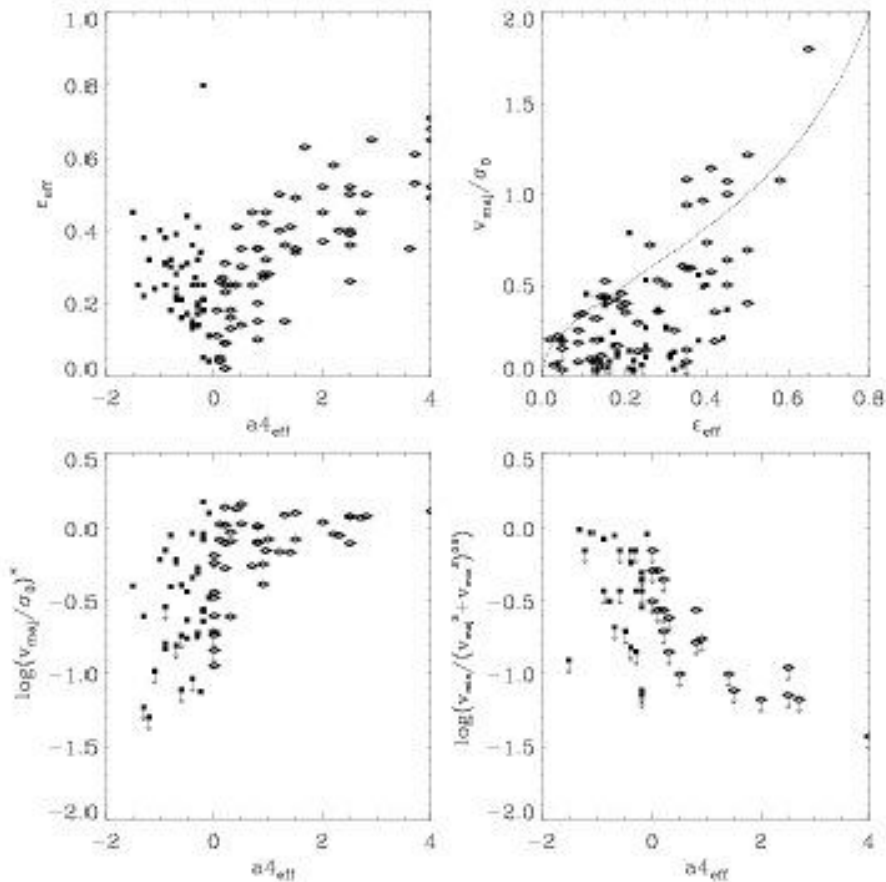
Figure 2.5: Kinematical and photometric properties of giant elliptical galaxies. The filled squares show the values for boxy ellipticals ($a4_{\mathrm{eff}} < 0$), while the open diamonds represent the values for disky ellipticals (all data provided by Ralf Bender). *Top left panel*: Ellipticity of the galaxies vs. $a4_{\mathrm{eff}}$. *Top right panel*: Rotational velocity over central velocity dispersion vs. ellipticity (upper limits are indicated by arrows). *Bottom left panel*: Anisotropy parameter $(v_{\mathrm{maj}}/\sigma_0)^*$ vs. $a4_{\mathrm{eff}}$. *Bottom right panel*: Amount of minor-axis rotation vs. $a4_{\mathrm{eff}}$, with v_{maj} and v_{min} being the maximum velocity along the major and the minor axes, respectively.

2.6 (e)). At the low luminosity end with $\log L_{B,solar} \leq 10.4$ (masses $\leq 10^{11} M_\odot$), almost all galaxies show disky isophotes. This is consistent with the finding of Davies et al. (1983) that faint ellipticals ($M_B > -20.5$) and bulges compare well with models for fast isotropic rotators (see also Illingworth, 1977; Davies & Illingworth, 1983). There are also long-known relations between radio activity and other properties of early-type galaxies (Bender et al., 1989). Radio activity predominantly occurs in luminous ellipticals (Heckman, 1983; Cordey, 1986).
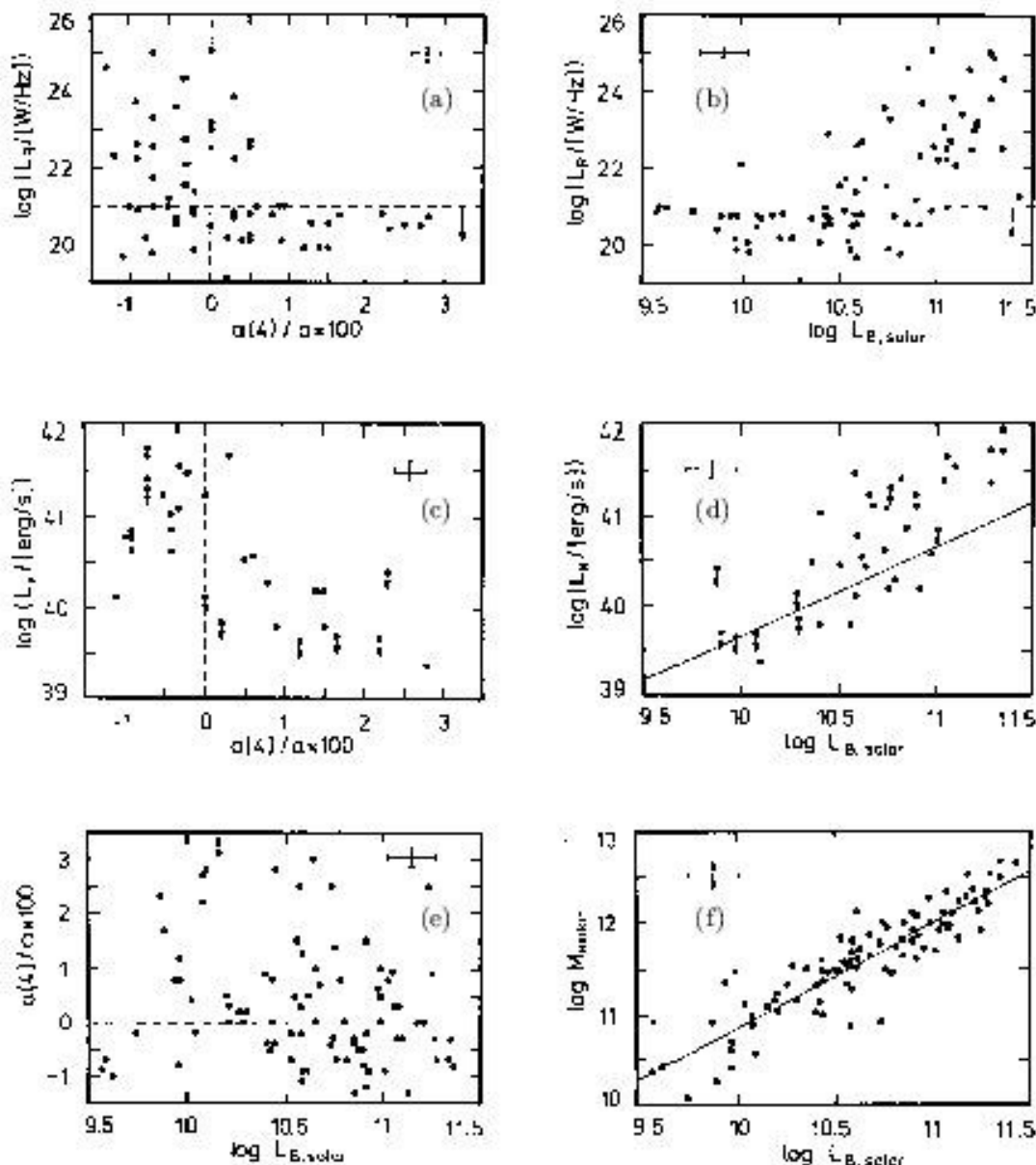
Figure 2.6: Summary of the main correlations for elliptical galaxies reproduced from the original paper of Bender et al. (1989). (a) Radio luminosities L_R at 1.4 GHz vs. the isophote shape parameter $a(4)/a \times 100$ (this is $a4_{\mathrm{eff}}$ in the notation used throughout this thesis). Error bars are calculated assuming a distance uncertainty of 15%. The arrow indicates that for $L_R \leq 10^{21}$ W/Hz the data points are either detections or upper limits. (b) Radio luminosities L_R at 1.4 GHz vs. the blue luminosities L_B. Error bars are calculated as in (a). (c) The X-ray luminosities L_X in the 0.5–4.5 kev band. The errors are calculated as in (a). The straight line indicates the assumed contribution of discrete X-ray sources. (d) X-ray luminosities against the shape parameter. (e) The isophote-shape parameter $a(4)/a$ vs. blue luminosities L_B. (f) Masses of the galaxies vs. their blue luminosities. The error in $\log M_{\mathrm{solar}}$ is only a lower limit.

Radio loud ellipticals are less flattened than ellipticals in general. Very powerful radio sources seem to be associated with disturbed galaxies. Many radio galaxies are triaxial in shape and radio-loud ellipticals have predominantly boxy isophotes, while disky ellipticals show no radio emission in general (Bender et al., 1987; see Figure 2.6 (a)).

Starting in the late 70s, observations using the *Einstein Observatory* (Giacconi et al., 1979) revealed significant X-ray emission from elliptical galaxies (Forman et al., 1979). The emission has been attributed to a hot interstellar medium (gaseous X-ray halos) because of the brightness of the emission as well as the softness of the spectrum (Forman et al., 1985; Canizares et al., 1987). For elliptical galaxies the amount of X-ray emission exceeds the emission from discrete stellar sources only in bright ($\log L_{B,solar} > 10.5$) ellipticals with boxy isophotes where the high X-ray luminosities ($\log L_x/[erg/s] > 40$) are consistent with emission from gaseous halos (see Figure 2.6 (c) and (d); Beuing et al., 1999). In contrast, faint and fast rotating ellipticals with disky isophotes do not show X-ray emission in excess of their discrete sources (Bender et al., 1989; Irwin & Sarazin, 1998; Hanlan & Bregman, 2000).
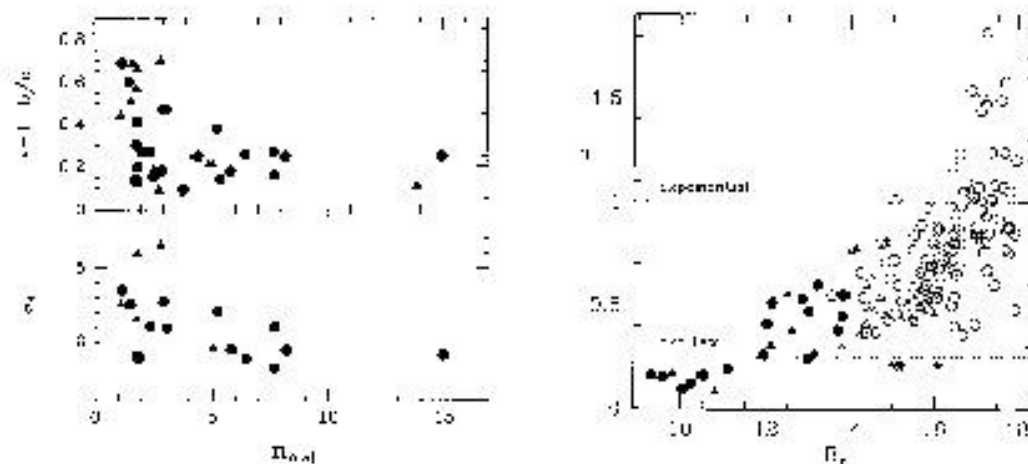

Figure 2.7: *Left:* Maximum ellipticity ϵ and characteristic isophotal shape a_4 versus Sersic-index n_{maj}. In our definition $n_{maj} = 1/n_{ser}$ (reproduced from Caon et al., 1993). *Right:* Sersic's shape parameter $n = n_{ser}$ versus total apparent blue magnitude for early type galaxies (open circles: dE, open triangles: dS0, filled circles: E, filled triangles: S0, compact M32-type Es: asterisk) in Virgo. The data for Es and S0s are taken from Caon et al. (1993). The plot is reproduced from Binggeli & Jerjen (1998).

Elliptical galaxies show deviations from a universal surface brightness distribution (Burkert, 1993; Hjorth & Madsen, 1995). Sersic (1968) proposed a generalized de Vaucouleurs law that can be written as

$$I(r) = I_0 e^{(-r)^{n_{ser}}}. \tag{2.9}$$

Introducing a scale radius r_e it can be rewritten as

$$I(r) = I_e \exp\left(-b_n[(r/r_e)^{n_{ser}} - 1]\right), \tag{2.10}$$

where I_e is the surface brightness at r_e. b_n can be chosen in such a way that the scale radius r_e is the radius encircling half of the total luminosity of the galaxy. For the special case of $n_{ser} = \frac{1}{4}$, equation (2.10) reduces to the de Vaucouleurs law, equation (2.2), with $b_n = 7.6692$. Caon et al. (1993) and D'Onofrio et al. (1994) used the Sersic law to fit the surface brightness profile of a sample of elliptical galaxies and S0s. They found that it provides a perfect fit with a very small scatter. The exponents lie in the range of $0.07 \leq n_{ser} \leq 0.6$ and correlate with the ellipticity ϵ_{eff} and the isophotal shape $a4_{eff}$ in the sense that boxy galaxies have smaller n_{ser} than disky galaxies and more elongated galaxies have higher values of n_{ser} (Caon et al., 1993). The exponent or profile shape parameter n_{ser} also correlates with global parameters as r_{eff} or the apparent blue magnitude of the galaxy (Caon et al., 1993; Binggeli & Jerjen, 1998; see Figure 2.7). Recent observations confirmed this trend for surface density profiles (Boselli et al., 2000; Gavazzi et al., 2000). Gavazzi et al. (2000) investigated the surface brightness profiles of 1157 galaxies with a model combining a de Vaucouleurs bulge and an exponential disk. They found that less than 50% of all elliptical galaxies show pure de Vaucouleurs profiles. The majority of E to Sb galaxies is best represented by a bulge + disk model. The fraction of exponential-dominated galaxies decreases with increasing luminosity and pure de Vaucouleurs profiles become dominant for galaxies with $L > 10^{10} L_\odot$.

Recent HST observations have shown that early type galaxies basically show two distinct core properties (Crane et al., 1993; Jaffe et al., 1994; Fisher et al., 1995; Lauer et al., 1995; Faber et al., 1997). Galaxies with cores (weak density cusps) show broken power-law surface brightness profiles that change slope significantly at a break radius r_b. Cores are found only in luminous ellipticals with $M_V \leq -22$ which can be associated with boxy, slowly rotating galaxies. A core galaxy is identified when the values of the inner logarithmic slope $\gamma = -\mathrm{d}(\log \Sigma)/\mathrm{d}(\log r)$ are smaller than 0.3. Low-luminosity elliptical galaxies ($M_V \geq -20.5$; mostly disky ellipticals) do not show a break in the profile slope and therefore do not show cores. Here the average slope is around $\gamma \simeq 0.8$ (Faber et al., 1997). At intermediate magnitudes ($-22 \leq M_V \leq -20.5$) core and power-law profiles coexist.

All these detailed observations show that elliptical galaxies can be subdivided into two groups with respect to their structural properties (Bender, 1988b; Bender et al., 1988; Kormendy & Bender, 1996; Bender & Saglia, 1999). Boxy ellipticals rotate slowly, have anisotropic velocity dispersions, have shallow cores, and show stronger than average radio and X-ray emission. Disky ellipticals rotate fast, are supposed to contain faint stellar disks, have power-law inner profiles and are radio and X-ray quiet. The distinct physical properties of disky and boxy elliptical galaxies point to the fact that both types of ellipticals could have different formation histories. It has been argued by Kormendy & Bender (1996) and Faber et al. (1997) that the observed stellar disks and the high density power law centers in disky ellipticals show that dissipation was essential for their formation. Since the angular momenta of the disks and bulges are parallel to each other it can be assumed that the disks were not randomly accreted after the elliptical has formed (Bender, 1993; Scorza & Bender, 1995). Boxy ellipticals with an even higher bulge to disk ratio show a stronger kinematical decoupling at their centers and no disk at all, indicating a merger origin that could also be responsible for irregular structures and X-ray emission from massive star formation. In this sense the Hubble sequence from S0s to massive ellipticals is a sequence of vanishing disks embedded in more prominent spheroidal bodies (Kormendy & Bender, 1996).

2.3 Line-of-sight velocity distributions (LOSVD)

The complete line-of-sight velocity distribution (LOSVD) of an elliptical galaxy at a given position contains all the accessible information about the kinematics of the system. The understanding of the dynamics of elliptical galaxies as given only by the first-order moment of the LOSVD — the bulk motion — and the second-order moment — the velocity dispersion (see Section 2.2) — therefore remains incomplete. Theoretical models have shown that it is not possible to constrain a model for an elliptical galaxy from the rotation velocity and the velocity dispersion alone. A large range of masses and central densities is consistent with a given velocity dispersion profile (Binney & Mamon, 1982; Dejonghe & Merritt, 1992). Theoretical investigations have indicated furthermore that more detailed information about higher-order moments of the LOSVD can help to break the degeneracy between anisotropy and mass (Dejonghe, 1987; Merrifield & Kent, 1990; Gerhard, 1991, 1993; Dejonghe & Merritt, 1992; Merritt, 1993; Dehnen & Gerhard, 1993, 1994; Evans, 1993, 1994; Cretton et al., 1999; Cretton et al., 2000b; Kronawitter et al., 2000). It is beyond the scope of this thesis to discuss these theoretical approaches. We refer the interested reader to the cited papers and references therein. New observational techniques and analytical tools (Bender, 1990b; Rix & White, 1992; van der Marel & Franx, 1993; Saha & Williams, 1994) provided the basis for measurements of LOSVD for real elliptical galaxies. Several observations have shown that the simple assumption of Gaussian LOSVDs has to be rejected. Many LOSVDs show asymmetries or are more or less peaked than a Gaussian (Bender, 1990b; Rix & White, 1992; Bender et al., 1994; Fisher, 1997; Mehlert et al., 2000; Koprolin & Zeilinger, 2000). To get a quantitative measurement for the deviations of the LOSVD from the Gaussian shape the velocity profile $P(v)$ can be parametrized in accordance with Gerhard (1993) and van der Marel & Franx (1993) by a Gaussian plus third- and fourth-order Gauss-Hermite functions (see Bender et al., 1994)

$$P(v) = \gamma \frac{\alpha(w)}{\sigma}[1 + h_3 H_3(w) + h_4 H_4(w)], \tag{2.11}$$

where $w = (v - v_{\text{fit}})/\sigma_{\text{fit}}$ and

$$\alpha(w) = \frac{1}{\sqrt{2\pi}} e^{-w^2/2} \tag{2.12}$$

$$H_3(w) = \frac{1}{\sqrt{6}}(2\sqrt{2}w^3 - 3\sqrt{2}w) \tag{2.13}$$

$$H_4(w) = \frac{1}{\sqrt{24}}(4w^4 - 12w^2 + 3). \tag{2.14}$$

H_3 and H_4 are the standard Hermite polynomials as defined by

$$\left(-\frac{d}{dx}\right)^j \alpha(x) = \sqrt{j!} H_j(x/\sqrt{2})\alpha(x). \tag{2.15}$$

The H_j form a set of orthogonal functions, $u_i = \exp(-w^2/2) \times H_i(w)$ are the Gauss-Hermite basis functions, and h_3 and h_4 are their amplitudes which represent the skewness and the kurtosis of the velocity profile, respectively. Note that the skewness/kurtosis and h_3/h_4 are not identical. The skewness and kurtosis are the normalized third- and fourth-order moments of the LOSVD and are more susceptible to the wings of the line profile which are ill-constrained by the observations (see van der Marel & Franx, 1993). γ is a normalization constant. Since

the observed LOSVDs are not Gaussian, the fit parameters v_{fit} and σ_{fit} correspond only to the first order to the real first (v_{rot}) and second (σ) moment of the velocity distribution (differences of up to 15%, see Bender et al., 1994; Magorrian & Binney, 1994). For $h_3 = 0$ and $h_4 = 0$ the resulting velocity profile is a Gaussian. For asymmetric profiles with the prograde (leading) wing steeper than the retrograde (trailing) one, h_3 and v_{fit} have opposite signs. This corresponds to a negative h_3 as defined by observers (van der Marel & Franx, 1993; Bender et al., 1994; Fisher, 1997). When v_{fit} and h_3 have the same sign, the leading wing is broad and the trailing wing is narrow. LOSVDs with $h_4 > 0$ have a 'triangular' or peaked shape, here the distribution's peak is narrow with broad wings. Flat-top LOSVDs have $h_4 < 0$ where the peak is broad and the wings are narrow. Figure 2.8 shows a Gaussian and the corresponding Gauss-Hermite functions of third and fourth order with amplitudes of 10% of the Gaussian.
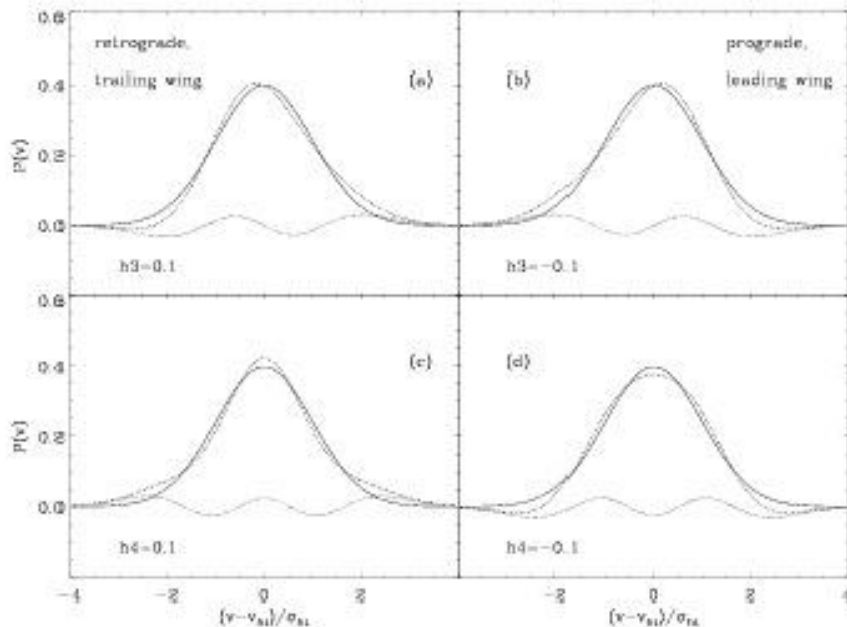

Figure 2.8: (a) Shows a Gaussian (full line), the third-order Gauss-Hermite basis function with the amplitude $h_3 = 0.1$ (dotted line) and the sum of the two (dashed line, see equation 2.11). In this case the retrograde wing ($v < v_{fit}$) is steeper than the prograde one. (b) Same as in (a) but with $h_3 = -0.1$. In this case the prograde wing is steeper than the retrograde wing. This is what is observed in elliptical galaxies to radii $\approx r_{eff}$ (Bender et al., 1994). (c) Shows a Gaussian (full line), the fourth-order Gauss-Hermite basis function with the amplitude $h_4 = 0.1$ (dotted line) and the sum of the two (dashed line). The resulting shape is peaked at the center with broad wings. (d) Same as (c) but with $h_4 = -0.1$. This produces a flat-top shape.

In general there is no reason why collisionless systems should have perfect Gaussian velocity distributions. There could be several origins for deviations from a perfect Gaussian shape. For example the superposition of a dynamically hot bulge component and a cold, fast rotating disk

would result in an asymmetric or even bimodal LOSVD which is characterized by a non-zero h_3 that has the opposite sign of v (Bender, 1990b; Rix & White, 1992; Bender et al., 1994). Theoretical predictions for LOSVDs of oblate anisotropic models indicate a positive value for h_4 resulting in a distribution that is more peaked than a Gaussian (Dehnen & Gerhard, 1993; Gerhard, 1993).
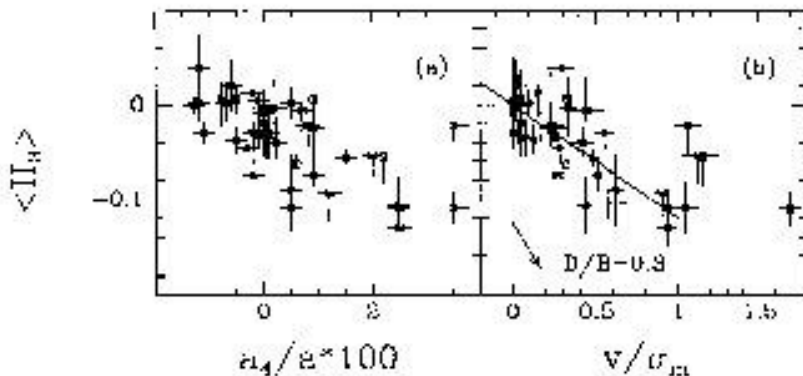

Figure 2.9: (a) The correlation between the global parameters $< H_3 >$ ($h3_{eff}$ in our notation) and $a_4/a * 100$ ($a4_{eff}$ in our notation). Filled squares represent boxy ellipticals, open squares are disky objects. Single sided error bars indicate upper limits. (b) The correlation between $< H_3 >$ and v/σ_0 (v_{maj}/σ_0 in our notation). Symbols are the same as in (a). The arrow indicates how the addition of a cold disk component with a disk-to-bulge ratio of 0.3 would move a point from the mean relation (see equation (2.16) shown by the straight line (see Bender et al. (1994) for details). The figure is reproduced from Bender et al. (1994).

Using a procedure similar to the definition for the isophotal parameter $a4_{eff}$ (Section 2.2) Bender et al. (1994) derived characteristic values $h3_{eff}$ and $h4_{eff}$ ($< H_3 >$ and $< H_4 >$ in their notation) by averaging the values of h_3 and h_4 up to one r_{eff} excluding the central part of the galaxy. These characteristic values show significant correlations with $a4_{eff}$ and v_{maj}/σ_0. As shown in Figure (2.9), $< H_3 >$ correlates with v_{maj}/σ_0 in the sense that $< H_3 >$ becomes more negative with increasing v_{maj}/σ_0. The same correlation is observed between $< H_3 >$ and $a4_{eff}$. Bender et al. (1994) find that a correlation between $< H_3 >$ and v_{maj}/σ_0 can be described by

$$h3_{eff} = < H_3 > = -0.12 \times v_{maj}/\sigma_0. \qquad (2.16)$$

They note that in their sample containing mostly ellipticals in low density environments and some cluster ellipticals, no galaxy shows significantly positive values for $h3_{eff}$. Recent observations of cluster ellipticals show that the correlation also holds for ellipticals in the Coma cluster (Ralf Bender, private communication; Mehlert et al., 2000) and therefore seems to be independent of the environment. Bender et al. (1994) conclude that *if rotation is present, the prograde wing of the LOSVD is always steeper than the retrograde wing.* They also investigated the local correlation between h_3 and v/σ (see also van der Marel et al., 1994). Here they find a steeper correlation than the global one for small values of v/σ
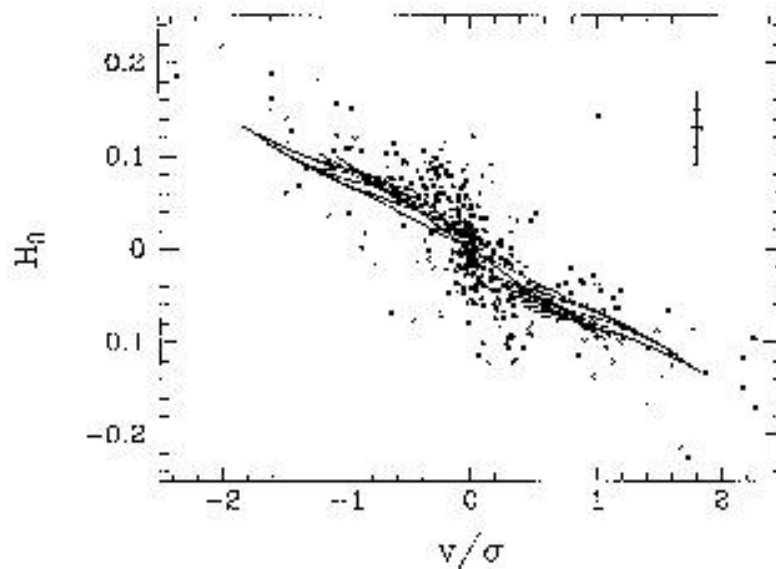
Figure 2.10: Local correlation between H_3 and v/σ as measured by Bender et al. (1994). Typical error bars are plotted in the upper right. Open squares represent disky ellipticals, filled squares all other ellipticals. The lines show model predictions for two-integral models (Dehnen & Gerhard, 1993, 1994) of different flattening and inclination. This figure is reproduced from Bender et al. (1994).

including all boxy ellipticals and a flatter one for large v/σ made up by disky ellipticals alone (see Figure 2.10). $h4_{\mathrm{eff}}$ hardly correlates with any of the other parameters (see Bender et al. (1994) for details).

2.4 Numerical simulations of interacting galaxies

In the 1970s, Toomre & Toomre (1972) and later on Toomre (1977) proposed on the basis of experiments with a restricted 3-body method that early type galaxies could originate from mergers of disk galaxies. Almost at the same time Ostriker & Tremaine (1975) suggested that dynamical friction and repeated mergers and accretion of galaxies near the centers of galaxy clusters could be responsible for the formation of massive cD galaxies. This *merger hypothesis* has become one of the most popular models for the formation of elliptical galaxies. The merger hypothesis has been tested in great detail by many authors. White (1978, 1979) investigated mergers of spherical galaxies, Gerhard (1981), Farouki & Shapiro (1982) and, later on, Negroponte & White (1983) were among the first who performed self-consistent merger simulations of disk galaxies. However, the resolution of these simulations was very low and the number of particles representing each galaxy did not exceed 500. The situation changed with the advent of Treecodes in the late 1980s (Appel, 1985; Jernigan, 1985; Barnes, 1986; Hernquist, 1987; Jernigan & Porter, 1989). The method allowed simulations without restrictions to the geometry of the problem and reduced the computational effort to simulate a system with N particles from $\mathcal{O}N^2$ to $\mathcal{O}(N \log N)$. Using this powerful tool, the merger hypothesis has been investigated by numerous authors in great detail (see Barnes & Hernquist (1992) for a review). Using the Treecode, the first fully self-consistent mergers of two equal mass, rotationally supported disk galaxies embedded in dark halos were performed by Barnes (1988) and Hernquist (1992). They found that mergers indeed lead to slowly rotating, pressure supported anisotropic systems. The remnants were triaxial and showed both disky and boxy isodensity contours in projection (Hernquist, 1992). In addition it was found, in contradiction to the common belief, that mergers of equal mass galaxies lead to the formation of loops and shells around the remnants in good agreement with observations of shells around elliptical galaxies (Hernquist & Spergel, 1992). The surface density of the remnants simulated by Barnes (1988) contained a central bulge component and followed an $r^{1/4}$ profile up to the central resolution limit, determined by the gravitational softening length. The half-mass radius of the system was slightly larger than the scale length of the initial disk. The pure disk mergers performed by Hernquist (1992) were too diffuse at the center, leading to strong deviations from the observed de Vaucouleurs profile. This result can be explained by limited phase space densities at the centers of observed disk galaxies that are in disagreement with the high phase space densities at the centers of elliptical galaxies and bulges (Carlberg, 1986; Wyse, 1998). Subsequent investigations by Hernquist et al. (1993b) showed that mergers of progenitors with massive bulge components (25% – 30% of the disk mass) could resolve this problem leading to core radii and surface brightness profiles that are in excellent agreement with observations. This result is expected since the mergers already start with galaxies that contain elliptical like components and therefore dissipation may not be needed to satisfy phase space constraints. Hernquist (1993a) and, subsequently, Heyl et al. (1994) and Steinmetz & Buchner (1995) investigated departures from pure ellipses in their equal mass merger remnants. However, Hernquist (1993a) did not investigate the shape qualitatively. Heyl et al. (1994) created false CCD images of their remnants and used the IRAF implementation of Jedrzejewski's ellipse fitting software (Jedrzejewski et al., 1987). Steinmetz & Buchner (1995) used MIDAS and the fitting procedure invented by Bender et al. (1988). Both found disky and boxy departures from pure ellipses that have the same magnitudes as in observed elliptical galaxies, depending on the viewing angle. Steinmetz & Buchner (1995) found predominantly boxy projections for their remnants but did not include a bulge component in their progenitor

galaxies. These results seem to be in contradiction with the observations. Since disky and boxy ellipticals have different radio and X-ray properties (see Chapter 2.2) that should not depend on their viewing angle, their isophotes should not change as a result of projection effects.

However, in agreement with observations of boxy ellipticals Barnes (1992) and Heyl et al. (1996) also found misalignments between the spin and the minor axis in major merger remnants that seemed to be larger than observed (Franx et al., 1991). Heyl et al. (1996) also investigated moments of the LOSVD inside 0.5 $r_{\rm eff}$ of their remnants. They found a significant amount of skewness but did not investigate the sign or the correlation with radius.

It has been argued by Kormendy & Bender (1996), Faber et al. (1997) and Rix et al. (1999) that gaseous mergers lead to distinct inner gaseous disks in the merger remnants which subsequently turn into stars, generating disky isophotes and strong rotational support in the outer regions. In contrast, boxy ellipticals would form from purely dissipationless mergers. This idea has theoretically been addressed in detail by Bekki & Shioya (1997) and Bekki (1998) and recently by Springel (2000). Bekki & Shioya (1997) simulated mergers including gaseous dissipation and star formation. They found that the rapidity of gas consumption affects the isophotal shapes. Secular star formation however leads to final density profiles which deviate significantly from the observed $r^{1/4}$-profiles in radial regimes where all ellipticals show almost perfect de Vaucouleurs laws (Burkert, 1993). These calculations and models of Mihos & Hernquist (1996) demonstrate that the effect of gas and star formation changes the structure of merger remnants as such a dissipative component would most likely lead to strong deviations from the $r^{1/4}$-profiles which seems to be a result of dissipationless, violent relaxation processes. Nevertheless the observations of metal enhanced, decoupled and rapidly spinning disk-like cores (see Chapter 2.1; Bender & Surma, 1992; Davies et al., 1993; Bender & Davies, 1996) show that even in boxy ellipticals gas must have been present. Numerical simulations show that these features would result naturally from gas infall during the merger process (Barnes & Hernquist, 1996; Mihos & Hernquist, 1996). The influence of gas on the global structure of elliptical galaxies is not well understood as it is sensitive to uncertain details about the star formation process (Barnes & Hernquist, 1996).

Recently, Barnes (1998) presented a set of 1:1 and 3:1 merger simulations. He proposed a scenario for the origin of rapidly rotating elliptical galaxies that does not require dissipation and showed that such systems could result from a merger of a large disk galaxy with a smaller companion. In addition, the edge-on view shows a disky morphology. However, he did not investigate projection effects or even quantify the isophotal deviations in detail. According to this model, boxy and disky elliptical galaxies should result from equal- and unequal-mass mergers, respectively (Naab et al., 1999). Bendo & Barnes (2000) took the sample of Barnes (1998) and investigated rotational support and the line-of-sight velocity distributions along the major axis of the remnant and parametrized it with Gauss-Hermite polynomials. They found only zero or positive values for h_3 but again they did not take projection effects into account. In addition, they compared the rotational support of the remnants with the observations of Rix et al. (1999) and found good agreement (see Section 4.1 for our view of this topic).

Chapter 3

Simulations of galaxy interactions

3.1 Numerical methods

In addition to theoretical and experimental physics, computational physics has become a powerful tool for answering relevant physical questions. The increase of computer speed and the development of special hardware and software have opened the opportunity to model a whole system directly. The data analysis following such a virtual experiment is then carried out in much the same way as an observer would do with data from a real observation. The N-body simulation technique has become one of the most powerful tools for the study of astronomical systems of gravitationally interacting subunits: the solar system, star clusters, galaxies, clusters of galaxies and the large scale structure of the universe.

3.1.1 The GRAPE-3/GRAPE-5 system

The simplest approach computing the gravitational interaction between particles is direct summation. Here the force exerted on a particle is given by adding up the contributions from all other particles in the simulation. This offers a large, controllable dynamic range in spatial resolution. In addition, there exists no limitation with respect to the geometry of the problem. The big disadvantage of this method is that it requires a computer processing power that scales with $\mathcal{O}(N^2)$ for the force calculation while all other actions (like time integration) scale with $\mathcal{O}(N)$. To increase the speed of a simulation it is in general possible to follow two different paths. One can use highly specialized algorithms (e.g. Treecodes) which can be used in combination with general-purpose computers or parallel supercomputers. They reduce the number of required inter-particle force calculations to $\mathcal{O}(N \log N)$ but contain approximations with respect to force contributions of distant particles. A different approach is to realize the time consuming force calculations directly in external hardware which can be connected to a standard workstation.

This approach has been realized by the family of GRAPE (GRAvity PipelinE) special-purpose hardware devices (Sugimoto et al., 1990; Makino & Taiji, 1998). They have a specially designed, pipelined and highly parallelized architecture to accelerate the computation of gravitational many-body interactions. Figure 3.1 shows the basic structure of a GRAPE system. The GRAPE hardware is connected to a host workstation. The host computer sends positions and masses of all particles of a simulation to the GRAPE system. Then GRAPE calculates the gravitational interaction (which is the $\mathcal{O}(N^2)$ part) between the particles and sends the
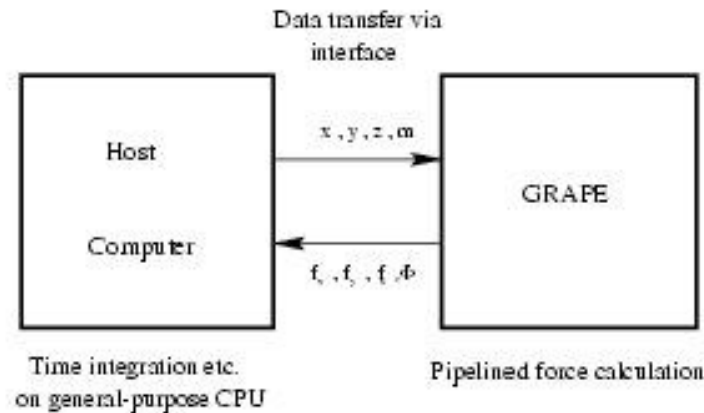
Figure 3.1: Basic structure of GRAPE systems.

resulting forces back to the host computer. In addition, GRAPE delivers a list of neighbors inside a given radius around a particle. This is especially important for the use of GRAPE in combination with Smoothed Particle Hydrodynamics (SPH). All other calculations like time integration and data diagnostics can then be performed on the host computer.
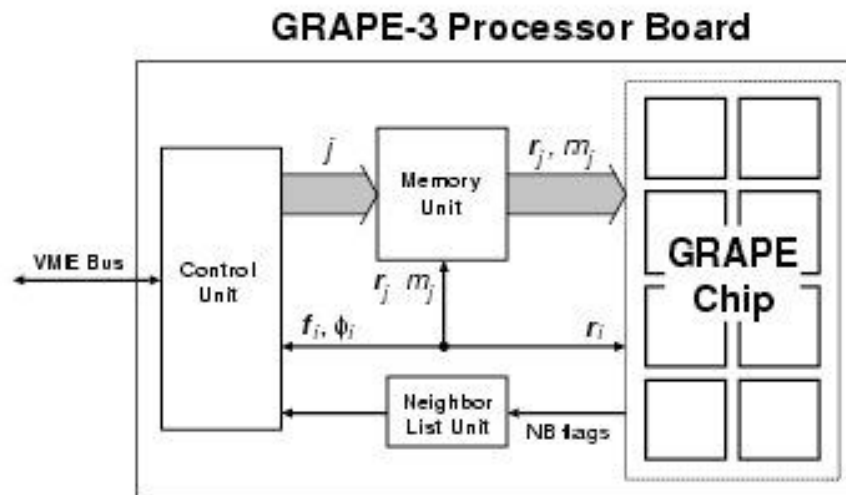

Figure 3.2: Block diagram of the GRAPE-3 processor board (reproduced from Kawai et al. (2000) with permission of Atsushi Kawai).

GRAPE-3 was the first GRAPE system using multiple pipelines for the force calculation (Okumura et al., 1993). Figure 3.2 shows the architecture of a GRAPE-3 board. This board has 8 pipelines and every pipeline is integrated into one G3 chip (Figure 3.3). Every pipeline

can calculate one pairwise gravitational force during each clock cycle according to

$$\mathbf{F}_i = -\sum_{j \neq i} \frac{Gm_i(\mathbf{x}_i - \mathbf{x}_j)}{(|\mathbf{x}_i - \mathbf{x}_j|^2 + \epsilon^2)^{3/2}}, \tag{3.1}$$

where $\mathbf{x}_i$ and $\mathbf{x}_j$ are the mass and position of the i-th and j-th particle, G is the gravitational constant and ϵ is the softening parameter to suppress the divergence of the forces at $x_i = x_j$.
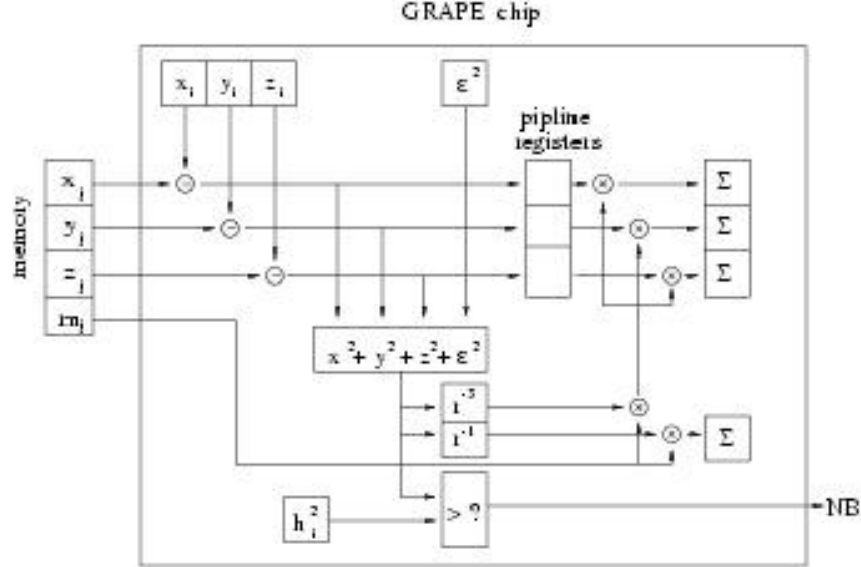

Figure 3.3: Block diagram of the G3 chip (see Okumura et al. (1993)).

The peak performance of one chip is 0.6 Gflops at a clock cycle of 20 MHz (Okumura et al., 1993; see also Kawai et al., 2000). This corresponds to 30 floating-point operations for the calculation of one gravitational interaction between two particles (Okumura et al., 1993). One GRAPE-3AF board has 8 GRAPE chips in total, resulting in a peak performance of 4.8 Gflops. The round-off error of GRAPE-3 has two main origins. One is the error that is generated when the positions are converted from floating-point format to fixed-point format. GRAPE-3 performs the subtraction $x_i - x_j$ in 20-bit fixed-point format. For the pairwise force calculation the round-off error due to this is $\mathcal{O}(10^{-3}/(x_i - x_j))$. This means that the error is larger for nearby pairs (Okumura et al., 1993). This error results just from the calculation of a distance between two particles. Another source of round-off error is the calculation of the force from the given distance $x_i - x_j$. This part is implemented in 13 bit unsigned logarithmic format with an error of about 1 percent. It has been tested by Okumura et al. (1993) that the round-off errors with respect to their size and their sign are independent of the errors resulting from other calculations performed on the board. In addition, the round-off errors have no offset. This results in an average mean error of 0. Taking this into account, the relative error of a pairwise force calculation is of the order of 2% which is precise enough to perform simulations of collisionless systems like galaxies (Hernquist et al., 1993a; Athanassoula et al., 1998, see Hernquist & Barnes, 1990 for a comparison between different N-body algorithms). The GRAPE-3AF cluster at the MPIA in Heidelberg — which is used for the simulations

presented in this thesis — consists of 10 boards in total. We grouped the boards into several subsystems. The fastest consists of three boards which work in parallel, occupying 3 slots in a Solflower SFVME Sbus/VMEbus interface unit with which it is linked to an ULTRA 2 (Sbus) host workstation. The peak performance of this GRAPE-3 system is $\approx$ 15 Gflops.

Since the beginning of summer 1999, GRAPE-5, the successor of GRAPE-3, has been on the market (Kawai et al., 2000). The GRAPE-5 board is connected to a PCI Host Interface Board (PHIB; Kawai et al., 1997) that can be connected to a general-purpose host computer. The connection is realized via Hlink (see Makino et al. (1997) for details of the implementation) which controls the data transfer between the GRAPE-5 and the PHIB (Figure 3.4). Every
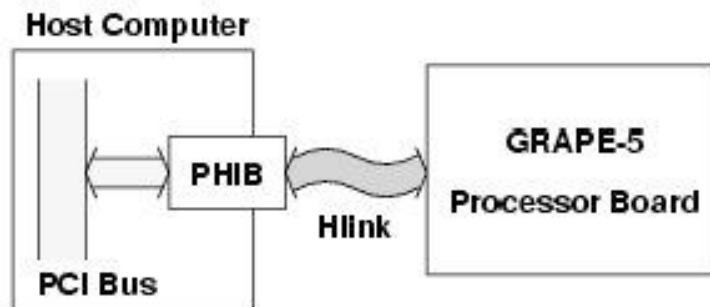
Figure 3.4: Basic structure of the GRAPE-5 system.

GRAPE-5 system consists of a GRAPE-5 processor board hosting eight G5 chips, a particle index unit, a memory unit that stores 131072 particles at one time, a neighbor list unit, and an on-board interface unit (Figure 3.5). The G5 chip itself hosts two real pipeline units which calculate the gravitational forces and an I/O unit which handles the data transfer between the pipeline unit and the external I/O port (Figure 3.6).

The G5 chip works with the *virtual multiple pipeline* architecture (Makino et al., 1993) where one real pipeline acts as multiple virtual pipelines at lower speed. The implementation on the G5 chip has two real pipeline units and six virtual pipelines per real pipeline unit. This results in 12 virtual pipelines in total per chip. The chip calculates two pairwise gravitational interactions per clock cycle at a clock speed of 80 MHz. This translates to 1.6×10^8 interactions per second or 4.8 Gflops if one assumes 30 floating-point operations for the calculation of the gravitational force between two particles. Thus the peak speed of a board with eight G5 chips is 38.4 Gflops. Therefore the G5 chip is 8 times faster than its predecessor G3. In addition, the communication speed is increased by a factor of 10 and the accuracy of the force calculation is increased to $\approx$ 0.2% (this is ten times more accurate than G3). Therefore GRAPE-5 is one of the fastest (and cheapest) available computers for the calculation of gravitational interactions (Gordon Bell Prize Winner 1999).

The GRAPE-5 system at the MPIA in Heidelberg consists of two GRAPE-5 boards that are used in parallel. The boards are connected to a Dec Alpha 20 SE double processor (500Mhz) workstation. The peak performance of this GRAPE-5 system is 76.8 Gflops.
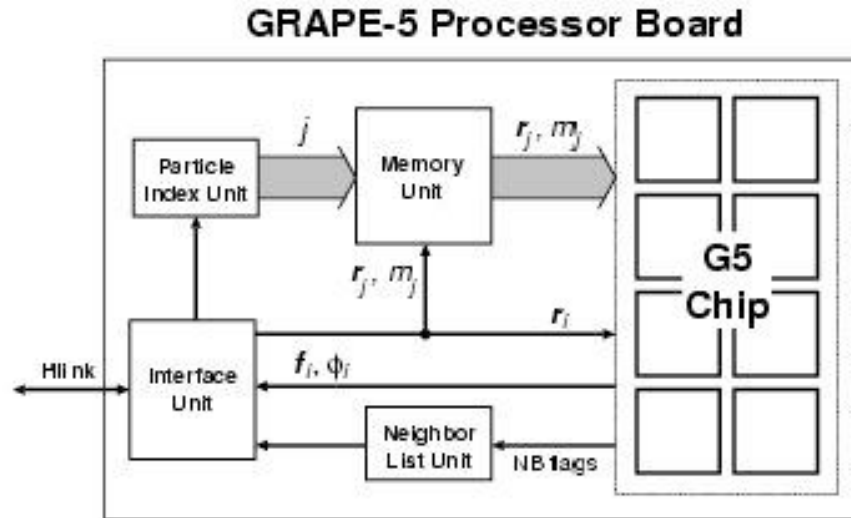
GRAPE-5 Processor Board

Figure 3.5: Block diagram of the GRAPE-5 processor board (reproduced from Kawai et al. (2000) with permission of Atsushi Kawai).
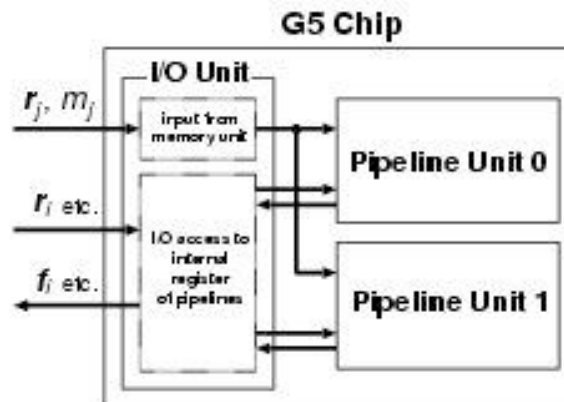
G5 Chip

Figure 3.6: Block diagram of the GRAPE-5 processor chip (G5 chip).

3.1.2 Time integration

In N-body simulations the particles move according to the Newtonian equations of motion

$$\frac{d\mathbf{x}}{dt} = \mathbf{v}$$
$$m\frac{d\mathbf{v}}{dt} = \mathbf{F}. \tag{3.2}$$

The functional form of $\mathbf{F}$ depends on the forces that are necessary for the simulations. For N-body simulations this reduces to the gravitational forces. To integrate this set of equations numerically it is necessary to replace them by linear algebraic relationships. The continuous

functions $\mathbf{x}$ and $\mathbf{v}$ are replaced by values at discrete time intervals. The most commonly used discretization for N-body simulations is the *leapfrog* scheme or Verlet method (see Hockney & Eastwood, 1981). It is the standard way of integrating the equations of motion of interacting particles whose interactions do not explicitly depend on velocity, like stellar dynamics. It has been used by a wide variety of authors investigating different problems (Barnes, 1988; Hernquist & Quinn, 1988, Barnes, 1988; Barnes & Hernquist, 1992; Hernquist et al., 1993a; Barnes & Hernquist, 1996; Velazquez & White, 1999 and many others). In this scheme the discretization of the equations (3.2) is realized by

$$
\begin{aligned}
\mathbf{x}^{(n+1)} &= \mathbf{x}^{(n)} + \mathbf{v}^{(n+\frac{1}{2})}\Delta t \\
\mathbf{v}^{(n+\frac{1}{2})} &= \mathbf{v}^{(n-\frac{1}{2})} + \frac{F(\mathbf{x}^{(n)})}{m}\Delta t.
\end{aligned}
\tag{3.3}
$$

Here Δt is the time step and the superscript n is the time level $t = n\Delta t$. This scheme is consistent in the sense that for $\Delta t \to 0$ the discretization (3.3) tends towards the continuous equations (3.2). Another desired consistency property is that the discrete approximations and the continuous equations have the same time symmetry. The Newtonian equations of motion are time-reversible, i.e., if a particle is integrated forwards in time on a trajectory and the time arrow is reversed, the particle will follow the same trajectory backwards returning to its starting point. Time reversible discretizations are obtained by time centered difference approximations. In the equations (3.3) the difference $(x^{(n+1)} - x^{(n)})$ is centered about $t^{(n+\frac{1}{2})}$ and the difference $(v^{(n+\frac{1}{2})} - v^{(n-\frac{1}{2})})$ is centered on $t^{(n)}$. The accuracy of the discretization scheme is given by round-off errors in the computer and truncation errors caused by representing the continuous variables by a discrete set of values. For stable integration schemes, round-off errors are smaller than truncation errors and can be neglected. Truncation errors can be seen as the difference between the differential equations and their algebraic approximations. The measure of the smallness of truncation errors is then given by the order p of the difference scheme, where the error is $\propto (\Delta t)^p$ for small Δt. If the overall time step Δt is held constant the leapfrog approximation is time-reversible and is a second-order accurate approximation to the equations of motion (see Hockney & Eastwood, 1981). In addition, the leapfrog scheme is stable for a small enough time step Δt. How the timestep has to be adjusted depends on the system that has to be integrated. For hydrodynamical simulations a criterium could be phrased as no information is allowed to travel farther than one resolution unit within one timestep. For dynamical simulations the timestep must be small enough to resolve the dynamics of the system. A typical value for a timestep of a collisionless system is $10^{-2} - 10^{-3}$ dynamical time scales. Small errors at any stage of the integration then do not lead to larger cumulative errors. In addition, the leapfrog scheme is easy to implement and requires little memory. If the time step is properly adjusted to the parameters of the simulations the scheme provides a good compromise between accuracy, stability and efficiency (Athanassoula, 1993; Barnes, 1998).

3.2   The initial conditions

Determining initial conditions for numerical simulations of disk galaxies is problematic in general. Galaxies are compound objects consisting of a luminous disk with interstellar gas, a stellar bulge or a bar, and an extended dark halo. The overall goal is to describe a dynamical equilibrium model with physical properties according to observations of the Milky Way and

other galaxies. Unfortunately, the distribution function that describes the dynamical evolution of a collisionless system like a galaxy (see Section 3.2.1) is very complex and not well known for systems of such a complexity. One way out is to realize only part of the galaxy with particles and describe the other components by fixed analytic potentials. The disadvantage of those methods is that they do not allow self-consistent interaction between the subsystems. In the standard cosmological model where dark matter halos consist of self-gravitating and collisionless particles those interactions are of fundamental importance for the evolution of the system as a whole.

In Section 3.2.1 we describe the basics of the dynamics of collisionless stellar systems and in Section 3.2.2 we review an approach to construct a model for disk galaxies in dynamical equilibrium that is used for the investigations in this thesis.

3.2.1 Dynamics of collisionless stellar systems

The dynamics of collisionless stellar systems is discussed extensively in the literature (e.g. Binney & Tremaine, 1987). Therefore we will focus only on the basic concepts that are needed to understand the description of the model for initial conditions in Section 3.2.2.

Gravitationally interacting stars in a galaxy can be assumed to form a collisionless dynamic system. Collisionless means that the motion of a star in a galaxy is determined by the overall potential of the system rather than by interactions with stars close by. Whether a stellar system can be assumed to be collisionless is determined by its relaxation time t_{relax}. The relaxation time gives the time-scale after which a star that moves in a system of N stars is deflected significantly by close encounters with nearby particles from its mean trajectory. The relaxation time can be defined as (see Binney & Tremaine (1987) for details)

$$t_{relax} = \frac{r_g}{v_t} \frac{N}{8 \ln N}. \tag{3.4}$$

Here $r_g/v_t = t_{cross}$ is the crossing time for a system of N particles with masses m, and the characteristic radius r_g is defined as

$$r_g \equiv \frac{GM^2}{|W|}. \tag{3.5}$$

G is the gravitational constant, W is the total potential energy of the system, and $M = N \cdot m$ is its total mass. v_t is the typical velocity

$$v_t^2 \approx \frac{GNm}{R} \tag{3.6}$$

of a particle in such a system with radius R. Galaxies consisting of $N = 10^{11}$ particles have relaxation times comparable to the age of the universe and can therefore be assumed to be collisionless systems. It has to be noted that every stellar system can be treated as a collisionless system if it is investigated on timescales significantly smaller than its relaxation time.

In classical mechanics the state of a system of particles is determined by the position $\mathbf{x}$ and velocity $\mathbf{v}$ of every particle. Using a discrete set of Newtonian equations of motion it is

then possible to determine the velocities and positions of every particle at every time. For the large number of particles involved in stellar dynamical processes it is not possible to follow exactly the trajectory of every particle. Since the particles in a collisionless system move under the influence of a smooth global potential $\Phi(\mathbf{x}, t)$, a continuous description of the system is more useful. The state of the system can be given by the number of stars $f(\mathbf{x}, \mathbf{v}, t)\mathrm{d}^3\mathbf{x}\mathrm{d}^3\mathbf{v}$ in a volume $\mathrm{d}^3\mathbf{x}$ centered on $\mathbf{x}$ and velocities in the range $\mathrm{d}^3\mathbf{v}$ centered on $\mathbf{v}$. The function $f(\mathbf{x}, \mathbf{v}, t) \geq 0$, defined in the 6-dimensional phase-space $(\mathbf{x}, \mathbf{v})$, is called the phase-space density or the distribution function of the system. To find a dynamical equation for $f(\mathbf{x}, \mathbf{v}, t)$, it can be assumed that the flow of matter through phase space can be described by a 6-dimensional vector $(\mathbf{x}, \mathbf{v})$ with

$$(\dot{\mathbf{x}}, \dot{\mathbf{v}}) = (\mathbf{v}, -\nabla\Phi(\mathbf{x}, t)), \tag{3.7}$$

where $\Phi(\mathbf{x}, t)$ is the gravitational potential. The flux $(\dot{\mathbf{x}}, \dot{\mathbf{v}})$ is conservative, therefore the change of mass in a phase-space volume $\mathbf{dxdv}$ is determined by inflow minus outflow, so

$$\frac{\partial f}{\partial t} + \frac{\partial}{\partial \mathbf{x}} \cdot (f\mathbf{x}) + \frac{\partial}{\partial \mathbf{v}} \cdot (f\mathbf{v}) = 0. \tag{3.8}$$

If we substitute equation (3.7) we obtain the collisionless Boltzmann equation (CBE)

$$\frac{\partial f}{\partial t} + \mathbf{v} \cdot \nabla f - \nabla\Phi \cdot \frac{\partial f}{\partial \mathbf{v}} = 0. \tag{3.9}$$

This equation is the fundamental equation of stellar dynamics. It has the property

$$\frac{\mathrm{d}f}{\mathrm{d}t} = 0. \tag{3.10}$$

This means that the local phase-space density f around a phase point of a given star always remains the same (Binney & Tremaine, 1987). The potential of a given density distribution $\rho(\mathbf{x})$ is given by the Poisson equation

$$\triangle\Phi(\mathbf{x}, t) = 4\pi G\rho(\mathbf{x}, t) = 4\pi G \int f(\mathbf{x}, \mathbf{v}, t)\mathrm{d}^3\mathbf{v}. \tag{3.11}$$

If a distribution function satisfies the Poisson equation (3.11) and the CBE (3.9) it provides a self-consistent solution to a collisionless problem. In the following equations we use the standard summation convention.

One can derive a continuity equation by integrating equation (3.9) over all possible velocities:

$$\int \frac{\partial f}{\partial t}\mathrm{d}^3\mathbf{v} + \int v_i\frac{\partial f}{\partial x_i}\mathrm{d}^3\mathbf{v} - \frac{\partial\Phi}{\partial x_i}\int \frac{\partial f}{\partial x_i}\mathrm{d}^3\mathbf{v} = 0. \tag{3.12}$$

For a spatial density of stars $\nu(x)$ and a mean stellar velocity $\overline{\mathbf{v}}(\mathbf{x})$ defined by

$$\nu \equiv \int f\mathrm{d}^3\mathbf{v} \quad , \quad \overline{v_i} \equiv \int fv_i\mathrm{d}^3\mathbf{v}, \tag{3.13}$$

this simplifies to the continuity equation

$$\frac{\partial\nu}{\partial t} + \frac{\partial(\nu\overline{v_i})}{\partial x_i} = 0. \tag{3.14}$$

If we multiply the CBE by v_j and integrate over all velocities we obtain

$$\frac{\partial}{\partial t} \int f v_j \mathrm{d}^3\mathbf{v} + \int v_i v_j \frac{\partial f}{\partial x_i} \mathrm{d}^3\mathbf{v} - \frac{\partial \Phi}{\partial x_i} \int v_j \frac{\partial f}{\partial v_i} \mathrm{d}^3\mathbf{v} = 0. \tag{3.15}$$

Using the fact that $f \to 0$ for large v and applying the divergence theorem, equation (3.15) can be written as

$$\frac{\partial \nu \overline{v}_j}{\partial t} + \frac{\partial (\nu \overline{v_i v_j})}{\partial x_i} + \nu \frac{\partial \Phi}{\partial x_j} = 0, \tag{3.16}$$

with

$$\overline{v_i v_j} \equiv \frac{1}{\nu} \int v_i v_j f \mathrm{d}^3\mathbf{v}. \tag{3.17}$$

Subtracting $\overline{v}_j$ times the equation of continuity (3.14) and substituting

$$\sigma_{ij}^2 \equiv \overline{(v_i - \overline{v}_i)(v_j - \overline{v}_j)} = \overline{v_i v_j} - \overline{v}_i \overline{v}_j \tag{3.18}$$

gives the Jeans equations

$$\nu \frac{\partial \overline{v}_j}{\partial t} + \nu \overline{v}_i \frac{\partial \overline{v}_j}{\partial x_i} = -\nu \frac{\partial \Phi}{\partial x_j} - \frac{\partial (\nu \sigma_{ij}^2)}{\partial x_i}. \tag{3.19}$$

The Jeans equations (3.19) are the stellar dynamical analogon to the ordinary Euler equation of hydrodynamics. Here $\nu \sigma_{ij}^2$ is a stress tensor that describes an anisotropic pressure. Applying an analogous sequence of steps one can obtain the Jeans equations in cylindrical coordinates by taking moments of the CBE in cylindrical coordinates (see Binney & Tremaine, 1987):

$$\frac{\partial (\nu \overline{v}_R)}{\partial t} + \frac{(\nu \overline{v_R^2})}{\partial R} + \frac{(\nu \overline{v_R v_z})}{\partial z} + \nu \left(\frac{\overline{v_R^2} - \overline{v_\phi^2}}{R} + \frac{\partial \phi}{\partial R} \right) = 0, \tag{3.20}$$

$$\frac{\partial (\nu \overline{v}_\phi)}{\partial t} + \frac{(\nu \overline{v_R v_\phi})}{\partial R} + \frac{(\nu \overline{v_\phi v_z})}{\partial z} + \frac{2\nu}{R} \overline{v_\phi v_R} = 0, \tag{3.21}$$

and

$$\frac{\partial (\nu \overline{v}_z)}{\partial t} + \frac{(\nu \overline{v_R v_z})}{\partial R} + \frac{(\nu \overline{v_z^2})}{\partial z} + \frac{\overline{v_R v_z}}{R} + \nu \frac{\partial \Phi}{\partial z} = 0. \tag{3.22}$$

In addition, we give the Jeans equations for a spherically symmetric system in steady state and for $\overline{v}_r = \overline{v}_\theta = 0$, calculated by integrating $\overline{v}_r$ times the CBE in spherical coordinates, as

$$\frac{d(\nu \overline{v_r^2})}{dr} + \frac{\nu}{r} \left[2\overline{v_r^2} - \left(\overline{v_\theta^2} + \overline{v_\phi^2} \right) \right] = -\nu \frac{d\Phi}{dr}. \tag{3.23}$$

3.2.2   A model for individual galaxies

The models for spiral galaxies consist of a disk component, a bulge, and an extended dark matter halo. They are constructed in dynamical equilibrium, adopting a method described by Hernquist (1993a). This method uses the fact that the lowest (second) order moments of the CBE are determined by the density distributions of the components. Since those are known from observations one can compute velocity moments and approximate the real distribution function in velocity space by known distribution functions (e.g. Gaussian) having these moments. This method is only an approximation but it can be assumed that the system initialized this way reaches an equilibrium state after a short evolution. Hereafter we describe the basic properties of the initial model.

We assume a **stellar disk** with a density which decreases exponentially with increasing cylindrical radius $R = \sqrt{x^2 + y^2}$ (Freeman, 1970) and is described by isothermal sheets perpendicular to the disk plane (Bahcall & Soneira, 1980; Spitzer, 1942)

$$\rho_d(R, z) = \frac{M_d}{4\pi h^2 z_0} \exp(-R/h) \operatorname{sech}^2\left(\frac{z}{z_0}\right), \tag{3.24}$$

where M_d is the disk mass, h is the radial scale length, and z_0 is a characteristic measure of the scale height perpendicular to the galactic plane. The scale height is assumed to be independent of the galactocentric distance (van der Kruit & Searle, 1981, 1982). To construct a velocity ellipsoid of the disk with the density given in equation (3.24) one can use moments of the CBE. Observations of velocity dispersions in disk galaxies show that the radial velocity dispersion is proportional to the surface density (Freeman, 1970; Lewis & Freeman, 1989; Bottema, 1993; Binney & Merrifield, 1998) implying that

$$\overline{v_R^2} \propto \exp(-R/h). \tag{3.25}$$

For an isothermal sheet (here $\overline{v_z^2}$ is independent of z) the vertical velocity dispersion is related to the disk surface density, $\Sigma(R)$, by

$$\overline{v_z^2} \propto \pi G \Sigma(R) z_0. \tag{3.26}$$

Observations of edge-on disk galaxies suggest that z_0 does not vary with radius and therefore $\overline{v_z^2} \propto \Sigma(R)$ (van der Kruit & Searle, 1981, 1982; van der Kruit & Freeman, 1984; see Bottema (1993) for an overview).

A small note: For a stellar system in equilibrium with density ρ, $\nabla P = -\rho \nabla \Phi$ with the "pressure" $P = \rho \sigma_z$ (this is related to the functional form of the Jeans equation as an analogon to the Euler equation, see Binney & Tremaine, 1987). We then get

$$\frac{1}{\rho} \frac{\partial(\rho \overline{v_z^2})}{\partial z} = -\frac{\partial \Phi}{\partial z}. \tag{3.27}$$

Near the plane of a highly flattened system Poisson's equation can be approximated by

$$\frac{\partial^2 \Phi}{\partial^2 z} = 4\pi G \rho. \tag{3.28}$$

Combining equations (3.27) and (3.28) gives

$$\frac{\partial}{\partial z}\left(\frac{1}{\rho}\frac{\partial\rho}{\partial z}\right) = -4\pi\rho\frac{G}{\sigma_z^2}, \tag{3.29}$$

assuming σ_z^2 is independent of z. The solution to equation (3.29) for constant σ_z^2 is

$$\rho = \rho_0\text{sech}^2\left(\frac{z}{z_0}\right) \tag{3.30}$$

with

$$z_0 = \left(\frac{\sigma_z^2}{2\pi G\rho_0}\right)^{\frac{1}{2}}. \tag{3.31}$$

The asymptotic behaviour of ρ is described by

$$\text{sech}^2(z/z_0) \approx \begin{cases} 1 - (z^2/4z_0^2) & : \quad \text{for } z \ll z_0 \\ 4e^{-2z/z_0} & : \quad \text{for } z \gg z_0. \end{cases} \tag{3.32}$$

The velocity structure in the radial and vertical directions in the disk plane is determined by equation (3.25) and (3.26). To quantify the normalization constant in equation (3.25) it is required that the radial dispersion at a critical radius $R = R_{\text{crit}}$ is determined by the Toomre Q parameter (Toomre, 1964). A critical velocity dispersion for the local stability of a thin gravitating disk at a given radius R_{crit} is defined by

$$\sigma_R|_{R_{\text{crit}}} > \frac{3.36G\Sigma}{\kappa}, \tag{3.33}$$

or defining the Toomre stability parameter Q:

$$Q \equiv \frac{\sigma_R\kappa}{3.36G\Sigma} > 1 \tag{3.34}$$

for the local stability of an axisymmmetric disk. The epicyclic frequency κ is defined by

$$\kappa^2 = \frac{3}{R}\left(\frac{\partial\Phi}{\partial R}\right) + \left(\frac{\partial^2\Phi}{\partial R^2}\right). \tag{3.35}$$

Here Φ is the total potential arising from all components of the galaxy model. For the models used in this thesis we assume a critical radius of $R_{\text{crit}} = 2.4h$. This corresponds to the solar radius $R_\odot$ if the model is scaled to the Milky Way.

To compute the azimuthal moments of the velocity field of the disk one needs the Jeans equation in cylindrical coordinates (3.20). For a star that lies close to the galactic equator, one can evaluate equation (3.20) at $z = 0$, and assume that $(\partial\nu/\partial z) = 0$, to find

$$\frac{R}{\Sigma}\frac{\partial(\Sigma\overline{v_R^2})}{\partial R} + R\frac{\partial(\overline{v_R v_z})}{\partial z} + \overline{v_R^2} - \overline{v_\phi^2} + R\frac{\partial\Phi}{\partial R} = 0 \tag{3.36}$$

if we substitute ν with Σ in the limit of a thin disk with $z = 0$. Substituting the azimuthal velocity dispersion

$$\sigma_\phi^2 = \overline{(v_\phi - \bar{v}_\phi)^2} = \overline{v_\phi^2} + \bar{v}_\phi^2 \tag{3.37}$$

and $R(\partial\Phi/\partial R) = v_c^2$, where v_c is the circular speed, in equation (3.36) gives the relevant second moment of the CBE to compute moments of the azimuthal velocity dispersions according to

$$\sigma_\phi^2 - \overline{v_R^2} - \frac{R}{\Sigma}\frac{\partial(\Sigma\overline{v_R^2})}{\partial R} - R\frac{\partial(\overline{v_R v_z})}{\partial z} = v_c^2 - \bar{v}_\phi^2. \tag{3.38}$$

The azimuthal dispersion was chosen to be related to the radial dispersion via the epicyclic approximation

$$\sigma_\phi^2 = \overline{v_R^2}\frac{\kappa^2}{4\Omega^2} \tag{3.39}$$

where Ω is the angular frequency and v_c is the circular velocity derived from the potential of all components by

$$\Omega^2 = \frac{1}{R}\frac{d\Phi_{\text{all}}}{dR}, \tag{3.40}$$

$$v_c^2 = R\frac{d\Phi_{\text{all}}}{dR}. \tag{3.41}$$

The equations (3.25),(3.26), and (3.39) fully specify the velocity ellipsoid in the disk plane. Assuming an exponential surface density profile for the disk and an exponential distribution for the radial velocity dispersion, equation (3.38) with equation (3.39) simplifies to

$$\overline{v_\phi^2} - v_c^2 = \overline{v_R^2}\left[1 - \frac{\kappa^2}{4\Omega^2} - \frac{R}{h} + \frac{\partial(\ln\overline{v_R^2})}{\partial\ln R} + \frac{R}{\overline{v_R^2}}\frac{\partial(\overline{v_R v_z})}{\partial z}\right]. \tag{3.42}$$

In addition some softening has to be applied to $\overline{v_R^2}$ at small radii (see Hernquist (1993a) for a detailed description). Velocities are then initialized by drawing v_z from a Gaussian with dispersion $(\overline{v_z^2})^{1/2}$, computing v_R by drawing from a Gaussian distribution with dispersion $(\overline{v_R^2})^{1/2}$, computing $\overline{v_\phi}$ from equation (3.42), and determining the random component by drawing from a Gaussian with dispersion $(\sigma_\phi^2)^{1/2}$.

The **dark matter halo** is assumed to follow a density profile that is characterized by isothermal spheres over some radial interval leading to a phenomenological potential-density pair of

$$\rho_h(r) = \frac{M_h}{2\pi^{3/2}}\frac{\alpha}{r_c}\frac{\exp(-r^2/r_c^2)}{r^2 + \gamma^2}, \tag{3.43}$$

$$\Phi_h(r) = -\frac{GM_h(r)}{r} + \frac{GM_h\alpha}{\sqrt{\pi}r_c}Ei\left[-\left(\frac{r}{r_c}\right)^2 - q^2\right], \tag{3.44}$$

where M_h is the total mass of the halo, r_c is a cutoff radius, and γ is a core radius. The normalization constant α is defined by

$$\alpha = \{1 - \sqrt{\pi}q\exp(q^2)[1 - \text{erf}(q)]\}^{-1}, \tag{3.45}$$

where $q = \gamma/r_c$. The halos are truncated exponentially at r_c. In general r_c is artificially small to reduce the computational task of integrating particles that are only loosely bound and do not affect the luminous component of the galaxy.

For a non-rotating spherical system with a mass distribution like equation (3.43) we have

$$\overline{v_\theta^2} = \overline{v_\phi^2}. \tag{3.46}$$

The velocity dispersion is defined by the Jeans equation in spherical coordinates (see equation 3.23)

$$\frac{1}{\rho_h}\frac{d}{dr}(\rho_h\overline{v_r^2}) + 2\beta(r)\frac{\overline{v_r^2}}{r} = -\frac{d\Phi}{dr}, \tag{3.47}$$

where $\beta(r)$ is defined as

$$\beta(r) \equiv 1 - \frac{\overline{v_\theta^2}}{\overline{v_r^2}} \tag{3.48}$$

and measures the degree of anisotropy. If the system is isotropic ($\beta(r) = 0$, $\overline{v_R^2} = \overline{v_\theta^2}$) one can integrate equation (3.47) to give

$$\overline{v_r^2} = \frac{1}{\rho_h(r)}\int_r^\infty \rho_h(r)\frac{d\Phi}{dr}dr \tag{3.49}$$

and

$$\overline{v_r^2} = \frac{1}{\rho_h(r)}\int_r^\infty \rho_h(r)GM(r)dr, \tag{3.50}$$

where Φ includes the self-gravity of the halo and of all other components which contribute to the gravitational field and $M(r)$ is the cumulative mass distribution. The absolute speeds of the particles are selected from

$$F(v,r) = 4\pi\left(\frac{1}{2\pi\sigma^2}\right)^{3/2} v^2 \exp(-v^2/2\overline{v_r^2}) \tag{3.51}$$

with

$$\int_0^\infty F(v,r)dv = 1. \tag{3.52}$$

The Cartesian velocities are then initialized from v assuming isotropy (see Hernquist, 1993a).

Observations of the **stellar bulge** of the Milky Way and external galaxies imply that they are spheroidal systems following an $r^{1/4}$ surface density law. A simple density profile that reproduces the $r^{1/4}$ law was proposed by Hernquist (1990) and is used for this galaxy model. The potential-density pair is

$$\rho_h(r) = \frac{M_b}{2\pi}\frac{a}{r}\frac{1}{(r+a)^3} \tag{3.53}$$

and

$$\Phi(r) = \frac{-GM_b}{r+a} \tag{3.54}$$

with a cumulative mass distribution of

$$M(r) = M_b \frac{r^2}{(r+a)^2}. \tag{3.55}$$

M_b is the total mass of the bulge and a is the scale length. The velocities are initialized in the same manner as for the halo.

For the simulations performed here we use the following **system of units** employed by Hernquist (1992, 1993b): gravitational constant $G = 1$, exponential scale length of the disk $h = 1$ and mass of the larger disk $M_d = 1$. In these units the galaxy model has $z_0 = 0.2$, $M_h = 5.8$, $\gamma = 1$, $r_c = 10$, $M_b = 1/3$, and $a = 0.1$. Scaled to the physical properties of the Milky Way or M31 this translates to $h = 3.5$ kpc and $M_d = 5.6 \times 10^{10} M_\odot$ with a unit time of $t = 1.31 \times 10^7$ yrs and a unit velocity of $v = 262$ km/s. The dynamical time of the disk measured as the rotation period at its half-mass radius is $T_{1/2} = 1.5 \times 10^8$ yrs.

This model has been proven as a valuable collisionless equilibrium model for disk galaxies and has been tested with several applications (Hernquist, 1992, 1993b; Quinn et al., 1993; Heyl et al., 1994; Mihos et al., 1995; Heyl et al., 1996; Walker et al., 1996; Weil & Hernquist, 1996; Velazquez & White, 1999; Naab et al., 1999). Figure 3.7 shows some spherically averaged properties of the initial disk galaxy like the ratio of dark to luminous mass, the density, and the circular velocities of the individual components.

3.2.3 Definition of the merger parameters

For all simulated mergers, the two galaxies approach each other on parabolic Keplerian orbits. In addition, we specify the initial separation of the centers of mass of the galaxies r_{sep}, the ratio $\eta = M_2/M_1 \leq 1$ of the total masses M_1 and M_2 (where $M_2 \leq M_1$) of each of the galaxies and the separation at closest approach, namely the pericenter distance r_p. Given these characteristic values for the galaxy orbits one can calculate the initial positions and velocities for the two galaxies as follows:

$$x_1 = \frac{M_2}{M_{tot}}(r_{sep} - 2r_p), \quad x_2 = -\frac{M_1}{M_{tot}}(r_{sep} - 2r_p), \tag{3.56}$$

$$y_1 = \frac{2M_2}{M_{tot}}\sqrt{r_{sep}r_p - r_p^2}, \quad y_2 = -\frac{2M_1}{M_{tot}}\sqrt{r_{sep}r_p - r_p^2}, \tag{3.57}$$

$$v_{x_1} = -\frac{M_2}{r_{sep}}\sqrt{\frac{2r_{sep} - 2r_p}{M_{tot}}}, \quad v_{x_2} = \frac{M_1}{r_{sep}}\sqrt{\frac{2r_{sep} - 2r_p}{M_{tot}}}, \tag{3.58}$$

$$v_{y_1} = -\frac{M_2}{r_{sep}}\sqrt{\frac{2r_p}{M_{tot}}}, \quad v_{y_2} = \frac{M_1}{r_{sep}}\sqrt{\frac{2r_p}{M_{tot}}}, \tag{3.59}$$

$$z_1 = z_2 = v_{z_1} = v_{z_2} = 0, \tag{3.60}$$

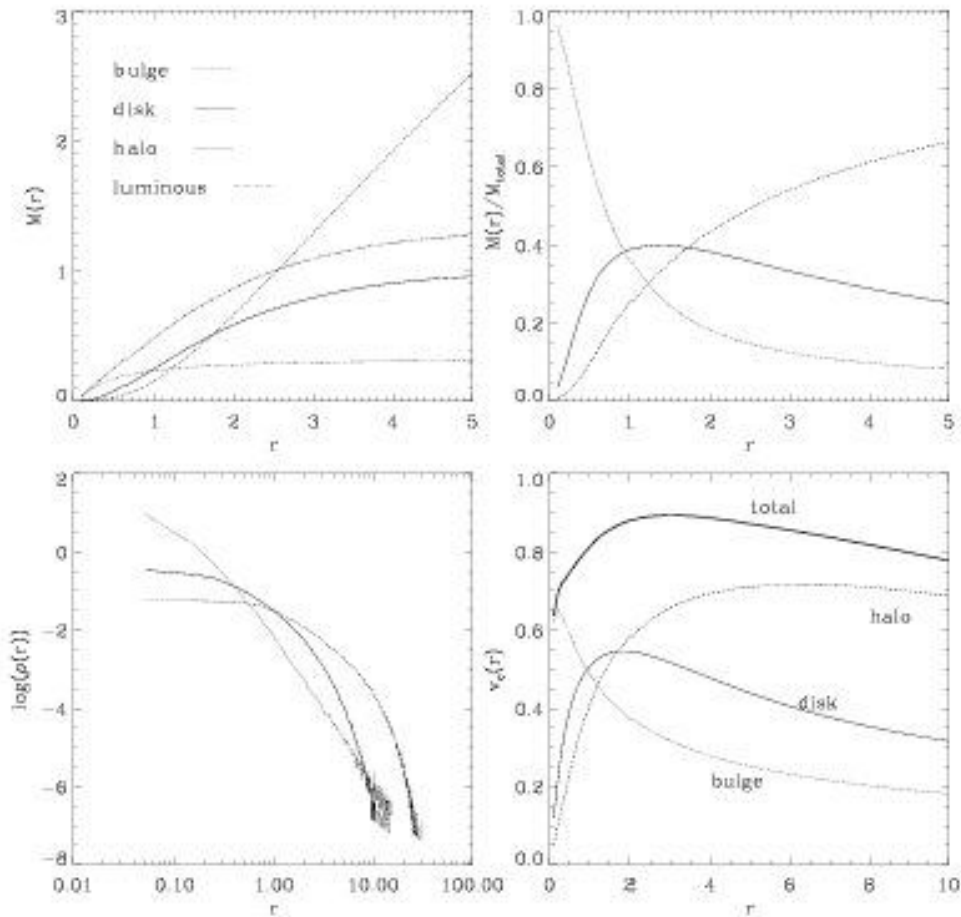where $M_{tot} = M_1 + M_2$ is the total mass of the two galaxies.

Figure 3.7: Spherically averaged properties of the initial disk galaxy vs. radius in units of disk scale lengths *Upper left panel*: Cumulative mass of bulge (dotted), disk (straight line), total luminous component (dash-dotted), and halo (dashed) vs. spherical radius. *Upper right panel*: Ratio of cumulative bulge, disk and halo mass and total cumulative mass vs. radius. *Lower left panel*: Density distribution for the different components. *Lower right panel*: Circular velocity of the model and separate contributions from disk, bulge, and halo vs. spherical radius. It has to be noted that the circular speed of the disk is underestimated by $\approx 15\%$ since the mass is spherically binned and therefore assumed to be spherically distributed (see Binney & Tremaine, 1987).

In addition to the orbits of the galaxies we have to define the inclinations of the two disks relative to the orbital plane. Here we follow Toomre & Toomre (1972) by defining the inclination angle i ranging from $i = 0°$ to $i = 180°$ as the angle between the spin and the orbit planes where $i = 0°$ for a prograde passage in the plane of the orbit, $i = 90°$ for a passage perpendicular to the orbital plane, and $i = 180°$ for a retrograde passage in the plane of the
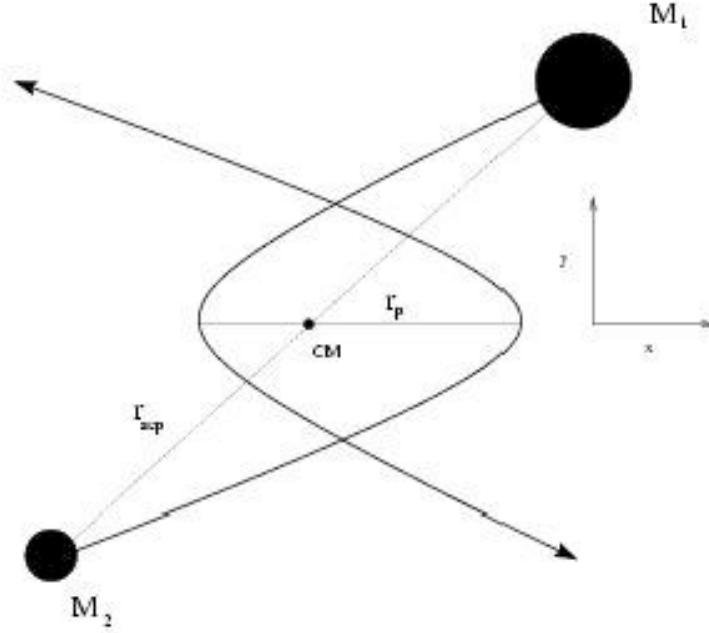
Figure 3.8: Schematic sketch of the initial conditions for a parabolic orbit for two galaxies with given masses M_1 and M_2, impact parameter r_p and initial separation r_{sep}.

orbit. The argument of pericenter ω, ranging from $\omega = -90°$ to $\omega = 90°$, measures the angle between the line of nodes and the separation vector at pericenter (Figure 3.9).

The lower mass merger partner is scaled by a factor of $\eta^{1/2}$ in radius and a factor of $\eta^{1/4}$ in velocity as expected from the Tully-Fisher relationship (Tully & Fisher, 1977) assuming a constant M/L ratio (Barnes, 1998). The Tully-Fisher relation describes a correlation between absolute magnitudes of spiral galaxies and their rotation velocities measured using the Doppler broadening in 21 cm emission (Tully & Fisher, 1977; Pierce & Tully, 1992; Giovanelli et al., 1997a; Giovanelli et al., 1997b). For the stellar component of disk galaxies this roughly corresponds to a relation between the luminosity L_d of a disk galaxy and its circular velocity v_{circ} which can be described as

$$L_d \propto v_{circ}^{n_{TF}}, \tag{3.61}$$

where n_{TF} ranges between 3 to 4. Here we assume a correlation of

$$L_d \propto v_{circ}^4. \tag{3.62}$$

Assuming centrifugal equilibrium for the disk

$$v_{circ}^2 \propto \frac{M_{tot}}{R_d} \tag{3.63}$$

and a given mass to light ratio M/L we get

$$v_{circ}^4 \propto \frac{M_{tot}}{M/L} \propto \frac{M_{tot}^2}{R_d^2}. \tag{3.64}$$
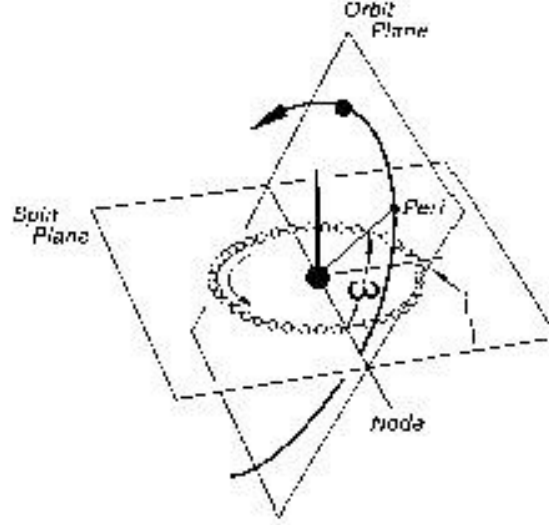
Figure 3.9: Definition of the angles i and ω for the relative orientation of the two galactic disks following Toomre & Toomre (1972).

If M/L is constant $M_d \propto R_d^2$ and we can calculate the scaling factors for the length scale h_r and for the velocities h_v for a given mass ratio η as

$$h_r \approx \eta^{1/2} \text{ and } h_v \approx \eta^{1/4}. \tag{3.65}$$

One can also assume a disk with an exponential surface brightness profile,

$$\Sigma(R) = \Sigma_0 \exp(-\frac{R}{R_d}). \tag{3.66}$$

Here R_d and Σ_0 are the disk scale length and central surface density, and are related to the disk mass through

$$M_d = 2\pi \Sigma_0 R_d^2. \tag{3.67}$$

The scaling relations (3.65) then correspond to the assumption that all disk galaxies have comparable values for Σ_0.

We performed simulations of merging disk galaxies with mass ratios $\eta = 1$, $\eta = 1/2$, $\eta = 1/3$, and $\eta = 1/4$.

The galaxies themselves were represented with two resolutions. In low-resolution simulations the more massive galaxy contains 20000 disk particles, 6666 bulge particles, and 40000 dark halo particles. The lower mass merger partner contains η times the particles in each component and its size and velocities are scaled according to equation (3.65). This results in a total number of 53332 luminous particles for 1:1 mergers ($\eta = 1$), 39999 luminous particles for 2:1 mergers ($\eta = 1/2$), 35554 luminous particles for 3:1 mergers ($\eta = 1/3$), and 33332 luminous

particles for 4:1 mergers ($\eta = 1/4$). The high-resolution simulations contain three times more particles in every component.

The time integration for the low-resolution runs were performed making use of the GRAPE-3 hardware (Section 3.1.1) using a leapfrog integrator with a fixed time step of $\Delta t = 0.08$. This corresponds to $\approx 1/140$ times the half mass rotation period of the larger disk. The gravitational softening (see equation 3.1) was chosen to be $\epsilon = 0.1$. Extensive tests of the evolution of disk galaxies in isolation have shown that this value provides the optimal compromise between relaxation effects (vertical heating of the disk) due to particle noise/two-body heating and errors introduced by a bias in the representation of the potential (Naab, Diploma Thesis, 1997, Heidelberg; for a discussion of the effects of force softening see Romeo, 1994; Merritt, 1996; Romeo, 1997; Athanassoula et al., 2000; Dehnen, 2000). A low-resolution 1:1 merger used $\approx 1.1 \times 10^5$ CPU seconds with direct summation on our parallel 24 processor GRAPE-3AF system. The same simulation with high resolution would need $\approx 1.2 \times 10^6$ CPU seconds with the same hardware configuration. Therefore we decided to perform the high-resolution simulations in combination with the GRAPE-5 hardware with a time step of $\Delta t = 0.04$ and a softening of $\epsilon = 0.07$. The simulation time for a 1:1 merger then reduces to $\approx 3.8 \times 10^5$ CPU seconds. The orbital parameters of the simulations we performed are given in Table 3.1. For the geometries 1 to 14 we performed simulations with mass ratios $\eta = 1$, $1/2$, $1/3$, and $1/4$. If we refer to a specific merger the notation will be as follows: the first two integer numbers indicate the mass ratio the following character denotes the resolution and the last integer characterizes the merger geometry. For example: a low–resolution merger, denoted by **L**, with $\eta = 1/2$ (**2_1_**) and the orbital geometry $\omega_1 = -30$, $i_1 = -30$, $\omega_2 = 30$, and $i_2 = 30$ (**_8**; the *Number of geometry* for this geometry given in Table 3.1 is 8) will be named as **2_1_L_8**; a high-resolution merger (**H**) with $\eta = 1/3$ (**3_1_**) and the orbital geometry $\omega_1 = 30$, $i_1 = 0$, $\omega_2 = 0$, and $i_2 = 0$ (**_2**) will be named as **3_1_H_2** and so on.

Number of geometry	i_1	ω_1	i_2	ω_2	r_p	r_{sep}
1	0	0	0	0	2	30
2	30	0	0	0	2	30
3	60	0	0	0	2	30
4	90	0	0	0	2	30
5	120	0	0	0	2	30
6	150	0	0	0	2	30
7	180	0	0	0	2	30
8	-30	-30	30	30	2	30
9	60	60	-60	-60	2	30
10	90	90	90	90	2	30
11	-90	90	90	90	2	30
12	-120	-30	60	-30	2	30
13	60	-30	-120	-30	2	30
14	60	-30	-60	-30	2	30
15	150	-30	30	30	2	30
16	-30	-30	30	30	0.5	30
17	-30	-30	30	30	4	30
18	-30	-30	30	30	8	30

Table 3.1: Orbital parameters for the merger simulations. The values for the more massive galaxy have subscript 1.

Chapter 4

Global properties of merger remnants

In this chapter we discuss the photometric and kinematic properties of the remnants resulting from the simulations described in Chapter 3. To compare our simulated merger remnants with observations we analyze the remnants with respect to observed global photometric and kinematical properties of giant elliptical galaxies. These include an elliptical's surface density profile, its isophotal deviation from a perfect ellipse, its isophotal twist, velocity dispersion, and major- and minor-axis rotation. We present numerical methods to investigate the simulated N-body remnants in a way that allows us to define characteristic values for physical quantities that are comparable to the quantities that observational astronomers measure (Bender et al., 1988). The chapter is organized as follows: we show some snapshots of characteristic mergers and give an overview of the global structure of the merger remnants (Section 4.1). In Section 4.2 we discuss how we determine the isophotal shape of simulated remnants and investigate its properties (isophotal twist, correlation with ellipticity). The kinematics of the remnants and the correlation with photometric properties are investigated in Section 4.3 in a statistical way comparing the results from remnants with mass ratios of 1:1, 2:1, 3:1, and 4:1. In the last section we discuss some individual remnants with remarkable properties (Section 4.4).

4.1   Global properties

To give a first overview of the simulations we performed, we show a time sequence of the prograde mergers 1.1_L_8, 1.1_L_15, 2.1_L_8, 3.1_L_8, 3.1_L_15 and 4.1_L_8 (Figures 4.1–4.12). Here the particle distribution is plotted in the orbital plane and then perpendicular to the orbital plane, respectively. The snapshots are shown at times $t = 0, 36, 60, 96, 150$, and 200, from the upper left to the lower right. For the equal mass merger 1.1_L_8 (Figures 4.1 and 4.2) one can clearly recognize the formation of extended tidal tails, shells and loops of luminous particles. The remnant becomes spheroidal in the end and is surrounded by tidal debris. The 2:1 merger 2.1_L_8 (Figures 4.5 and 4.6) also leads to the formation of extended tails but does not form extended loops. The 3:1 merger 3.1_L_8 (Figures 4.7 and 4.8) and the 4:1 merger 4.1_L_8 (Figures 4.11 and 4.12) are much less violent and lead to more flattened remnants.
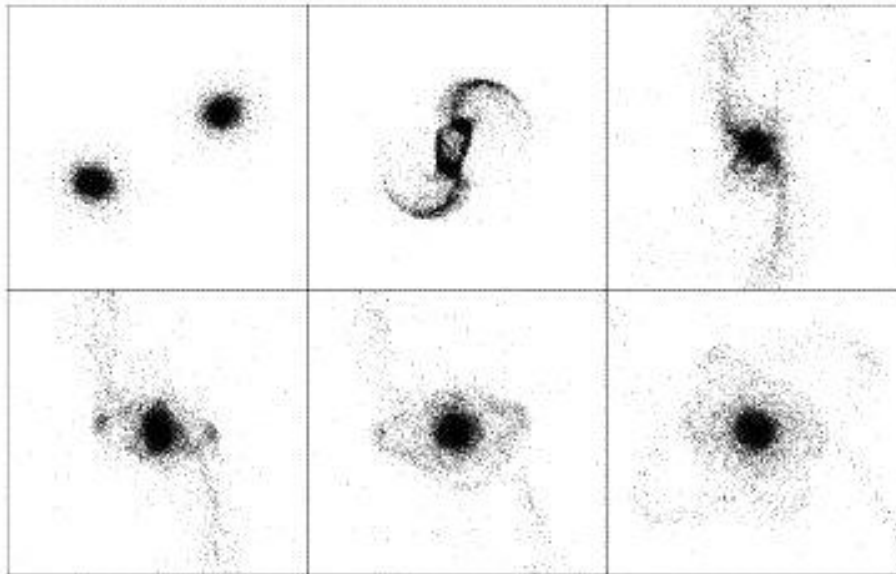
Figure 4.1: Evolution of the luminous particles for the merger 1.1.L.8 seen in the orbital plane. For better visualization only 20% of the luminous particles are shown. Every box has a size of 60 unit lengths. See text for details.
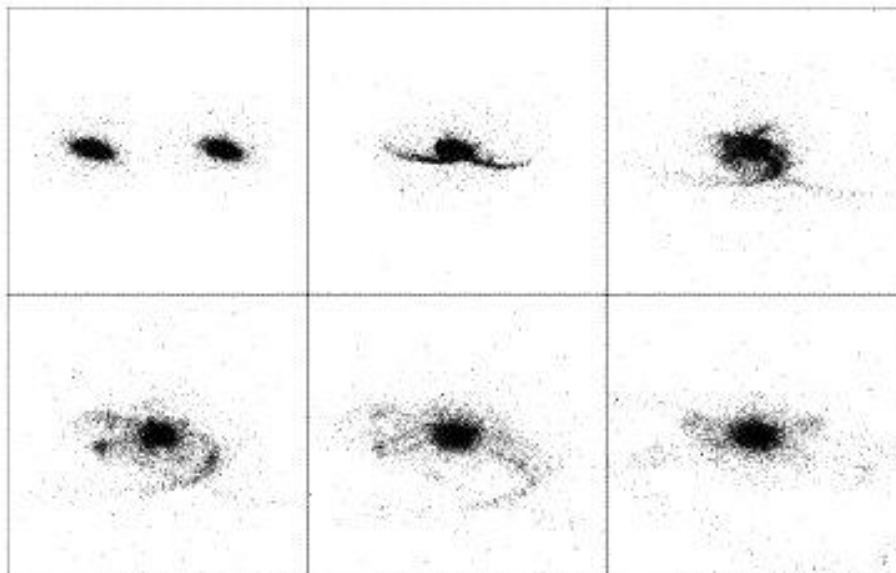

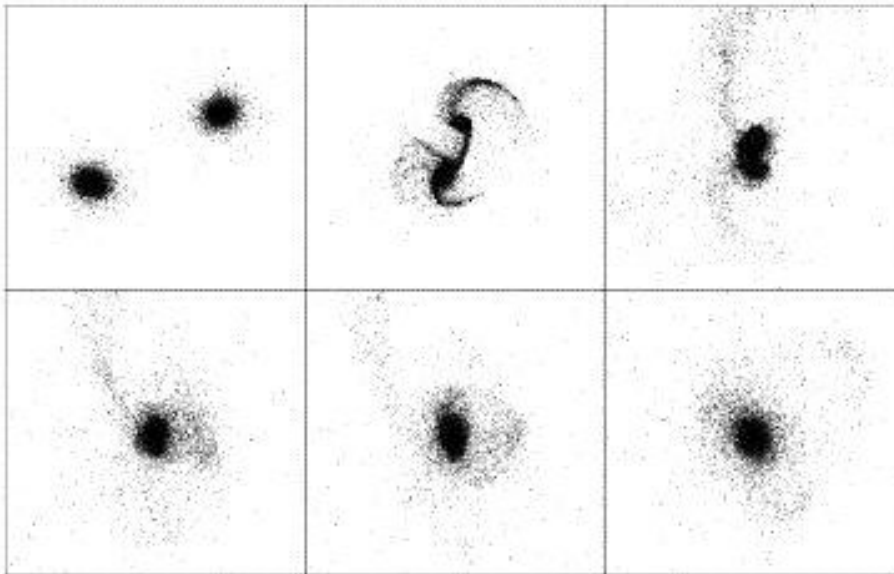Figure 4.2: Same as Figure 4.1, but seen perpendicular to the orbital plane.

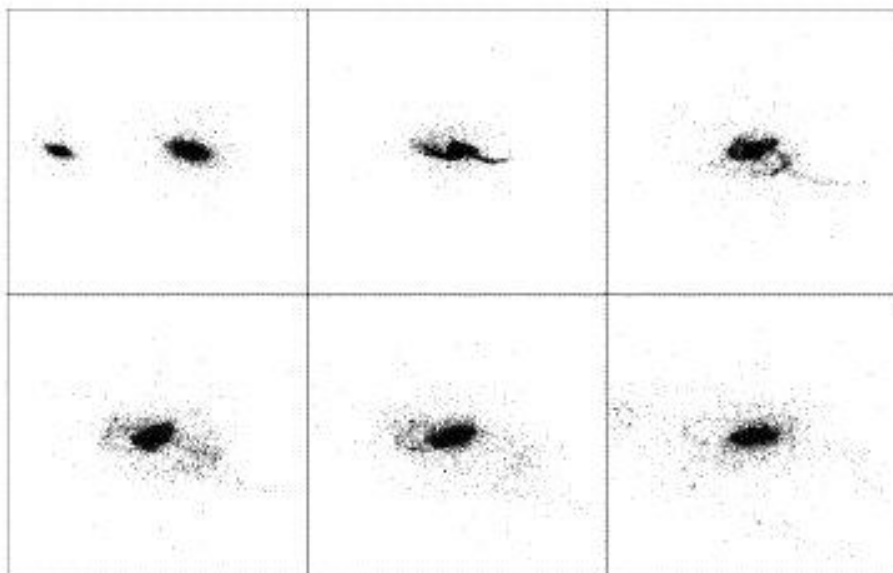Figure 4.3: Evolution of the luminous particles for the merger 1_1_L_15 seen in the orbital plane. Scales are the same as in Figure 4.1. In contrast to the merger 1_1_L_8 the galactic disks are now counter-rotating.
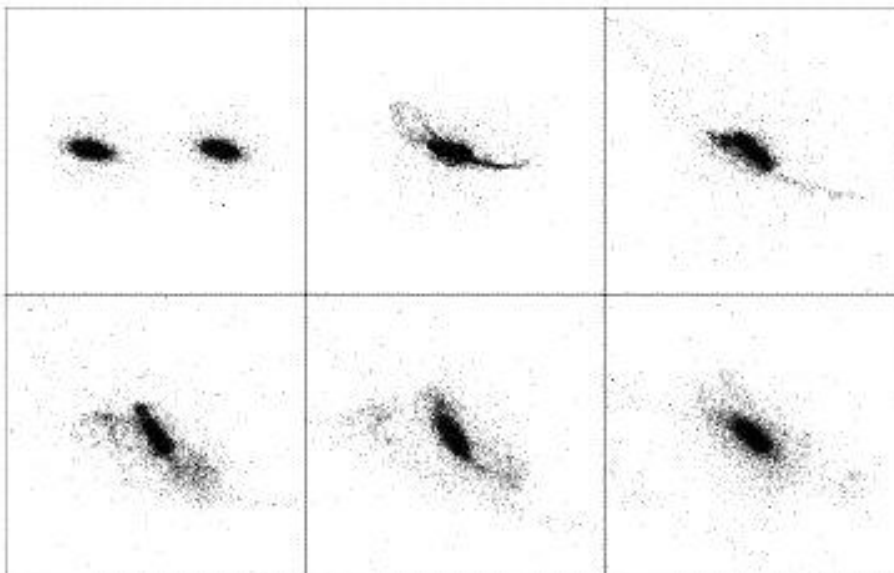
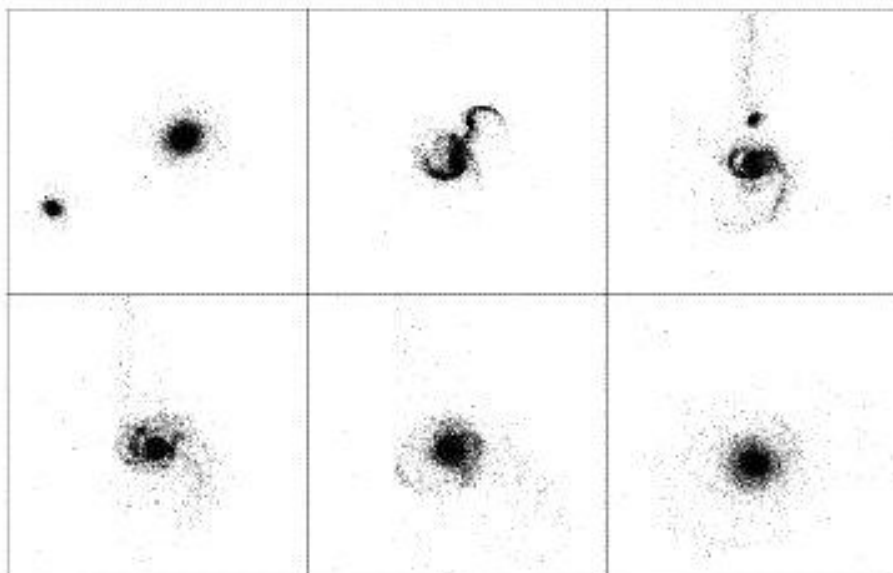Figure 4.4: Same as Figure 4.3, but seen perpendicular to the orbital plane.
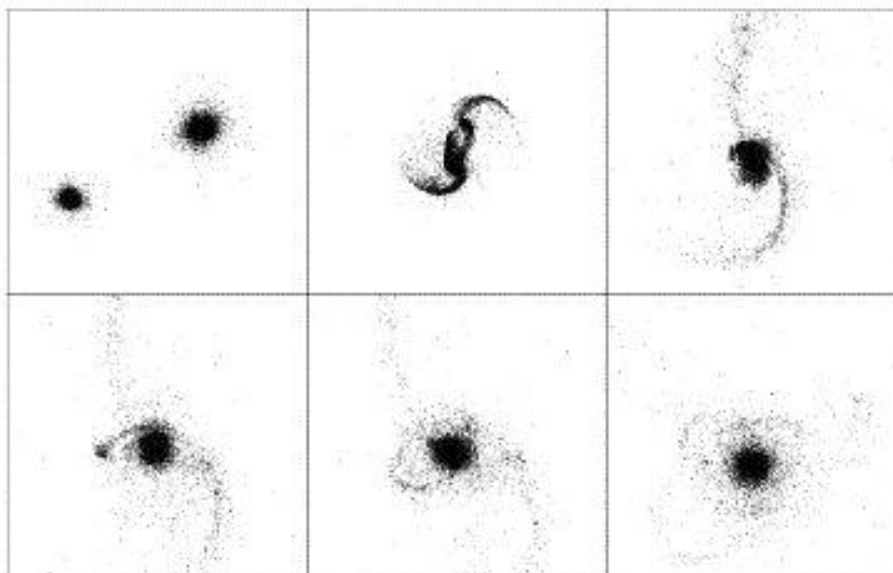
Figure 4.5: Same as Figure 4.1, but for the merger 2_1_L_8.
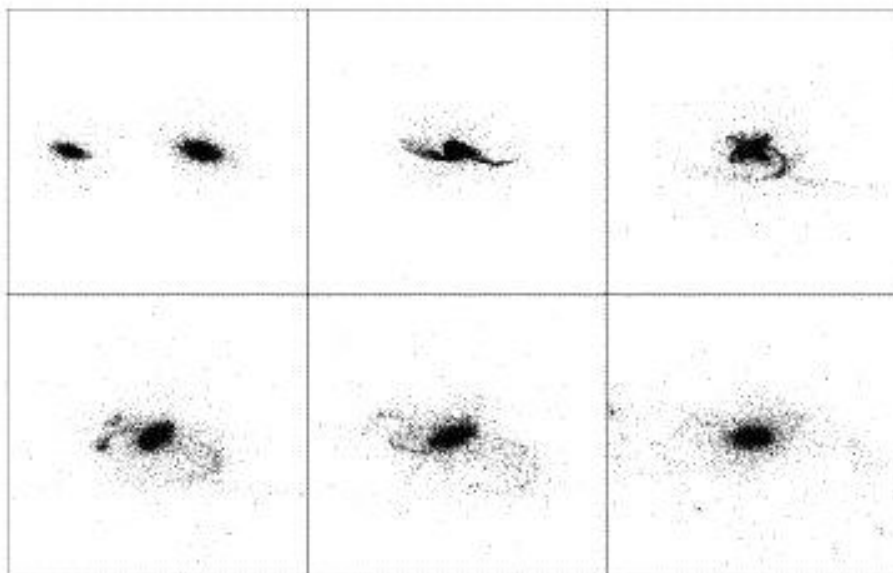
Figure 4.6: Same as Figure 4.5, but seen perpendicular to the orbital plane.
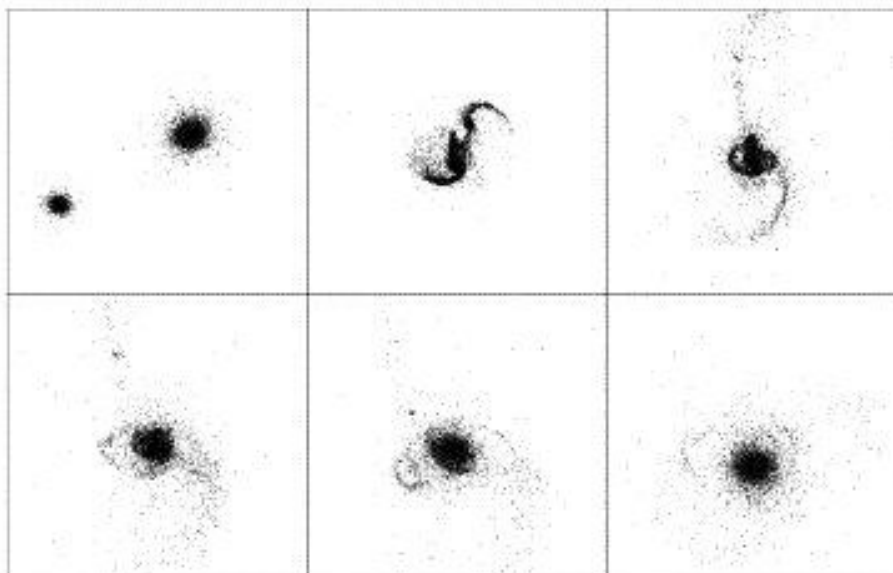
Figure 4.7: Same as Figure 4.1, but for the merger 3_1_L_8.

Figure 4.8: Same as Figure 4.7, but seen perpendicular to the orbital plane.
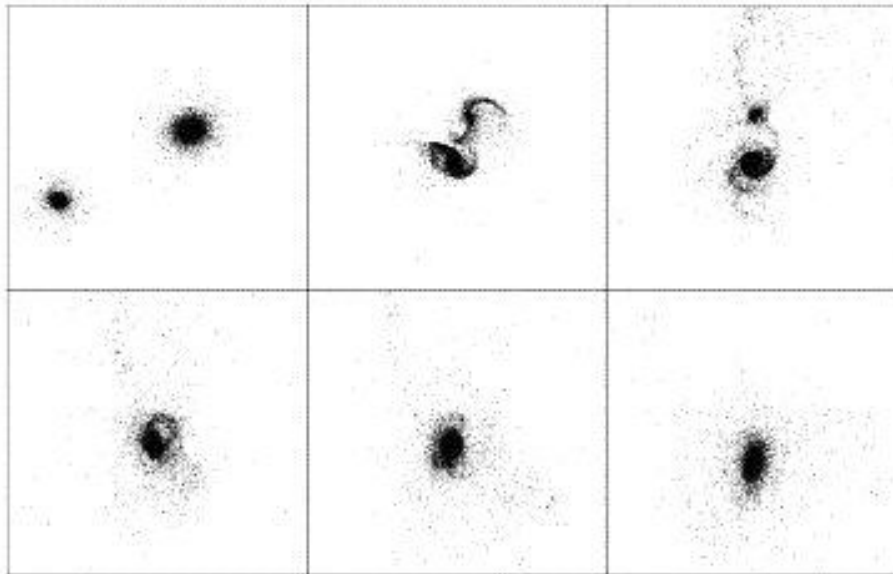
Figure 4.9: Evolution of the luminous particles for the merger 3_1_L_15 seen in the orbital plane. Scale as in Figure 4.7. In contrast to the merger 3_1_L_8 the large disks is now counter-rotating.
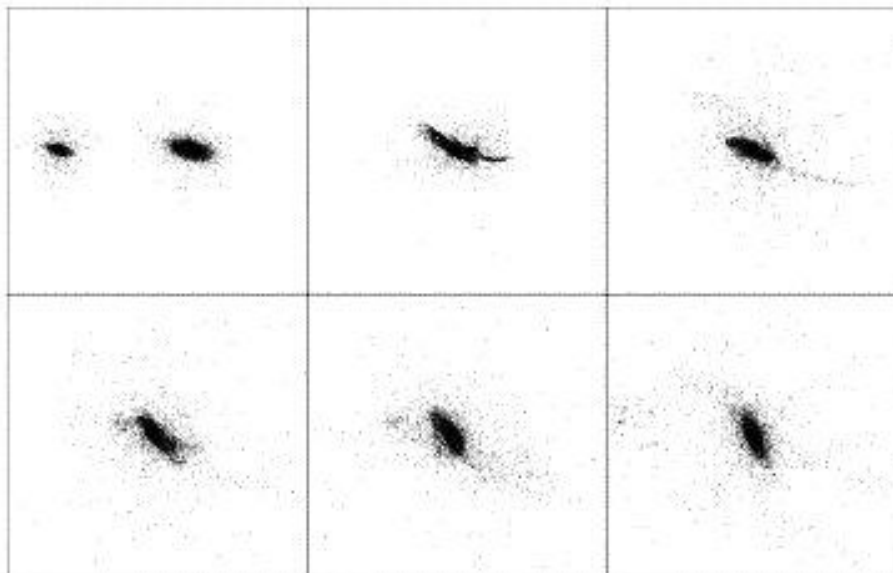
Figure 4.10: Same as Figure 4.9, but seen perpendicular to the orbital plane.

Figure 4.11: Same as Figure 4.1, but for the merger 4.1.L.8.
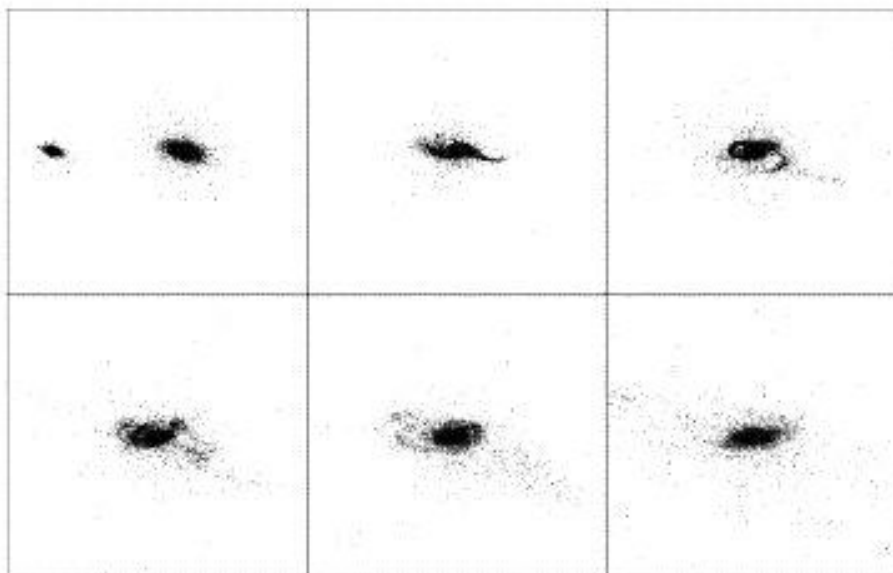
Figure 4.12: Same as Figure 4.11, but seen perpendicular to the orbital plane.
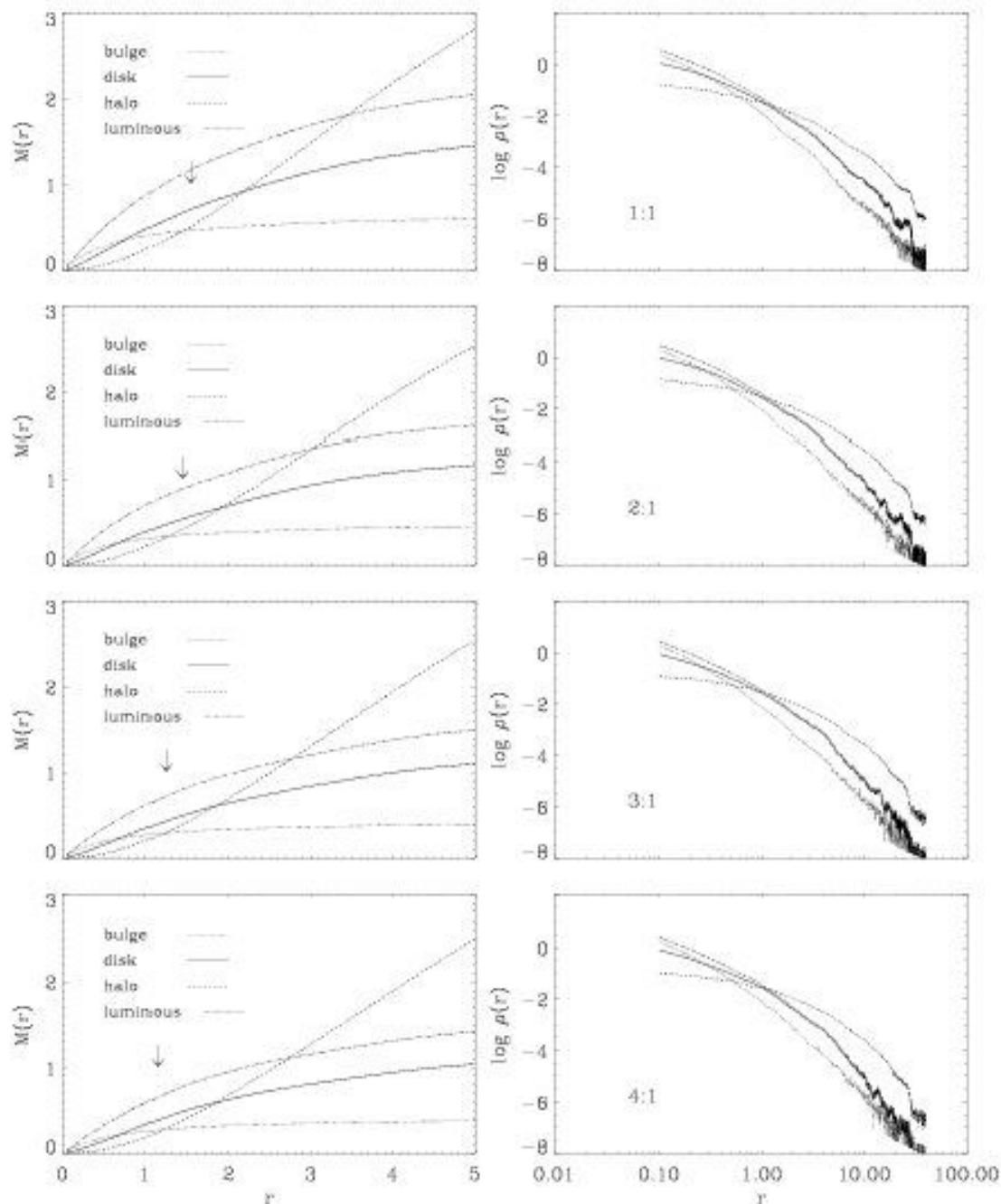
Figure 4.13: Characteristic distribution of matter for 1:1, 2:1, 3:1, and 4:1 merger remnants, respectively. The column on the left side shows the remnant's cumulative mass distribution vs. radius ordered by the different contributions of the progenitor galaxies. The half mass radius of the remnants is indicated by an arrow. The column on the right side shows the corresponding density contributions.

As will be shown later on, equal mass mergers with one retrograde rotating disk (the orbital angular momentum and the spin of the disk point in opposite directions) and unequal mass mergers where the massive disk rotates in a retrograde sense show interesting kinematical properties (Section 4.4). Therefore we show the merger 1_1_L_15 and 3_1_L_15 in Figures 4.3, 4.4, 4.9, and 4.10. In both cases the retrograde rotating disk forms less extended tidal arms. All mergers lead to spheroidal remnants in the end.

Figure 4.13 shows the distribution of matter and the density profiles for characteristic remnants with mass ratios 1:1, 2:1, 3:1, and 4:1 (remnants with geometry 8). It becomes clear from this plot that all remnants show a similar amount of mixing between dark and luminous matter inside one effective radius r_{eff} which is the projected half mass radius of the simulated remnants. This trend is extended up to large radii, regardless of the initial mass ratio. Therefore it seems difficult to explain the tilt of the Fundamental Plane (Section 2.1) by a varying dark matter content of elliptical galaxies with different masses. The detailed implications of the merger scenario for the Fundamental Plane are not discussed in this thesis and need further investigation.

After these first impressions we describe the methods to investigate the merger remnants in more detail. To prepare the analysis of the kinematical and photometric properties of every simulated galaxy we shift the galaxy to the densest central region which can be assumed to be the center of the potential. Thereafter we transform the luminous part of the remnant (disk and bulge particles) to the principal axes of its three-dimensional moment-of-inertia tensor I,

$$I = \sum_i m_i x_i \otimes x_i. \tag{4.1}$$

Here m_i is the mass of a particle and x_i are the coordinates of a particle relative to the center of the potential (Barnes, 1992). The tensor is evaluated using 40% of the most tightly bound particles since we are basically interested in the properties of the inner, bound part of the galaxy (inside one half-mass radius). If we used all luminous particles, we would take unrelaxed, large scale structures like shells and tidal tails into account, resulting in a moment-of-inertia tensor which could be dominated by loosely bound or unbound particles. The eigenvalues λ of the moment-of-inertia tensor I can be used to determine the three-dimensional shape of every merger remnant. The axis ratios b and c can be computed according to $b = (\lambda_2/\lambda_1)^{1/2}$ and $c = (\lambda_3/\lambda_1)^{1/2}$. The triaxiality parameter $\mathcal{T} = (1 - b^2)/(1 - c^2)$ (de Zeeuw & Franx, 1991) characterizes the shape of the remnant. A value of $\mathcal{T} = 0$ then corresponds to a perfectly oblate, lens-like shape and a value of $\mathcal{T} = 1$ corresponds to a prolate, cigar-like shape. Figure 4.14 shows the axis ratios of the merger remnants with orbital geometries 1–14 (given by their numbers) for mass ratios of 1:1, 2:1, 3:1, and 4:1, respectively. The value for their triaxiality parameter can be derived from the location of the numbers in the two-dimensional plot. The arrows indicate the change in shape if 60% of the most tightly bound particles instead of 40% are used to calculate the moment-of-inertia tensor. We find that 1:1 and 2:1 merger remnants are more triaxial than 3:1 or 4:1 merger remnants which are more oblate. For all remnants the three-dimensional shape changes with radius (arrows in Figure 4.14). The remnants are more triaxial in the inner part and clearly tend to have a more oblate shape in the outer parts. If real galaxies show the same behaviour it will be very difficult to derive uniquely the intrinsic shape of observed galaxies (Binney & de Vaucouleurs, 1981; Franx et al., 1991; Ryden, 1992; Tremblay & Merritt, 1995; Ryden, 1996; Tremblay
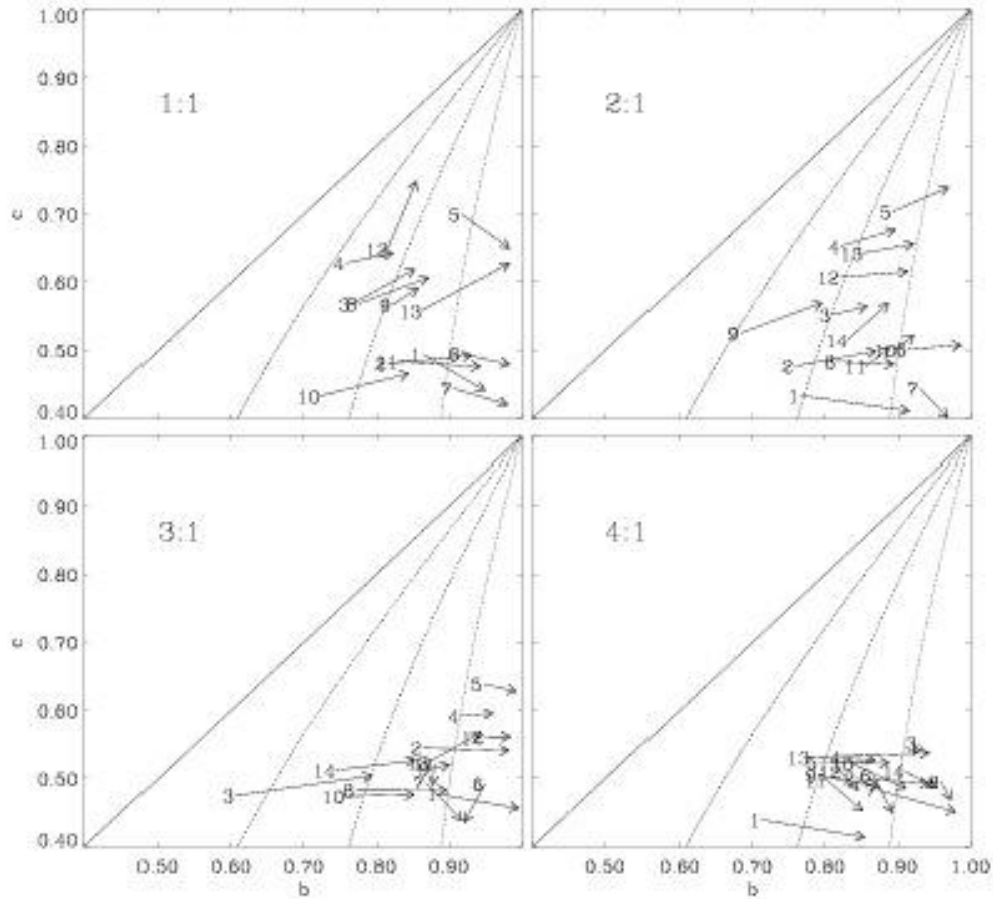
Figure 4.14: Axis ratios of 1:1, 2:1, 3:1, and 4:1 merger remnants. The numbers indicate the axis ratios for the 40% most tightly bound particles of remnants with orbital geometries given in Table 3.1. Solid, dash-dotted, dashed, and dotted lines are contours of triaxiality $T = 1$, 0.75, 0.5, and 0.25, respectively. The arrows indicate the shift in shape if one uses 60% of the most tightly bound particles to calculate the moment-of-inertia tensor.

& Merritt, 1996; Bak & Statler, 2000). It is beyond the scope of this thesis to compare the intrinsic shapes of merger remnants with measurements of real galaxies and we refer the interested reader to the cited literature.

Figure 4.15 shows the surface density profiles for characteristic 1:1, 2:1, 3:1, and 4:1 merger remnants. The profiles are given for projections along the three principal axes for every mass ratio. The index n_{ser} is the shape parameter for the best fitting Sersic profile (see Section 2.2). $n_{ser} = 0.25$ corresponds to a de Vaucouleurs profile. 3:1 and 4:1 remnants show slightly larger values for the shape parameters than 1:1 and 2:1 remnants pointing to more exponential-like
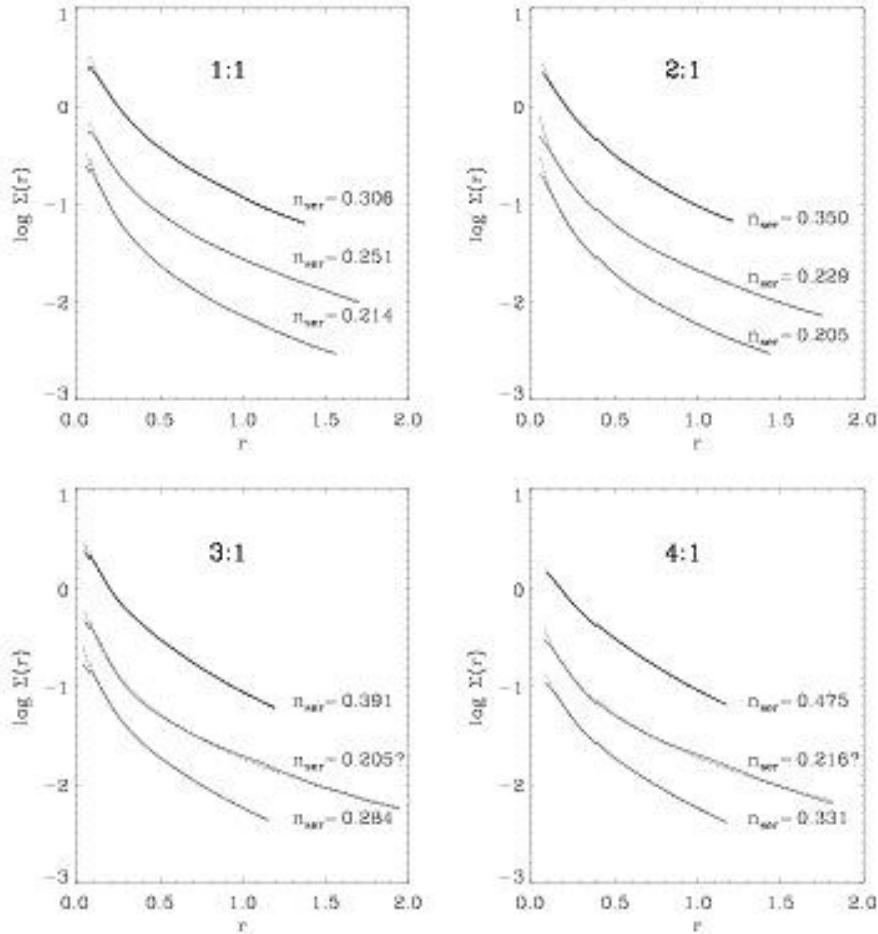
Figure 4.15: Surface density for characteristic 1:1, 2:1, 3:1, and 4:1 merger remnants seen along the long (upper line), short (middle line), and intermediate axis (lower line) of the moment-of-inertia tensor, respectively. The offset between the lines is artificial. The dashed line shows the best fitting Sersic profile between $0.1r_{\rm eff}$ and $1.5r_{\rm eff}$. The shape parameter $n_{\rm ser}$ is given for each projection. Question marks indicate fits that are not well described by a Sersic law.

($n_{\rm ser} = 1$) surface density profiles. This is supported by the fact that the Sersic fit does not converge for some 3:1 and 4:1 remnants where a two component model with a bulge and an exponential disk could give more consistent results. In general, the absolute values of $n_{\rm ser}$ are consistent with observations of elliptical galaxies and future investigations will show if the profile type of simulated merger remnants can serve as an additional global parameter for the classification of elliptical galaxies (see Chapter 2.1).

4.2   Isophotal shape

We have seen in Section 2.2 that the isophotal shape of an elliptical galaxy is a good indicator for its global properties. Therefore it is very important to investigate the isophotal shape of simulated merger remnants. For this analysis we create an artificial surface density map of every simulated remnant seen in projection by binning the mass points of the central 10 length units into 128×128 pixels. As an example we show the grid used for binning the point mass distribution in Figure 4.16 for a characteristic 3:1 merger remnant.
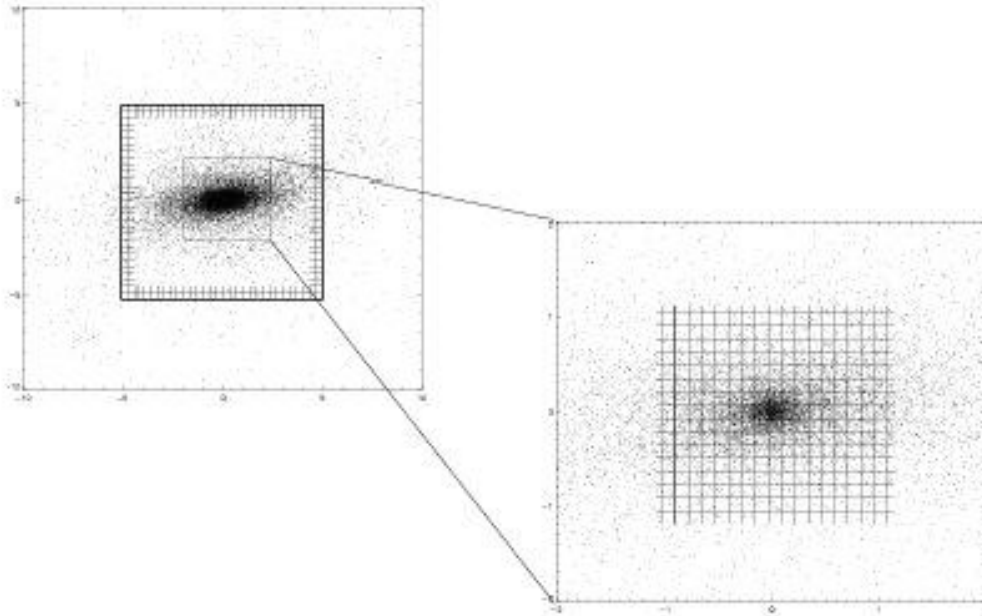
Figure 4.16: Particle distribution of a 3:1 merger remnant (only 10% of the luminous particles are plotted) with the artificial grid at its maximal extension over-plotted. The blow-up of the central region demonstrates the grid coverage inside the half mass radius which ranges between 1.0 and 1.4 length units for the simulated remnants.

We decided to use "pixels" of a size between $\approx 1/15$ to $\approx 1/25$ times the half mass radius r_{eff} of the remnant. This artificial picture is then smoothed with a Gaussian filter of standard deviation $\sigma_{\mathrm{Gauss}} = 1.5$ pixels which corresponds to "seeing" values between $\approx r_{\mathrm{eff}}/4$ and $\approx r_{\mathrm{eff}}/7$. This roughly imitates the detector properties and the seeing conditions for most of the observed galaxies (except the apparently very large ones) at the time when the data was taken (see Bender et al., 1988). Figure 4.17 shows an example of a binned picture derived directly from the particle distribution in comparison with convolved pictures with $\sigma_{\mathrm{Gauss}} = 0.5$, 1.5, and 3.0 pixels.

The effect of "seeing" or convolution with a Gaussian reduces the central surface density of the remnant. It spreads "light" from the center outwards and increases the surface density in the outer regions (Figure 4.18 (a), see also Saglia et al. (1993b) and references therein).
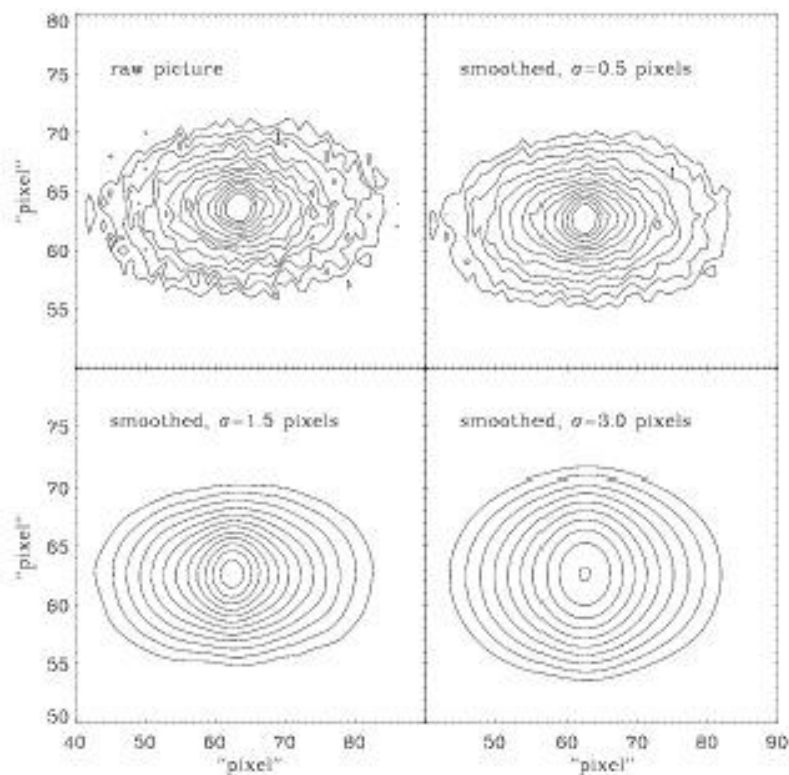
Figure 4.17: Raw surface density contours after binning the particle distribution and the surface density convolved with a Gaussian of standard deviation $\sigma = 0.5$, $\sigma = 1.5$, and $\sigma = 3.0$ pixels.
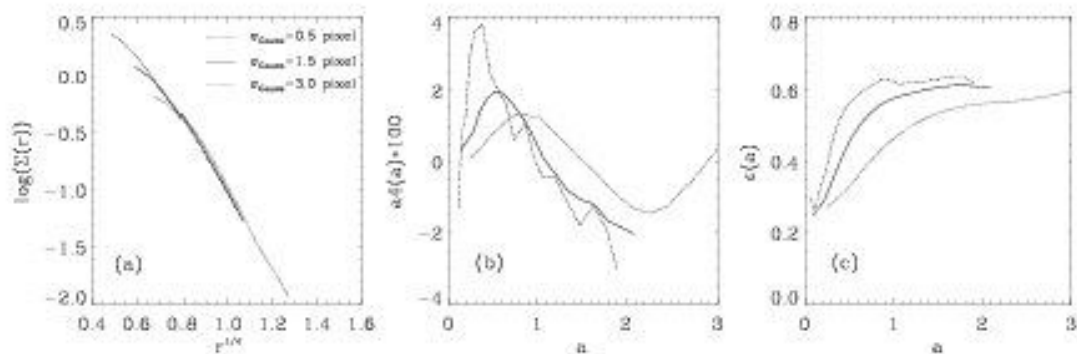

Figure 4.18: Properties of an "observed" merger remnant. Surface densities are convolved with a Gaussian of standard deviation $\sigma = 0.5$ (dashed), $\sigma = 1.5$ (solid line, used for all the data reduction in this thesis), and $\sigma = 3.0$ (dotted).

The isophotes of the central parts of the remnants are in general rounder and closer to
a perfect elliptical shape. Therefore the ellipticities (ϵ) and fourth order deviations from
perfect ellipses ($a4$, see below for the definition) are reduced in the central regions. This
effect becomes stronger for larger values of σ_{Gauss}. Therefore ϵ and the absolute value of $a4$ at
a given distance from the center are always underestimated for $\sigma > 0$ but the characteristic
shape of the curves is conserved (see Figure 4.18 (a) and (b)). Another reason for choosing
$\sigma_{Gauss} = 1.5$ pixels is the following: for $\sigma_{Gauss} < 1.0$ the surface density still is too noisy
to get consistent fits for all the low-resolution simulations. We could avoid this problem by
increasing the distance between two isophote fits, but then we loose resolution in the radial
direction. If, in contrast, we use values of $\sigma > 3.0$ the isophotes are too distorted due to
smoothing (see Figure 4.17 and 4.18). Note again that the main reason for the choice of the
specific seeing parameter was the condition under which the real observation was taken with
which we compare our results. Any change in the "seeing" will change the absolute values of
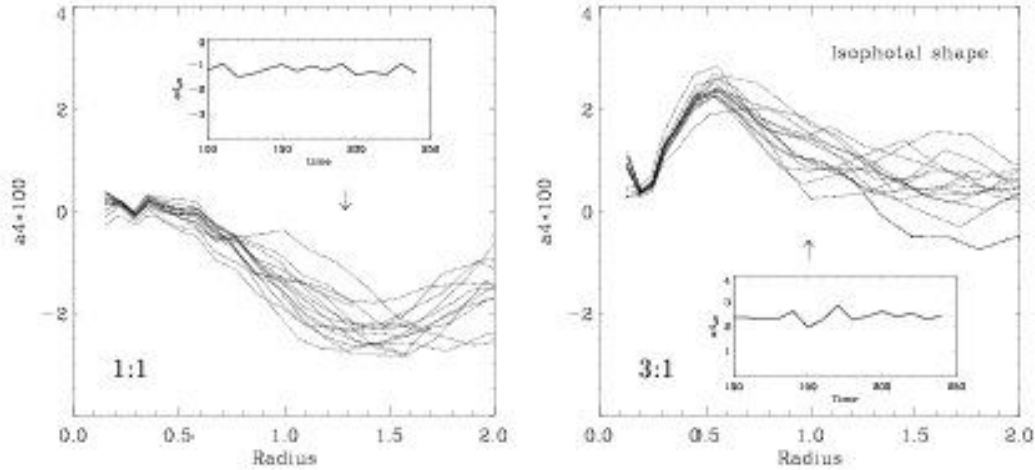the measured properties but will not change the global trend.

Figure 4.19: Dashed lines show the variation of $a4$ along the apparent long axis for different
time steps with $\Delta t = 10$ for a 1:1 merger remnant (left) and a 3:1 merger remnant (right).
The arrow indicates the value of the projected half mass radius r_{eff}. The small viewgraph
shows the time evolution of the effective $a4_{eff}$ value assigned to each of the dashed curves.

The isophotes and their deviations from perfect ellipses are determined following the data re-
duction procedure described in Bender et al. (1988) (see Section 2.2). Using their definitions
for the global properties of observed giant elliptical galaxies, we determine for every projection
the fourth-order Fourier coefficient $a4_{eff}$ as the mean value of $a4 \times 100$ between $0.25r_{eff}$ and
$1.0r_{eff}$, with r_{eff} being the projected spherical half-mass radius. In case of a strong peak in
the $a4$-distribution with an absolute value that is larger than the above absolute mean value,
we choose the peak value.

Since the evolutionary state for which we analyze the $a4$ profile of the remnant is somewhat
arbitrary we investigated the time evolution of the isophotal shape starting ≈ 20 time units

after the merger of the bulge components was completed. Beginning at $t = 100$, after every 10 time units the luminous part of the remnant was transformed to the principal axes of its moment-of-inertia tensor as described above. The $a4$ profile was then analyzed as seen along the major axis. Figure 4.19 shows the $a4$ profiles at different times for a characteristic 1:1 and 3:1 merger remnant plotted as dashed lines. Although the details of the individual $a4$ profiles vary with time, the global characteristic shape is conserved. This is reflected in the time evolution of the characteristic value $a4_{eff}$ which is shown in the small diagrams of Figure 4.19.

The characteristic ellipticity ϵ_{eff} for each projection is defined as the isophotal ellipticity at $1.5r_{eff}$. Figure 4.20 shows the ellipticity profiles for a characteristic merger remnant (here a 3:1 merger) at different times starting at $t = 100$. Once the system has achieved dynamical equilibrium, its characteristic shape does not evolve with time and ϵ_{eff} stays constant.
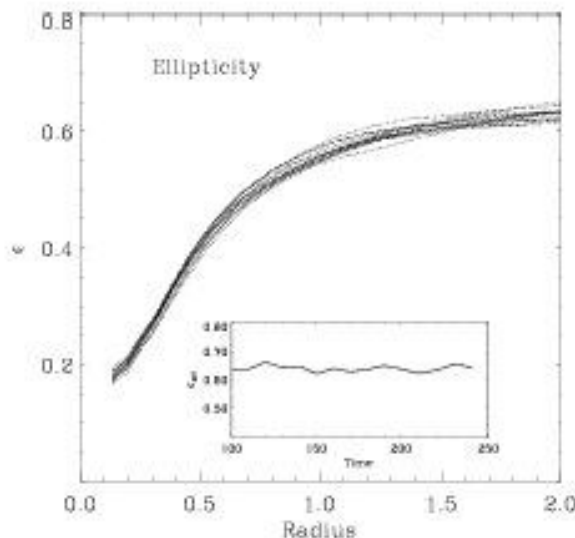

Figure 4.20: Radial change of the ellipticity ϵ at different times (dashed lines) and the time evolution of the characteristic value ϵ_{eff} for a 3:1 remnant.

Ellipticals on the sky are observed only in projection. To include projection effects in our investigation we determined for each simulation $a4_{eff}$ and ϵ_{eff} for 500 random projections. These values were used to calculate a probability density for a given simulated remnant to be "observed" at a given location in the $a4_{eff}$ - ϵ_{eff} plane. In addition, we determined the cumulative probabilities for all geometries at a given mass ratio assuming that mergers occur randomly without preferred relative inclinations.

Figure 4.21 shows the results for 1:1, 2:1, 3:1, and 4:1 mergers. The contours indicate the areas of 50% (thick line), 70% (thin line) and 90% (dashed line) probability to detect a merger remnant with the given properties. Observed data points from Bender et al. (1988) are overplotted. Filled boxes are ellipticals with $a4_{eff} \leq 0$ while open diamonds indicate those with
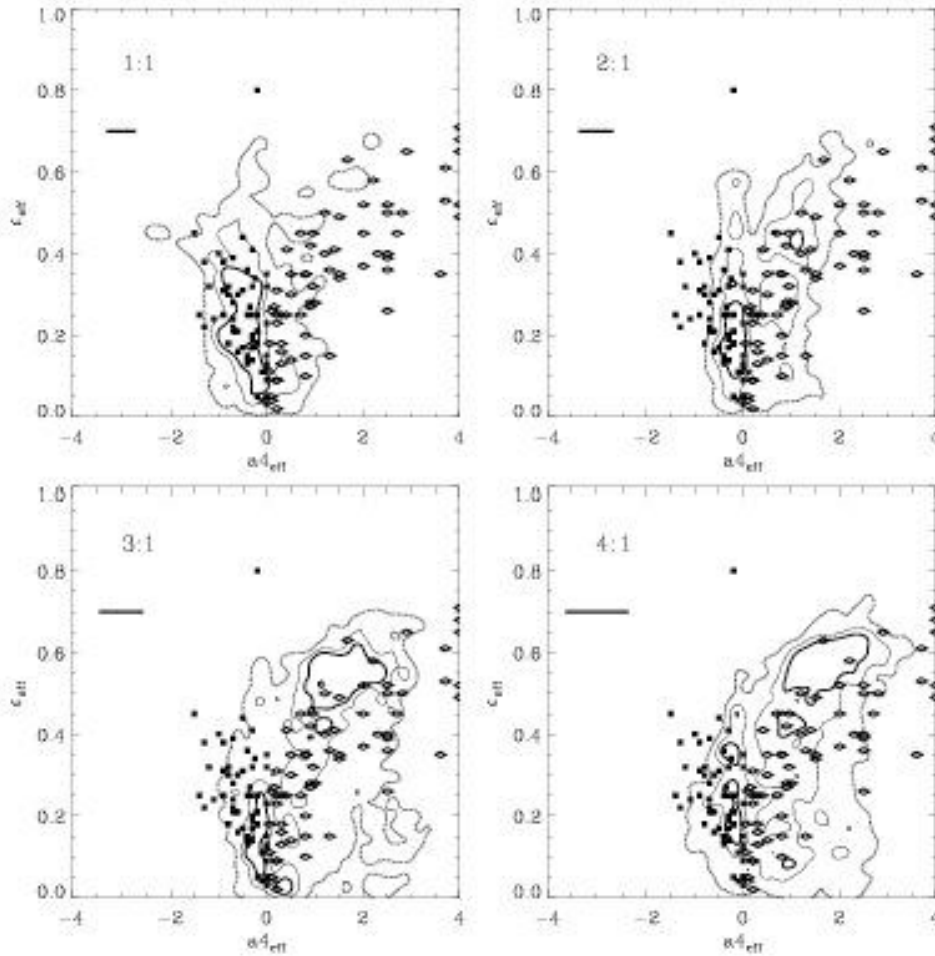
Figure 4.21: Ellipticities ϵ_{eff} versus the characteristic shape parameter $a4_{\text{eff}}$ for low-resolution 1:1, 2:1, 3:1, and 4:1 mergers. The contours indicate the 50% (thick line), the 70% (thin line) and the 90% (dashed line) probability to find a merger remnant in the enclosed area. The error bars for $a4_{\text{eff}}$ are derived applying statistical bootstrapping. Errors for ϵ_{eff} are too small to be plotted here. Black boxes indicate values for observed boxy elliptical galaxies, open diamonds those for observed disky ellipticals (data from Bender et al., 1988).

$a4_{\text{eff}} > 0$. The given errors for $a4_{\text{eff}}$ are estimated applying the statistical bootstrapping method (see Heyl et al., 1994). The area covered by 1:1 remnants is in very good agreement with the observed data for boxy elliptical galaxies (Figure 4.21). In particular, the observed trend for more boxy galaxies to have higher ellipticities is reproduced.

The peak of the shape distribution is around $a4_{\text{eff}} \approx -0.5$ (Figure 4.22) where 2/3 of all projected remnants show boxy isophotes. 2:1 remnants show a double peaked shape distribution. They can appear slightly boxy ($a4_{\text{eff}} \approx -0.2$) or disky ($a4_{\text{eff}} \approx 1.0$) depending on the merger geometry and the projection angle (Figure 4.22). In contrast to 1:1 mergers, 2/3
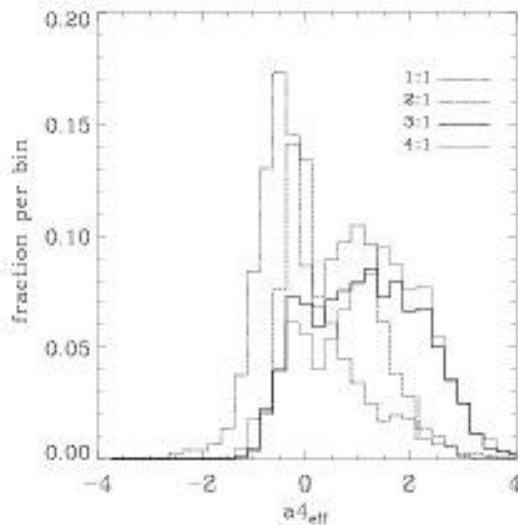
Figure 4.22: Normalized histograms of the shape parameter $a4_{eff}$ for 1:1, 2:1, 3:1, and 4:1 low-resolution mergers.

of the projected remnants show disky isophotes. If the isophote shape is boxy then only the area for small ellipticities $\epsilon \leq 0.2$ is covered. The disky projections have ellipticities predominantly around $\epsilon \approx 0.4$ (Figure 4.21). 3:1 and 4:1 remnants show a rather similar behaviour. They have a double-peaked shape distribution with one peak around elliptical and slightly boxy isophotes and a clear peak for $0.5 \leq a4_{eff} \leq 2.0$ and $\epsilon_{eff} \approx 0.6$. For 3:1 and 4:1 mergers around 82% of the projections have a positive $a4_{eff}$. Therefore there is a clear trend for mergers with mass ratios of 3:1 or 4:1 to produce predominantly disky remnants. The distribution of the particles of the massive disk is responsible for the disky appearance of the 3:1 and 4:1 remnants. To show this behaviour, we investigate the remnant 3.1.H.8 as being representative for 3:1 and 4:1 mergers. Figure 4.23 shows the different contributions from the small and the large progenitor galaxy and the resulting isophotal map. The particles originating from the small progenitor accumulate in an elongated torus-like structure that clearly has boxy isophotes. In contrast, the luminous material from the larger progenitor galaxy still has a disk-like appearance. In combination, the contribution from the larger progenitor – since it is three times more massive – dominates the overall properties of the remnant. This result holds for all 3:1 and 4:1 merger remnants. The more massive disk is not completely destroyed during the merger event and determines the overall structure of the remnant. For equal mass remnants both disk components are destroyed during the merger and they loose the memory of their initial state. Therefore both progenitors contribute equally and no dominant contribution from one of the progenitor disks is visible (Figure 4.24).

The isophotal analysis also provides further information with respect to the change of the relative orientation of the major axes of the isophotes. In general we can state that for the simulated merger remnants the amount of isophotal twist depends on the projection. This is demonstrated in Figure 4.25 for a more elongated and a nearly round projection of a 3:1
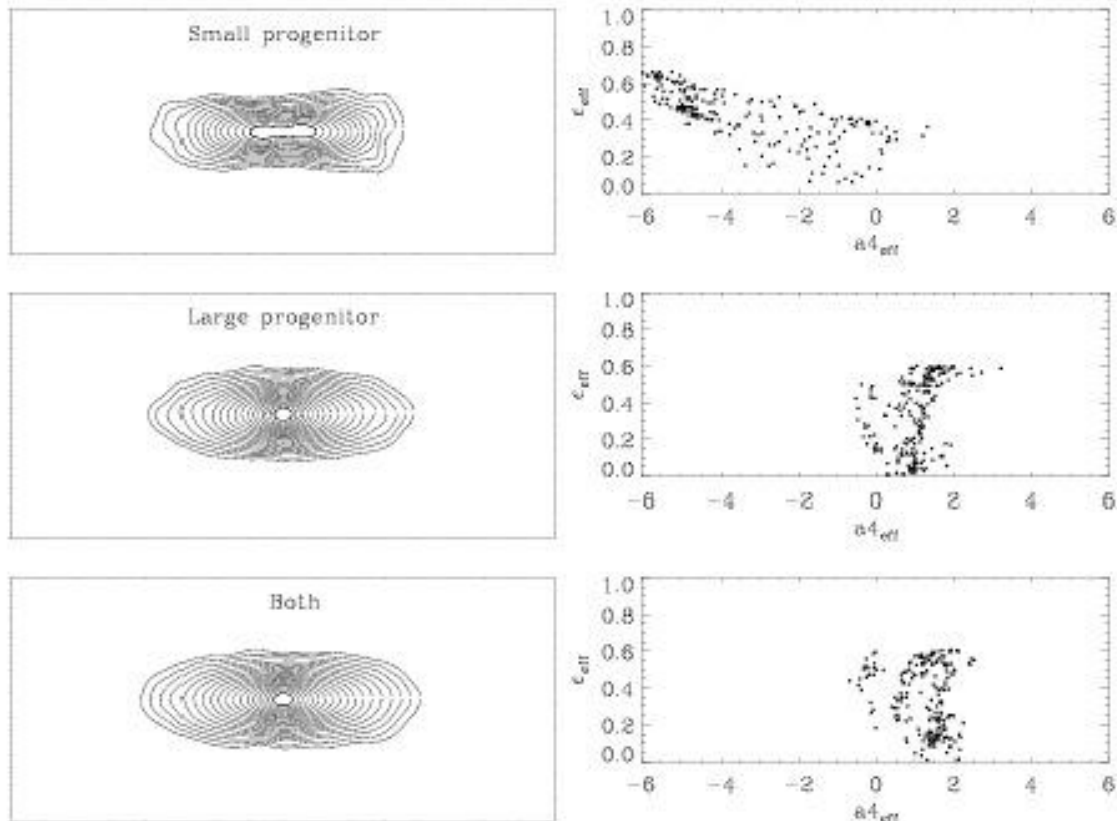
Figure 4.23: *Left row:* Characteristic isodensity contours of the remnant 3_1_H_8. The two upper panels shows the results for the luminous particles originating from the smaller and the larger progenitor, respectively. The lower panel shows the contours for both components together. *Right row:* Corresponding values for $a4_{eff}$ vs. ϵ_{eff} for 200 random projections of the chosen particle subset.

merger remnant. To get a quantitative measure for the isophotal twist we determined the relative position angle $\Delta\Phi$ between the isophote at $0.5\ r_{eff}$ and $1.5\ r_{eff}$ for every projection of the remnant. Figure 4.26 shows a comparison of isophotal twists for the characteristic remnants 1_1_H_8, 2_1_H_8, 3_1_H_8, and 4_1_H_8. The isophotal twist is in general larger for projections that appear nearly round. For ellipticities larger than $\epsilon_{eff} \approx 0.4$ the isophotal twist is $\Delta\Phi \leq 20°$. The distribution of $\Delta\Phi$ versus ϵ_{eff} for random projections of every remnant is almost consistent with observations of elliptical galaxies. However, the simulated remnants have larger isophotal twists at high ellipticities than the observed galaxies (see Figure 2.4 for comparison). Figure 4.27 shows nine 3:1 merger remnants with different initial disk orientations. The geometry of the merger seems to have a stronger influence on the isophotal twist than the mass ratio of the progenitor galaxies. However, it becomes clear that isophotal twist can be attributed to intrinsic triaxiality (see Section 4.1, Figure 4.14). The more oblate remnants 3_1_H_4, 3_1_H_5, and 3_1_H_6 clearly show smaller isophotal twist than the more prolate remnants 3_1_H_3 or 3_1_H_8.
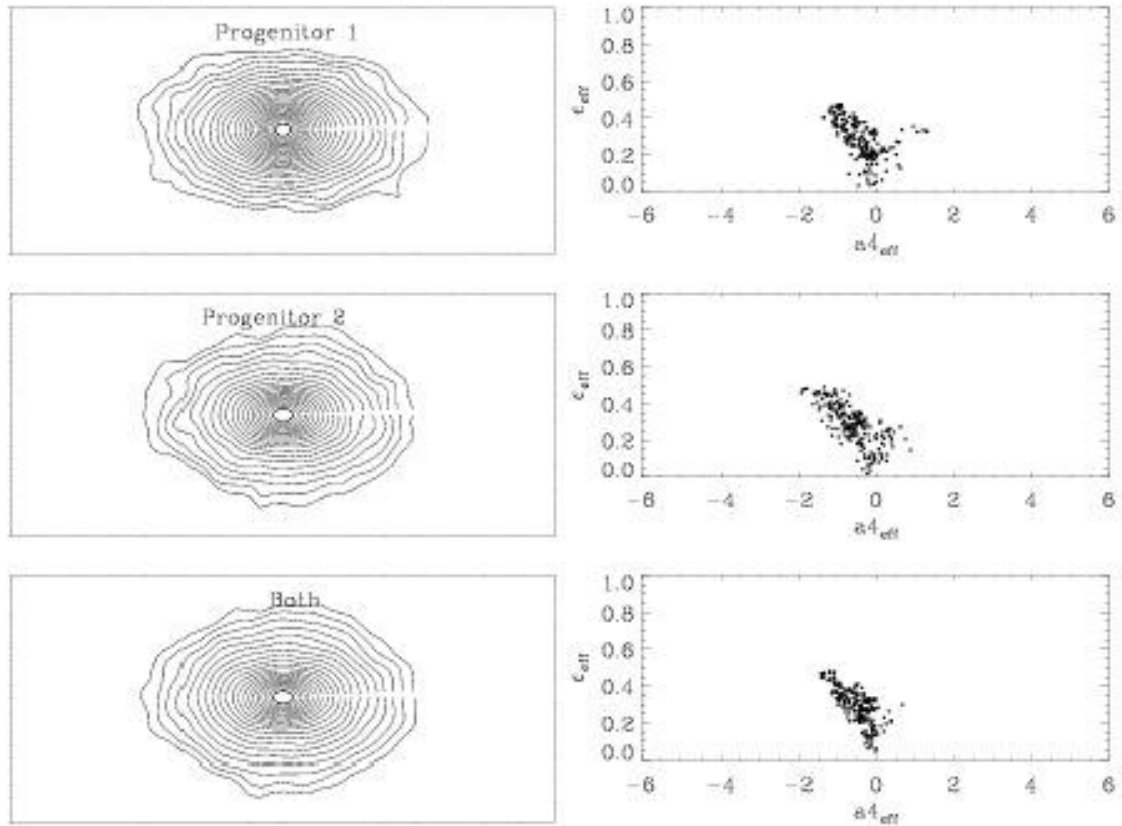
Figure 4.24: *Left row:* Characteristic isodensity contours of the remnant 1_1_H_8. The two upper panels show results for the luminous particles originating from the two progenitor galaxies, respectively. The lower panel shows the contours for both components together. *Right row:* Corresponding values for $a4_{\rm eff}$ vs. $\epsilon_{\rm eff}$ for 200 random projections of the chosen particle subset.
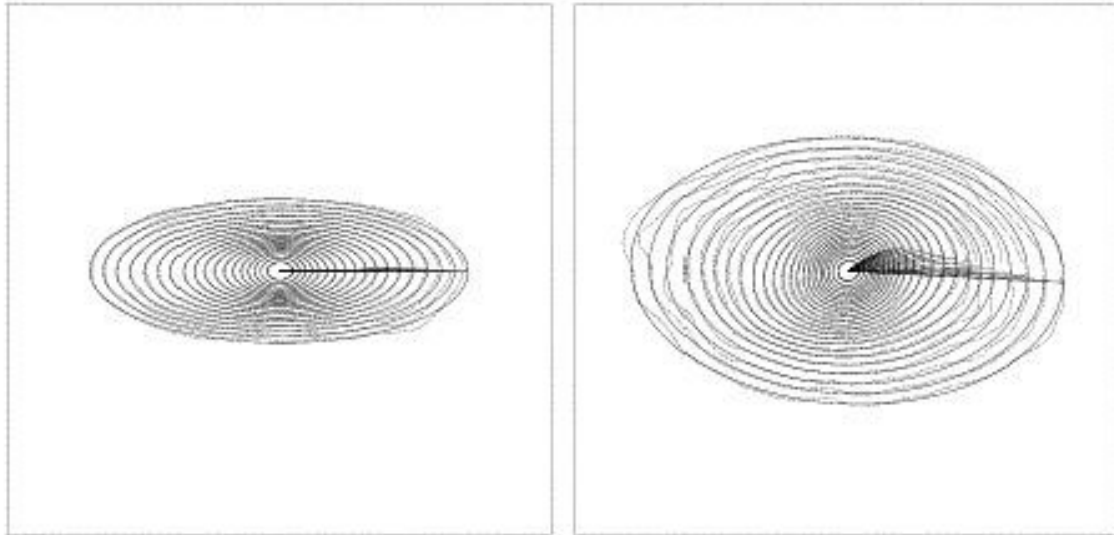
Figure 4.25: The real isophotes (dotted) and the best fitting ellipses (solid line) for the merger remnant 3_1_H_8 seen in a more elongated (left) and rounder (right) projection. The major axes are plotted for every isodensity contour. The change of direction of the axes indicates the isophotal twist. The box length is 3 length units.
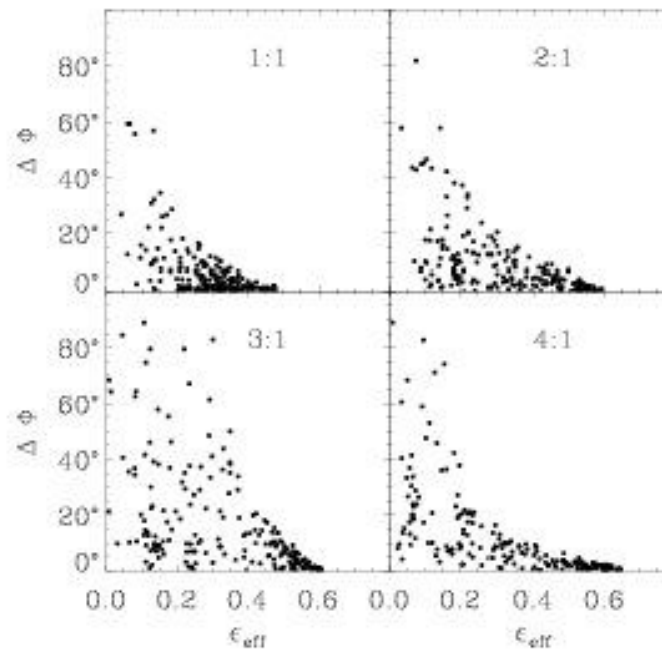

Figure 4.26: Isophotal twists $\Delta\Phi$ vs. ellipticity ϵ for the merger remnants 1_1_H_8, 2_1_H_8, 3_1_H_8, and 4_1_H_8. For every mass ratio 100 random projections are shown.
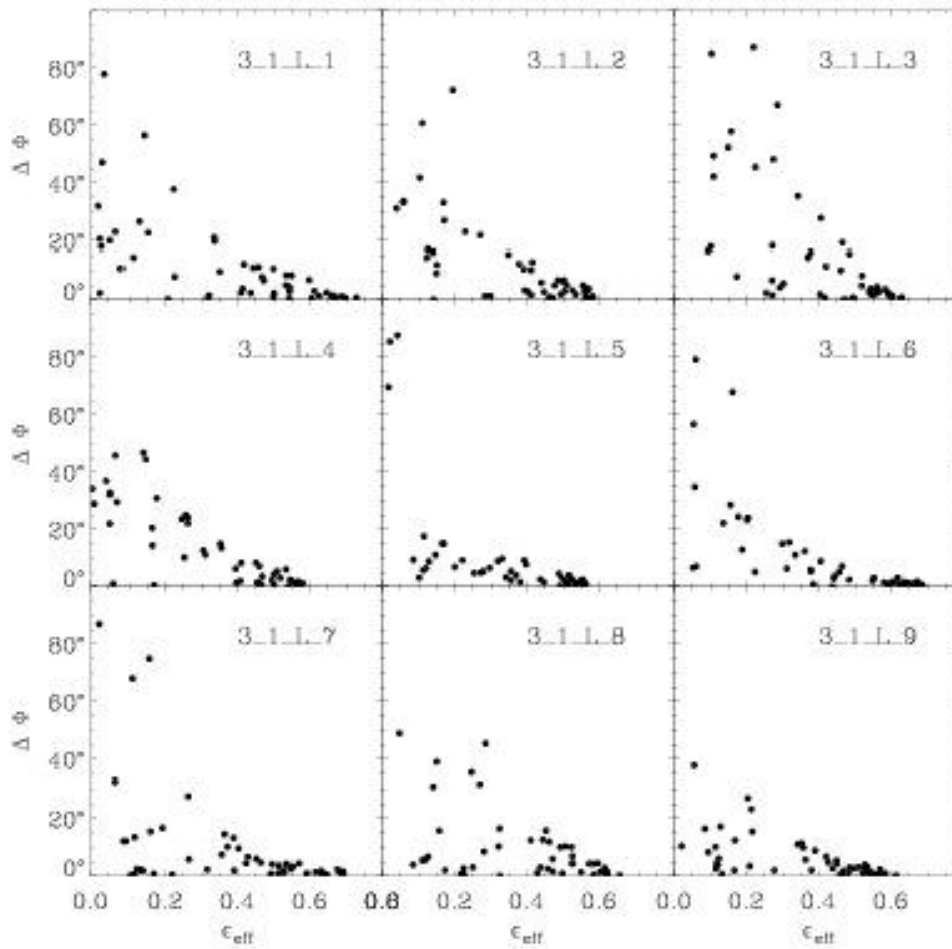
Figure 4.27: Isophotal twists for nine 3:1 merger remnants with different orbital geometries. For every geometry 50 random projections are shown.

4.3   Kinematics

To get kinematic information about the merger remnants we shift the densest region of the two-dimensional projection to the origin and perform a principal axis analysis of the two-dimensional moment-of-inertia tensor. Then we place a binned slit along the long and short apparent axis of each projection of the remnants and determine the mean velocity and the velocity dispersion for every bin. The central velocity dispersion σ_0 is determined as the average projected velocity dispersion of the stars inside a projected galactocentric distance of $0.2r_{\rm eff}$. We define the characteristic rotational velocity along the major and the minor axis as the projected rotational velocity determined around $1.5r_{\rm eff}$ and $0.5r_{\rm eff}$, respectively.
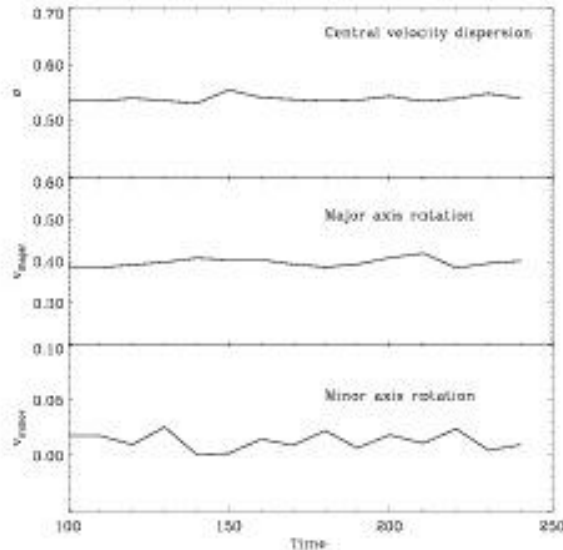

Figure 4.28: Time evolution of the characteristic kinematical parameters: projected central velocity dispersion $\sigma = \sigma_0$, major-axis rotation velocity $v_{\rm major} = v_{\rm maj}$ at $1.5\ r_{\rm eff}$, and minor-axis rotation velocity $v_{\rm minor} = v_{\rm min}$ at $0.5\ r_{\rm eff}$.

Figure 4.28 shows the time evolution for σ_0, $v_{\rm maj}$ and $v_{\rm min}$ for a 3:1 merger simulation which shows a behaviour characteristic for all simulations. The derived kinematical properties of the remnants stay nearly constant for a long time period and are therefore a good measure of the intrinsic kinematics of the simulated remnants. Similar to our approach in determining the isophotal shape, we construct probability density plots for the kinematical properties of the simulated remnants and compare them with observational data.

The normalized histograms for $v_{\rm maj}/\sigma_0$ are shown in Figure 4.29. There is a clear trend for 1:1 mergers to produce either non-rotating or slowly rotating ellipticals with $v_{\rm maj}/\sigma_0 \approx 0.2$. For 2:1 mergers the peak value is around $v_{\rm maj}/\sigma_0 \approx 0.35$. 3:1 and 4:1 merger remnants show significant rotation with peaks around $v_{\rm maj}/\sigma_0 \approx 0.5$ and 0.75, respectively. Figure 4.30 shows the distribution for $v_{\rm maj}/\sigma_0$ versus $\epsilon_{\rm eff}$. The area for slowly rotating boxy ellipticals (filled boxes) is almost completely covered by the data of 1:1 mergers while 2:1 mergers have rotational properties similar to faster rotating boxy and slowly rotating disky ellipticals. 3:1
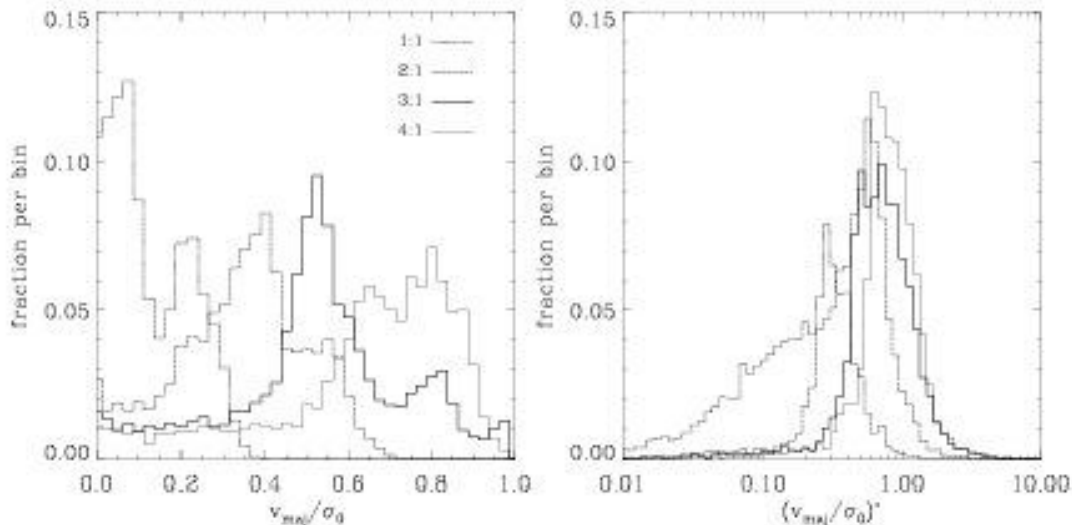
Figure 4.29: *Left:* Normalized histograms of $v_{\mathrm{maj}}/\sigma_0$ for 1:1, 2:1, 3:1, and 4:1 low-resolution mergers. *Right:* Normalized histograms of the anisotropy parameter $(v_{\mathrm{maj}}/\sigma_0)^*$.

and 4:1 are clearly fast rotating and show high ellipticities. They can be associated with observed fast rotating disky ellipticals (open diamonds). There is a clear trend for mergers with an increasing mass ratio to produce faster rotating ellipticals with higher ellipticities. All simulations are in good agreement with observations although the simulated remnants have slightly larger ellipticities than observed (see also Hernquist, 1993b).

It becomes clear from Figure 4.30 that our models do not lead to remnants with $v_{\mathrm{maj}}/\sigma_0 > 1$ around one effective radius. However, there exist observed ellipticals with higher values of $v_{\mathrm{maj}}/\sigma_0$. In addition, Rix et al. (1999) observed rotational properties of a small sample of fast rotating faint ellipticals up to large radii $\approx 2 - 3 r_{\mathrm{eff}}$ and found that some of the galaxies show extremely large values for local $v/\sigma \approx 3$ around two effective radii. Cretton et al. (2000a) used the simulations described in this thesis to perform a detailed comparison between the observed data and the simulated values. Figure 4.31 shows the results. The data of Rix et al. (1999) show both a steep rise of v/σ in the central parts and larger absolute values in the outer parts. Therefore our simulated remnants are unable to reproduce this observed trend of low-luminosity ellipticals. The implications of this result for the merger picture will be discussed in Chapter 6.

The anisotropy parameter $(v_{\mathrm{maj}}/\sigma_0)^*$ is defined as the ratio of the observed value of $v_{\mathrm{maj}}/\sigma_0$ and the theoretical value for an isotropic oblate rotator $(v/\sigma)_{\mathrm{theo}} = \sqrt{\epsilon/(1-\epsilon)}$ evaluated using the observed ellipticity ϵ_{eff} (Binney, 1978). This parameter has been used to determine whether a given galaxy with observed v_{maj}, σ_0 and ϵ_{eff} is flattened by rotation $[(v_{\mathrm{maj}}/\sigma_0)^* > 0.7]$ or by velocity anisotropy $[(v_{\mathrm{maj}}/\sigma_0)^* < 0.7]$ (e.g. Davies et al. (1983); Bender (1988b); Nieto et al. (1988) and Scorza & Bender (1995); see Section 2.2). Figure 4.29 shows the normalized histograms for the $(v_{\mathrm{maj}}/\sigma_0)^*$ values of the simulated remnants.
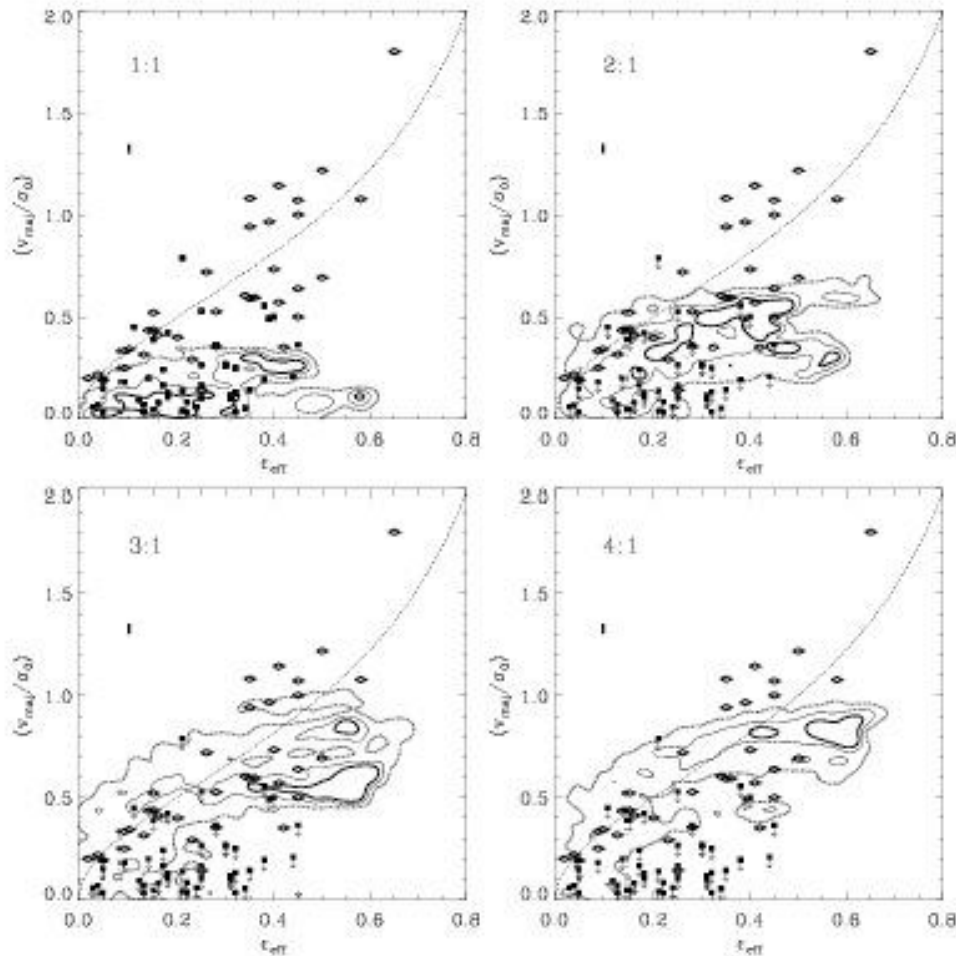
Figure 4.30: The ratio of rotational velocity along the major axis v_{maj} and central velocity dispersion σ_0 versus characteristic ellipticity ϵ_{eff} for 1:1, 2:1, 3:1, and 4:1 mergers. Values for observed ellipticals are overplotted. Filled boxes indicate data for boxy elliptical galaxies, open diamonds show data for disky ellipticals. The dashed line shows the theoretical value for an oblate isotropic rotator.

The 1:1 remnants show a peak at $(v_{maj}/\sigma_0)^* \approx 0.28$ with a more extended tail towards lower values. The anisotropy parameter is almost never larger than $(v_{maj}/\sigma_0)^* = 0.7$. In summary, equal mass merger remnants are systems with anisotropic velocity dispersions. 2:1 mergers show a median of $(v_{maj}/\sigma_0)^* \approx 0.5$ and are slightly more isotropic. 3:1 and 4:1 mergers with $(v_{maj}/\sigma_0)^* \approx 0.7$ and $(v_{maj}/\sigma_0)^* \approx 0.8$ are consistent with the model prediction for oblate isotropic rotators. Since the 3:1 and 4:1 remnants also have disky isophotes they perfectly cover the area populated by observed disky ellipticals in the $\log(v_{maj}/\sigma_0)^*$-$a4_{eff}$ diagram (Figure 4.32). 1:1 merger remnants are predominantly boxy and anisotropic. Therefore they are in good agreement with data from boxy ellipticals. 2:1 remnants cover the intermediate range.

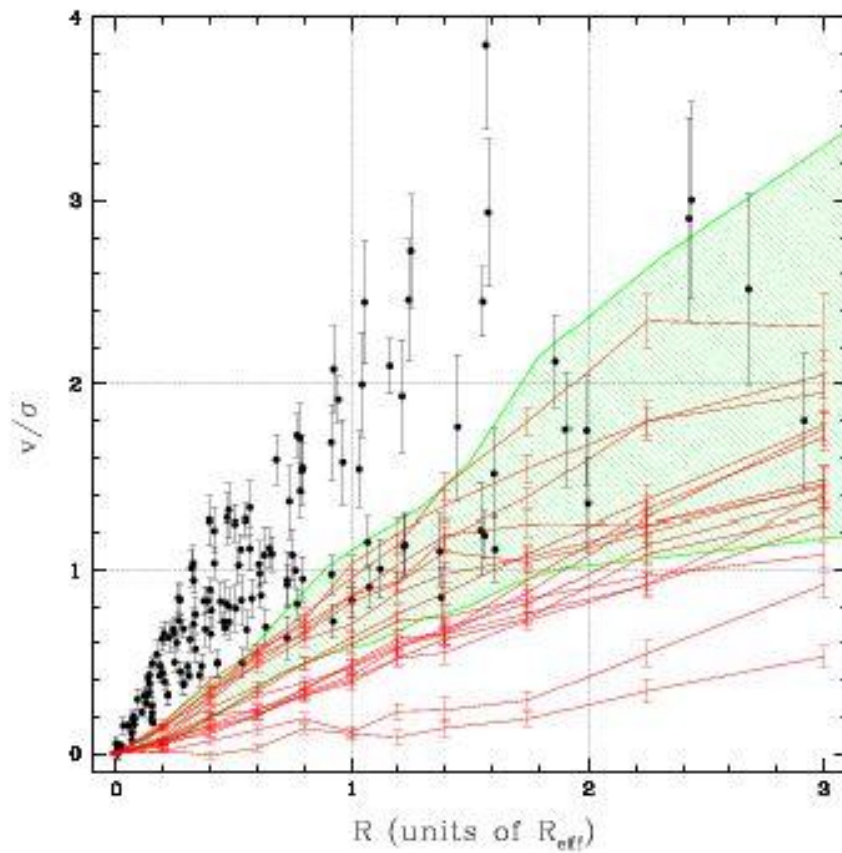Figure 4.31: Comparison of observed local (v/σ) (black dots, data from Rix et al., 1999) and local (v/σ) for the simulated merger remnants with geometries 1–14 seen edge on (lines with error bars). The shaded area corresponds to the range occupied by the edge-on models of Bendo & Barnes (2000). Both distributions are not compatible with the observed data. The figure is taken from Cretton et al. (2000a).
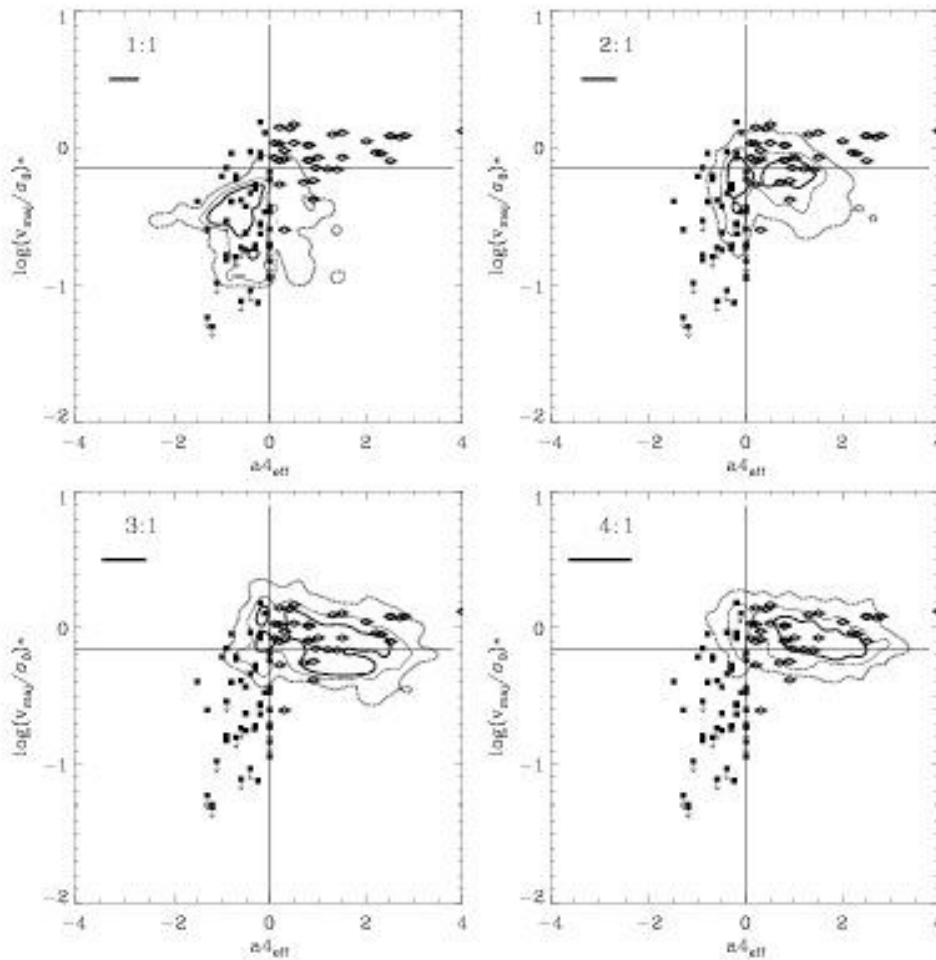
Figure 4.32: Anisotropy parameter $(v_{maj}/\sigma_0)^*$ versus $a4_{eff}$ for 1:1, 2:1, 3:1, and 4:1 mergers. Values for observed ellipticals are over-plotted. Filled boxes indicate data for boxy elliptical galaxies, open diamonds show data for disky ellipticals.

Figure 4.33: Amount of minor-axis rotation $\log(v_{\min}/\sqrt{v_{\mathrm{maj}}^2 + v_{\min}^2})$ versus $a4_{\mathrm{eff}}$ for 1:1, 2:1, 3:1, and 4:1 mergers. Values for observed ellipticals are over-plotted. Filled boxes indicate data for boxy elliptical galaxies, open diamonds show data for disky ellipticals.
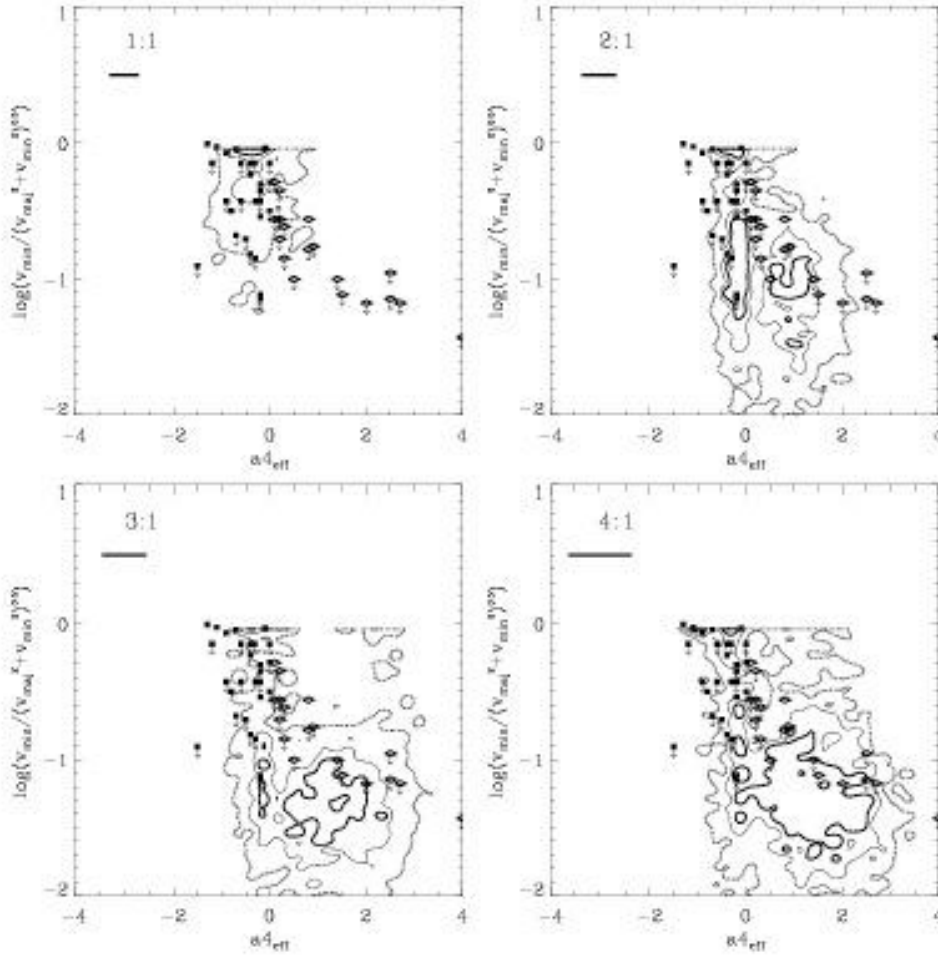
Minor-axis rotation in elliptical galaxies, in addition to isophotal twist (see Section 2.2), has been suggested as a sign for a triaxial shape of the main body of elliptical galaxies (Wagner et al., 1988; Franx et al., 1991). We investigate the minor-axis kinematics of the simulated remnants by parametrizing the amount of minor-axis rotation as $v_{\min}/\sqrt{v_{\mathrm{maj}}^2 + v_{\min}^2}$ (Binney, 1985). Since almost all 1:1 mergers show a significant amount of minor-axis rotation (Figure 4.33) they cannot be oblate objects from the theoretical point of view. This is consistent with the result that 1:1 mergers are intrinsically triaxial (see Figure 4.14). 3:1 and 4:1 remnants show significantly less minor-axis rotation than 1:1 merger remnants although the spread in the data is very large. This finding is consistent with the more oblate shape of 3:1 and 4:1 mergers. The theoretical expectation is that they also show smaller isophotal twists. This trend, however, cannot clearly be seen in the data (see Figure 4.26, but see Section 4.4).

4.4   Individual examples

It has been argued by Naab et al. (1999) on the basis of two high-resolution simulations that equal mass mergers lead to slowly rotating, pressure supported systems with boxy isophotes and, in contrast, 3:1 mergers lead to fast rotating systems with disky isophotes. In the previous section we have shown that this result is statistically true for all simulated geometries. 2:1 mergers show intermediate properties while 4:1 mergers have almost the same properties as 3:1 remnants. Further insight into the process of collisionless merging is provided by investigating four individual mergers in detail. Part of these show peculiar properties that are not observed. Figures 4.34–4.37 show the observed data (open squares) and 50 random projections of the simulated remnant over-plotted with filled circles, respectively.
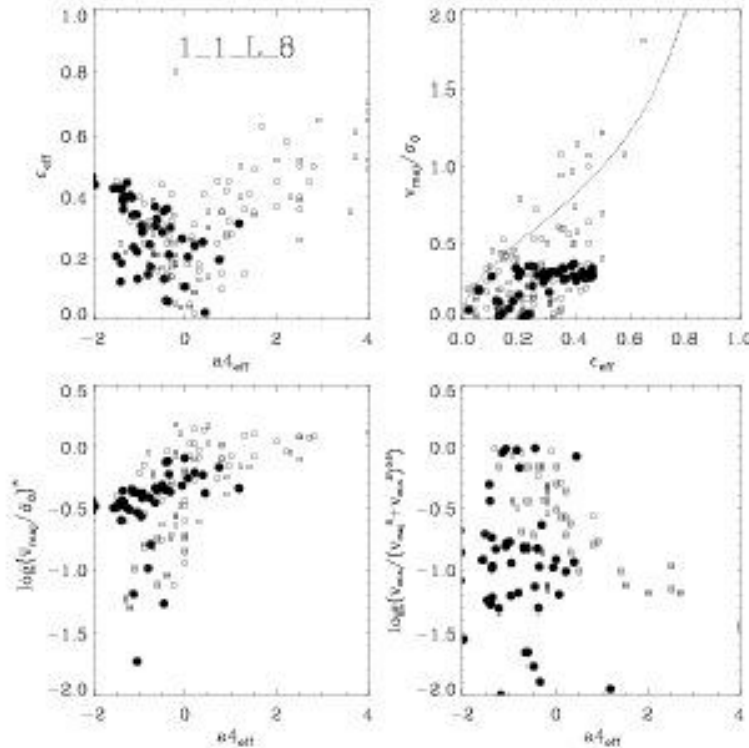

Figure 4.34: Same as Figure 2.5 with the observed data plotted as open squares. The measurement for 50 random projections of the merger remnant 1_1_L_8 are over-plotted (black dots).

The equal mass merger 1_1_L_8 (Figure 4.34) has two prograde rotating disks slightly inclined with respect to the orbital plane. The isophotal shape is clearly boxy with $a4_{\mathrm{eff}} \approx 1.5$. However, the remnant exhibits significant rotational support. $v_{\mathrm{maj}}/\sigma_0$ can reach values up to 0.3–0.4 for apparent ellipticities $\epsilon_{\mathrm{eff}} \approx 0.4$. This leads to values for the anisotropy parameter of $\log(v_{\mathrm{maj}}/\sigma_0)^* \approx -0.5$ which only covers the less anisotropic part of the observed distribution of boxy ellipticals. The distribution for minor-axis rotation is rather broad and

projection effects alone can almost account for the observed spread in the boxy regime.
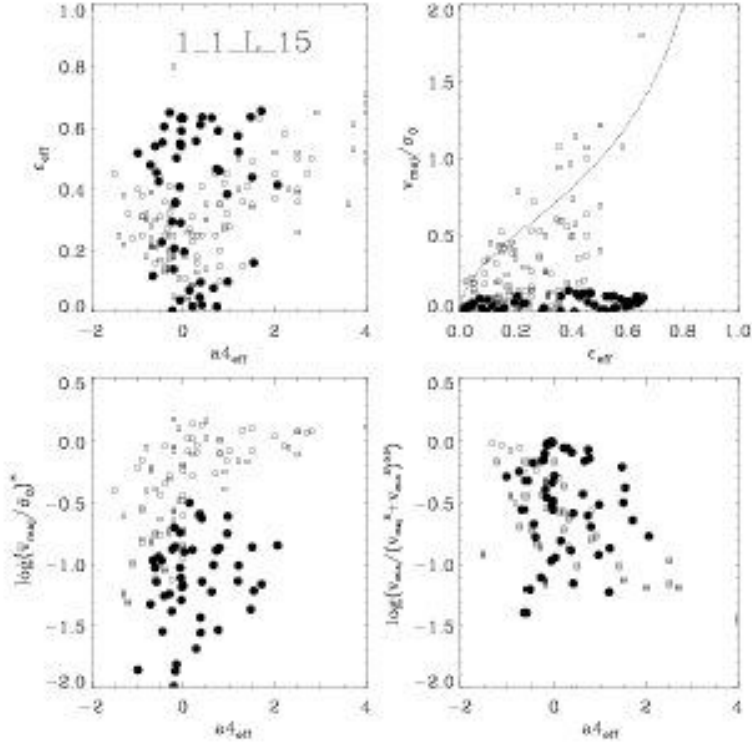

Figure 4.35: Same as Figure 4.34 for the equal mass merger remnant 1_1_L_15

Another example is the equal mass merger 1_1_L_15 which has one retrograde rotating disk, in contrast to the merger 1_1_L_8. The effect can be seen in Figure 4.35. There is no clear correlation between ϵ_{eff} and $a4_{\mathrm{eff}}$. Nearly half of the projected remnants show disky isophotes. In total, this remnant is almost not rotating and $v_{\mathrm{maj}}/\sigma_0 < 0.1$ for all projections. For the anisotropy parameter we get $\log(v_{\mathrm{maj}}/\sigma_0)^* \leq -0.5$. This indicates that the remnant is completely supported by anisotropic velocity dispersions. We find a significant amount of disky projections with a high degree of anisotropy and a large amount of minor-axis rotation. Both trends are not observed for real elliptical galaxies. However the impact of comparable merger geometries on the statistical investigation is only weak for $(v_{\mathrm{maj}}/\sigma_0)^*$ versus $a4_{\mathrm{eff}}$ (see Figure 4.32) or not detectable for $v_{\mathrm{min}}/\sqrt{v_{\mathrm{maj}}^2 + v_{\mathrm{min}}^2}$ versus $a4_{\mathrm{eff}}$ (see Figure 4.33). The different rotational properties of the two 1:1 mergers discussed here can be understood from the fact that the spins of the galaxies were aligned for 1_1_L_8 and pointed in opposite directions for 1_1_L_15, therefore the resulting angular momentum is larger for the merger 1_1_L_8.

The merger 3_1_L_5 is the fastest rotator among all the simulated 3:1 remnants. Its shape is almost oblate with $\mathcal{T} \approx 0.2$ (see Figure 4.14). It reaches a maximum value of $v_{\mathrm{maj}}/\sigma_0 \approx 1$ (Figure 4.36). The isophotes are disky and perfectly follow the observed trend for ϵ_{eff} versus
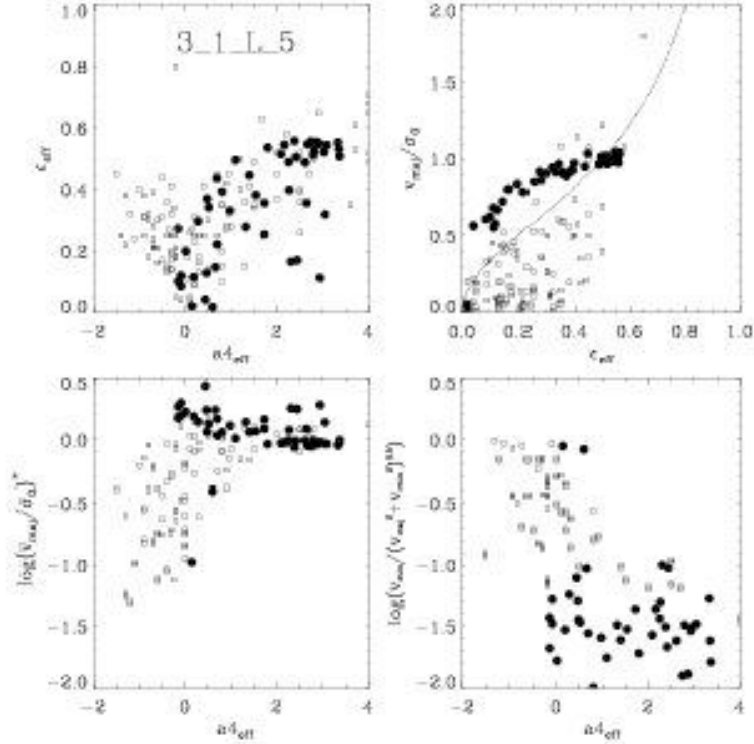
Figure 4.36: Same as Figure 4.35 for the 3:1 merger remnant 3_1_L_5.

$a4_{\mathrm{eff}}$. $\log(v_{\mathrm{maj}}/\sigma_0)^* > 1$ for all projections and is in excellent agreement with observations. Minor-axis rotation is very small and also in good agreement with observations. For this merger the more massive disk rotates in retrograde direction and the small disk rotates in prograde direction.

The merger 3_1_L_3 is the slowest rotator among all the simulated 3:1 remnants. Only a maximum value of $v_{\mathrm{maj}}/\sigma_0 \approx 0.5$ is reached (Figure 4.37). The isophotes are predominantly disky but do not strictly follow the observed trend for ϵ_{eff} versus $a4_{\mathrm{eff}}$. Although the remnant is disky, $\log(v_{\mathrm{maj}}/\sigma_0)^*$ is generally smaller than -0.2 for all projections, in contradiction with observations. Significant minor-axis rotation can be detected for projections with disky isophotes which is also not observed for elliptical galaxies. The merger remnant has an almost prolate shape with $\mathcal{T} \approx 0.8$ (see Figure 4.14). As we have already seen, the remnant shows large isophotal twist already for ellipticities $\epsilon_{\mathrm{eff}} \leq 0.4$ (see Figure 4.27). For this merger both disks rotate in a prograde sense. This result is puzzling since one would naively assume that the prograde merger rotates faster than the retrograde one. Possible explanations for this behaviour will be discussed in Chapter 6.
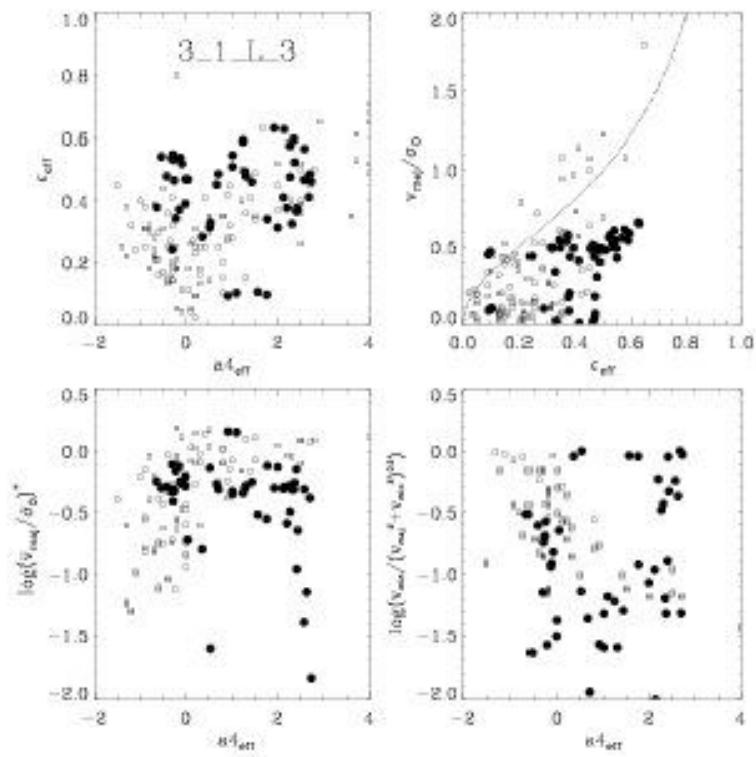
Figure 4.37: Same as Figure 4.36 for the 3:1 merger remnant 3_1_L_3

Chapter 5

LOSVDs of merger remnants

In addition to isophotal shape and global kinematic properties, we determine the line-of-sight velocity distributions (LOSVD) of the simulated merger remnants and compare them in detail with observed global and local correlations (Bender et al., 1994; see Section 2.3).

5.1 Line-of-sight velocity distributions

To measure the line-of-sight velocity distribution of a merger remnant we shifted the densest region of every two-dimensional projection to the origin and performed a principal axis analysis of the two-dimensional moment-of-inertia tensor (see Section 4.3). Then we placed a slit with a width of 0.3 unit lengths along the apparent long axis of each projected remnant. Thereafter we binned all particles falling within each grid cell in velocity along the line-of-sight. The grid spacing was chosen to be 0.2 which corresponds to $\approx 15\%$ of the projected half-mass radius. Figure 5.1 shows a schematic sketch of the grid we used to derive the LOS-VDs for every remnant. The shaded bins indicate the location at one projected half-mass radius r_{eff}. For the derivation of the amplitudes h_3 and h_4 only information up to this radius was used. The width of the velocity bins was set to a value of 0.2 for line-of-sight velocities v_{los} in the range $-4 \geq v_{\text{los}} \geq 4$. This results in 80 velocity bins over the whole interval. Using the binned velocity data we constructed the histograms of the line-of-sight velocity for each bin along the grid. This quantity is called the velocity profile $P(v)$ or line-of-sight velocity distribution (LOSVD). Subsequently we parametrized the velocity profile using Gauss-Hermite basis functions (see Section 2.3) to extract the kinematic parameters of each profile (σ_{fit}, v_{fit}, h_3, h_4). Technically we performed a least squares fit for each profile using the appropriate NAG Fortran library subroutines. We checked that the resulting parameters do not depend on the chosen bin size for v_{los}. For simulations with low resolution this procedure might lead to relatively large errors for the resulting velocity profile. To overcome the resolution problems Bendo & Barnes (2000) proposed to overlay 5 frames equally spaced over small intervals in time. However, it is not clear how susceptible this procedure is to errors in the derivation of the three-dimensional shape of the remnant. Cretton et al. (2000a) averaged the profiles of 10 different position angles of the slit between $0°$ and $90°$ in the equatorial plane. This might lead to problems if one takes into account that the specific shape of the velocity profiles of the simulated remnants strongly depends on projection effects (see Figure 5.6, later this Chapter). The simple approach we followed here was to increase the resolution of the
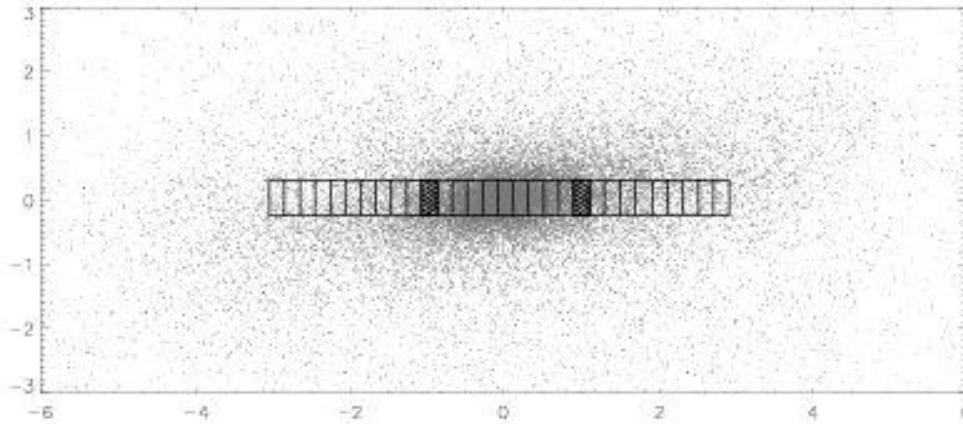
Figure 5.1: Schematic illustration of the artificial grid used to determine the LOSVDs of a 3:1 merger remnant. The bins at r_{eff} are marked and can be found in Figures 5.2, 5.3, and 5.5.

simulations to 160000 luminous particles for 1:1 mergers and 106666 particles for 3:1 mergers, whereas Bendo & Barnes (2000) only used 65532 luminous particles. The large number of particles in combination with the relatively large slit width guarantees that at least 2000 particles fall within each slit inside one effective radius. Because of the large computational effort to perform direct summation simulations for particle numbers of ≈ 40000 (even with GRAPE-5) we restricted ourselves to a small subset of mass ratios and orbital geometries. We used only mergers with a mass ratio of 1:1 and 3:1 and geometries 8 and 15 since these are representative for the slowly rotating and fast rotating class of collisionless merger remnants (Naab et al., 1999, see Chapter 4).

Figure 5.2 and 5.3 show typical examples for the LOSVDs of the remnants 1_1_H_8 and 3_1_H_8 seen edge on. The profiles are shown for each bin inside a radius d of two unit lengths. The measured profiles are indicated by open squares while the solid line gives the best Gauss-Hermite fit (as described in Section 2.3) for each bin. Additionally, the number of particles and the values for h_3 and h_4 for each bin are given. Figures 5.4 and 5.5 show a blow up of the bins at $\pm r_{\text{eff}}$ (indicated by the shaded bins in Figures 5.2 and 5.2). Here the measured LOSVDs (open squares) with the errors and the decomposition into the Gauss-Hermite basis functions are given. These plots are characteristic for all simulated remnants and show that the LOSVDs of merger remnants deviate from a pure Gaussian. The absolute values for h_3 (this parameter measures the asymmetries of the LOSVD) lie in the range $0.001 \leq h_3 \leq 0.1$ and are in good agreement with observations. However, the effective h_3 is always positive (at least here, see below for the discussion of projection effects). This indicates line profiles with a steep retrograde wing and a broad prograde wing (note that the sign of v_{fit} should be multiplied with that of h_3 to get a correct measure of the asymmetry of the LOSVD).

Figure 5.2: The measured LOSVD (open squares) along the major axis of the 1_1_H_8 merger remnant shown for the 20 innermost bins starting at the upper left at a distance of $d = -1.9$ from the center. The dotted lines indicate the best fitting Gaussian. The solid lines give the best Hermite fit including the third- and fourth-order Gauss-Hermite functions with the given amplitudes h_3 and h_4. The marked plots show the LOSVD at $\pm r_{\text{eff}}$.
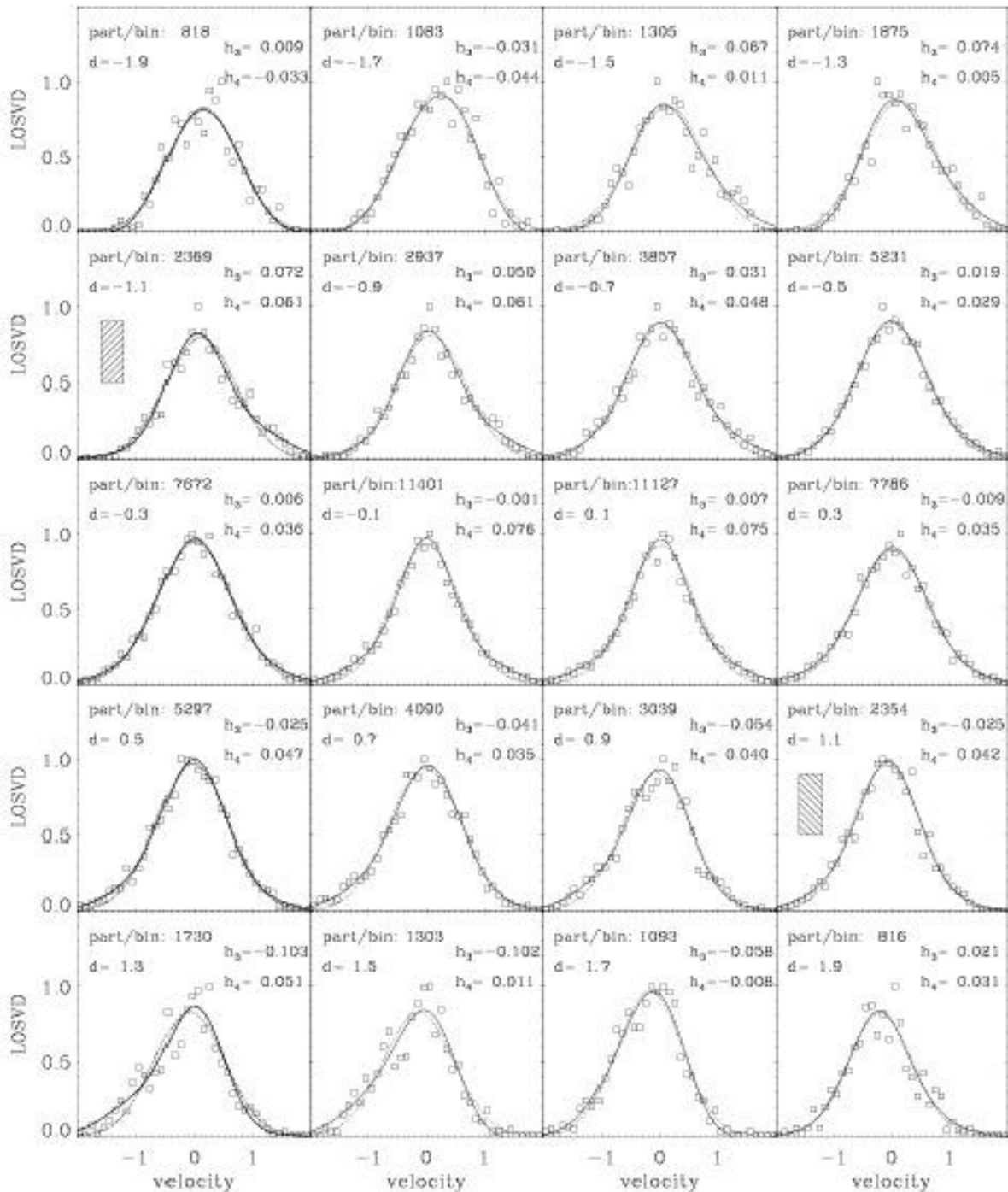
Figure 5.3: The measured LOSVD (open squares) along the major axis of the 3_1_H_8 merger remnant shown for the 20 innermost bins starting at the upper left at a distance of $d = -1.9$ from the center. The dotted lines indicate the best fitting Gaussian. The solid lines give the best Hermite fit including the third- and fourth-order Gauss-Hermite functions with the given amplitudes h_3 and h_4. The marked plots show the LOSVD at $\pm r_{\mathrm{eff}}$.
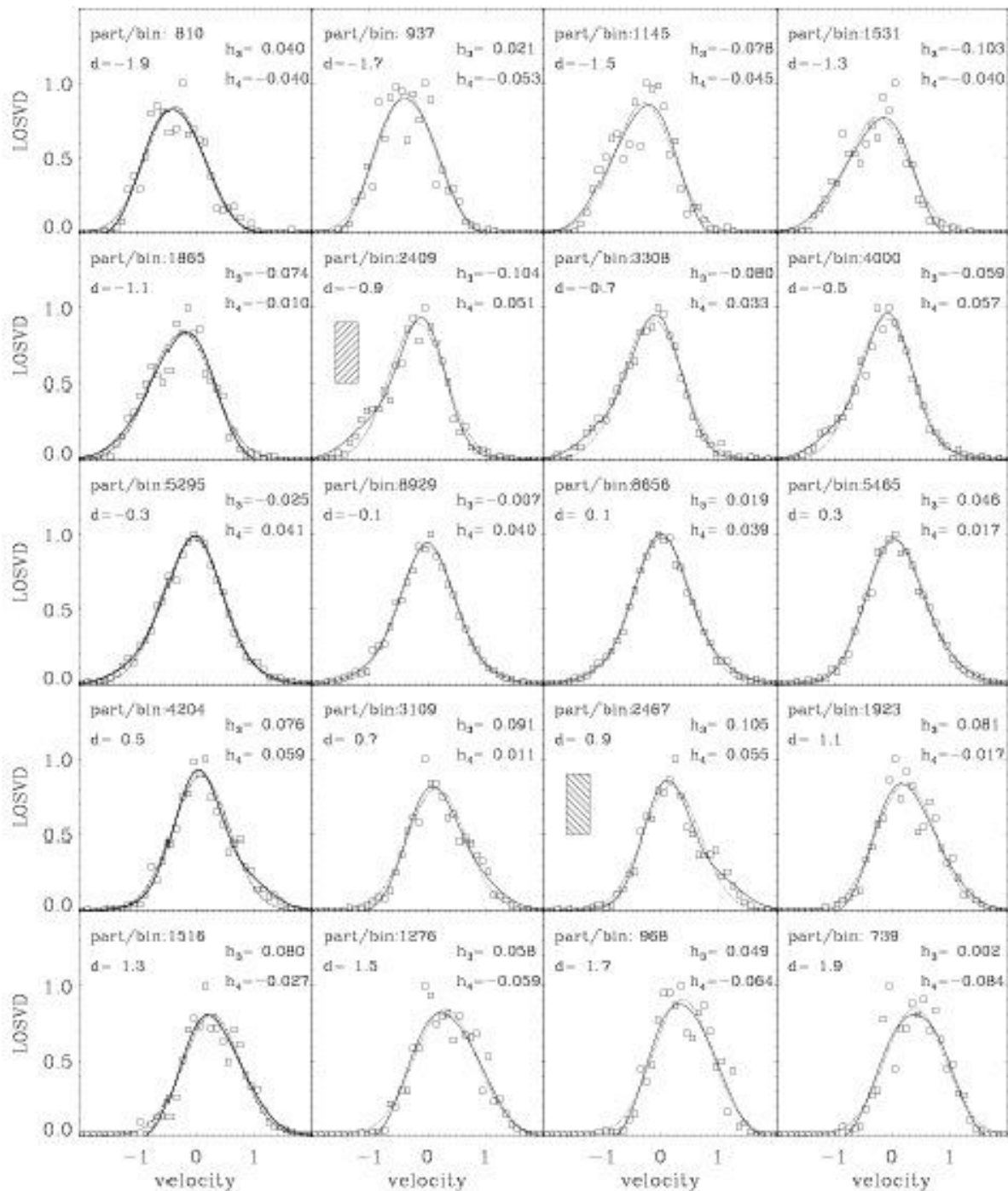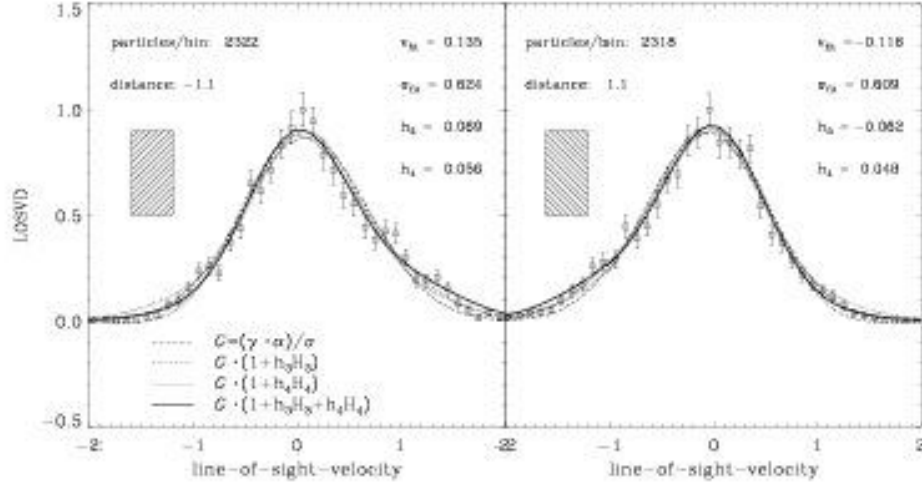
Figure 5.4: Mean data (open squares) for the LOSVD at $d = -1.1$ (left) and $d = 1.1$ (right) for the equal-mass merger remnant 1_1_H_8. The errors were derived by bootstrapping. The best fitting Gaussian G (long dashes), the sum of G and the third-order Gauss-Hermite basis function H_3 with amplitude h_3 (short dashes), the sum of G and the fourth-order Gauss-Hermite basis function H_4 with amplitude h_4 (dotted), and the sum $G \times (1 + h_3 H_3 + h_4 H_4)$ (thick line) is shown.

Figure 5.5: Same as Figure 5.4 but for the 3:1 merger remnant 3_1_H_8. Data are taken at $d = -0.9$ (left) and $d = 0.9$ (right)

The parameter measuring the symmetric deviation of the LOSVD from a Gaussian h_4 is always positive for radii inside r_{eff}. Here the line profile is more peaked than a Gaussian. At larger radii h_4 can become negative corresponding to a flat-top velocity distribution. The errors in the measurements are relatively small (see Figures 5.4 and 5.5) and are consistent with the fits.

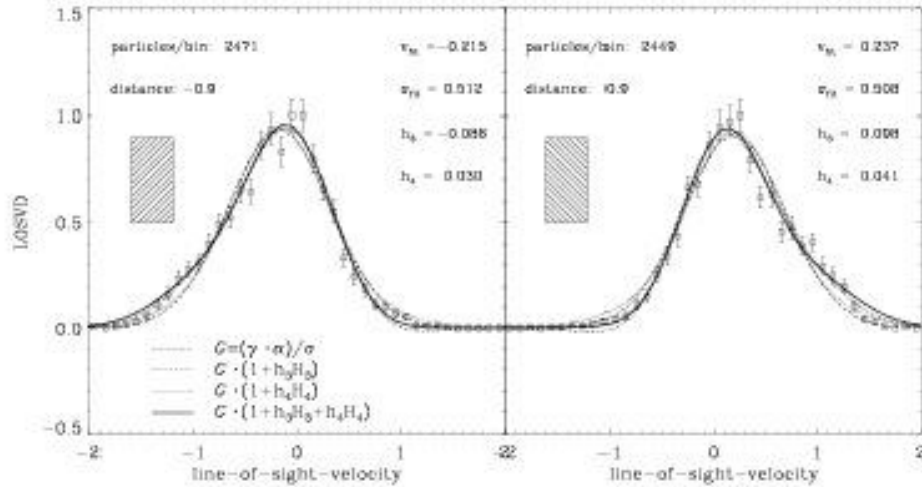Now we can take each simulated remnant and derive radial profiles for v_{fit}, σ_{fit}, h_3, and h_4 with small errors over a large range in radius. Figure 5.6 shows the radial profiles of v_{rot}, σ, v_{rot}/σ, h_3, and h_4 for projections along the three principal axes of the remnant 3.1.H.8. We must note that v_{rot} and σ as plotted here are the true moments of the velocity distribution while v_{fit} and σ_{fit} are the values derived from the best fitting Gaussian. However, the difference is less than 10%. This figure already suggests that projection effects change the characteristic shape of the kinematic profiles. The velocity dispersion σ shows a stronger peak at the center of the remnant if the long axis of the slightly prolate shaped remnant is aligned with the line-of-sight. h_3 is correlated with v_{rot} for the projection perpendicular to the long axis. This corresponds to LOSVDs that have a steep retrograde wing and broad prograde one (see Figure 2.8 and Figures 5.2 and 5.3). For the projections along the two remaining axes the LOSVDs are almost symmetric with an h_3 that is almost zero or slightly anti-correlated with v_{fit}. The parameter h_4 is always positive inside r_{eff} (≈ 1 unit length) describing a LOSVD that is more peaked than a Gaussian (see Figure 2.8). Figure 5.7 shows the local correlations for h_3 versus v_{fit}/σ_{fit} again for the projections along the long, intermediate, and short principal axis, respectively. Here we plot the values of h_3 versus v_{fit}/σ_{fit} for every bin along the slit inside two r_{eff}. However, observations only extend to r_{eff}. It becomes clear from this plot that projection effects can also change the shape of this local correlation dramatically. Therefore it will be necessary to investigate projection effects in detail.

In addition to projection effects and the mass ratio, the initial merger geometry could have a strong influence on the shape of the LOSVD. The computational effort for high-resolution studies of the parameter space is, however, too large. Therefore it is necessary to test whether low-resolution simulations result in remnants with comparable kinematic properties and to use those to investigate the parameter space. Figure 5.8 and Figure 5.9 show a comparison between a high-resolution and low-resolution 1:1 and 3:1 merger, respectively. Besides local deviations we find in general a good agreement for all measured kinematic data. The errors for radii larger than $r \approx 1$ are significantly larger for low-resolution simulations. However, the influence on our conclusions should be small since for further investigations we use only data inside one effective radius of every remnant and this never gets larger than 1.3 unit lengths.

Following Bender et al. (1994) we define a characteristic line-shape parameter $h3_{eff}$ as the mean value of h_3 between 0.25 r_{eff} and 0.75 r_{eff} for every projection. Thereafter we can test correlations between all global parameters we have defined up to now if we investigate the remnants from different viewing angles. Figure 5.10 shows the correlation between $h3_{eff}$ and v_{rot}/σ_0 for 14 different orbital geometries of equal-mass mergers seen from 50 random viewing angles, respectively. The observed correlations (see Figure 2.9) are indicated by a straight line. There seem to exist two classes of merger remnants. The extremely slowly rotating remnants with $v_{rot}/\sigma_0 \leq 0.1$ result from mergers with counterrotating disks as is indicated by the letter (r) in the plot. The data points fall perfectly on the observed correlation. This is not surprising since the only limitation here is the spread in $h3_{eff}$ which is always in

good agreement with observations. The faster rotating remnants $v_{rot}/\sigma_0 \leq 0.3$ originate from corotating progenitor disks. They clearly show positive values for $h3_{eff}$ even for $v_{rot}/\sigma_0 \geq 0.15$ and do not follow the correlation of observed ellipticals.

The correlation between $h3_{eff}$ and $a4_{eff}$ for the equal-mass remnants is shown in Figure 5.11. In general, all the data for almost all remnants is consistent with observations. $h3_{eff}$ is always around zero or even positive and the observational data allow those values only for boxy elliptical galaxies. Retrograde remnants show some very disky projections that do not follow the observed correlation (see remnant 1.1.L.6 in Figure 5.11).

Figure 5.12 shows the local correlation between h_3 and v_{fit}/σ_{fit}. To be consistent with observations we only use data inside r_{eff}. We can assume that galaxies on the sky have random orientations. Therefore the observed correlation must already contain projection effects. In case we want to choose a successful model for elliptical galaxies, the projected properties of this model must not be in disagreement with the observed distribution. However, the observed distribution is relatively complex (see Figure 2.10). Nevertheless, we approximate the observations with two straight lines for comparison. The innermost one shows the correlation for $-0.3 \leq v_{fit}/\sigma_{fit} \leq 0.3$. This gives only a mean correlation for all observed ellipticals. The slope for boxy ellipticals is slightly steeper, but never becomes positive. For the simulated equal-mass merger remnants we can state that there is a correlation between h_3 and v_{fit}/σ_{fit}. The tilt of the correlation depends on the orbital geometry. The mergers with geometries 1–7 clarify this trend. Here one of the disks changes its sense of rotation stepwise from corotating to counterrotating (see Table 3.1) during the same time that the tilt changes stepwise from positive values to negative values. All mergers with counterrotating disks (indicated by (r) in Figure 5.12) agree perfectly with the observed distribution. In contrast, most of the corotating mergers that rotate faster show a positive slope and are therefore inconsistent with observations.

Now the same correlations can be investigated for the low resolution mergers with a mass ratio of 3:1. The correlation between $h3_{eff}$ and v_{rot}/σ_0 for 15 geometries is shown in Figure 5.13. All merger remnants rotate fast with $v_{rot}/\sigma_0 \leq 0.5$ to $v_{rot}/\sigma_0 \leq 0.8$. For most of the geometries where the massive disk is rotating in a prograde sense, $h3_{eff}$ is predominantly positive for all projections. If the massive disk is rotating in a retrograde sense $h3_{eff}$ becomes zero or slightly negative. However, absolute values for $h3_{eff}$ (and therefore the asymmetry in the line profiles) are still too small to fit the observations. No remnant has $h3_{eff} < -0.05$. To summarize, for all projections with $v_{rot}/\sigma_0 \geq 0.4$ the properties are not in agreement with observations, since we find no remnant with $h3_{eff} \leq -0.05$.

Testing the correlation between $h3_{eff}$ and $a4_{eff}$ we find no correlation at all (Figure 5.14). $h3_{eff}$ is distributed around zero regardless of the isophotal shape.

For the local relation between h_3 and v_{fit}/σ_{fit} the slope of the correlation depends on the merger geometry, like for equal mass mergers. Prograde mergers, e.g. those with geometries 1–3 or 8, lead to correlations showing a positive slope over the whole interval. For retrograde mergers, e.g. geometries 5, 6 or 12, the slope in the outer parts changes sign and points in the "observed" direction, but most of the projections still show positive h_3 for positive velocities. In the inner part, $-0.3 \leq v_{fit}/\sigma_{fit} \leq 0.3$, no merger is able to reproduce the observed trend. The slope is either positive or zero with a large spread.
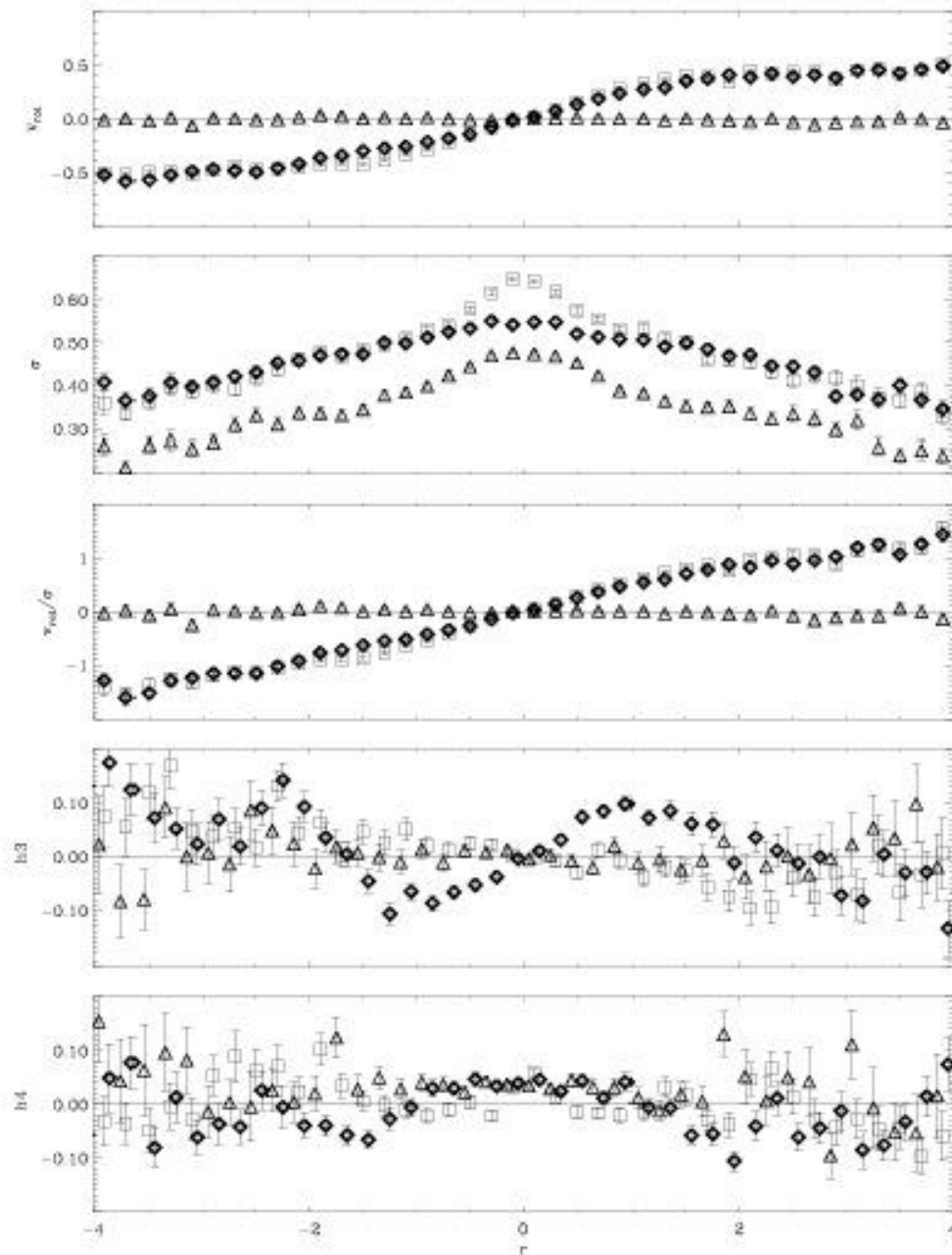
Figure 5.6: Properties of a 3:1 merger remnant measured along a slit aligned with the major axis (open squares), the intermediate axis (diamonds) and the small axis (open triangles). Rotational velocity $v_{\rm rot}$, local velocity dispersion σ, $v_{\rm rot}/\sigma$, $h3$, and $h4$ versus radius in units of $r_{\rm eff}$. The values for $h3$ and $h4$ along the intermediate (diamonds) and short (triangles) have an artificial offset of ± 0.05 in radius to identify individual error-bars.
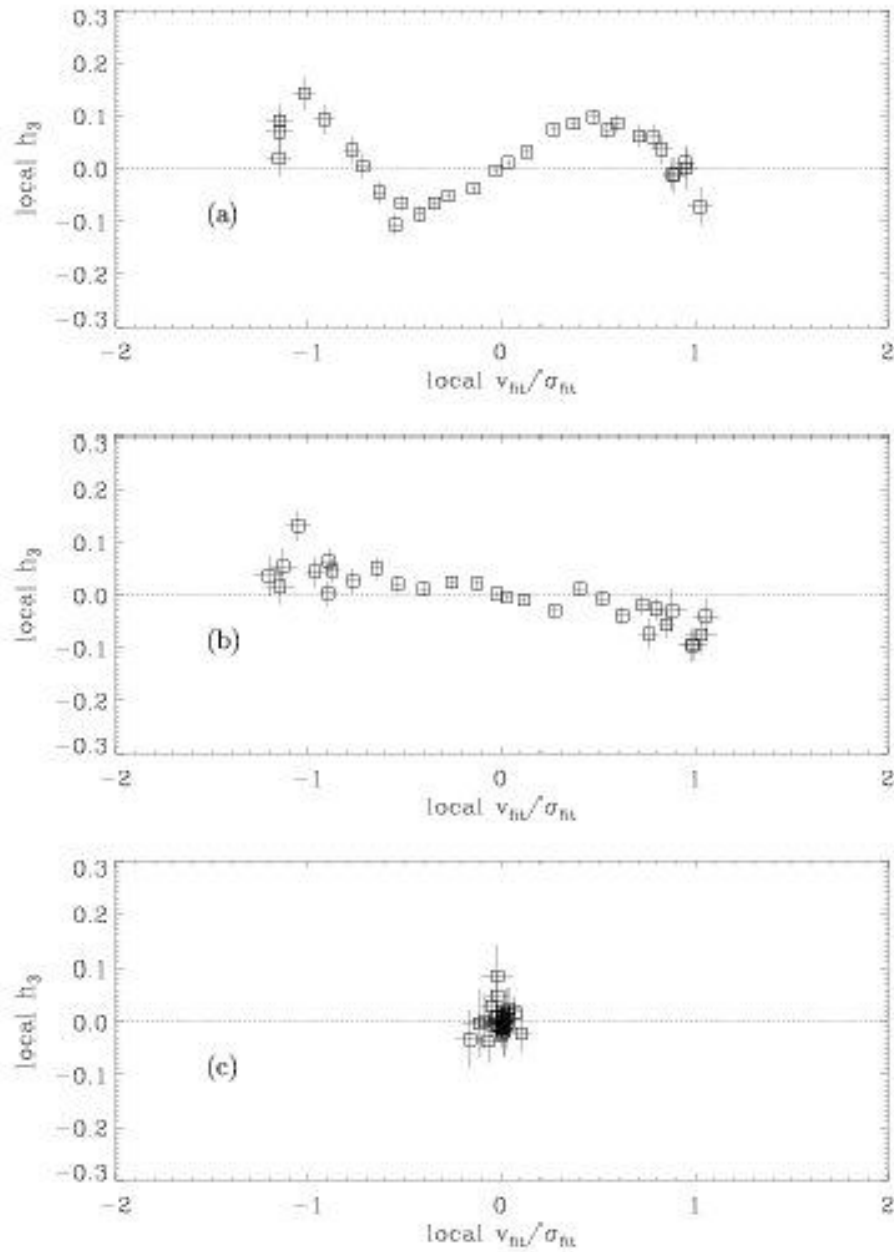
Figure 5.7: Local correlation between $h3$ and v_{maj}/σ_0 for data inside $3\,r_{eff}$. The data is shown for 3 different projections: along the long (a), the intermediate (b) and the short principal axis (c) of the remnant.
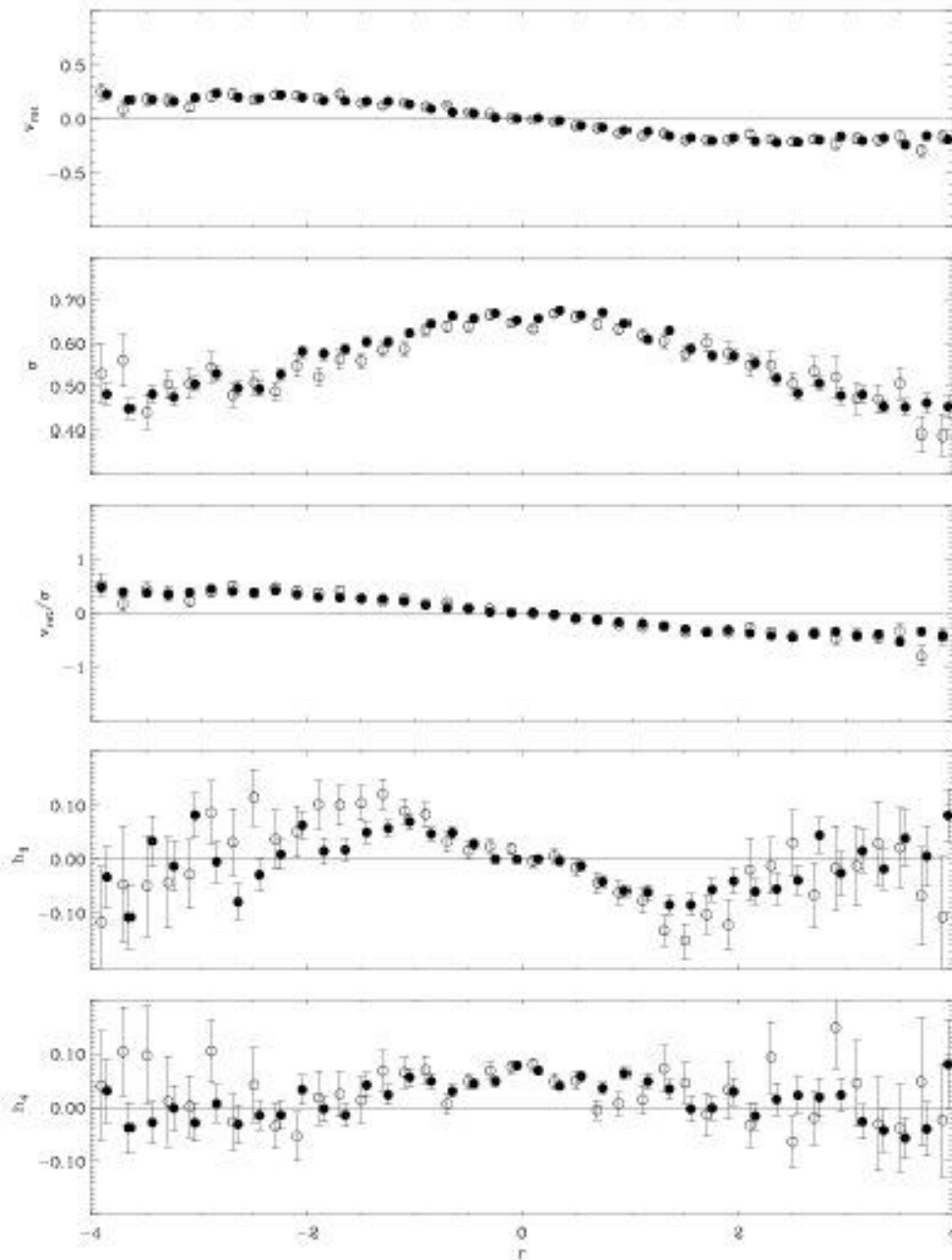
Figure 5.8: Comparison between the kinematic properties of the 1:1 merger remnants 1_1_L_8 and 1_1_H_8 with different resolutions. Data for the low-resolution simulation (53332 luminous particles) are given by open circles, those for the high-resolution simulation (160000 luminous particles) are given by filled circles. Errors are determined by bootstrapping.
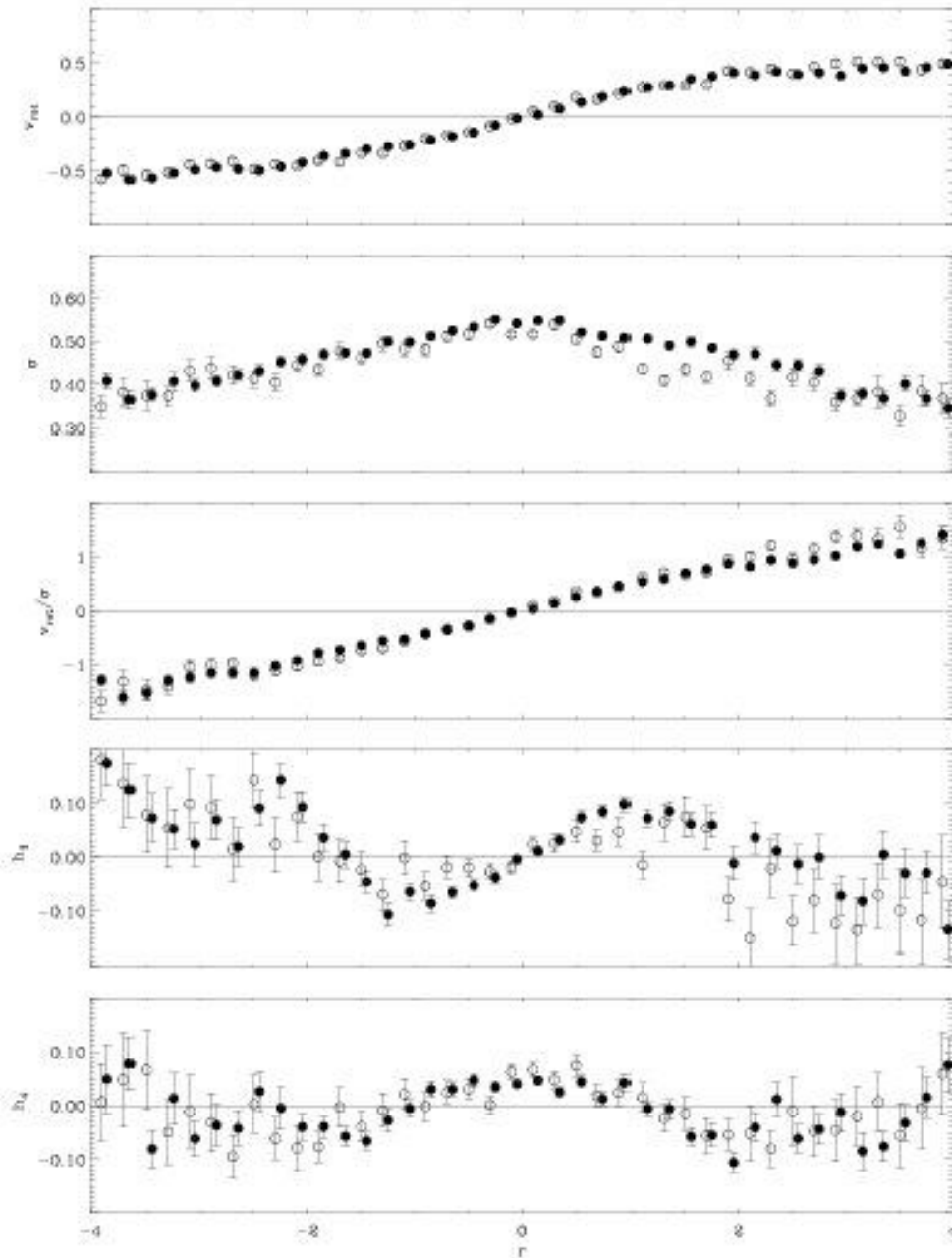
Figure 5.9: Comparison between the kinematic properties of the 3:1 merger remnants 3_1_L_8 and 3_1_H_8 with different resolutions. Data for the low-resolution simulation (35554 luminous particles) are given by open circles, those for the high-resolution simulation (106666 luminous particles) are given by filled circles. Errors are determined by bootstrapping.

Figure 5.10: Global correlation between $h3_{\text{eff}}$ and v_{rot}/σ_0 for 14 different orbital geometries of equal mass mergers. Every merger is investigated from 50 random viewing angles (black dots). The observed correlation (Bender et al., 1994) is shown by a straight line. The maximum spread around this correlation is indicated by the dashed lines. The dotted line shows $h3_{\text{eff}} = 0$. Mergers with one retrograde rotating disk are indicated by an (r). The typical error is given in the upper right plot.

Figure 5.11: Global correlation between $h3_{eff}$ and $a4_{eff}/\sigma_0$ for 14 different orbital geometries of equal mass mergers. Every merger is investigated from 50 random viewing angles (black dots). The observed correlation (Bender et al., 1994) is shown by a straight line. The maximum spread around this correlation is indicated by the dashed lines. Mergers with one retrograde rotating disk are indicated by an (r). The typical error is given in the upper right plot.

Figure 5.12: Local correlation between h_3 and v_{fit}/σ_{fit} for 14 different orbital geometries of equal mass mergers. Every merger is investigated from 50 random viewing angles (black dots). Data are taken inside r_{eff}. The observed correlation (Bender et al., 1994) is approximated by two straight lines (see Figure 2.10 for details). Mergers with one disk rotating retrograde are indicated by an (r). The typical error is given in the upper right plot. The small error bar is valid for measurements inside $0.7r_{eff}$, the larger one for the rest.
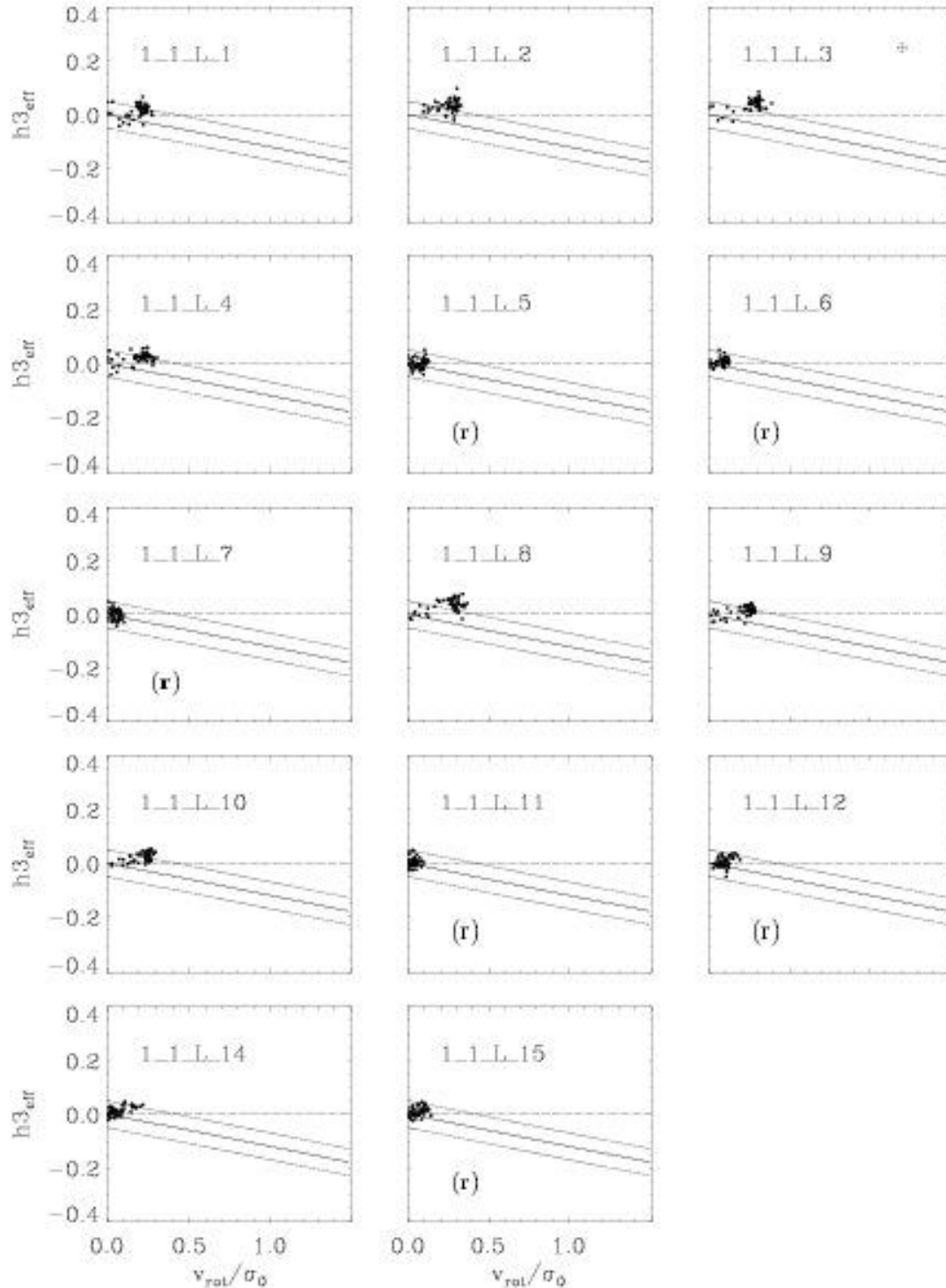
Figure 5.13: Global correlation between $h3_{eff}$ and v_{rot}/σ_0 for 15 different orbital geometries of 3:1 mergers. Every merger is investigated from 50 random viewing angles (black dots). The observed correlation (Bender et al., 1994) is shown by a straight line. The maximum spread around this correlation is indicated by the dashed lines. The dotted line shows $h3_{eff} = 0$. Mergers with the more massive disk rotating retrograde are indicated by an (r). The typical error is given in the upper right plot.
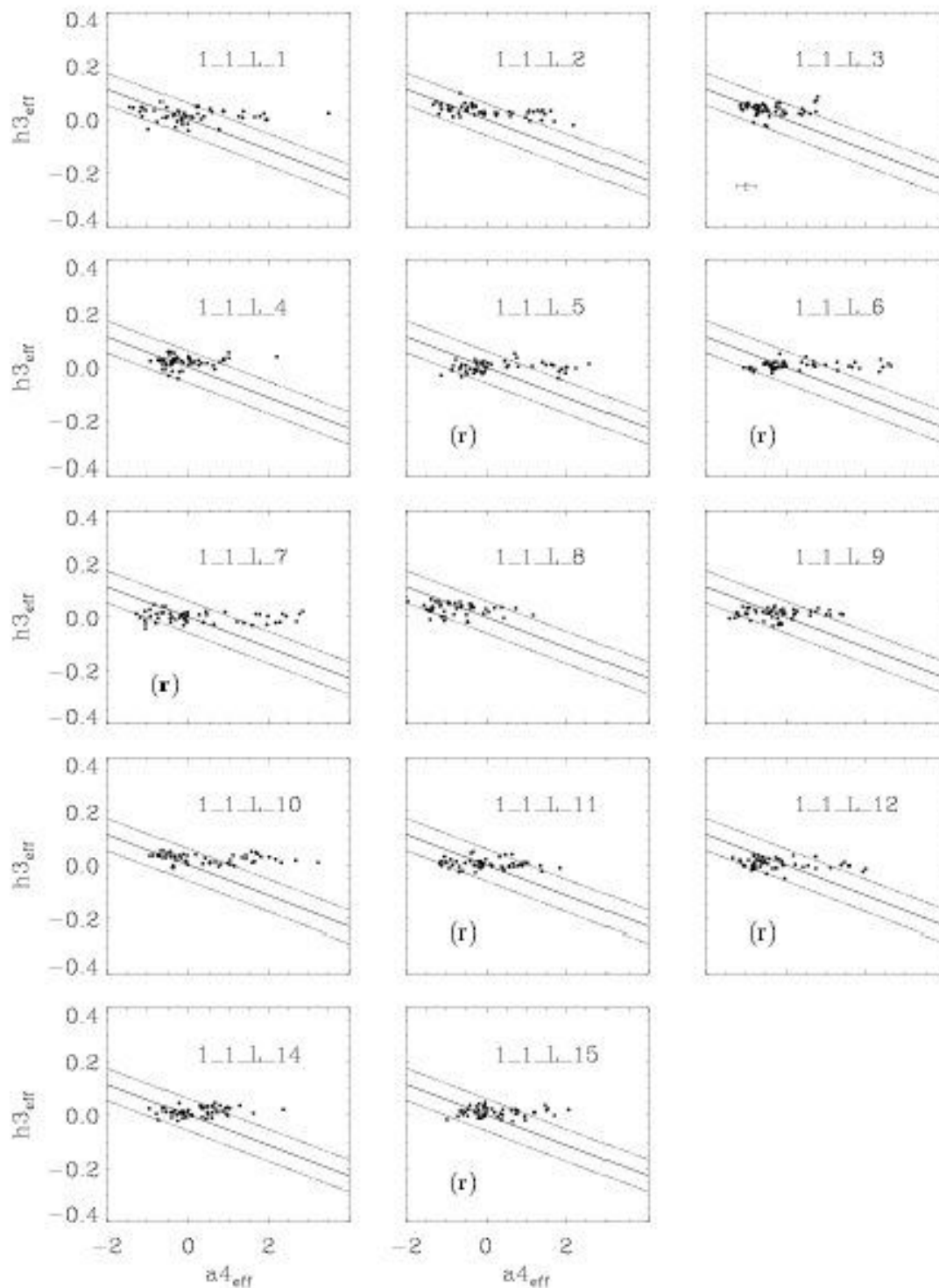
Figure 5.14: Global correlation between $h3_{\mathrm{eff}}$ and $a4_{\mathrm{eff}}$ for 15 different orbital geometries of 3:1 mergers. Every merger is investigated from 50 random viewing angles (black dots). The observed correlation (Bender et al., 1994) is shown by a straight line. The maximum spread around this correlation is indicated by the dashed lines. Mergers with the more massive disk rotating retrograde are indicated by an (r). The typical error is given in the upper right plot.
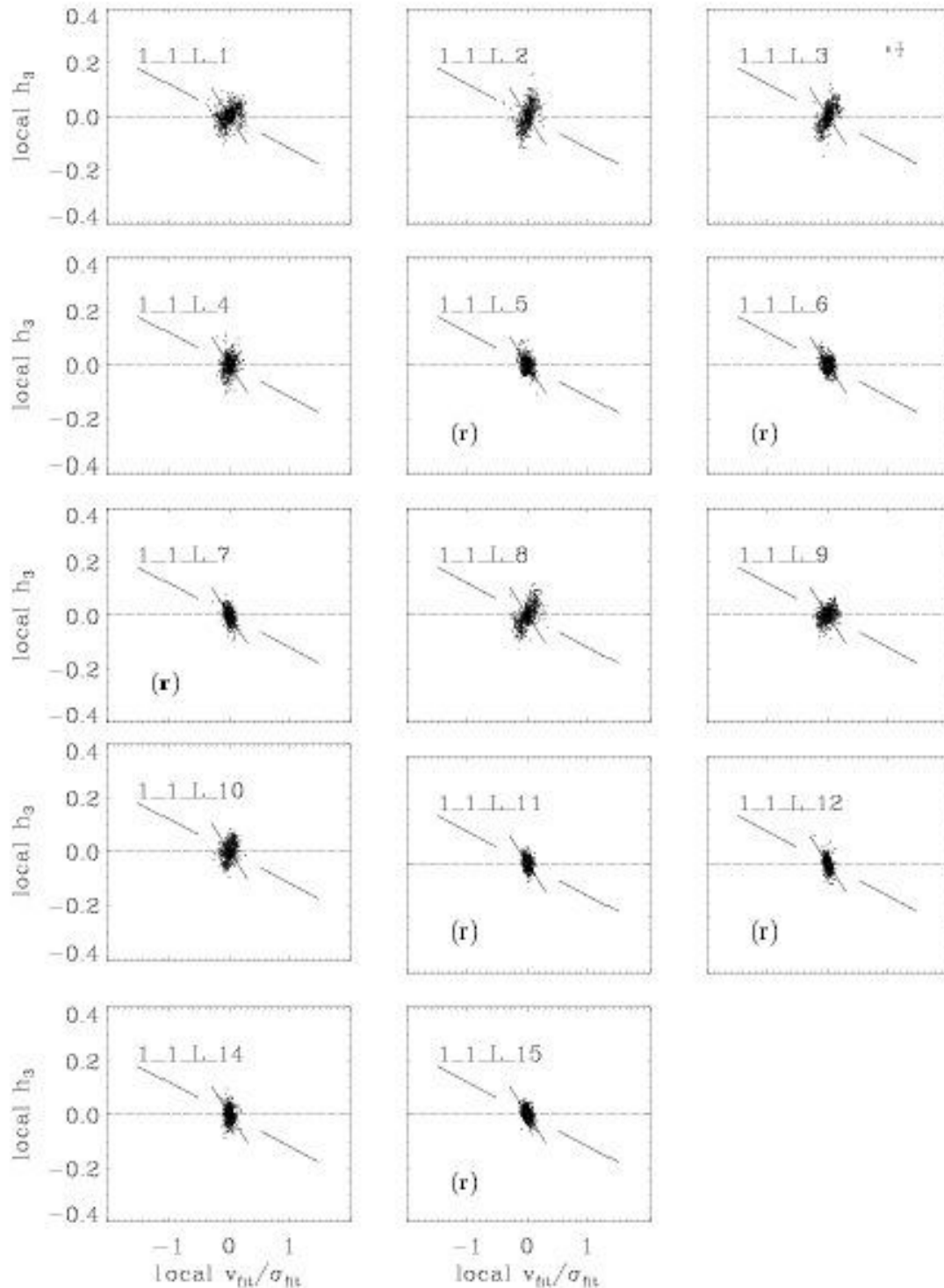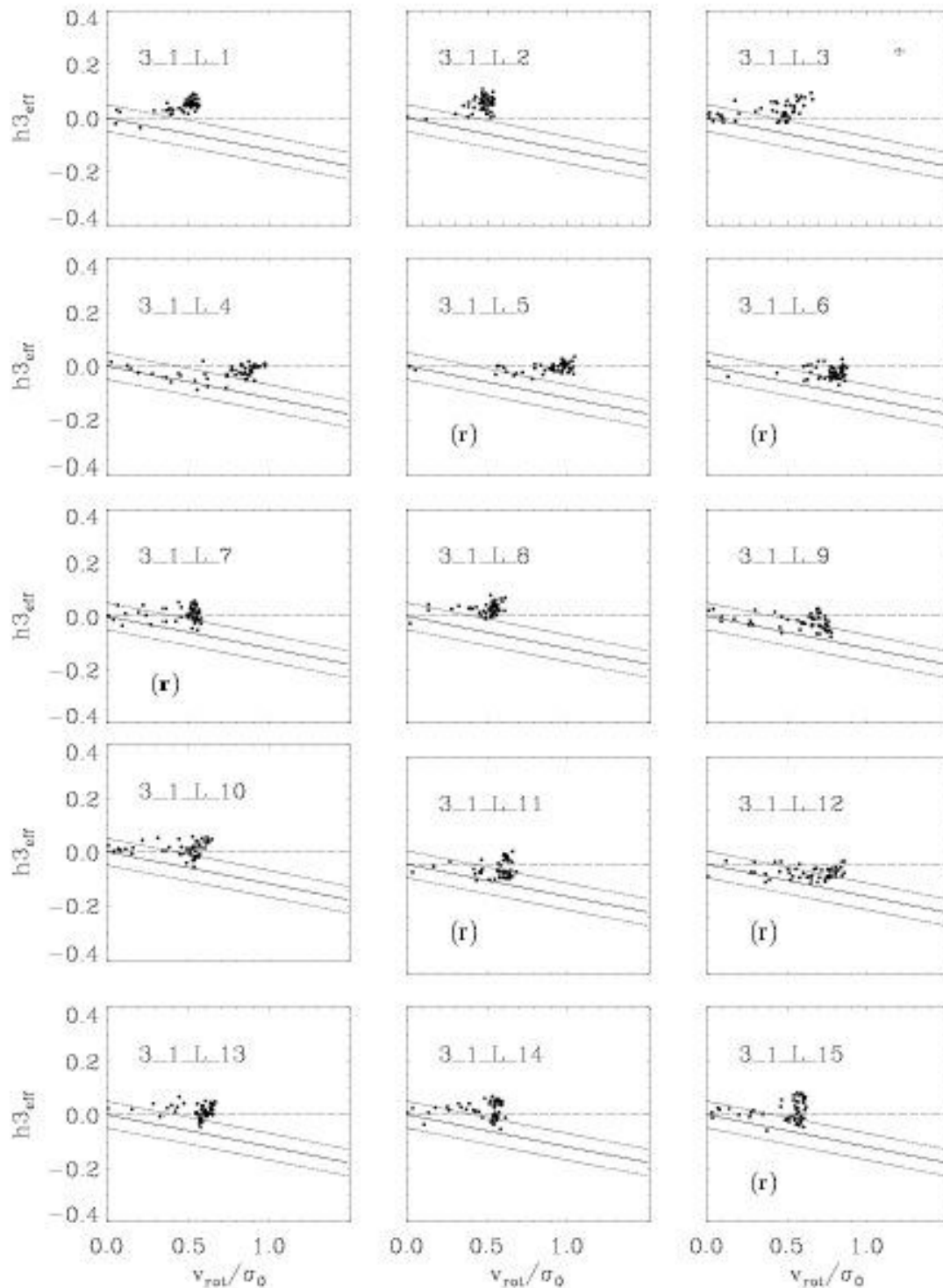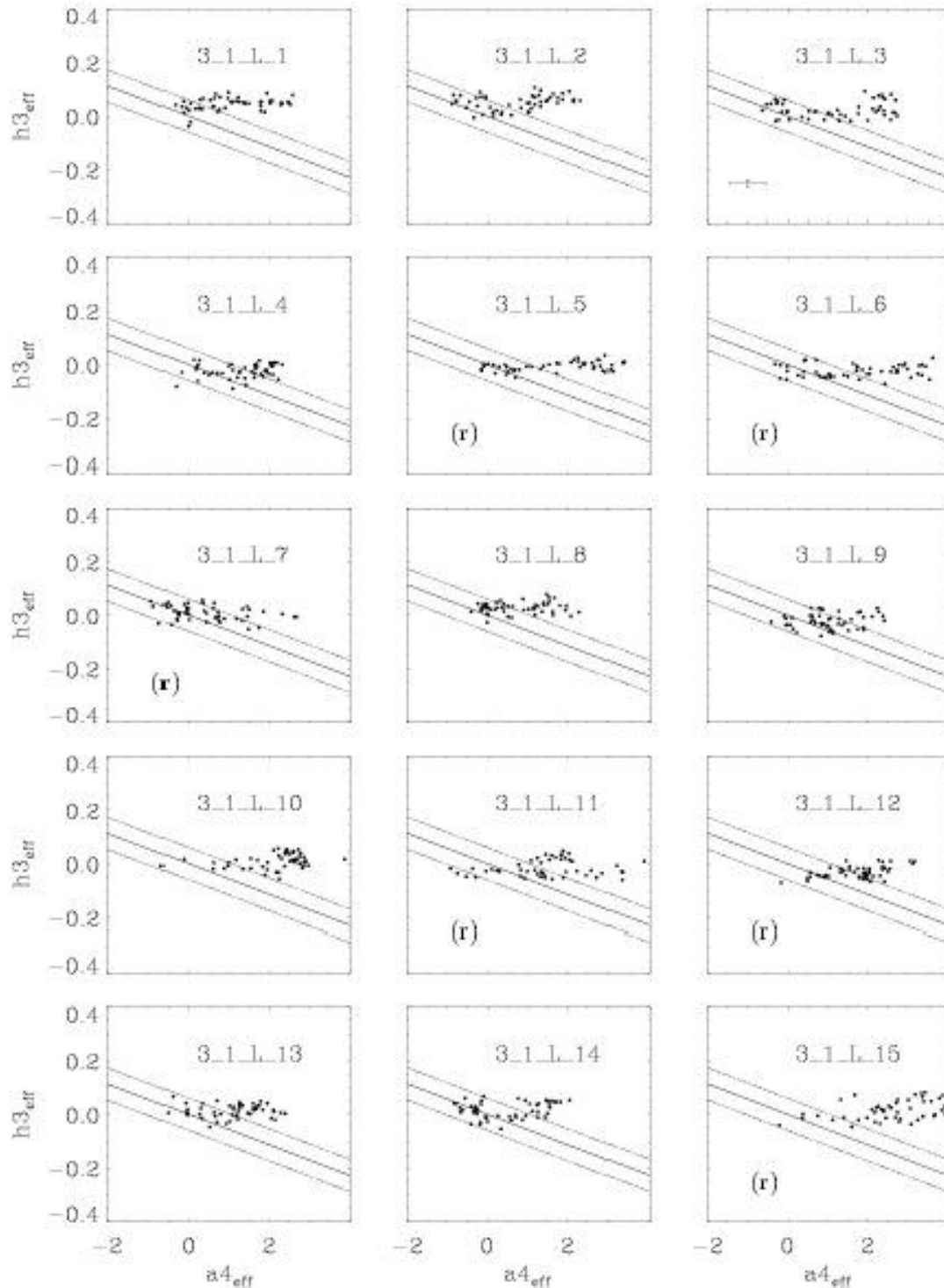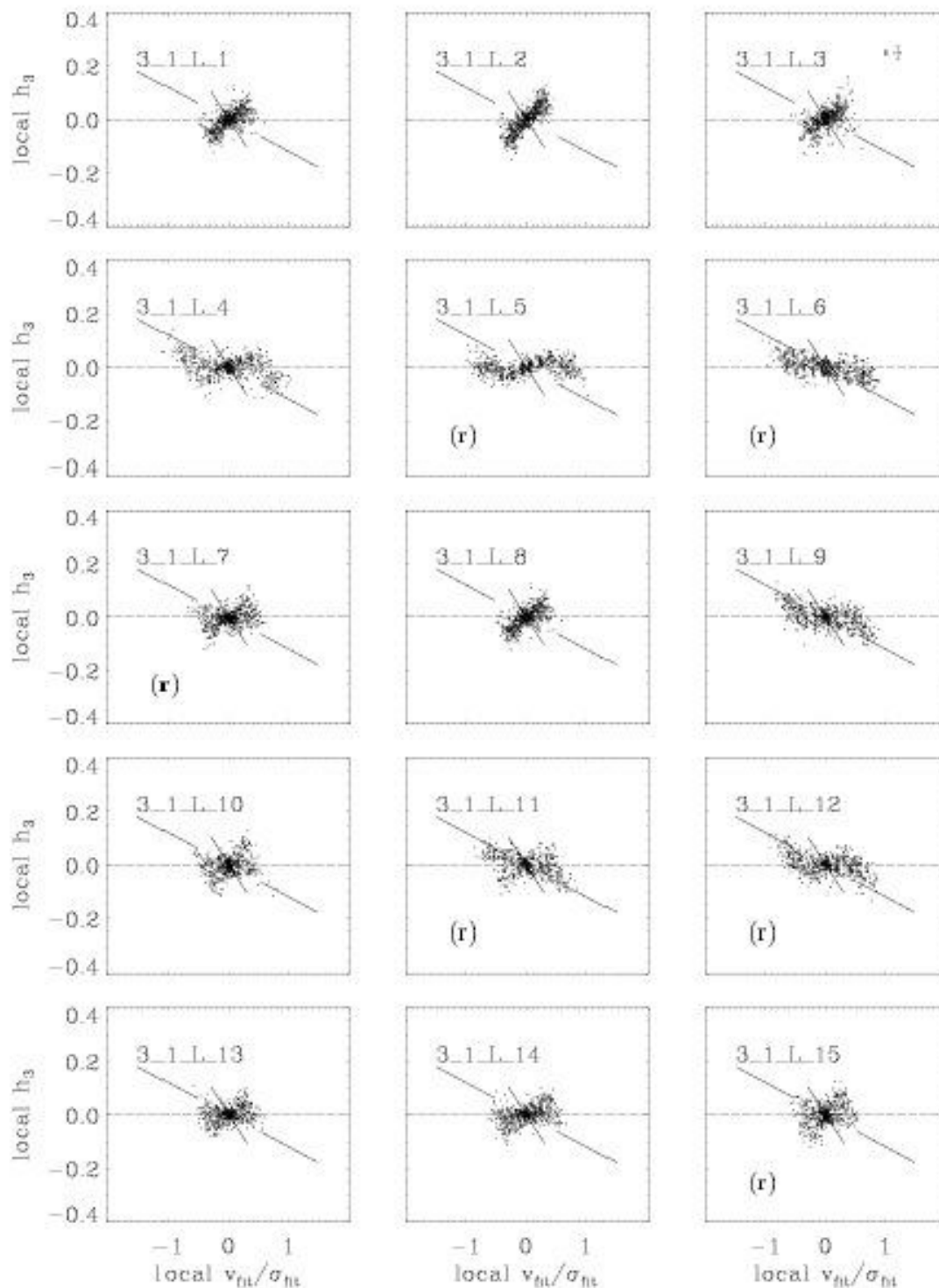
Figure 5.15: Local correlation between h_3 and v_{fit}/σ_{fit} for 15 different orbital geometries of 3:1 mergers. Every merger is investigated from 50 random viewing angles (black dots). The observed correlation (Bender et al., 1994) is approximated by two straight lines. Mergers with the more massive disk rotating retrograde are indicated by an (r). Errors as in Figure 5.12.

5.2   Correlations with other parameters

Observations suggest that the correlation between h_3 on the one hand and $a4_{\text{eff}}$ and v_{rot}/σ_0 on the other hand are the strongest among the observed quantities for elliptical galaxies (Bender et al., 1994). h_4 which defines the symmetric deviation from a Gaussian hardly correlates with any other quantity. Our simulated merger remnants show the same trend for h_4. In the following we want to show a set of possible correlations between the parameters we derived for the merger remnants 1_1_H_8, 1_1_H_15, 3_1_H_8, 3_1_H_15. We find them as being representative for all co- and counterrotating 1:1 and 3:1 mergers.

In addition to the previously investigated properties, we correlate the effective asymmetry parameter $h3_{\text{eff}}$ with the effective ellipticity ϵ_{eff}, the Sersic shape parameter n_{ser} and the anisotropy parameter $(v_{\text{rot}}/\sigma_0)^*$. We also show correlations for the parameter h_4 (see Chapter 2.3). Its characteristic value $h4_{\text{eff}}$ is determined the same way as $h3_{\text{eff}}$. We correlate $h4_{\text{eff}}$ with v_{rot}/σ_0, $a4_{\text{eff}}$, ϵ_{eff}, n_{ser} and $(v_{\text{rot}}/\sigma_0)^*$. The local correlation between h_4 and $v_{\text{fit}}/\sigma_{\text{fit}}$ is also analyzed.

Figure 5.16 and 5.17 show the results for a corotating and a counterrotating equal-mass merger with high resolution. $h3_{\text{eff}}$ does not correlate with any other given parameter. The same is true for $h4_{\text{eff}}$. If one is willing to see a correlation, there is only a slight trend for the faster rotating projected remnants to have a symmetric part of the LOSVD that is closer to a Gaussian ($h4_{\text{eff}}$ vs. v_{rot}/σ_0 in Figure 5.16). $h4_{\text{eff}}$ is in general positive. This fact and its measured spread are in good agreement with observations.

The results for the two 3:1 counterparts are shown in Figure 5.18 and 5.19. Here we just want to describe a few trends: projections with small $h3_{\text{eff}}$ are closer to a de Vaucouleurs surface density profile ($n_{\text{ser}} = 0.25$); projections where the remnant seems to be more anisotropic [smaller $(v_{\text{rot}}/\sigma_0)^*$] show a more positive $h3_{\text{eff}}$; rounder and more slowly rotating projected remnants have more positive values of $h4_{\text{eff}}$; and, probably the most interesting trend, the local correlation of h_4 versus $v_{\text{fit}}/\sigma_{\text{fit}}$ shows a characteristic hat-like structure. Unfortunately, there is no published data available to confirm if this shape is consistent with measurements of real elliptical galaxies.

To summarize the properties of LOSVDs of collisionless merger remnants we find that they indeed show asymmetric line profiles. The deviations from a Gaussian as measured by h_3 and h_4 are of the same order as observed elliptical galaxies. In general, h_3 is zero or positive for our simulated merger remnants. In contradiction to observations, the LOSVDs have a retrograde wing that is steeper than the prograde wing (see Figure 2.8 for definition). All simulated remnants show predominantly positive h_4. This indicates that their profile shape is more peaked than a Gaussian. This is in good agreement with observations. The simulated characteristic values $h3_{\text{eff}}$ and $h4_{\text{eff}}$ hardly correlate with any other global quantity. However, one important exception is the local correlation between h_3 and $v_{\text{fit}}/\sigma_{\text{fit}}$. Except for counterrotating equal mass mergers, this correlation is not compatible with the observed one. In the following section we try to find out in how far the effect of a dissipative component could change the results. If gas is involved during the merger event this could result in the formation of an additional thin stellar disk after the merger is complete and it could change the kinematical properties of the merger remnant.

Figure 5.16: Correlations between the line shape parameters h_3 and h_4 and other kinematic and photometric properties for 50 random projections of the merger remnant 1_1_H_8.

Figure 5.17: Correlations between the line shape parameters h_3 and h_4 and other kinematic and photometric properties for 50 random projections of the merger remnant 1_1_H_15.

Figure 5.18: Correlations between the line shape parameters h_3 and h_4 and other kinematic and photometric properties for 50 random projections of the merger remnant 3_1_H_8.
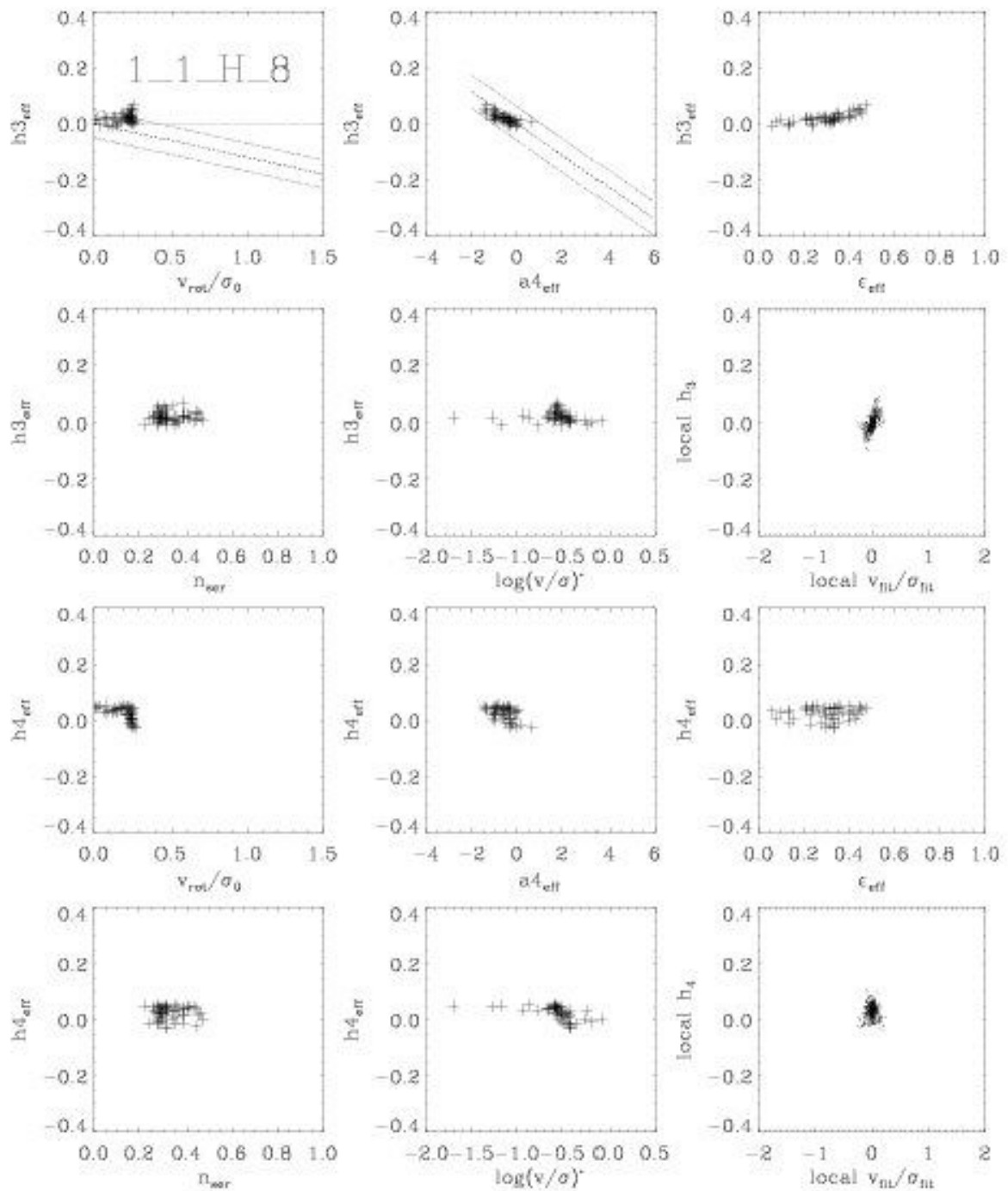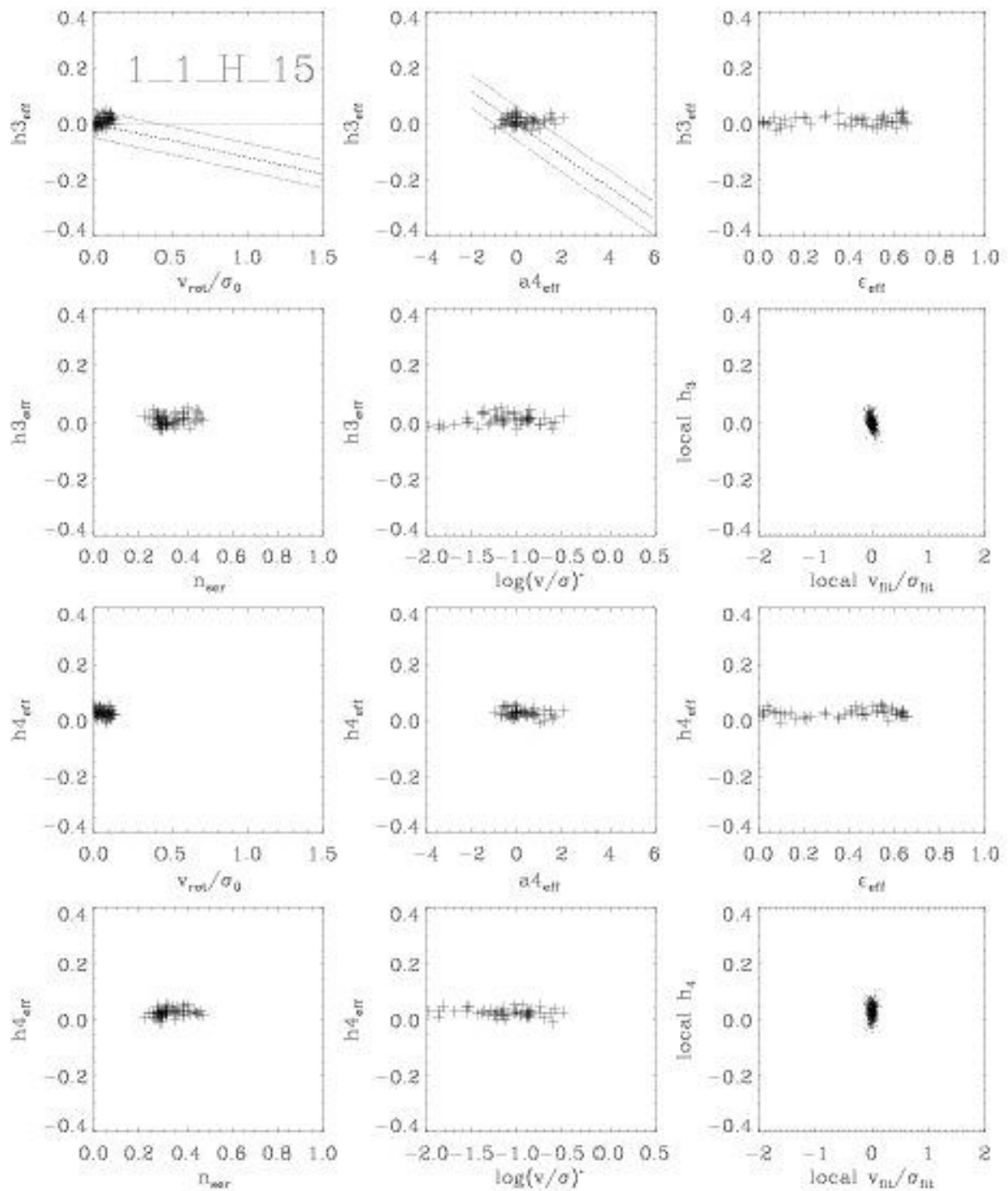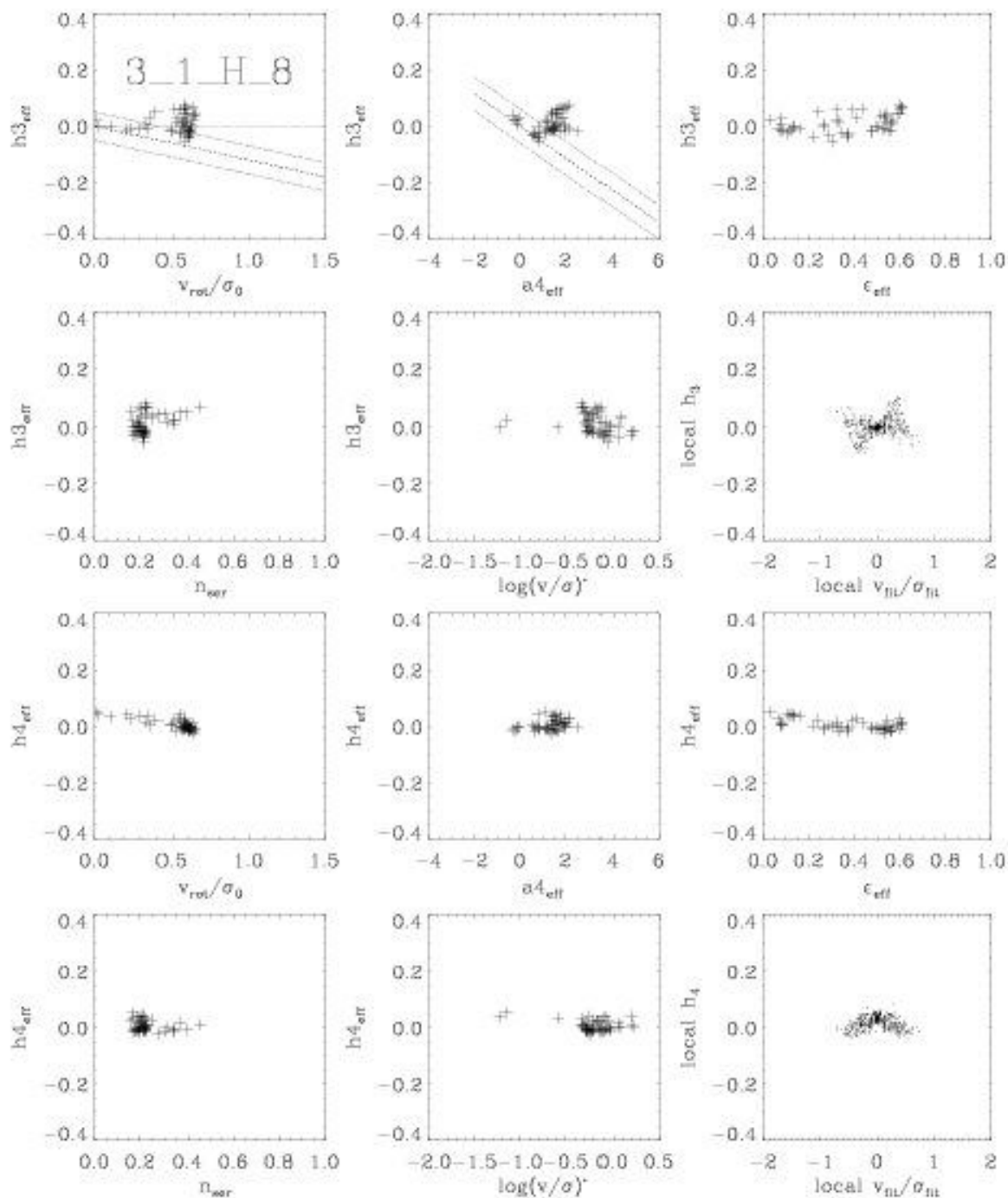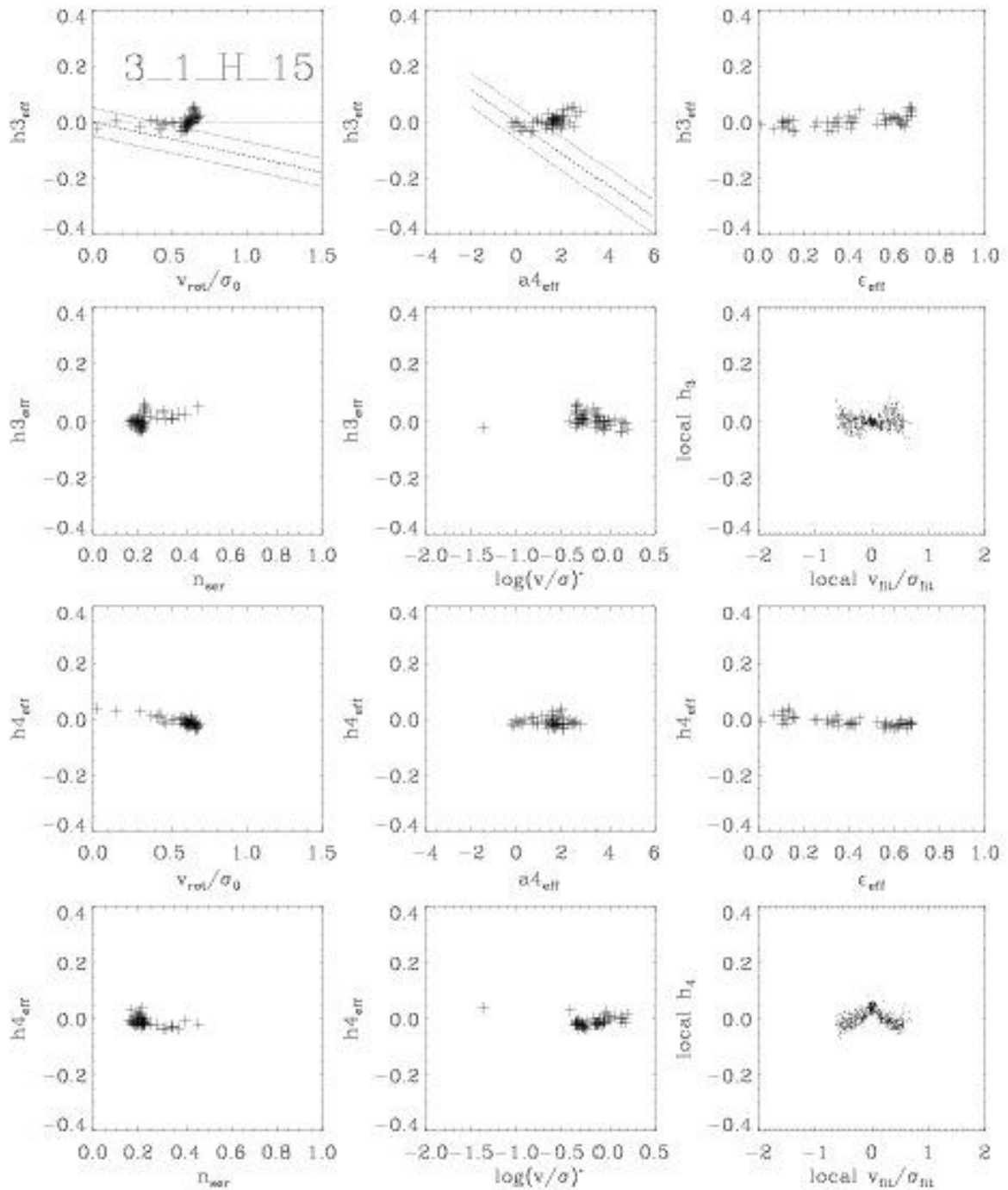
Figure 5.19: Correlations between the line shape parameters h_3 and h_4 and other kinematic and photometric properties for 50 random projections of the merger remnant 3_1_H_15.

5.3   What about a disk?

As we have seen in the previous section, the LOSVDs from simulated collisionless merger remnants are almost never in agreement with observations. The only exception are remnants of equal-mass mergers with counterrotating disk components that do not rotate in the end. All other remnants show wrong global correlations between $h3_{\text{eff}}$, $a4_{\text{eff}}$, and v_{rot}/σ and wrong local correlations between h_3 and $v_{\text{fit}}/\sigma_{\text{fit}}$. One plausible explanation for line-of-sight velocity distributions with negative h_3 is the superposition of a spheroidal body with a disk-like component (see Chapter 2; Bender et al., 1994). We performed a simple experiment to test if the wrong correlations for our remnants result from a lack of such a disk-like component. We artificially added a thin (scale height $\approx 0.05 r_{\text{eff}}$), cold ($\sigma_z = 0$), stellar disk with an exponential surface density profile. The disk was placed in the plane defined by the long and intermediate axes of the main stellar body and rotates the same way as the main stellar body. The disk particles move around the center of the galaxy in centrifugal equilibrium with the gravitational potential arising from the total enclosed mass. No additional random motion was added. Under these simple assumptions only two parameters remain free. The total mass of the disk M_d and its scale length r_d. From now on we always refer measurements to the main stellar body of the remnant and we measure M_d in units of the total luminous mass of the remnant and r_d in units of the projected half-light radius r_{eff}. Figure 5.20 shows a sequence of particle distributions for a merger remnant with an additional disk with a scale length of $r_d = 0.5 r_{\text{eff}}$ and $r_d = 1.0 r_{\text{eff}}$. If seen edge on the large disk looks like a spike coming out of both sides of the spheroidal remnant. An observer probably would immediately classify a galaxy like this as Sa or S0. However, as soon as the remnant is tilted by only $10°$ with respect to the line-of-sight the disk disappears and is not obviously visible any more. The strength of this effect depends on the mass of the disk. For disk masses larger than 40% of the mass of the spheroid the disk would still be visible, even for larger inclinations.

To test the effect of an additional disk component on the kinematic and photometric properties of the remnants we selected the characteristic merger remnants 3_1_H_8, and 3_1_H_15 and added disks with masses of $M_d = 5\%, 10\%, 15\%, 20\%, 25\%, 30\%, 35\%$ and 40% of the total luminous mass and scale lengths of $r_d = 0.25, 0.5, 0.75, 1.0, 1.25, 1.5, 1.75,$ and $2.0 r_{\text{eff}}$. Thereafter the remnants were analyzed as seen from 50 random viewing angles as described before. To select a successful model we expect that projection effects alone do not lead to deviations from the observed correlations since we can assume that real galaxies are distributed on the sky with random orientations.

As an example we show the results for the merger 3_1_H_8 when we add a sequence of disks with a fixed mass of 15% of the total mass but with increasing scale radii (Figures 5.21, 5.22, and 5.23). The global relations between $h3_{\text{eff}}$, $a4_{\text{eff}}$, and v_{rot}/σ start to follow the observed trend as soon as a small disk with $r_d = 0.25 r_{\text{eff}}$ is added. However, for small disks $h3_{\text{eff}}$ becomes too negative and the LOSVD is more asymmetric than observed (Figures 5.21 and 5.22). In this case the influence of the disk for radii inside r_{eff} is too strong. If the disk gets as large as r_{eff} the influence is smaller and the agreement with observed correlations is good. The effect of the disk on the local correlation between h_3 and $v_{\text{fit}}/\sigma_{\text{fit}}$ is even stronger. As soon as a small disk is added the correlations change their previous positive slope to the observed slope for $-0.3 \leq v_{\text{fit}}/\sigma_{\text{fit}} \leq 0.3$ (Figure 5.23). However, for small disks the absolute values for h_3 become too large for $\text{abs}(v_{\text{fit}}/\sigma_{\text{fit}}) \geq 0.3$. For scale lengths larger than r_{eff} even
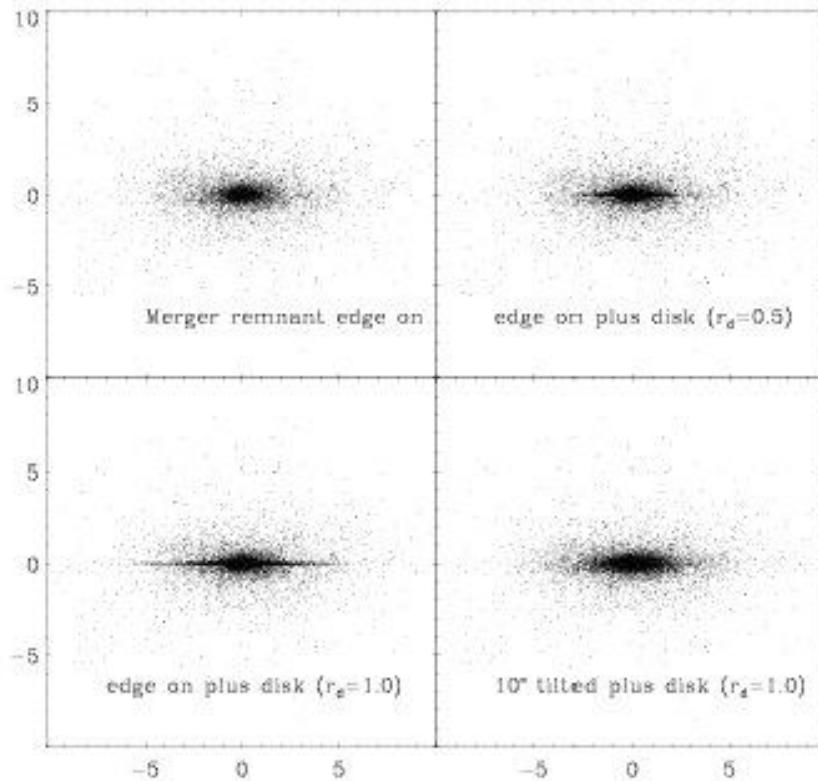
Figure 5.20: Sequence of disks added to the main body of the galaxy. *Upper left panel*:
Luminous particles of a 3:1 merger remnant (only 20% of all particles are plotted here).
Upper right panel: Like before, but with an additional disk component having a scale length
of $0.5r_{\text{eff}}$ and a scale height of $0.5r_{\text{eff}}$. *Lower left panel*: With an additional disk with a scale
length of r_{eff}. *Lower right panel*: The same model as before, but inclined by 10° with respect
to the line-of-sight. Note that the disk component is not easily visible any more.

the slope in the outer part is in good agreement with observations.

In Figures 5.24, 5.25, and 5.26 we show the results of adding a sequence of disks with a scale
length of $r_d = 1.25r_{\text{eff}}$ but increasing masses. The effect of 5% disk seems to be too small to
change the initial properties significantly. Remnants with disk masses of 10% or 15% of the
total luminous mass can reproduce the observed correlations. For disk masses $M_d \geq 20\%$ the
absolute values of $h3_{\text{eff}}$ are too large (Figures 5.24 and 5.25) and the local asymmetry of the
LOSVDs for abs($v_{\text{fit}}/\sigma_{\text{fit}}$) > 0.3 as measured by abs($h_3 > 0.2$) is too strong.
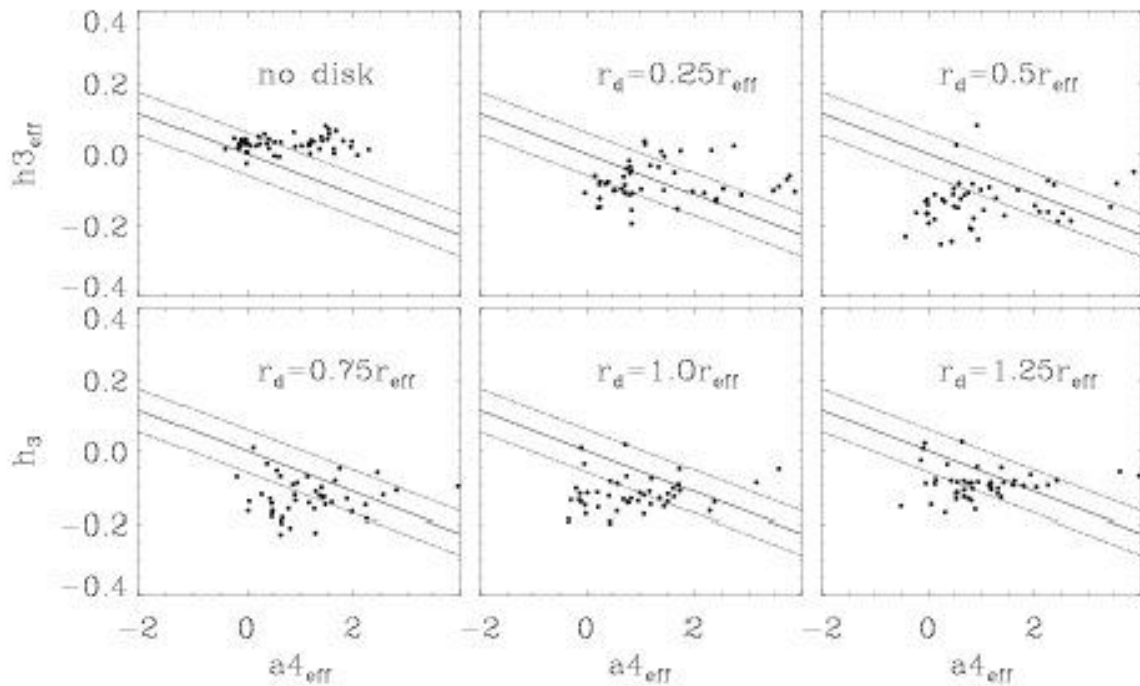
Figure 5.21: Global correlation between $h3_{eff}$ and $a4_{eff}$ for 50 random projections, respectively. From the upper left to the lower right an exponential disk with a fixed mass of 15% of the luminous body and increasing scale length r_d is added.
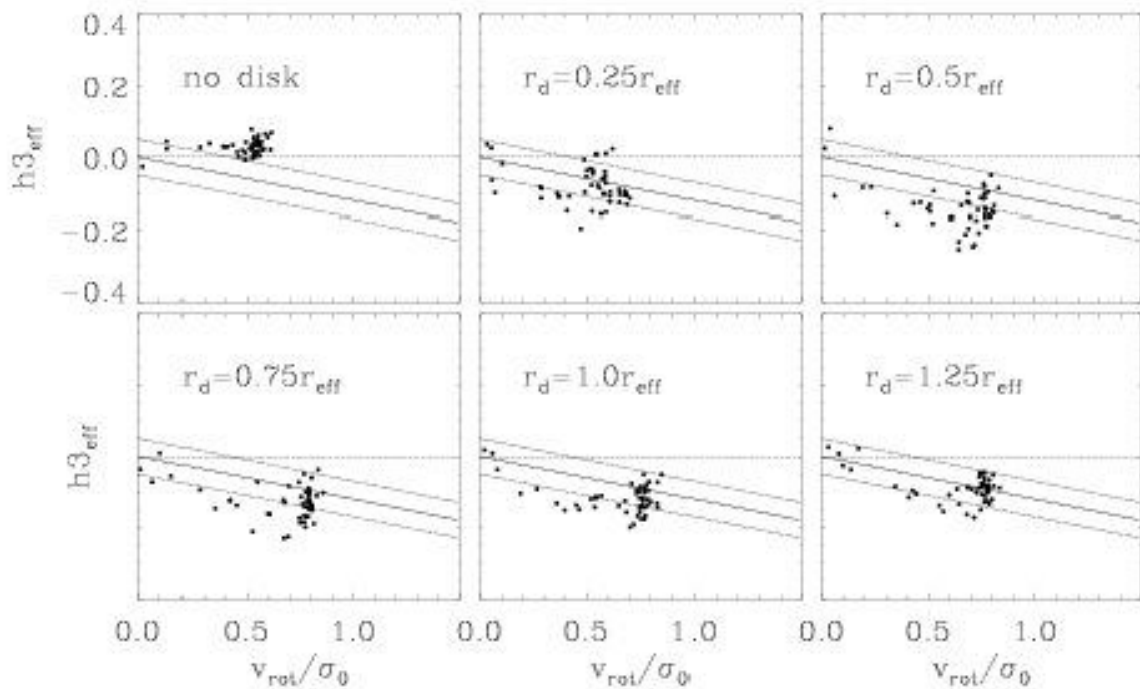
Figure 5.22: Same as Figure 5.21 but for $h3_{eff}$ vs. v_{rot}/σ_0.
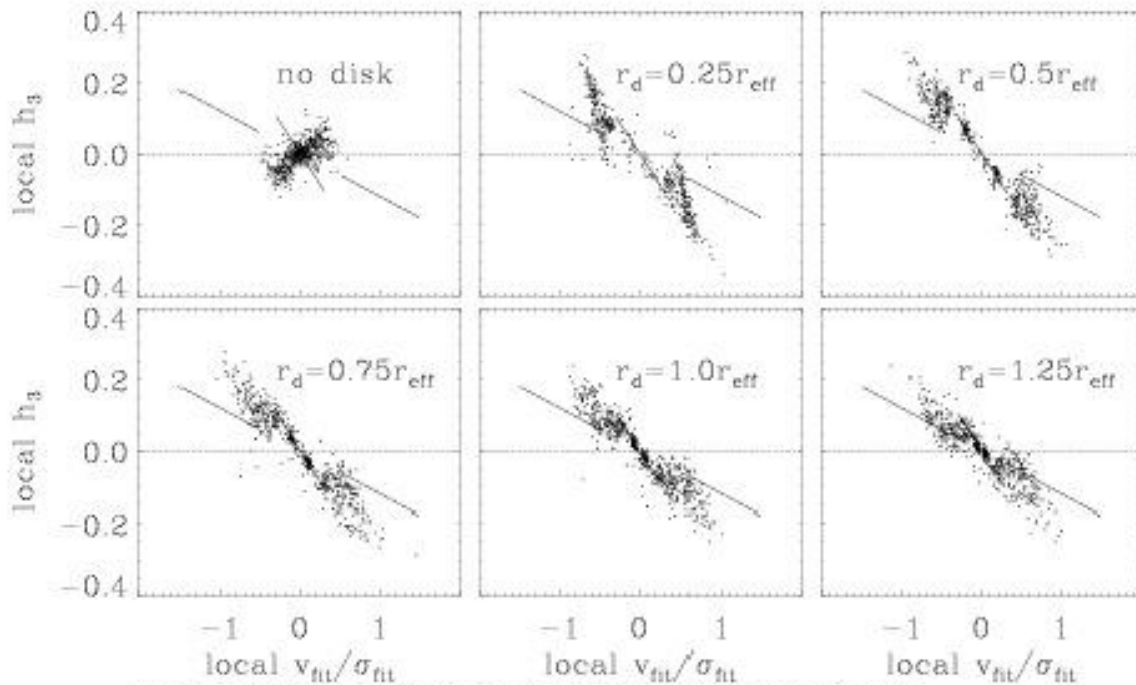
Figure 5.23: Same as Figure 5.22, but for local h_3 vs. local v_{fit}/σ_{fit}.

Figure 5.24: Global correlation between $h3_{eff}$ and $a4_{eff}$ for 50 random projections, respectively. From the upper left to the lower right an exponential disk with a fixed scale length of $r_d = 1.25$ and increasing mass M_d is added.
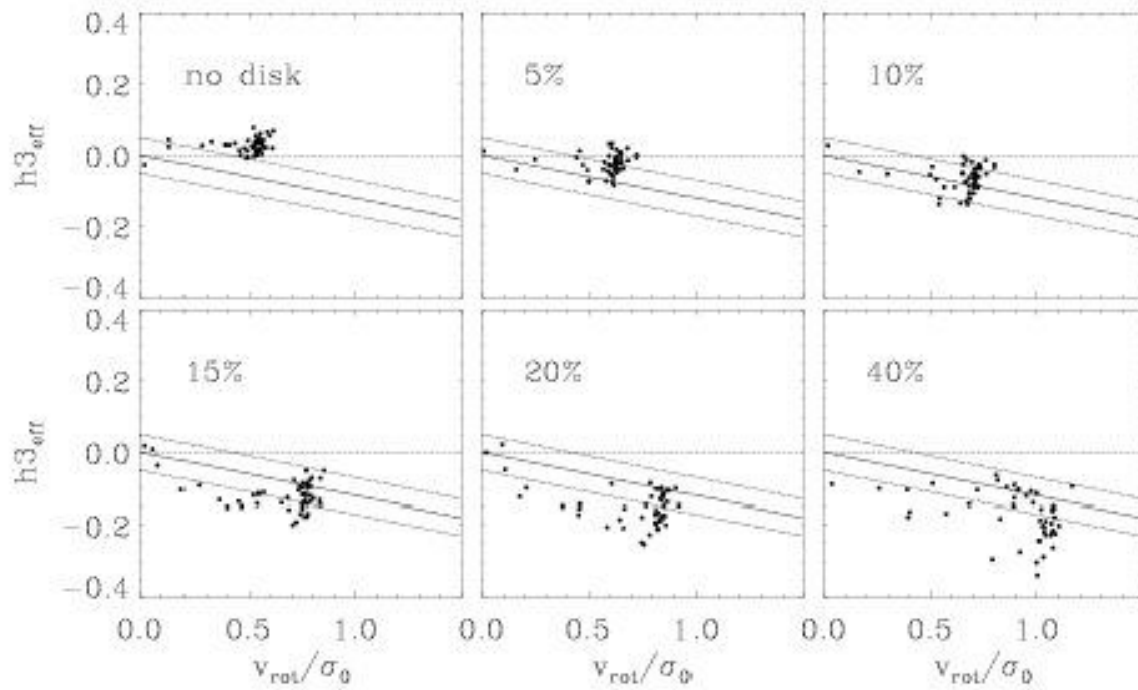
Figure 5.25: Same as Figure 5.24 but for $h3_{\rm eff}$ vs. $v_{\rm rot}/\sigma_0$.
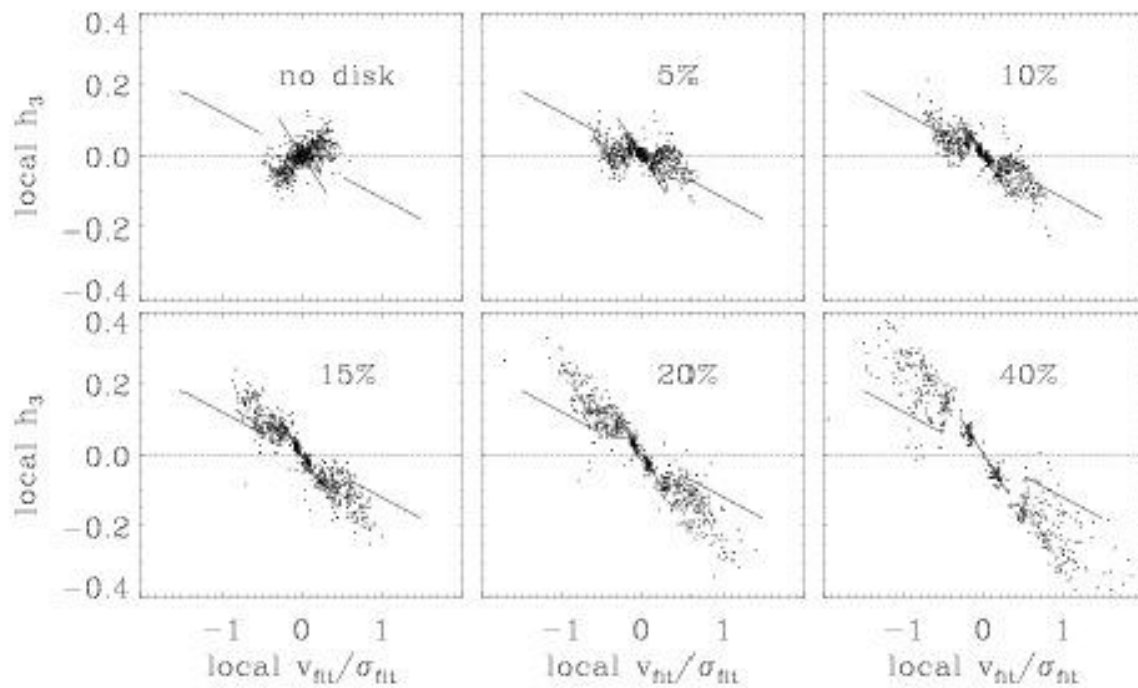
Figure 5.26: Same as Figure 5.25, but for local h_3 vs. local $v_{\rm fit}/\sigma_{\rm fit}$.
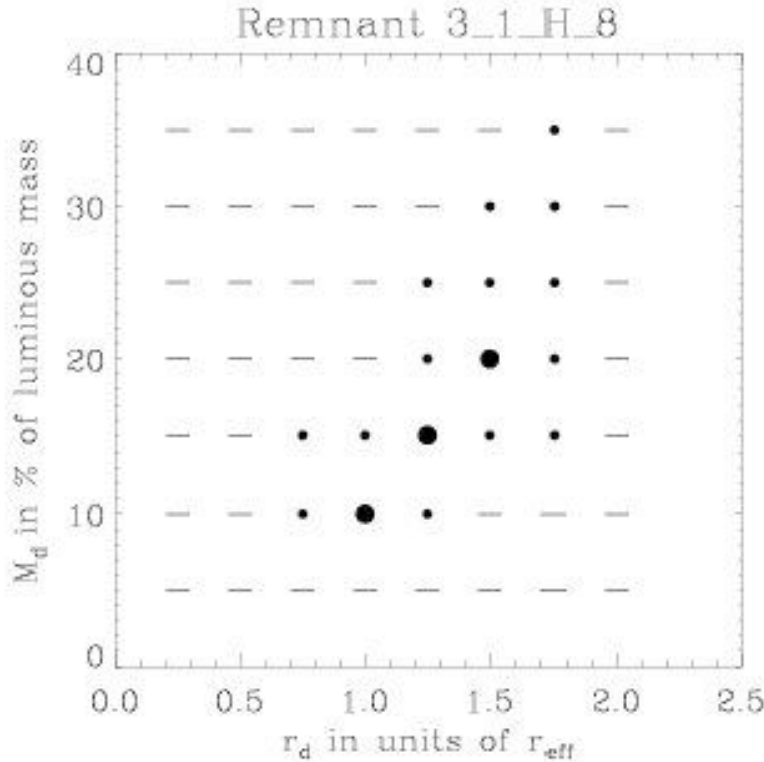
Figure 5.27: Mass M_d versus scale radius r_d for a disk added to the merger remnant 3_1_L_8. Combinations that are able to reproduce (big dot), almost reproduce (small dot) or fail to reproduce (minus sign) the observed correlations are shown.

If we analyze the properties of all given combinations of M_d and r_d we can get an estimate of the disk mass and size that is needed to fit the observed correlations. Figures 5.27 and 5.28 show the results of this analysis for the remnant 3_1_H_8 and its retrograde counterpart 3_1_H_15. We placed a minus sign if more than half of the projections of a given remnant clearly fail to reproduce one of the observed global correlations. In addition, we exclude all models with significantly positive local h_3 for abs(v_{fit}/σ_{fit}) < 0.3 and those with a maximum abs$h_3 > 0.2$. Disks with $r_d > 1.75$ were also excluded because they result in ellipticities $\epsilon > 0.7$ for disk masses $M_d > 30\%$. The models that fit the data best are indicated by a large dot. Intermediate models are indicated by a small dot. Although we only apply "soft" criteria for the success of a model, we can estimate an optimal disk-contribution. For both 3:1 merger simulations we get the best results for disks with scale lengths between $1.0r_{eff}$ and $1.5r_{eff}$ and masses ranging between $M_d = 10\%$ and $M_d = 20\%$. Both models seem to require disks of comparable dimensions, although the merger remnants show different kinematical properties. However, the disk required for remnant 3_1_L_15 can be less massive and slightly smaller. Of course this simple model does not place final constraints on the dimension of the disk since we did not consider the possible formation mechanism and we did not account for
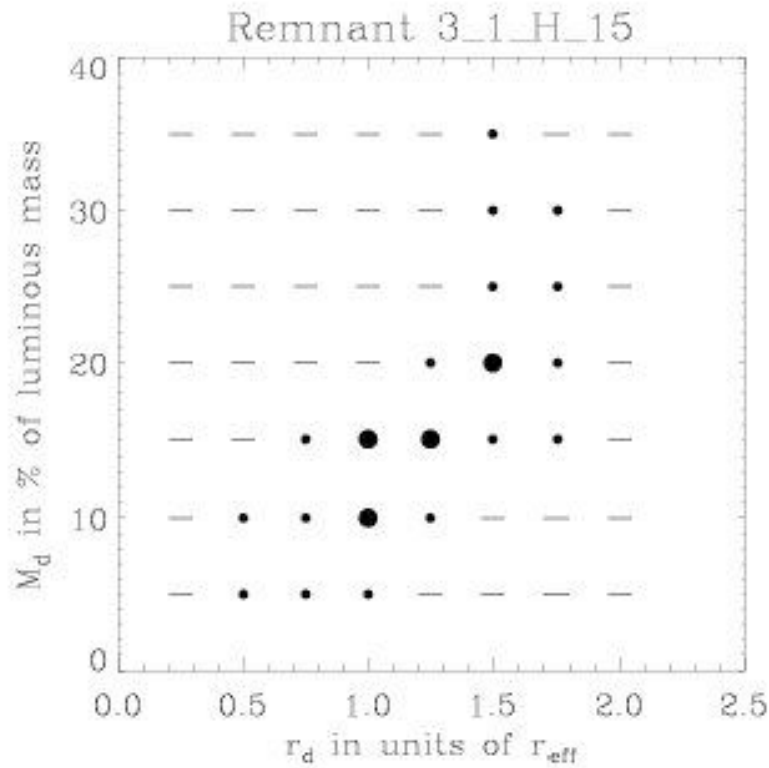
Figure 5.28: Same as Figure 5.27 for the merger remnant 3_1_L_15.

the dynamical response of the remnant.
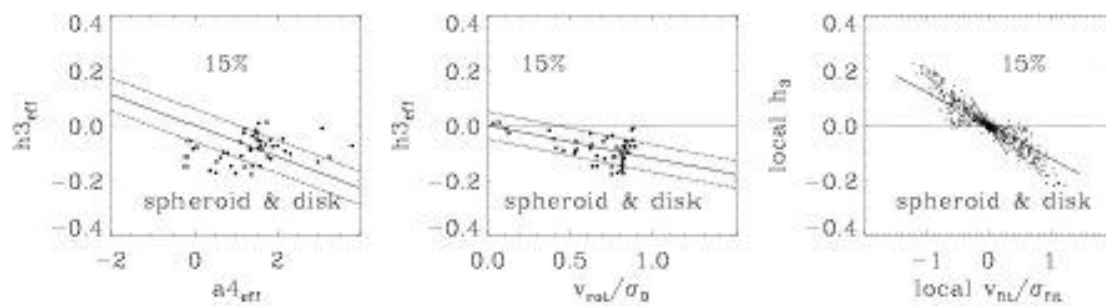
Figure 5.29: Correlations for the model where the dynamically active disk component has reached a mass of 15% of the mass of the remnant. Both, the luminous particles and the additional disk particles are analyzed.
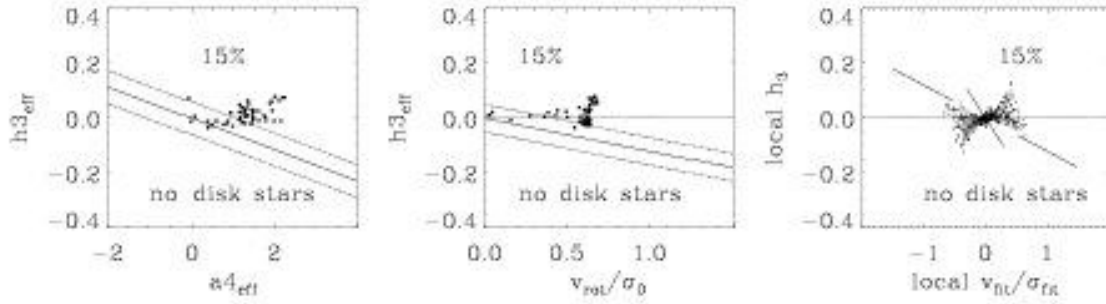
Figure 5.30: Same as Figure 5.29, but without the contribution of the disk particles.

In the next step we test the dynamical response of the merger remnant to an additional disk component that would have formed after the merger was complete. Therefore we place a disk with a size of $r_d = 1.25 r_{eff}$, realized by 10000 massless particles, at the center of the remnant and evolve the remnant dynamically with time. We increase the total mass of the disk every time step at a constant rate of $10^7 M_\odot/\mathrm{Myr}$. After the disk mass has reached 15% of the total mass of the remnant we analyze the remnant again. The result is shown in Figure 5.29. The global relations as well as the local correlations resemble those of the simple model with $r_d = 1.25$ and a disk mass of $M_d = 15\%$. However, the steep gradient for $\mathrm{abs}(v_{fit}/\sigma_{fit}) < 0.3$ disappears (Figure 5.29). If the same remnant is analyzed without the additional disk component we can quantify the influence on the spheroidal component. Figure 5.30 indicates that the structure of the merger remnant is almost unchanged (see Figures 5.21, 5.22, and 5.23) besides a small influence on the h_3-v_{fit}/σ_{fit} correlation.

Chapter 6

Discussion and Conclusions

The aim of this thesis was to study the dynamics of interacting disk galaxies represented by collisionless particles and the possible formation of elliptical galaxies originating from the resulting mergers. After a short summary of the thesis we will discuss the results in a broader context.

We performed a large set of fully self-consistent collisionless simulations of two merging spiral galaxies with mass ratios of 1:1, 2:1, 3:1, and 4:1. For every mass ratio, we simulated mergers with different orbital geometries that coarsely cover the parameter space for relative spin orientations between the galactic disks (Chapter 3). In general, isophotal shape, ellipticity and rotational properties of the simulated remnants change with radius. Therefore for every projected merger remnant we derived global photometric and kinematic parameters applying the methods used by observational astronomers. We showed that the parameters do not change with time once the remnant has reached dynamical equilibrium (Section 4.2) and we performed a statistical comparison of the projected properties of simulated merger remnants with data of observed elliptical galaxies (Section 4.2 and 4.3). In addition, for individual examples, we discussed the kinematic and photometric properties in details (Section 4.4). We determined the line-of-sight velocity distribution along the major axis for every projected remnant (Chapter 5). After parametrizing the asymmetric and symmetric deviations from a Gaussian we compared it with observations of elliptical galaxies (Section 5.1). Thereafter the influence of a thin stellar disk component on the properties of 3:1 merger remnants was investigated and we estimated a possible mass and size for such a component (Section 5.3).

The derived global parameters demonstrate that the observed dichotomy between boxy and disky ellipticals could originate from variations in the mass ratios of the progenitor galaxies.

Equal-mass mergers lead to remnants that predominantly show boxy isophotes, rotate slowly and are supported by anisotropic velocity dispersions. They are intrinsically triaxial, show a large amount of minor-axis rotation and have significantly twisted isophotes, depending on the viewing angle. Their surface density profile is close to an $r^{1/4}$ law. During the violent merger both progenitor disks are completely destroyed and loose the memory of their initial state.

A trend for equal-mass mergers to form preferentially boxy ellipticals has already been noted before by Steinmetz & Buchner (1995) and Heyl et al. (1994). However, those investigations

suffer from important limitations. Steinmetz & Buchner (1995), on the one hand, neglected the bulge component leading to remnants that were too diffuse at the center to follow a de Vaucouleurs law. Heyl et al. (1994), on the other hand, used simulations with only a small set of relative orientations which allowed them to draw only weak conclusions. In addition, they did not correlate the isophotal shape with kinematic parameters. Our simulations show that statistically, the "observed" data of simulated equal-mass merger remnants agrees perfectly with data for observed boxy elliptical galaxies with respect to ellipticity, rotation, anisotropy and minor-axis rotation. The observed spread in the data can be explained by projection effects (see Naab et al., 1999).

Within the group of equal-mass merger remnants there exist two subgroups with distinct kinematical properties (see the double-peaked distribution of v_{rot}/σ_0 in Figure 4.29). Those with corotating progenitor disks still contain a significant amount of rotation up to $v_{rot}/\sigma_0 \approx 0.4$. They are less anisotropic with $\log(v_{rot}/\sigma_0)^* \approx -0.5$ and the vast majority of their projected remnants shows boxy isophotes. The faster rotating projections show asymmetric LOSVDs with steep retrograde wings characterized by a positive $h3_{eff}$. This trend is in contradiction to observations by Bender et al. (1994) and Mehlert et al. (2000) who find only negative $h3_{eff}$ for significantly rotating galaxies. The local correlations for simulated remnants show a positive slope for the measured interval, again in contradiction to the observations mentioned above. Equal-mass mergers with counterrotating progenitor disks almost do not rotate ($v_{rot}/\sigma_0 \leq 0.1$) and show a high degree of velocity anisotropy [$(v_{rot}/\sigma_0)^* \approx -1$]. In contradiction to observations they have a significant number of projected remnants that show disky isophotes. The kinematic differences to corotating mergers can be explained by the fact that mergers with counterrotating disks will lead to a remnant with a smaller angular momentum in the end. The reason why the most anisotropic remnants show a relatively large portion of disky projections is unclear and has to be investigated in the future. The remnants of counterrotating equal-mass mergers perfectly follow the observed global and local correlations for LOSVDs.

Remnants of 3:1 and 4:1 mergers are more oblate than equal-mass mergers and rotate fast ($v_{rot}/\sigma_0 \leq 1.0$). It has already been suggested by Barnes (1998) that 3:1 mergers lead to fast rotating flattened remnants. However, he did not quantify the results using directly observable physical parameters. Almost all of our simulated 3:1 and 4:1 mergers have disky isophotes. During the merger the large progenitor disk is not completely destroyed and keeps the memory of its initial state. After the merger is complete the particles from the large progenitor dominate the properties of the merger remnant. 3:1 merger remnants show small minor-axis rotation and are less anisotropic than equal-mass mergers [$(v_{rot}/\sigma_0)^* \approx 0.7$]. They can therefore be assumed to be flattened by rotation. Their surface density profile cannot be described by a pure $r^{1/4}$ law. The Sersic shape parameter lies in the range of $0.28 \leq n_{ser} \leq 0.45$, pointing towards a more exponential-like distribution. These values are consistent with observations of giant elliptical galaxies with lower luminosity (Caon et al., 1993; Gavazzi et al., 2000).

Like equal-mass mergers, the merger geometry influences the resulting kinematical properties of the 3:1 merger remnants. Prograde 3:1 mergers tend to have a more prolate shape, rotate more slowly, show a higher degree of anisotropy and a larger amount of minor-axis rotation than retrograde mergers. In addition, they have stronger twisted isophotes than retrograde mergers. Prograde encounters experience a much stronger tidal perturbation of

the more massive disk component. The formation of strong tidal arms leads to strong radial motions. In addition, tidal material looses angular momentum by dynamical friction with the outer halo. The detailed influence of these processes on the structure of the remnants is still unclear. Further investigations will be needed to understand the dominant processes determining the structure of 3:1 merger remnants. The LOSVDs of 3:1 merger remnants can be characterized by positive values of h_3 for all values of rotational support. This finding contradicts the observations of LOSVDs of fast rotating elliptical galaxies.

Remnants with a mass ratio of 2:1 show properties that are intermediate between those of equal-mass and 3:1 or 4:1 merger remnants with respect to all observed global and local parameters.

There is a fundamental difference between 1:1 remnants and 3:1 or 4:1 (unequal-mass) remnants which does not change with projection effects. They do however lead to a large spread in the global parameters. This is is in very good agreement with the observed parameter distribution (Bender et al., 1988; Bender et al., 1989).

We tested different initial conditions like closer or wider passages, cuspy halo profiles (Hernquist, 1990) resembling the profiles from cosmological large-scale simulations (Navarro et al., 1997), rotating bulges or significantly colder initial disks. The basic results remained unchanged. In contradiction to the common belief that disky E/S0 galaxies are formed involving dissipative processes like star formation (Kormendy & Bender, 1996; Faber et al. (1997); Bekki & Shioya, 1997) we therefore conclude on the basis of isophotal shape and rotation properties that pure stellar mergers can in principle explain the observed dichotomy between disky and boxy ellipticals. The following comparison summarizes the basic results (plus and minus signs indicate whether the result is consistent with observations or not):

1:1 merger, counterrotating

- $r^{1/4}$ surface density profile: ⊕

- triaxial structure, isophotal twist, large amount of minor-axis rotation: ⊕

- no rotation and high degree of velocity anisotropy: ⊕

- boxy and disky isophotes depending on viewing angle: ⊖

- follows observed correlations for LOSVDs: ⊕⊕

1:1 merger, corotating

- $r^{1/4}$ surface density profile: ⊕

- triaxial structure, isophotal twist, large amount of minor-axis rotation: ⊕

- small rotation and modest degree of velocity anisotropy: ⊕

- boxy isophotes ⊕

- does not follow observed global and local correlations for LOSVDs: ⊖⊖

3:1 merger, counterrotating

- surface density profile with $n_{ser} \approx$ 0.4: $\oplus$

- oblate structure, isophotal twist, small amount of minor-axis rotation: $\oplus$

- fast rotation and small degree of velocity anisotropy: $\oplus$

- disky isophotes $\oplus$

- does not follow observed global and local correlations for LOSVDs: $\ominus$

3:1 merger, corotating

- surface density profile with $n_{ser} \approx$ 0.4: $\oplus$

- oblate/prolate structure, isophotal twist, intermediate amount of minor-axis rotation: $\oplus\ominus$

- significant rotation and intermediate degree of velocity anisotropy: $\oplus\ominus$

- disky isophotes $\oplus$

- does not follow observed global and local correlations for LOSVDs: $\ominus\ominus$

However, the properties of LOSVDs of most simulated merger remnants are in disagreement with observations. Where they do agree, as in the case of equal-mass mergers with counterrotating progenitor disks, we find disky projections which are not observed. The negative h_3 for observed fast rotating elliptical galaxies indicates an additional stellar disk component superimposed on a spheroidal stellar body. This finding is supported by detailed surface photometry of disky ellipticals (Nieto et al., 1991a; Scorza & Bender, 1995; Scorza et al., 1998) and kinematical investigations of low-luminosity ellipticals (Rix et al., 1999). The comparison of rotation properties of low-luminosity elliptical galaxies (Rix et al., 1999) with our simulated 3:1 merger remnants has shown, that our remnants are dynamically too hot to be in agreement with observations (Cretton et al., 2000a) in contrast to the results published by Bendo & Barnes (2000). But this is only true for the low-luminosity end of giant elliptical galaxies and cannot lead to conclusions concerning the global population of elliptical galaxies. Since dissipative features are observed in all types of elliptical galaxies (see Section 2.1) it cannot generally be ruled out that gas dynamics and star formation have also played an important role in the formation of boxy ellipticals.

We tested the influence of a dissipative component on the dynamics of our 3:1 merger remnants by artificially adding a thin stellar disk with a scalable mass and size after the merger is complete. We found that a disk with a mass of $\approx 15\%$ of the remnant's mass and a scale length of $r_d \approx 1.0 r_{eff}$ leads to properties of the remnant which are in excellent agreement with observations. The line shapes of the remnants change from having a steep retrograde wing to having a steep prograde wing. The remnants particularly follow the observed local correlation between h_3 and v_{fit}/σ_{fit}. The minor-axis rotation for prograde encounters is reduced to the observed value for all projections and all remnants are as isotropic and rotate as fast as expected from observations.

These results indicate that for the formation of disky elliptical galaxies a dissipative component with a mass of at least 15% of the stellar mass of the progenitor galaxies must have been present during the merger event. This amount of gas must have survived the merger itself to form a disk after the merger was complete. The gaseous disk could then successively have turned into stars that have determined the final properties of present day disky elliptical galaxies. We know from simulations of equal-mass merging gas rich galaxies (Mihos & Hernquist, 1996; Barnes & Hernquist, 1996) that a large amount of gas can be driven to the center leading to a starburst or gas can accumulate in dense gas knots where it could very effectively be transformed into stars. At the end of these simulations most of the gas has turned into stars located in the very central region of the remnant. Therefore it is not clear from these simulations how an extended disk could have formed in equal-mass mergers. Recent simulations of gas rich 3:1 mergers indicate that a significant amount of the gas of the progenitor galaxies can form a large-scale disk after the merger is complete (Naab & Burkert, 2000b). These simulations do not include star formation therefore it is not at all clear if there will be enough gas left to form a disk if the gas is allowed to form stars during the merger. Hence we do not know in how far processes like star formation and energy feedback into the interstellar medium will influence the properties of the merger remnant. For a more detailed discussion of this topic we refer to Chapter 7.

Taking all results of this thesis into account we can draw the following conclusions for collisionless mergers of disk galaxies:

- Global properties of merger remnants like isophotal shape and velocity anisotropy agree with observations of elliptical galaxies. The dominant parameter is the mass ratio of the progenitor galaxies.

- Local properties like LOSVD-shape or rotational support (in case of 3:1 and 4:1 mergers) are in disagreement with observations with the exception of counterrotating equal-mass mergers.

- Merging of equal-mass disk galaxies is the most likely process for the formation of boxy and anisotropic elliptical galaxies.

- Disky elliptical galaxies cannot have formed from initially gas free 3:1 mergers of disk galaxies.

- A disk, with a mass of $\approx 15\%$ of the initial stellar mass, formed after the 3:1 merger is complete leads to a perfect agreement with observations. Therefore gas must have been present during the formation of disky elliptical galaxies.

Observations show that disky ellipticals have on average lower luminosities than boxy ellipticals (Bender et al., 1988). Our results indicate that low-mass elliptical galaxies preferentially formed by unequal-mass mergers of disk galaxies whereas equal-mass mergers dominated the formation of high-mass ellipticals. This result is puzzling as there is no convincing argument for why low mass ellipticals should have suffered mainly unequal-mass mergers while high mass ones should have evolved mainly through equal-mass mergers. However, there is a possible solution to this problem. Boxy ellipticals could predominantly form from mergers of early type galaxies. Observations of high redshift clusters suggest this process to be very frequent in the early universe (e.g. van Dokkum et al., 1999). We tested this formation

scenario by taking two merger remnants of corotating equal-mass galaxies and merging them on a parabolic orbit. The resulting remnant is indeed very anisotropic (see Figure 6.1). The amount of boxiness and the ellipticities are larger than observed. However, the LOSVD fits the observed data. Naab & Burkert (2000a) also investigated unequal-mass mergers of early type galaxies and found a significant amount of disky projections with anisotropic kinematics, in contradiction with observations.
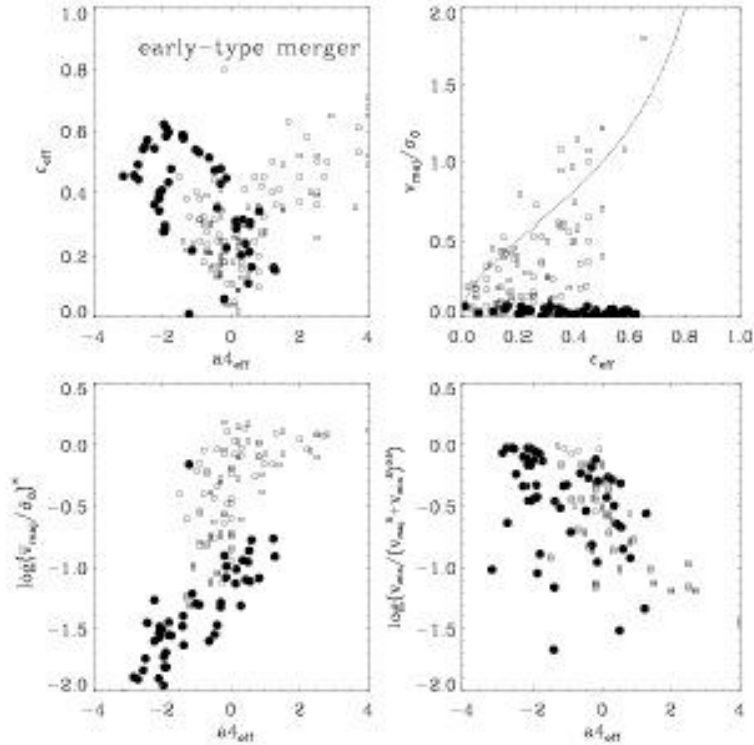
Figure 6.1: Same as Figure 4.36 but for a merger of two remnants of equal-mass disk mergers.

Therefore, some of our problems are still unsolved. Numerical resolution does not seem to be the problem. We performed simulations with varying numbers of particles and different timestep sizes getting the same results. The errors for the measured quantities are in general very small. If they are large, as in the case of $a4_{eff}$ for low-resolution simulations, they do not have any influence on the basic results at all.

A possible solution to the problem of making massive ellipticals could be the influence of gas. A significant amount of gas must have also been present in equal-mass mergers as we know from the existence of metal enhanced and/or kinematically decoupled cores. If previous simulations of gas rich equal-mass mergers are correct most of the gas settles into the central region of the merger remnant. The additional potential could change the orbits of the stars (see e.g. Merritt & Quinlan, 1998; Valluri & Merritt, 1998). This could lead to much rounder

remnants (as it has been found by Barnes & Hernquist, 1996) thereby avoiding extremely boxy or disky shapes.

The formation of a large-scale disk after an equal-mass merger is complete seems very unlikely since most of the gas in simulations is driven to the center. However, we could test the influence of such an additional gas disk in the same way as we did for 3:1 mergers (Section 5.3). The result for the best fitting disk dimensions is almost the same as for 3:1 mergers (Figure 6.2).
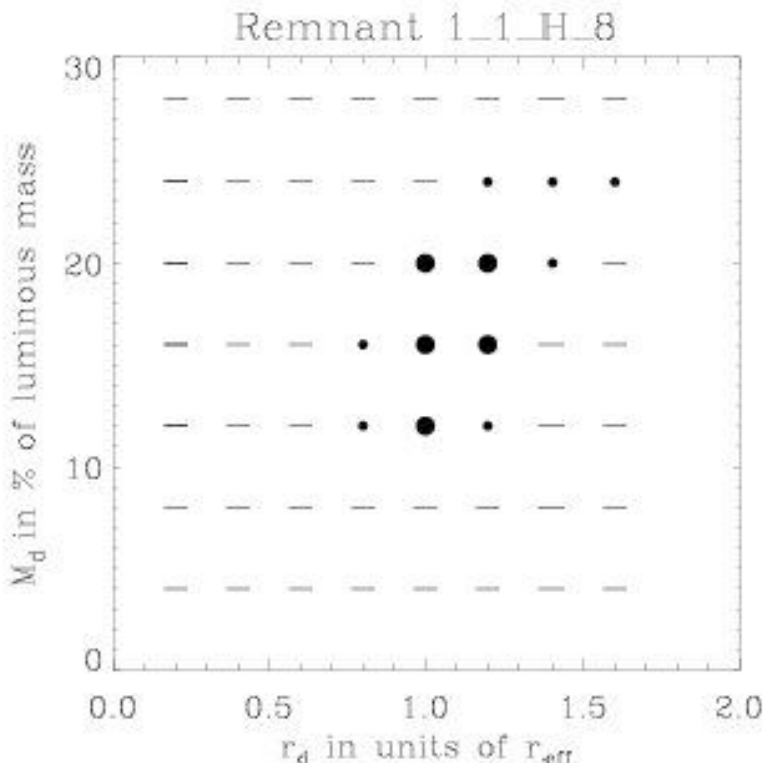
Figure 6.2: Mass M_d versus scale radius r_d for a disk added to the merger remnant 1_1_H_8. Combinations that are able to reproduce (big dot), almost reproduce (small dot) or fail to reproduce (minus sign) the observed correlations are shown.

If this behaviour was realistic it would break the strict association of equal-mass mergers with boxy ellipticals. The properties like diskiness/boxiness or isotropy/anisotropy would then strongly depend on the projection effects. Surprisingly, the spread in the data points perfectly agrees with the observed distribution (Figure 6.3).

In addition, the model follows the observed correlations for the LOSVDs (Figure 6.4). Such a merger remnant would however not represent the class of observed massive boxy ellipticals since observed radio and X-ray emission connected to those galaxies does not depend on
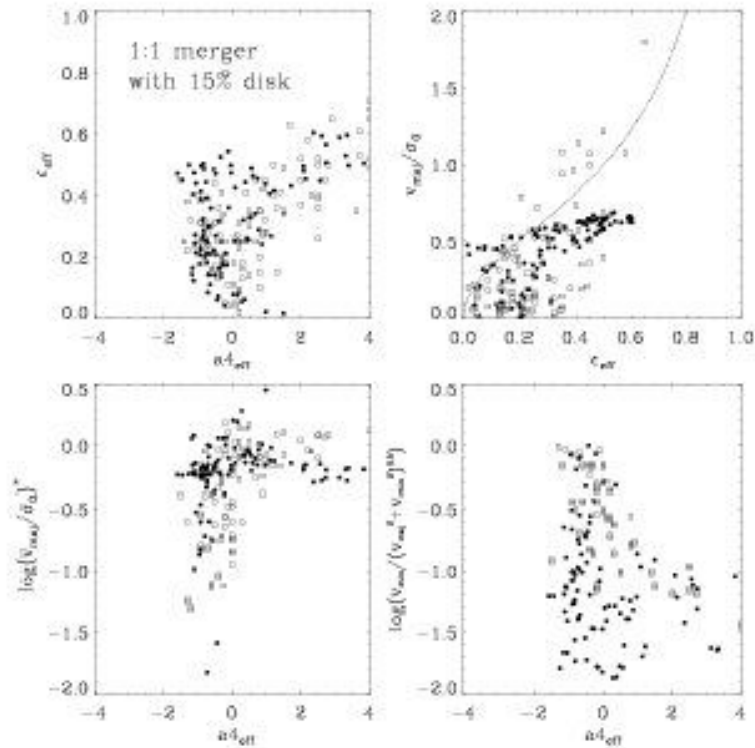
Figure 6.3: Same as Figure 4.36 but for an equal-mass merger with an additional disk with a mass of $M_d = 15\%$ of the luminous mass and a scale length of $r_d = 1.25 r_{\text{eff}}$.
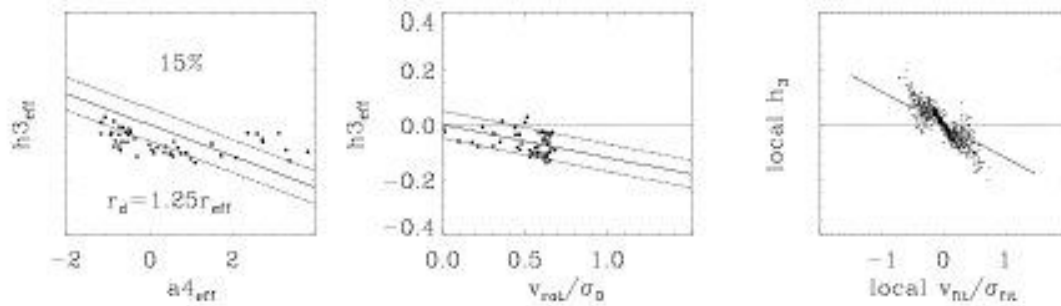
Figure 6.4: Same as figure 5.29 but for an equal-mass merger with a disk with $M_d = 15\%$ and $r_d = 1.25 r_{\text{eff}}$ added after the merger was complete.

the viewing angle. However, it could represent a class of objects connecting boxy and disky galaxies at intermediate masses (Bender et al., 1988). In addition, previous models of gas-rich equal-mass mergers might have missed important physical processes. A plausible way to form

such a large-scale disk is to heat the gas at the time when it still has a significant amount of angular momentum and decouple it from the stars. After the merger has taken place, the gas would cool down and form a disk. This scenario, however, is very speculative and can only be tested with further simulations incorporating more physical processes. Some of them will be discussed in Chapter 7.

Finally, there is at least one problem left. When did massive elliptical galaxies really form? The traditional view on the formation and evolution of giant elliptical galaxies is that they are very old stellar systems and all formed very early at a redshift of more than two (Searle et al., 1973). After an intensive initial star formation phase they experienced very little mass evolution (Bruzual A. & Charlot, 1993). It has been argued by many authors that the stellar evolution of ellipticals is compatible with pure passive evolution models (e.g. Bower et al., 1992, Aragon-Salamanca et al., 1993, Bender et al., 1996 , Ellis et al., 1997, Ziegler & Bender, 1997) or models with exponentially decaying star formation (Ziegler et al., 1999). Alternatively, hierarchical theories of galaxy formation predict that massive galaxies were assembled relatively late in many generations of mergers of disk galaxies or smaller subunits and mass accretion. It has been argued by Kauffmann (1996) and Kauffmann & Charlot (1998) that this merger scenario is consistent with observations of galaxies at different redshifts.

We have shown that simulated remnants of merging spiral galaxies have properties resembling observed elliptical galaxies. This is an argument for the merger picture. On the other hand it is very unlikely that Milky Way sized galaxies could have existed 5 Gyrs or 10 Gyrs ago in sufficient numbers to account for the population of ellipticals in total. Probably the process is a combination of dissipative collapse and mergers. Massive ellipticals and bulges form by early dissipative collapse and faint disky and intermediate ellipticals form by mergers of evolved Sb or Sa galaxies. However, for a self-consistent model of the formation of ellipticals it will be necessary to investigate the merger history of individual galaxies in large-scale cosmological simulations to draw conclusions on the masses, mass ratios, orbits, gas contents, halo shapes, and time scales of individual mergers. Those mergers have then to be investigated in great detail. Therefore we need further improvements in computer power, in the software for time integration of physical processes, and in the way we analyze and visualize our results.

Chapter 7

Outlook

We have seen that gas must have played an important role during the formation of disky elliptical galaxies. The observations can be explained if gas with a mass of at least 15% of the initial luminous mass survives the encounter and forms a disk after the merger is complete. We have used this information to resimulate the 3:1 mergers 3_1_L_8 and 3_1_L_15 adding a gas component with 20% of the total stellar mass (thereafter 3_1_LG_8 and 3_1_LG_15). The gas was represented by SPH particles using an isothermal equation of state (Gingold & Monaghan, 1977; Lucy, 1977; Monaghan, 1992). The N-body/SPH formalism and numerical models will not be discussed in detail here (see e.g. Hernquist & Katz, 1989). This first step to more self-consistent simulations of unequal-mass mergers focuses on the gas dynamics and neglects the effects of star formation. Figures 7.1 and 7.2 show snapshots of the gas distribution during the encounter. The prograde and retrograde rotating massive progenitor disks are easily recognizable. Figures 7.3 and 7.4 show the final distribution of stellar and gaseous particles for the two mergers. In contrast to the collisionless merger the stellar distribution here is almost perfectly oblate with $\mathcal{T} = 0.1$ for 3_1_LG_8 and $\mathcal{T} = 0.06$ for 3_1_LG_15. The surface density of the stellar population for the prograde merger has a Sersic index of $n_{ser} \approx 0.24$. The retrograde merger 3_1_LG_15 has $n_{ser} \approx 0.48$ and is therefore more exponential. The gas in both cases is distributed in a large-scale disk and is surrounded by dense gas knots. In case of the merger 3_1_LG_8, the gas disk is clearly tilted in the outer parts. As already noted by Barnes & Hernquist (1996), based on their SPH simulations of equal-mass mergers, even a small amount of gas has a strong influence on the stellar population of the remnant. In addition to their finding that equal-mass mergers with gas look more round we find that unequal-mass mergers with gas are more elongated

If we investigate the LOVSDs of only the stellar part we find negative values for h_3 in excellent agreement with observations (see upper rows of Figures 7.5 and 7.6), although the inner tilt of the local correlation is not reproduced. Therefore the gas must have changed the dynamics of the stars significantly during the merger event. We have seen that a disk, added after the merger is complete, does not lead to such a significant change in stellar kinematics. If we assume that the gas transforms into stars after it has settled into a disk we can treat the gas particles as stellar particles and investigate the remnant again. We still find a good agreement of the LOSVDs with observations (see lower rows of Figures 7.5 and 7.6). However, now the absolute values of h_3 tend to be slightly too large. Taking the stellar surface density, triaxiality, and ellipticity into account, the remnant 3_1_LG_8 (G is for "gas") resembles more

a S0 than an elliptical one. These first results already suggest that negative values for h_3 do not have to result from a newly formed stellar disk alone.
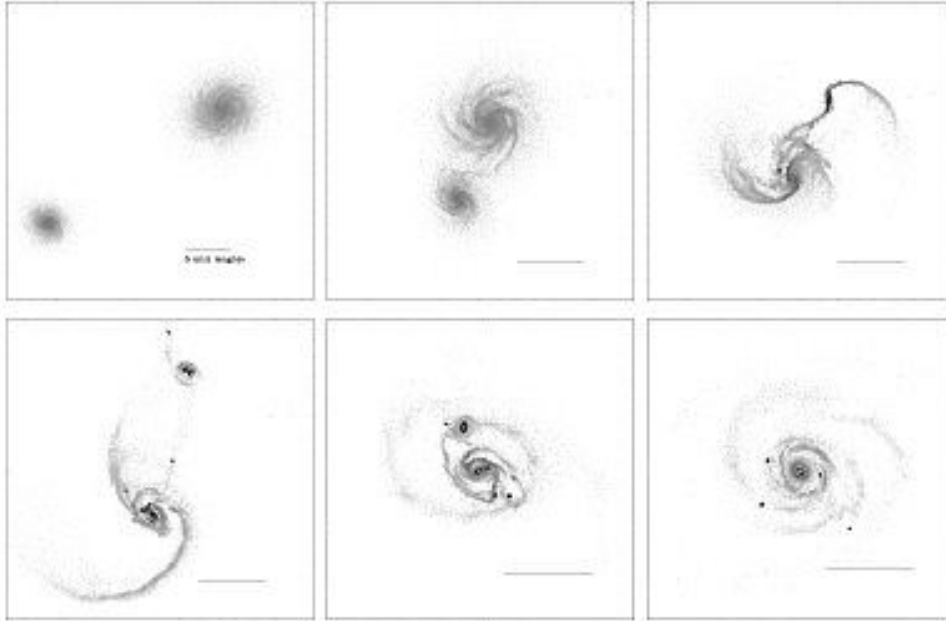
Figure 7.1: Time sequence of the gaseous component of the merger 3_1_LG_8.
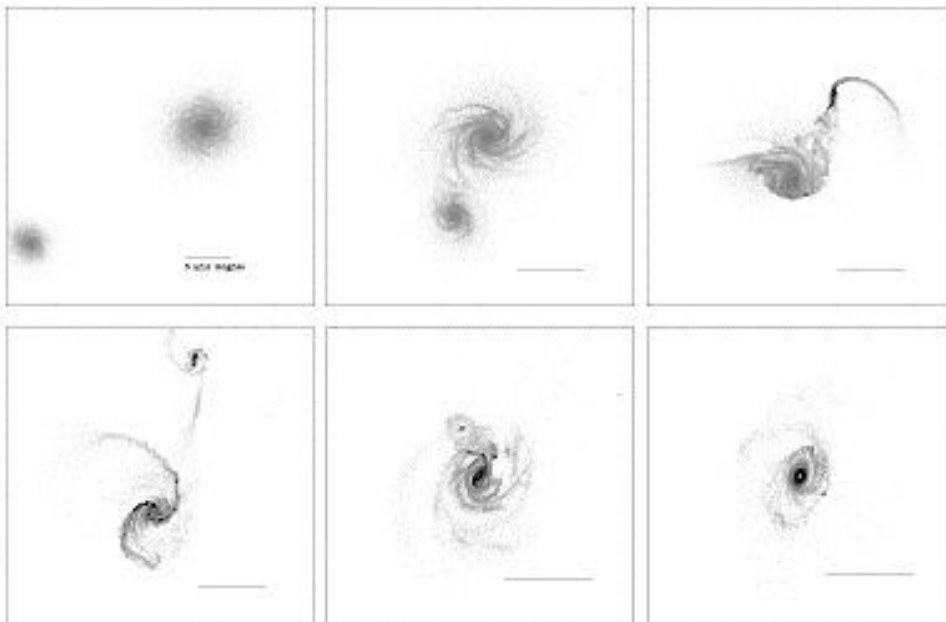
Figure 7.2: Time sequence of the gaseous component of the merger 3_1_LG_15.
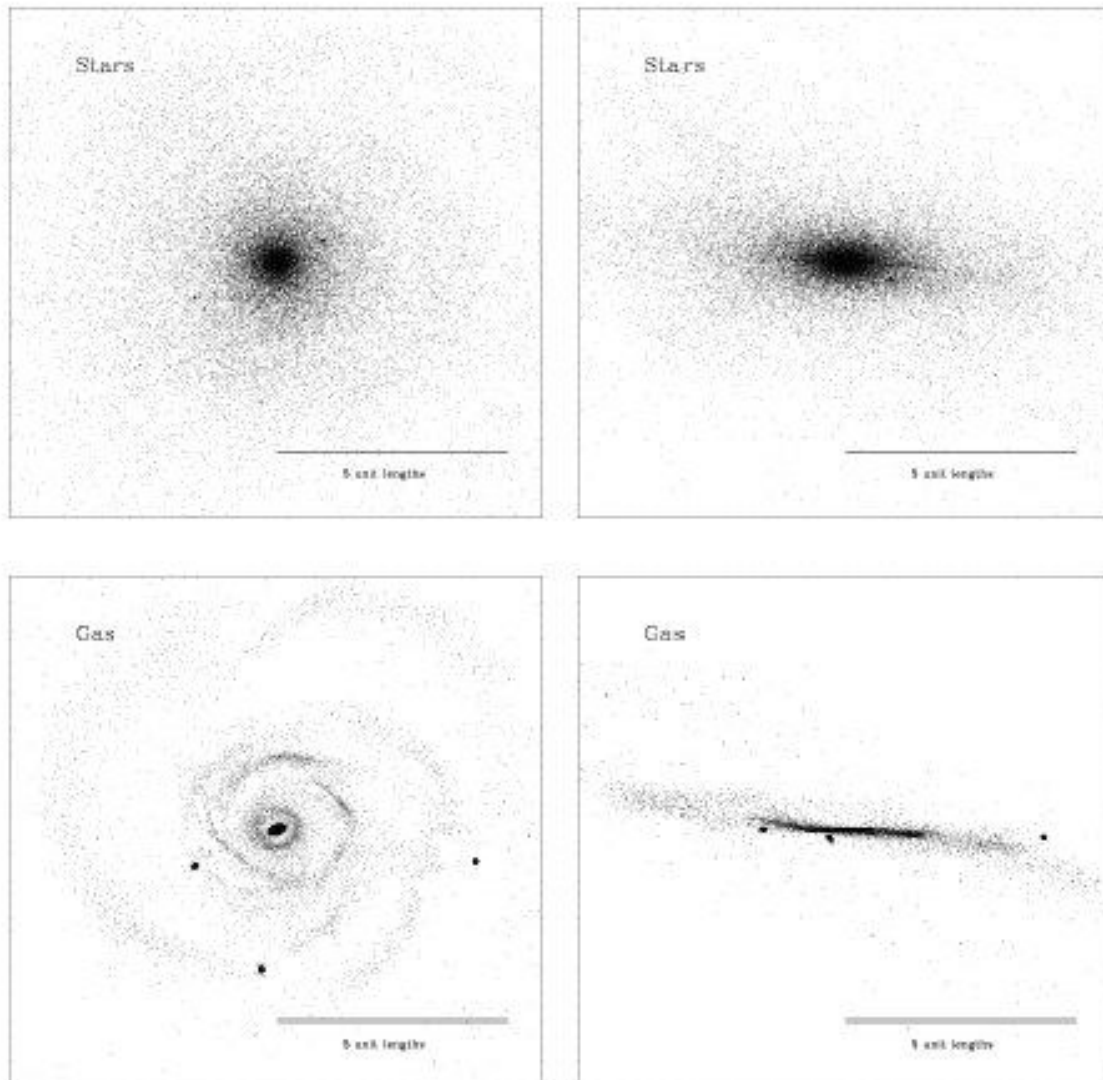
Figure 7.3: Final distribution of the stars and the gas of the merger 3_1_LG_8.

Instead, they can result from the influence of a gaseous (collision dominated) component during the merger event. Therefore, collisionless and collisional dynamics both determine the structure of merger remnants.

The end products of the mergers with gas show properties that are in very good agreement with properties of observed elliptical galaxies. In addition, they are in good agreement with predictions from observations that suggest that disky elliptical galaxies have formed from processes which include dissipative physics. Kormendy & Bender (1996) proposed a modified Hubble sequence in the sense that there is a continuous sequence from S0 galaxies to disky ellipticals to boxy ellipticals (Figure 7.7). They predict that the influence of dissipation de-
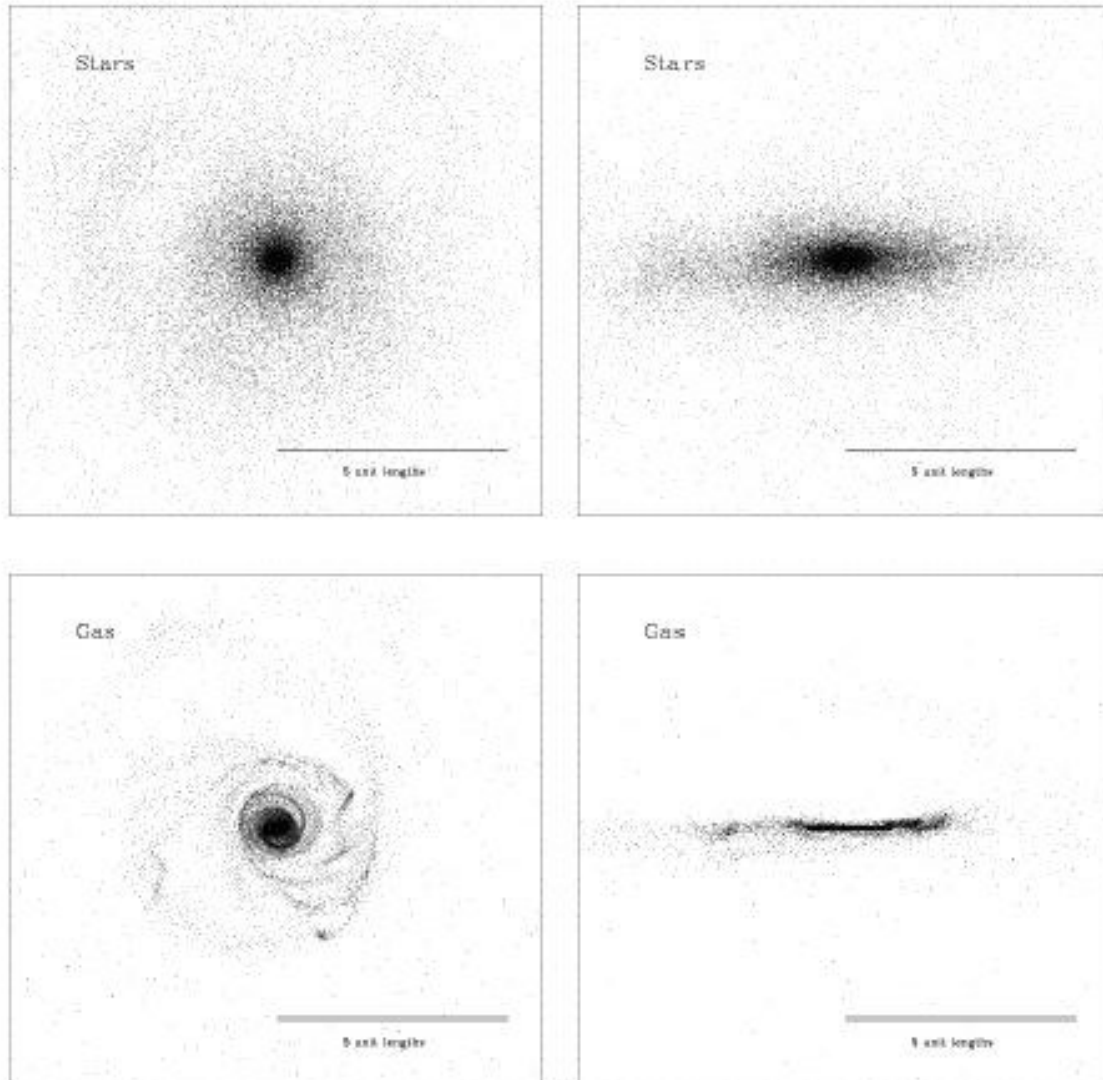
Figure 7.4: Final distribution of the stars and the gas of the merger 3_1_LG_15.

creases from the right hand side to the left hand side.

We find strong theoretical evidence that this picture is correct. Collisionless unequal-mass mergers lead to remnants that are inconsistent with observations. Adding a significant amount of gas, which is likely if one assumes that the mergers must have taken place in the earlier phases of the universe, leads to disky ellipticals or even S0 galaxies with observed kinematical properties. Equal-mass mergers might lead to intermediate type galaxies as discussed before and mergers of gas poor early type galaxies make up the population of massive anisotropic ellipticals.
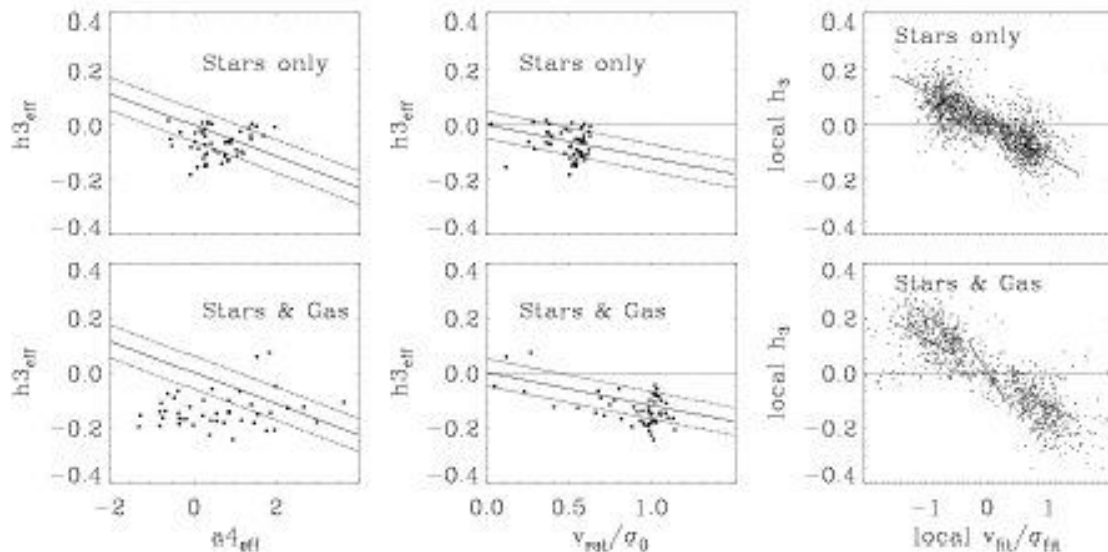
Figure 7.5: Correlations for the merger 3_1_L_8 with gas. *Upper row:* Correlations with h_3 for the stellar part only.*Lower row:* Correlations with h_3 assuming that all the gas turned into stars after the disk has formed.
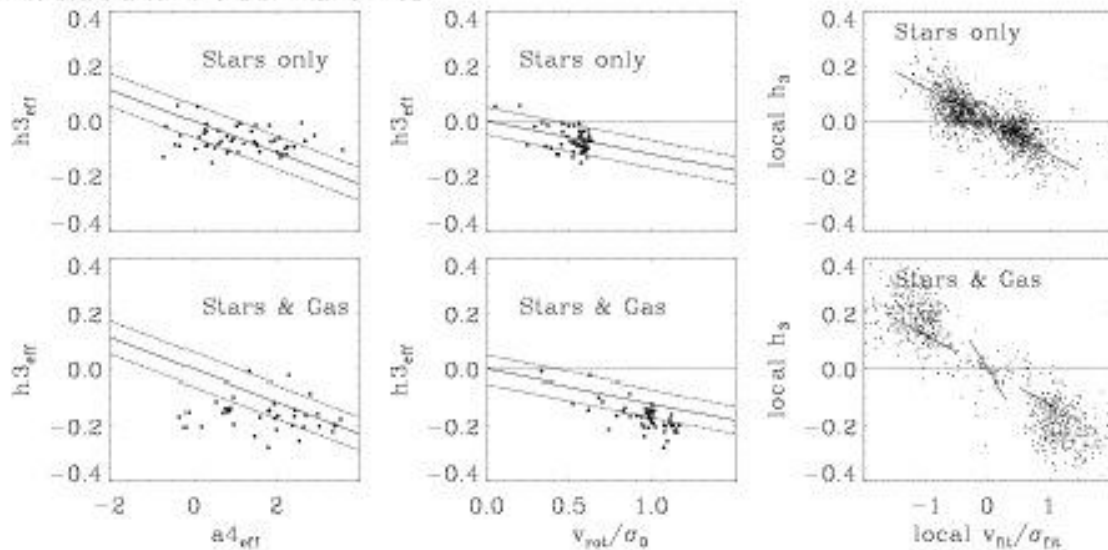
Figure 7.6: Same as Figure 7.5 but with a prograde rotating massive disk.

However, there are a lot of outstanding issues that could, in addition, have a significant influence on the theory of the formation of elliptical galaxies:

- The **interstellar medium** is by far more complex than it is treated in these very simplified simulations. We only simulate gas with a temperature of 10^4 Kelvin with an isothermal equation of state. However, we know that hot massive gaseous coronae exist around massive elliptical galaxies at a temperature of some 10^6 Kelvin and cold molecular gas exists in molecular clouds at a temperature of ≈ 10 Kelvin in disks of
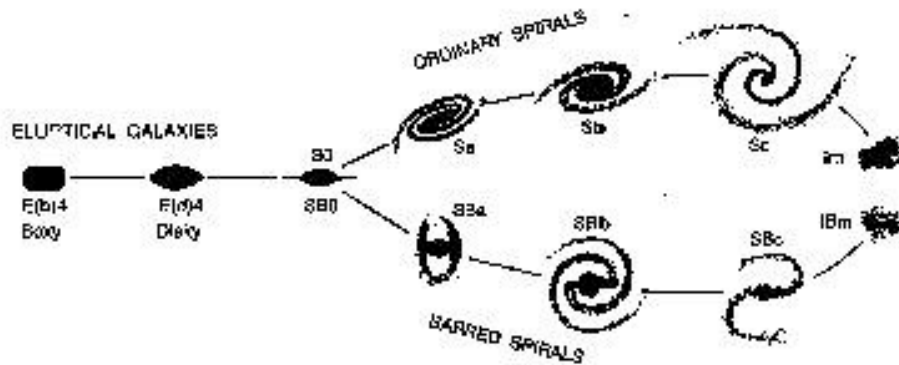
Figure 7.7: Revised Hubble sequence as proposed by Kormendy & Bender (1996).

spiral galaxies. These components contain a significant amount of dynamical mass that could (and will, as we have seen) change the properties of the resulting merger remnant. As we know from cosmological simulations, there exists a severe angular momentum problem since cold gas clumps that form relatively early in the universe loose too much angular momentum by dynamical friction to lead to the formation of spiral galaxies with smaller than the observed rotation (see e.g. Navarro & Steinmetz, 1997; Steinmetz & Navarro, 1999). It is not yet clear, at least to me, why a related problem should not exist for merging galaxies. Here we also find the formation of bound gas clumps within tidal tails. These gas clumps loose angular momentum by dynamical friction and fall back to the center of the galaxy to make up a disk. If there is no problem at all with this we can conclude that the simulated formation of tidal clumps is real and those clumps can be associated with dwarf galaxies or massive star clusters. If there exists an angular momentum problem, part of the gas must have been heated by star formation processes to keep its angular momentum and form a new large-scale disk after the merger is complete as it has been suggested by Rix et al. (1999). Therefore it will be necessary to simulate a multi-phase interstellar medium on the scale of the entire galaxy.

- The **spatial resolution** of the present day simulations does not go far beyond 100pc. This is the scale of giant molecular clouds. Properties on smaller scales cannot be simulated self-consistently. For example, we can barely resolve the structure of the bound clumps that form in tidal tails of interacting galaxies. We do not exactly know on which (probably resolution-dependent) scales these clumps could form. On small scales they could be the seeds of **star clusters**. If they are more massive, they could be identified with **tidal dwarf galaxies**. Those clumps are extremely interesting since they do not contain dark matter at all. Therefore they are *a priory* candidates for globular clusters which do not contain dark matter. Also the question of whether there exist dwarf galaxies without dark matter could be addressed. Dwarfs that are observed around merging systems could have a tidal origin (e.g. Deeg et al., 1998). Therefore we need high-resolution simulations to resolve the internal structure of those regions in detail (e.g. Kroupa, 1997; Klessen & Kroupa, 1998; Duc et al., 2000).

- We also want to know where exactly the dense regions form that will be the seeds of star formation. High-resolution simulations could be compared with high-resolution observations of nearby merging spirals like the Antennae galaxies or Cartwheel (e.g. Mirabel et al., 1998; Horellou et al., 1998). In addition, it is impossible up to now to follow infalling gas on its way to the center. However, this process could be crucial for the formation of **massive galactic black holes**. There is a strong correlation between bulge masses and masses of their black holes (Gebhardt et al., 2000). If bulges of spiral galaxies host black holes of the order of $10^6 M_\odot$ and elliptical galaxies host black holes of the order $10^9 M_\odot$ it is not possible that elliptical galaxies have formed from collisionless mergers of spiral galaxies (even if their black holes will merge in the end, we would need ≈ 1000 progenitor galaxies of Milky Way size which is very unlikely). Gas accretion during a major merger is a very attractive way of explaining the large black hole masses. However, future simulations should be able to follow the infall of gas up to the innermost regions where relativistic processes become important. This would enable us to calculate accretion rates and estimate the strength of central starbursts and the grow rate of nuclear black holes.

- Another related topic are the **core properties** of elliptical galaxies. It has been argued by Faber et al. (1997) that the steep central density profiles in disky elliptical galaxies originate from central disk-like structures with a power-law density distribution resulting from dissipative processes. Naab & Burkert (2000b) found first evidence for the formation of such a central power-law gas distribution. The flat cores in massive ellipticals are assumed to be a result of black holes interacting with each other or the surrounding stars (e.g. Nakano & Makino, 1999; Cruz & Merritt, 2000). Since the dynamical timescale is very short at the centers of galaxies, it is necessary to use methods of collision dominated dynamics in the inner parts of galaxies in combination with collisionless dynamics for the large-scale evolution of the system. The development of numerical models to treat those problems is an important step to fully understand the dynamics of interacting galaxies in the future (e.g. Hemsendorf, 2000 and others).

- The **influence of gas on the stellar dynamics during a merger event** is not well understood. Barnes & Hernquist (1996) already noted that the stellar distribution of equal-mass mergers with gas look significantly rounder than their collisionless counterparts. In contrast, as we have shown here, 3:1 remnants with gas are significantly more flattened than collisionless 3:1 mergers. Furthermore, the difference in the LOSVDs point to a major change in the stellar distribution function. However, it is far beyond the scope of this thesis to investigate this issue. Specialists working within this field might be able to deal with it analytically (Dehnen, private communication). We have already seen that the formation of a thin stellar disk that formed after the collisionless merger is complete cannot be responsible for a significant change of the shape and the dynamics of the spheroidal part of the remnant (Section 5.3). Therefore the gas itself must influence the stellar population during the merger event. The details of this process are still not understood and need further investigation.

- We did not incorporate **star formation** into our simulations. The formation of molecular clouds which are the seeds of star formation on scales of 10pc to 100pc is not yet understood. Since we are not able to resolve these small scales it is even more problematic to apply simple large-scale star formation rules. It seems plausible that

small-scale effects would not change the global star formation properties, but it is not proven at all. However first steps have been taken in the past (Barnes & Hernquist, 1996; Mihos & Hernquist, 1996; Springel, 2000). Feedback from star-forming regions through the input of thermal and kinetic energy into the surrounding interstellar medium will change the resulting gas flow. First attempts at incorporating star formation and feedback by Mihos & Hernquist (1996) and others indicate that star formation does not change large-scale gas flows as for example the bar-induced funneling of gas to the center of the merger remnant. Since only very simple rules describing star formation on a kpc scale have been applied, the complex small scale processes related to star formation are neglected. It has been argued by Bekki & Shioya (1997) and Springel (2000) that the isophotal shape depends on the star formation history of the merger remnant. However, those simulations did not investigate the influence of merger geometry and different mass ratios. Therefore it is not yet clear which is the dominant process.

- There must be some influence of the merging process on the **dark matter halos**. We can expect that the dramatic change of shape of the luminous part will also change the shape of the dark matter halos. Collisionless merger simulations show that the resulting halos are almost spheroidal. This is not surprising since we start with spherical objects. Large-scale collisionless simulations suggest a prolate shape (Warren et al. (1992)) whereas a small fraction of dissipative gas ($\approx 10\%$) results in halos of a more oblate shape (Dubinski, 1994). Observations suggest that halos in real galaxies are most likely flattened oblate objects (see Sackett (1999) for an overview). Therefore it is unclear if we need oblate halos already as models for disk galaxies or if oblate halos form during the merger process itself. In addition, it has to be investigated how in detail the shape of dark matter halos influences the evolution of merging galaxies. Especially the influence of initially rotating dark halos of the progenitor galaxies should be investigated in the future.

- At the present epoch most elliptical galaxies are found in high-density regions like galaxy groups or galaxy clusters. Nevertheless, the **environmental influence** at the time of their formation is still unclear. Massive old clusters like Coma are most likely dynamically relaxed systems with velocity dispersions of ≈ 1000 km/s. Galaxies with relative velocities of this order do not merge. There is evidence that younger clusters show a significant amount of dynamically cold substructure, probably infalling groups of galaxies with velocity dispersions of the order of 100 km/s. Here merging is very likely. Therefore galaxy groups or galaxy clusters in early evolutionary phases are good candidates for being the locations of elliptical galaxy formation. It has been shown theoretically that the potential of a cluster and repeated close high-speed encounters with cluster galaxies can significantly change the morphology of an infalling spiral galaxy (Moore et al., 1998). Gnedin et al. (2000) argue on the basis of cosmological large-scale simulations that bulges and moderate size ellipticals could form at very early phases of the universe. However, it is still unclear how massive ellipticals could have formed thereafter. More theoretical work has to be done in the future to understand in detail possible formation processes and interactions with the environment in detail.

Bibliography

APPEL, A. W.: 1985. *SIAM J. Sci. Stat. Comp.*, **6**, 85.

ARAGON-SALAMANCA, A., ELLIS, R. S., COUCH, W. J., CARTER, D.: 1993. Evidence for systematic evolution in the properties of galaxies in distant clusters. *Monthly Notices of the Royal Astronomical Society*, **262**, 764.

ATHANASSOULA, E.: 1993. N-body techniques and their impact on galactic stellar dynamics. In F., C. E., A., editors, *N-body Problems and Gravitational Dynamics*, page 116.

ATHANASSOULA, E., BOSMA, A., LAMBERT, J. ., MAKINO, J.: 1998. Performance and accuracy of a GRAPE-3 system for collisionless N-body simulations. *Monthly Notices of the Royal Astronomical Society*, **293**, 369.

ATHANASSOULA, E., FADY, E., LAMBERT, J. C., BOSMA, A.: 2000. Optimal softening for force calculations in collisionless N-body simulations. *Monthly Notices of the Royal Astronomical Society*, **314**, 475.

BAHCALL, J. N. SONEIRA, R. M.: 1980. The universe at faint magnitudes. I - Models for the Galaxy and the predicted star counts. *Astrophysical Journal Supplement Series*, **44**, 73.

BAK, J. STATLER, T. S.: 2000. The intrinsic shape distribution of a sample of elliptical galaxies. *Astronomical Journal*, **120**, 110.

BARNES, J.: 1998. Dynamcis of galaxy interactions. In Friedly, D., Martinet, L., Pfenniger, D., editors, *Galaxies: Interactions and induced star formation: lecture notes 1996 / Saas Fee Advanced Course 26*, page 276. Berlin: Springer.

BARNES, J. E.: 1986. A hierarchical $\mathcal{O}(N \log N)$ force-calculation algorithm. *Nature*, **324**, 446.

BARNES, J. E.: 1988. Encounters of disk/halo galaxies. *Astrophysical Journal*, **331**, 699.

BARNES, J. E.: 1992. Transformations of galaxies. I - Mergers of equal-mass stellar disks. *Astrophysical Journal*, **393**, 484.

BARNES, J. E. HERNQUIST, L.: 1992. Dynamics of interacting galaxies. *Annual Review of Astronomy and Astrophysics*, **30**, 705.

BARNES, J. E. HERNQUIST, L.: 1996. Transformations of galaxies. II. Gasdynamics in merging disk galaxies. *Astrophysical Journal*, **471**, 115.

BEKKI, K.: 1998. Unequal-mass galaxy mergers and the creation of cluster S0 galaxies. *Astrophysical Journal Letters*, **502**, L133.

BEKKI, K. SHIOYA, Y.: 1997. Formation of boxy and disky elliptical galaxies in early dissipative mergers. *Astrophysical Journal Letters*, **478**, L17.

BENDER, R.: 1988a. Rotating and counter-rotating cores in elliptical galaxies. *Astronomy and Astrophysics*, **202**, L5.

BENDER, R.: 1988b. Velocity anisotropies and isophote shapes in elliptical galaxies. *Astronomy and Astrophysics*, **193**, L7.

BENDER, R.: 1990a. In Wielen, R., editor, *Dynamics and interactions of galaxies. Berlin, Springer-Verlag, 1990*, page 212.

BENDER, R.: 1990b. Unraveling the kinematics of early-type galaxies - Presentation of a new method and its application to NGC4621. *Astronomy and Astrophysics*, **229**, 441.

BENDER, R.: 1996. Mergers and the formation of massive ellipticals. In Bender, R. Davies, R. L., editors, *IAU Symp. 171: New Light on Galaxy Evolution (Dordrecht: Kluwer)*, volume 171, page 181.

BENDER, R., BURSTEIN, D., FABER, S. M.: 1992. Dynamically hot galaxies. I - Structural properties. *Astrophysical Journal*, **399**, 462.

Bender, R. Davies, R. L., editors: 1996. *New light on galaxy evolution. The IAU Symposium 171, held at Max Planck Haus in Heidelberg, Germany from 25th-30th June 1995.*, volume 171.

BENDER, R., DOEBEREINER, S., MOELLENHOFF, C.: 1987. Radio activity and the shape of elliptical galaxies. *Astronomy and Astrophysics*, **177**, L53.

BENDER, R., DOEBEREINER, S., MOELLENHOFF, C.: 1988. Isophote shapes of elliptical galaxies. I - The data. *Astronomy and Astrophysics Supplement Series*, **74**, 385.

BENDER, R. SAGLIA, R. P.: 1999. Elliptical galaxies: Detailed structure, scaling relations and formation. In Merritt, D., Sellwood, J. A., Valluri, M., editors, *ASP Conf. Ser. 182: Galaxy Dynamics - A Rutgers Symposium*, page 113.

BENDER, R., SAGLIA, R. P., GERHARD, O. E.: 1994. Line-of-sight velocity distributions of elliptical galaxies. *Monthly Notices of the Royal Astronomical Society*, **269**, 785.

BENDER, R. SURMA, P.: 1992. Mg2 line-strength profiles of elliptical galaxies with kinematically decoupled cores. *Astronomy and Astrophysics*, **258**, 250.

BENDER, R., SURMA, P., DOEBEREINER, S., MOELLENHOFF, C., MADEJSKY, R.: 1989. Isophote shapes of elliptical galaxies. II - Correlations with global optical, radio and X-ray properties. *Astronomy and Astrophysics*, **217**, 35.

BENDER, R., ZIEGLER, B., BRUZUAL, G.: 1996. The redshift evolution of the stellar populations in elliptical galaxies. *Astrophysical Journal Letters*, **463**, L51.

BENDER, R. E.: 1993. In Danziger, J., editor, *Structure, Dynamics and chemical evolution of elliptical galaxies ,ESO/EICP workshop*, page 113.

BENDO, G. J. BARNES, J. E.: 2000. The line-of-sight velocity distributions of simulated merger remnants. *Monthly Notices of the Royal Astronomical Society*, **316**, 315.

BEUING, J., DOBEREINER, S., BOHRINGER, H., BENDER, R.: 1999. X-ray luminosities for a magnitude-limited sample of early-type galaxies from the ROSAT All-Sky Survey. *Monthly Notices of the Royal Astronomical Society*, **302**, 209.

BINGGELI, B. JERJEN, H.: 1998. Is the shape of the luminosity profile of dwarf elliptical galaxies an useful distance indicator? *Astronomy and Astrophysics*, **333**, 17.

BINNEY, J.: 1978. On the rotation of elliptical galaxies. *Monthly Notices of the Royal Astronomical Society*, **183**, 501.

BINNEY, J.: 1985. Testing for triaxiality with kinematic data. *Monthly Notices of the Royal Astronomical Society*, **212**, 767–781.

BINNEY, J. DE VAUCOULEURS, G.: 1981. The apparent and true ellipticities of galaxies of different Hubble types in the Second Reference Catalogue. *Monthly Notices of the Royal Astronomical Society*, **194**, 679.

BINNEY, J., KORMENDY, J., WHITE, S., MARTINET, L., MAYOR, M.: 1982. *Morphology and dynamics of galaxies : twelfth advanced course of the Swiss Society of Astronomy and Astrophysics (member society of the Swiss National Academy of Science)*. Sauverny, Switzerland : Geneva Observatory, [1982].

BINNEY, J. MAMON, G. A.: 1982. M/L and velocity anisotropy from observations of spherical galaxies, or must M87 have a massive black hole. *Monthly Notices of the Royal Astronomical Society*, **200**, 361.

BINNEY, J. MERRIFIELD, M.: 1998. *Galactic Astronomy*. Galactic astronomy / James Binney and Michael Merrifield. Princeton, NJ : Princeton University Press, 1998.

BINNEY, J. TREMAINE, S.: 1987. *Galactic Dynamics*. Princeton University Press.

BOSELLI, A., GAVAZZI, G., FRANZETTI, P., PIERINI, D., SCODEGGIO, M.: 2000. 1.65 μm (H-band) surface photometry of galaxies. IV. Observations of 170 galaxies with the Calar Alto 2.2 m telescope. *Astronomy and Astrophysics Supplement Series*, **142**, 73.

BOTTEMA, R.: 1993. The stellar kinematics of galactic disks. *Astronomy and Astrophysics*, **275**, 16.

BOWER, R. G., LUCEY, J. R., ELLIS, R. S.: 1992. Precision photometry of early-type galaxies in the Coma and Virgo clusters: A test of the universality of the colour-magnitude relation. I - The data. II. Analysis. *Monthly Notices of the Royal Astronomical Society*, **254**, 589.

BRUZUAL A., G. CHARLOT, S.: 1993. Spectral evolution of stellar populations using isochrone synthesis. *Astrophysical Journal*, **405**, 538.

BURKERT, A.: 1993. Do elliptical galaxies have $r^{(1/4)}$ brightness profiles? *Astronomy and Astrophysics*, **278**, 23.

CANIZARES, C. R., FABBIANO, G., TRINCHIERI, G.: 1987. Properties of the X-ray emitting gas in early-type galaxies. *Astrophysical Journal*, **312**, 503.

CAON, N., CAPACCIOLI, M., D'ONOFRIO, M.: 1993. On the shape of the light profiles of early type galaxies. *Monthly Notices of the Royal Astronomical Society*, **265**, 1013.

CARLBERG, R. G.: 1986. The phase space density in elliptical galaxies. *Astrophysical Journal*, **310**, 593.

CARTER, D.: 1987. Weak disks in rapidly rotating elliptical galaxies. *Astrophysical Journal*, **312**, 514.

CORDEY, R. A.: 1986. Radio sources in giant E and S0 galaxies. *Monthly Notices of the Royal Astronomical Society*, **219**, 575.

CRANE, P., STIAVELLI, M., KING, I. R., DEHARVENG, J. M., ALBRECHT, R., BARBIERI, C., BLADES, J. C., BOKSENBERG, A., DISNEY, M. J., JAKOBSEN, P., KAMPERMAN, T. M., MACHETTO, F., MACKAY, C. D., PARESCE, F., WEIGELT, G., BAXTER, D., GREENFIELD, P., JEDRZEJEWSKI, R., NOTA, A., SPARKS, W. B.: 1993. High resolution imaging of galaxy cores. *Astronomical Journal*, **106**, 1371.

CRETTON, N., DE ZEEUW, P. T., VAN DER MAREL, R. P., RIX, H.: 1999. Axisymmetric three-integral models for galaxies. *Astrophysical Journal Supplement Series*, **124**, 383.

CRETTON, N., NAAB, T., RIX, H.-W., BURKERT, A.: 2000a. The kinematics of 3:1-merger remnants and the formation of low-luminosity eliptical galaxies. *submitted to Astrophysical Journal*.

CRETTON, N., RIX, H., DE ZEEUW, P. T.: 2000b. The distribution of stellar orbits in the giant elliptical galaxy NGC 2320. *Astrophysical Journal*, **536**, 319.

CRUZ, F. MERRITT, D.: 2000. Mergers of galaxies with nuclear black holes. In *American Astronomical Society Meeting*, volume 196, page 2917.

DAVIES, R. L.: 1996. The star formation history of elliptical galaxies. In Bender, R. Davies, R. L., editors, *IAU Symp. 171: New Light on Galaxy Evolution (Dordrecht: Kluwer)*, volume 171, page 37.

DAVIES, R. L., EFSTATHIOU, G., FALL, S. M., ILLINGWORTH, G., SCHECHTER, P. L.: 1983. The kinematic properties of faint elliptical galaxies. *Astrophysical Journal*, **266**, 41.

DAVIES, R. L. ILLINGWORTH, G.: 1983. Dynamics of yet more ellipticals and bulges. *Astrophysical Journal*, **266**, 516.

DAVIES, R. L., SADLER, E. M., PELETIER, R. F.: 1993. Line-strength gradients in elliptical galaxies. *Monthly Notices of the Royal Astronomical Society*, **262**, 650.

DE VAUCOULEURS, G.: 1948. Recherches sur les nebuleuses extragalactiques. *Annales d'Astrophysique*, **11**, 247.

DE ZEEUW, T. FRANX, M.: 1991. Structure and dynamics of elliptical galaxies. *Annual Review of Astronomy and Astrophysics*, **29**, 239.

DEEG, H. J., MUNOZ-TUNON, C., TENORIO-TAGLE, G., TELLES, E., VILCHEZ, J. M., RODRIGUEZ-ESPINOSA, J. M., DUC, P. A., MIRABEL, I. F.: 1998. A catalogue of dwarf galaxy candidates around interacting galaxies. *Astronomy and Astrophysics Supplement Series*, **129**, 455.

DEHNEN, W.: 2000. Towards optimal softening in N-body codes: I. Minimizing the force error. *submitted to Monthly Notices of the Royal Astronomical Society.*

DEHNEN, W. GERHARD, O. E.: 1993. Three-integral models of oblate elliptical galaxies. *Monthly Notices of the Royal Astronomical Society*, **261**, 311.

DEHNEN, W. GERHARD, O. E.: 1994. Two-integral models for oblate elliptical galaxies with cusps. *Monthly Notices of the Royal Astronomical Society*, **268**, 1019.

DEJONGHE, H.: 1987. A completely analytical family of anisotropic Plummer models. *Monthly Notices of the Royal Astronomical Society*, **224**, 13.

DEJONGHE, H. MERRITT, D.: 1992. Inferring the mass of spherical stellar systems from velocity moments. *Astrophysical Journal*, **391**, 531.

DJORGOVSKI, S. DAVIS, M.: 1987. Fundamental properties of elliptical galaxies. *Astrophysical Journal*, **313**, 59.

D'ONOFRIO, M., CAPACCIOLI, M., CAON, N.: 1994. On the shape of the light profiles of early type galaxies - Part two - The diagram. *Monthly Notices of the Royal Astronomical Society*, **271**, 523.

DRESSLER, A.: 1980. Galaxy morphology in rich clusters - Implications for the formation and evolution of galaxies. *Astrophysical Journal*, **236**, 351.

DRESSLER, A., LYNDEN-BELL, D., BURSTEIN, D., DAVIES, R. L., FABER, S. M., TERLEVICH, R., WEGNER, G.: 1987. Spectroscopy and photometry of elliptical galaxies. I - A new distance estimator. *Astrophysical Journal*, **313**, 42.

DUBINSKI, J.: 1994. The effect of dissipation on the shapes of dark halos. *Astrophysical Journal*, **431**, 617.

DUC, P. ., BRINKS, E., SPRINGEL, V., PICHARDO, B., WEILBACHER, P., MIRABEL, I. F.: 2000. Formation of a tidal dwarf galaxy in the interacting system Arp 245 (NGC 2992/93). *Astronomical Journal*, **120**, 1238.

ELLIS, R. S., SMAIL, I., DRESSLER, A., COUCH, W. J., OEMLER, A. J., BUTCHER, H., SHARPLES, R. M.: 1997. The homogeneity of spheroidal populations in distant clusters. *Astrophysical Journal*, **483**, 582.

EVANS, N. W.: 1993. Simple galaxy models with massive haloes. *Monthly Notices of the Royal Astronomical Society*, **260**, 191.

EVANS, N. W.: 1994. The power-law galaxies. *Monthly Notices of the Royal Astronomical Society*, **267**, 333.

FABER, S. M., TREMAINE, S., AJHAR, E. A., BYUN, Y., DRESSLER, A., GEBHARDT, K., GRILLMAIR, C., KORMENDY, J., LAUER, T. R., RICHSTONE, D.: 1997. The centers of early-type galaxies with HST. IV. Central parameter relations. *Astronomical Journal*, **114**, 1771.

FAROUKI, R. T. SHAPIRO, S. L.: 1982. Simulations of merging disk galaxies. *Astrophysical Journal*, **259**, 103.

FISHER, D.: 1997. Kinematic profiles of S0 galaxies. *Astronomical Journal*, **113**, 950.

FISHER, D., FRANX, M., ILLINGWORTH, G.: 1995. Line strength gradients in elliptical and brightest cluster galaxies. *Astrophysical Journal*, **448**, 119.

FORBES, D. A., FRANX, M., ILLINGWORTH, G. D.: 1994. Ellipticals with kinematically distinct cores : HST imaging of the nuclear structure of IC 1459. *Astrophysical Journal Letters*, **428**, L49.

FORBES, D. A., FRANX, M., ILLINGWORTH, G. D.: 1995. Ellipticals with kinematically distinct cores: WFPC1 imaging of nearby ellipticals. *Astronomical Journal*, **109**, 1988.

FORBES, D. A., FRANX, M., ILLINGWORTH, G. D., CAROLLO, C. M.: 1996. Ellipticals with kinematically distinct cores: WFPC2 imaging of globular clusters. *Astrophysical Journal*, **467**, 126.

FORMAN, W., JONES, C., TUCKER, W.: 1985. Hot coronae around early-type galaxies. *Astrophysical Journal*, **293**, 102.

FORMAN, W., SCHWARZ, J., JONES, C., LILLER, W., FABIAN, A. C.: 1979. X-ray observations of galaxies in the Virgo cluster. *Astrophysical Journal Letters*, **234**, L27.

FRANX, M., ILLINGWORTH, G., DE ZEEUW, T.: 1991. The ordered nature of elliptical galaxies - Implications for their intrinsic angular momenta and shapes. *Astrophysical Journal*, **383**, 112.

FRANX, M., ILLINGWORTH, G., HECKMAN, T.: 1989. Major and minor axis kinematics of 22 ellipticals. *Astrophysical Journal*, **344**, 613.

FRANX, M. ILLINGWORTH, G. D.: 1988. A counterrotating core in IC 1459. *Astrophysical Journal Letters*, **327**, L55.

FREEMAN, K. C.: 1970. On the disks of spiral and S0 galaxies. *Astrophysical Journal*, **160**, 811.

FUKUGITA, M. PEEBLES, P. J. E.: 1999. A galaxy X-ray Fundamental Plane? *Astrophysical Journal Letters*, **524**, L31.

GAVAZZI, G., FRANZETTI, P., SCODEGGIO, M., BOSELLI, A., PIERINI, D.: 2000. 1.65 μm (H-band) surface photometry of galaxies. V. Profile decomposition of 1157 galaxies. *submitted to Astronomy and Astrophysics*.

GEBHARDT, K., BENDER, R., BOWER, G., DRESSLER, A., FABER, S. M., FILIPPENKO, A. V., GREEN, R., GRILLMAIR, C., HO, L. C., KORMENDY, J., LAUER, T. R., MAGORRIAN, J., PINKNEY, J., RICHSTONE, D., TREMAINE, S.: 2000. A relationship between nuclear black hole mass and galaxy velocity dispersion. *Astrophysical Journal Letters*, **539**, L13.

GERHARD, O. E.: 1981. N-body simulations of disc-halo galaxies - Isolated systems, tidal interactions and merging. *Monthly Notices of the Royal Astronomical Society*, **197**, 179.

GERHARD, O. E.: 1991. A new family of distribution functions for spherical galaxies. *Monthly Notices of the Royal Astronomical Society*, **250**, 812.

GERHARD, O. E.: 1993. Line-of-sight velocity profiles in spherical galaxies: Breaking the degeneracy between anisotropy and mass. *Monthly Notices of the Royal Astronomical Society*, **265**, 213.

GIACCONI, R., BRANDUARDI, G., BRIEL, U., EPSTEIN, A., FABRICANT, D., FEIGELSON, E., FORMAN, W., GORENSTEIN, P., GRINDLAY, J., GURSKY, H., HARNDEN, F. R., HENRY, J. P., JONES, C., KELLOGG, E., KOCH, D., MURRAY, S., SCHREIER, E., SEWARD, F., TANANBAUM, H., TOPKA, K., VAN SPEYBROECK, L., HOLT, S. S., BECKER, R. H., BOLDT, E. A., SERLEMITSOS, P. J., CLARK, G., CANIZARES, C., MARKERT, T., NOVICK. R., HELFAND, D., LONG, K.: 1979. The Einstein /HEAO 2/ X-ray observatory. *Astrophysical Journal*, **230**, 540.

GINGOLD, R. A. MONAGHAN, J. J.: 1977. Smoothed particle hydrodynamics - Theory and application to non-spherical stars. *Monthly Notices of the Royal Astronomical Society*, **181**, 375.

GIOVANELLI, R., HAYNES, M. P., HERTER, T., VOGT, N. P., DA COSTA, L. N., FREUDLING, W., SALZER, J. J., WEGNER, G.: 1997a. The I-band Tully-Fisher relation for cluster galaxies: A template relation, its scatter and bias corrections. *Astronomical Journal*, **113**, 53.

GIOVANELLI, R., HAYNES, M. P., HERTER, T., VOGT, N. P., WEGNER, G., SALZER, J. J., DA COSTA, L. N., FREUDLING, W.: 1997b. The I-band Tully-Fisher relation for cluster galaxies: data presentation. *Astronomical Journal*, **113**, 22.

GNEDIN, N. Y., NORMAN, M. L., OSTRIKER, J. P.: 2000. Formation of galactic bulges. *Astrophysical Journal*, **540**, 32.

HANLAN, P. C. BREGMAN, J. N.: 2000. X-Ray emission from rotating elliptical galaxies. *Astrophysical Journal*, **530**, 213.

HECKMAN, T. M.: 1983. Radio emission and the masses of elliptical galaxies. *Astrophysical Journal*, **273**, 505.

HEMSENDORF, M.: 2000. Dynamics of dense stellar clusters: Binary black holes in galactic centres. In *Massive Stellar Clusters, Proceedings of the international workshop held in Strasbourg, France, November 8-11, 1999. Eds.: A. Lanßon, and C. Boily, Astronomical Society of the Pacific Conference Series., p.197*, page 197.

HERNQUIST, L.: 1987. Performance characteristics of tree codes. *Astrophysical Journal Supplement Series*, **64**, 715.

HERNQUIST, L.: 1990. An analytical model for spherical galaxies and bulges. *Astrophysical Journal*, **356**, 359.

HERNQUIST, L.: 1992. Structure of merger remnants. I - Bulgeless progenitors. *Astrophysical Journal*, **400**, 460.

HERNQUIST, L.: 1993a. N-body realizations of compound galaxies. *Astrophysical Journal Supplement Series*, **86**, 389.

HERNQUIST, L.: 1993b. Structure of merger remnants. II: Progenitors with rotating bulges. *Astrophysical Journal*, **409**, 548.

HERNQUIST, L. BARNES, J. E.: 1990. Are some N-body algorithms intrinsically less collisional than others? *Astrophysical Journal*, **349**, 562.

HERNQUIST, L., HUT, P., MAKINO, J.: 1993a. Discreteness noise versus force errors in N-body simulations. *Astrophysical Journal Letters*, **402**, L85.

HERNQUIST, L. KATZ, N.: 1989. Treesph - A unification of SPH with the hierarchical tree method. *Astrophysical Journal Supplement Series*, **70**, 419.

HERNQUIST, L. QUINN, P. J.: 1988. Formation of shell galaxies. I - Spherical potentials. *Astrophysical Journal*, **331**, 682.

HERNQUIST, L. SPERGEL, D. N.: 1992. Formation of shells in major mergers. *Astrophysical Journal Letters*, **399**, L117.

HERNQUIST, L., SPERGEL, D. N., HEYL, J. S.: 1993b. Structure of merger remnants. III: Phase-space constraints. *Astrophysical Journal*, **416**, 415.

HEYL, J. S., HERNQUIST, L., SPERGEL, D. N.: 1994. Structure of merger remnants. IV: Isophotal shapes. *Astrophysical Journal*, **427**, 165.

HEYL, J. S., HERNQUIST, L., SPERGEL, D. N.: 1996. Structure of merger remnants. V: Kinematics. *Astrophysical Journal*, **463**, 69.

HIBBARD, J. E. VACCA, W. D.: 1997. The apparent morphology of peculiar galaxies at intermediate to high redshifts. *Astronomical Journal*, **114**, 1741.

HIBBARD, J. E. VAN GORKOM, J. H.: 1996. HI, HII, and R-band observations of a galactic merger sequence. *Astronomical Journal*, **111**, 655.

HIBBARD, J. E. YUN, M. S.: 1999. Luminosity profiles of merger remnants. *Astrophysical Journal Letters*, **522**, L93.

HJORTH, J. MADSEN, J.: 1995. Small deviations from the $r^{1/4}$ law, the Fundamental Plane, and phase densities of elliptical galaxies. *Astrophysical Journal*, **445**, 55.

HOCKNEY, R. W. EASTWOOD, J. W.: 1981. *Computer simulations using particles*. McGraw-Hill Inc.

HORELLOU, C., CHARMANDARIS, V., COMBES, F., APPLETON, P. N., CASOLI, F., MI-
RABEL, I. F.: 1998. Molecular gas in the Cartwheel galaxy. *Astronomy and Astrophysics*,
340, L51.

HUBBLE, E.: 1936. *The realm of the nebulae*. Yale University Press, New Haven and London,
1936 and 1982.

HUBBLE, E. HUMASON, M. L.: 1931. The velocity-distance relation among extra-galactic
nebulae. *Astrophysical Journal*, **74**, 43.

ILLINGWORTH, G.: 1977. Rotation in 13 elliptical galaxies. *Astrophysical Journal Letters*,
218, L43.

IRWIN, J. A. SARAZIN, C. L.: 1998. ROSAT X-ray colors and emission mechanisms in
early-type galaxies. *Astrophysical Journal*, **499**, 650.

JAFFE, W., FORD, H. C., O'CONNELL, R. W., VAN DEN BOSCH, F. C., FERRARESE, L.:
1994. Hubble space telescope photometry of the central regions of Virgo cluster elliptical
galaxies. 1: Observations, discussion, and conclusions. *Astronomical Journal*, **108**, 1567.

JEDRZEJEWSKI, R. SCHECHTER, P. L.: 1988. Evidence for dynamical subsystems in elliptical
galaxies. *Astrophysical Journal Letters*, **330**, L87.

JEDRZEJEWSKI, R. I.: 1987. CCD surface photometry of elliptical galaxies. I - Observations,
reduction and results. *Monthly Notices of the Royal Astronomical Society*, **226**, 747.

JEDRZEJEWSKI, R. I., DAVIES, R. L., ILLINGWORTH, G. D.: 1987. CCD surface photometry
of the bright elliptical galaxies NGC 720, NGC 1052, and NGC 4697. *Astronomical Journal*,
94, 1508.

JERNIGAN, J. G.: 1985. Direct N-body simulations with a recursive center of mass reduction
and regularization. In *Dynamics of star clusters; Proceedings of the Symposium, Princeton,
NJ, May 29-June 1, 1984 (A86-38176 17-90). Dordrecht, D. Reidel Publishing Co., 1985.
Research supported by the University of California.*, page 275.

JERNIGAN, J. G. PORTER, D. H.: 1989. A tree code with logarithmic reduction of force
terms, hierarchical regularization of all variables, and explicit accuracy controls. *Astro-
physical Journal Supplement Series*, **71**, 871.

JORGENSEN, I., FRANX, M., KJAERGAARD, P.: 1996. The fundamental plane for cluster E
and S0 galaxies. *Monthly Notices of the Royal Astronomical Society*, **280**, 167.

KAUFFMANN, G.: 1996. The age of elliptical galaxies and bulges in a merger model. *Monthly
Notices of the Royal Astronomical Society*, **281**, 487.

KAUFFMANN, G. CHARLOT, S.: 1998. The K-band luminosity function at z=1: A powerful
constraint on galaxy formation theory. *Monthly Notices of the Royal Astronomical Society*,
297, L23.

KAWAI, A., FUKUSHIGE, T., TAIJI, M., MAKINO, J., SUGIMOTO, D.: 1997. The PCI
interface for GRAPE systems: PCI-HIB. *Publications of the Astronomical Society of Japan*,
49, 607.

KAWAI, A., FUKUSHIGE, T., TAIJI, M., MAKINO, J., SUGIMOTO, D.: 2000. GRAPE-5: A special-purpose computer for N-body simulations. *Publications of the Astronomical Society of Japan*, **52**, 659.

KELSON, D. D., VAN DOKKUM, P. G., FRANX, M., ILLINGWORTH, G. D., FABRICANT, D.: 1997. Evolution of early-type galaxies in distant clusters: The Fundamental Plane from Hubble Space Telescope imaging and Keck spectroscopy. *Astrophysical Journal Letters*, **478**, L13.

KLESSEN, R. S. KROUPA, P.: 1998. Dwarf spheroidal satellite galaxies without dark matter: Results from two different numerical techniques. *Astrophysical Journal*, **498**, 143.

KOPROLIN, W. ZEILINGER, W. W.: 2000. Line-of-sight velocity distributions of 53 early-type galaxies. *Astronomy and Astrophysics Supplement Series*, **145**, 71.

KORMENDY, J.: 1982. Rotation of the bulge components of barred galaxies. *Astrophysical Journal*, **257**, 75.

KORMENDY, J. BENDER, R.: 1996. A proposed revision of the Hubble sequence for elliptical galaxies. *Astrophysical Journal Letters*, **464**, L119.

KORMENDY, J. DJORGOVSKI, S.: 1989. Surface photometry and the structure of elliptical galaxies. *Annual Review of Astronomy and Astrophysics*, **27**, 235.

KRONAWITTER, A., SAGLIA, R. P., GERHARD, O., BENDER, R.: 2000. Orbital structure and mass distribution in elliptical galaxies. *Astronomy and Astrophysics Supplement Series*, **144**, 53.

KROUPA, P.: 1997. Dwarf spheroidal satellite galaxies without dark matter. *New Astronomy*, **2**, 139.

LAUER, T. R.: 1985. Boxy isophotes, discs and dust lanes in elliptical galaxies. *Monthly Notices of the Royal Astronomical Society*, **216**, 429.

LAUER, T. R., AJHAR, E. A., BYUN, Y. ., DRESSLER, A., FABER, S. M., GRILLMAIR, C., KORMENDY, J., RICHSTONE, D., TREMAINE, S.: 1995. The centers of early-type galaxies with HST. I .An observational survey. *Astronomical Journal*, **110**, 2622.

LEWIS, J. R. FREEMAN, K. C.: 1989. Kinematics and chemical properties of the old disk of the Galaxy. *Astronomical Journal*, **97**, 139.

LUCY, L. B.: 1977. A numerical approach to the testing of the fission hypothesis. *Astronomical Journal*, **82**, 1013.

MAGORRIAN, J. BINNEY, J.: 1994. Predicting line-of-sight velocity distributions of elliptical galaxies. *Monthly Notices of the Royal Astronomical Society*, **271**, 949.

MAKINO, J., KOKUBO, E., TAIJI, M.: 1993. HARP: A special-purpose computer for N-body problem. *Publications of the Astronomical Society of Japan*, **45**, 349.

MAKINO, J. TAIJI, M.: 1998. *Scientific simulations with special-purpose computers : The GRAPE systems*. Toronto : John Wiley & Sons, c1998.

MAKINO, J., TAIJI, M., EBISUZAKI, T., SUGIMOTO, D.: 1997. GRAPE-4: A massively parallel special-purpose computer for collisional N-body simulations. *Astrophysical Journal*, **480**, 432.

MEHLERT, D., SAGLIA, R. P., BENDER, R., WEGNER, G.: 1998. The kinematically peculiar cores of the Coma cluster early-type galaxies NGC 4816 and IC 4051. *Astronomy and Astrophysics*, **332**, 33.

MEHLERT, D., SAGLIA, R. P., BENDER, R., WEGNER, G.: 2000. Spatially resolved spectroscopy of Coma cluster early-type galaxies. I. The database. *Astronomy and Astrophysics Supplement Series*, **141**, 449.

MELNICK, J. SARGENT, W. L. W.: 1977. The radial distribution of morphological types of galaxies in X-ray clusters. *Astrophysical Journal*, **215**, 401.

MERRIFIELD, M. R. KENT, S. M.: 1990. Fourth moments and the dynamics of spherical systems. *Astronomical Journal*, **99**, 1548.

MERRITT, D.: 1993. Dynamical mapping of hot stellar systems. *Astrophysical Journal*, **413**, 79.

MERRITT, D.: 1996. Optimal smoothing for N-body codes. *Astronomical Journal*, **111**, 2462.

MERRITT, D. QUINLAN, G. D.: 1998. Dynamical evolution of elliptical galaxies with central singularities. *Astrophysical Journal*, **498**, 625.

MIHOS, J. C. HERNQUIST, L.: 1996. Gasdynamics and starbursts in major mergers. *Astrophysical Journal*, **464**, 641.

MIHOS, J. C., WALKER, I. R., HERNQUIST, L., MENDES DE OLIVEIRA, C., BOLTE, M.: 1995. A merger origin for X structures in S0 galaxies. *Astrophysical Journal Letters*, **447**, L87–L90.

MIRABEL, I. F., VIGROUX, L., CHARMANDARIS, V., SAUVAGE, M., GALLAIS, P., TRAN, D., CESARSKY, C., MADDEN, S. C., DUC, P. .: 1998. The dark side of star formation in the Antennae galaxies. *Astronomy and Astrophysics*, **333**, L1.

MOBASHER, B., GUZMAN, R., ARAGON-SALAMANCA, A., ZEPF, S.: 1999. The near-infrared Fundamental Plane of elliptical galaxies. *Monthly Notices of the Royal Astronomical Society*, **304**, 225.

MOELLENHOFF, C., HUMMEL, E., BENDER, R.: 1992. Optical and radio morphology of elliptical dust-lane galaxies - Comparison between CCD images and VLA maps. *Astronomy and Astrophysics*, **255**, 35.

MONAGHAN, J. J.: 1992. Smoothed particle hydrodynamics. *Annual Review of Astronomy and Astrophysics*, **30**, 543.

MOORE, B., LAKE, G., KATZ, N.: 1998. Morphological transformation from galaxy harassment. *Astrophysical Journal*, **495**, 139.

NAAB, T. BURKERT, A.: 2000a. Formation of massive elliptical galaxies in a mixed merger scenario. In *ASP Conf. Ser. 197: Dynamics of Galaxies: From the Early Universe to the Present*, page 267.

NAAB, T. BURKERT, A.: 2000b. Gas dynamics and disk formation in 3:1 mergers. In *to appear in ASP Conf. Ser.:Galaxy Disks and Disk Galaxies*.

NAAB, T., BURKERT, A., HERNQUIST, L.: 1999. On the formation of boxy and disky elliptical galaxies. *Astrophysical Journal Letters*, **523**, L133.

NAKANO, T. MAKINO, J.: 1999. On the cusp around central black holes in luminous elliptical galaxies. *Astrophysical Journal Letters*, **525**, L77.

NAVARRO, J. F., FRENK, C. S., WHITE, S. D. M.: 1997. A universal density profile from hierarchical clustering. *Astrophysical Journal*, **490**, 493.

NAVARRO, J. F. STEINMETZ, M.: 1997. The effects of a photoionizing ultraviolet background on the formation of disk galaxies. *Astrophysical Journal*, **478**, 13.

NEGROPONTE, J. WHITE, S. D. M.: 1983. Simulations of mergers between disc-halo galaxies. *Monthly Notices of the Royal Astronomical Society*, **205**, 1009.

NIETO, J. L. BENDER, R.: 1989. Boxiness in elliptical galaxies. *Astronomy and Astrophysics*, **215**, 266.

NIETO, J. L., BENDER, R., ARNAUD, J., SURMA, P.: 1991a. The shape of central regions in elliptical galaxies. *Astronomy and Astrophysics*, **244**, L25.

NIETO, J. L., BENDER, R., POULAIN, P., SURMA, P.: 1992. The origin of inner isophotal twists in elliptical galaxies. *Astronomy and Astrophysics*, **257**, 97.

NIETO, J. L., CAPACCIOLI, M., HELD, E. V.: 1988. More isotropic oblate rotators in elliptical galaxies. *Astronomy and Astrophysics*, **195**, L1.

NIETO, J. L., DAVOUST, E., BENDER, R., PRUGNIEL, P.: 1990. The low-mass extension of the Fundamental Plane of elliptical galaxies. *Astronomy and Astrophysics*, **230**, L17.

NIETO, J. L., POULAIN, P., DAVOUST, E.: 1994. The nature of elongated ellipticals. *Astronomy and Astrophysics*, **283**, 1.

NIETO, J. L., POULAIN, P., DAVOUST, E., ROSENBLATT, P.: 1991b. Isophotal shapes of early-type galaxies. I - Elongated ellipticals. *Astronomy and Astrophysics Supplement Series*, **88**, 559.

OEMLER, A. J.: 1974. The systematic properties of clusters of galaxies. Photometry of 15 clusters. *Astrophysical Journal*, **194**, 1.

OKUMURA, S. K., MAKINO, J., EBISUZAKI, T., FUKUSHIGE, T., ITO, T., SUGIMOTO, D., HASHIMOTO, E., TOMIDA, K., MIYAKAWA, N.: 1993. Highly parallelized special-purpose computer, GRAPE-3. *Publications of the Astronomical Society of Japan*, **45**, 329.

OSTRIKER, J. P. TREMAINE, S. D.: 1975. Another evolutionary correction to the luminosity of giant galaxies. *Astrophysical Journal Letters*, **202**, L113.

PAHRE, M. A., DE CARVALHO, R. R., DJORGOVSKI, S. G.: 1998. Near-infrared imaging of early-type galaxies. IV. The physical origins of the Fundamental Plane scaling relations. *Astronomical Journal*, **116**, 1606.

PIERCE, M. J. TULLY, R. B.: 1992. Luminosity-line width relations and the extragalactic distance scale. I - Absolute calibration. *Astrophysical Journal*, **387**, 47.

POSTMAN, M. GELLER, M. J.: 1984. The morphology-density relation - The group connection. *Astrophysical Journal*, **281**, 95.

POULAIN, P., NIETO, J. L., DAVOUST, E.: 1992. Isophotal shapes of early-type galaxies. II - The Perseus cluster. *Astronomy and Astrophysics Supplement Series*, **95**, 129.

QUINN, P. J., HERNQUIST, L., FULLAGAR, D. P.: 1993. Heating of galactic disks by mergers. *Astrophysical Journal*, **403**, 74.

RIGOPOULOU, D., SPOON, H. W. W., GENZEL, R., LUTZ, D., MOORWOOD, A. F. M., TRAN, Q. D.: 1999. A large mid-infrared spectroscopic and near-infrared imaging survey of Ultraluminous Infrared Galaxies: Their nature and evolution. *Astronomical Journal*, **118**, 2625.

RIX, H., CAROLLO, C. M., FREEMAN, K.: 1999. Large stellar disks in small elliptical galaxies. *Astrophysical Journal Letters*, **513**, L25.

RIX, H. WHITE, S. D. M.: 1992. Optimal estimates of line-of-sight velocity distributions from absorption line spectra of galaxies - Nuclear discs in elliptical galaxies. *Monthly Notices of the Royal Astronomical Society*, **254**, 389.

RIX, H.-W. WHITE, S. D. M.: 1990. Disks in elliptical galaxies. *Astrophysical Journal*, **362**, 52.

ROMEO, A. B.: 1994. How faithful are N-body simulations of disc galaxies? *Astronomy and Astrophysics*, **286**, 799.

ROMEO, A. B.: 1997. Dynamical effects of softening in N-body simulations of disc galaxies. Method and first applications. *Astronomy and Astrophysics*, **324**, 523.

RYDEN, B.: 1992. The intrinsic shapes of elliptical galaxies. *Astrophysical Journal*, **396**, 445.

RYDEN, B. S.: 1996. The intrinsic shapes of stellar systems. *Astrophysical Journal*, **461**, 146.

SACKETT, P. D.: 1999. The shape of dark matter halos. In *ASP Conf. Ser. 182: Galaxy Dynamics - A Rutgers Symposium*, page 393.

SAGLIA, R. P., BENDER, R., DRESSLER, A.: 1993a. The intrinsic shape of early-type galaxies and the scatter around the Fundamental Plane. *Astronomy and Astrophysics*, **279**, 75.

SAGLIA, R. P., BERTSCHINGER, E., BAGGLEY, G., BURSTEIN, D., COLLESS, M., DAVIES, R. L., McMAHAN, R. K., WEGNER, G.: 1993b. The effects of seeing on the photometric properties of elliptical galaxies. *Monthly Notices of the Royal Astronomical Society*, **264**, 961.

SAHA, P. WILLIAMS, T. B.: 1994. Unfolding kinematics from galaxy spectra: A Bayesian method. *Astronomical Journal*, **107**, 1295.

SANDAGE, A. TAMMAN, G. A.: 1981. *A Revised Shapley-Ames Catalouge of Bright Galaxies*. The Carnegie Institute of Washington, Washington.

SANDERS, D. B. MIRABEL, I. F.: 1996. Luminous Infrared Galaxies. *Annual Review of Astronomy and Astrophysics*, **34**, 749.

SANROMA, M. SALVADOR-SOLE, E.: 1990. Evidence for a large-scale environmental dependence of galaxy morphology in clusters. *Astrophysical Journal*, **360**, 16.

SCORZA, C. BENDER, R.: 1990. A disk in the elliptical galaxy NGC 3610. *Astronomy and Astrophysics*, **235**, 49.

SCORZA, C. BENDER, R.: 1995. The internal structure of disky elliptical galaxies. *Astronomy and Astrophysics*, **293**, 20.

SCORZA, C., BENDER, R., WINKELMANN, C., CAPACCIOLI, M., MACCHETTO, D. F.: 1998. Stellar disks and embedded bars in early-type galaxies. I. 2-D photometric decomposition of 28 southern early-type galaxies. *Astronomy and Astrophysics Supplement Series*, **131**, 265.

SEARLE, L., SARGENT, W. L. W., BAGNUOLO, W. G.: 1973. The history of star formation and the colors of late-type galaxies. *Astrophysical Journal*, **179**, 427.

SERSIC, J. L.: 1968. *Atlas de galaxias australes*. Cordoba, Argentina: Observatorio Astronomico, 1968.

SPITZER, L. J.: 1942. The dynamics of the interstellar medium. III. Galactic distribution. *Astrophysical Journal*, **95**, 329.

SPRINGEL, V.: 2000. Modelling star formation and feedback in simulations of interacting galaxies. *Monthly Notices of the Royal Astronomical Society*, **312**, 859.

STEINMETZ, M. BUCHNER, S.: 1995. In Hippelein, K., Meisenheimer, K., Röser, H.-J., editors, *Galaxies in the young Universe (Lecture Notes in Physiscs 463; Berlin: Springer)*, page 215.

STEINMETZ, M. NAVARRO, J. F.: 1999. The cosmological origin of the Tully-Fisher relation. *Astrophysical Journal*, **513**, 555.

SUGIMOTO, D., CHIKADA, Y., MAKINO, J., ITO, T., EBISUZAKI, T., UMEMURA, M.: 1990. A special-purpose computer for gravitational many-body problems. *Nature*, **345**, 33–35.

TOOMRE, A.: 1964. On the gravitational stability of a disk of stars. *Astrophysical Journal*, **139**, 1217.

TOOMRE, A.: 1977. In Tinsley, B. Larson, R., editors, *The evolution of galaxies and stellar populations (New Haven: Yale Univ. Press)*, page 401.

TOOMRE, A. TOOMRE, J.: 1972. Galactic bridges and tails. *Astrophysical Journal*, **178**, 623.

TREMBLAY, B. MERRITT, D.: 1995. The frequency function of elliptical galaxy intrinsic shapes. *Astronomical Journal*, **110**, 1039.

TREMBLAY, B. MERRITT, D.: 1996. Evidence from intrinsic shapes for two families of elliptical galaxies. *Astronomical Journal*, **111**, 2243.

TULLY, R. B. FISHER, J. R.: 1977. A new method of determining distances to galaxies. *Astronomy and Astrophysics*, **54**, 661.

VALLURI, M. MERRITT, D.: 1998. Regular and chaotic dynamics of triaxial stellar systems. *Astrophysical Journal*, **506**, 686.

VAN DER KRUIT, P. C. FREEMAN, K. C.: 1984. The vertical velocity dispersion of the stars in the disks of two spiral galaxies. *Astrophysical Journal*, **278**, 81.

VAN DER KRUIT, P. C. SEARLE, L.: 1981. Surface photometry of edge-on spiral galaxies. I - A model for the three-dimensional distribution of light in galactic disks. II - The distribution of light and colour in the disk and spheroid of NGC 891. *Astronomy and Astrophysics*, **95**, 105.

VAN DER KRUIT, P. C. SEARLE, L.: 1982. Surface photometry of edge-on spiral galaxies. III - Properties of the three-dimensional distribution of light and mass in disks of spiral galaxies. *Astronomy and Astrophysics*, **110**, 61.

VAN DER MAREL, R. P. FRANX, M.: 1993. A new method for the identification of non-Gaussian line profiles in elliptical galaxies. *Astrophysical Journal*, **407**, 525.

VAN DER MAREL, R. P., RIX, H. W., CARTER, D., FRANX, M., WHITE, S. D. M., DE ZEEUW, T.: 1994. Velocity profiles of galaxies with claimed black-holes - Part one - Observations of M31 M32 NGC3115 and NGC4594. *Monthly Notices of the Royal Astronomical Society*, **268**, 521.

VAN DOKKUM, P. G., FRANX, M., FABRICANT, D., KELSON, D. D., ILLINGWORTH, G. D.: 1999. A high merger fraction in the rich cluster MS 1054-03 at z = 0.83: Direct evidence for hierarchical formation of massive galaxies. *Astrophysical Journal Letters*, **520**, L95.

VELAZQUEZ, H. WHITE, S. D. M.: 1999. Sinking satellites and the heating of galaxy discs. *Monthly Notices of the Royal Astronomical Society*, **304**, 254.

WAGNER, S. J., BENDER, R., MOELLENHOFF, C.: 1988. Minor-axis rotation and triaxiality in elliptical galaxies. *Astronomy and Astrophysics*, **195**, L5.

WALKER, I. R., MIHOS, J. C., HERNQUIST, L.: 1996. Quantifying the fragility of galactic disks in minor mergers. *Astrophysical Journal*, **460**, 121.

WARREN, M. S., QUINN, P. J., SALMON, J. K., ZUREK, W. H.: 1992. Dark halos formed via dissipationless collapse. I - Shapes and alignment of angular momentum. *Astrophysical Journal*, **399**, 405.

WEIL, M. L. HERNQUIST, L.: 1996. Global properties of multiple merger remnants. *Astrophysical Journal*, **460**, 101.

WHITE, S. D. M.: 1978. Simulations of merging galaxies. *Monthly Notices of the Royal Astronomical Society*, **184**, 185.

WHITE, S. D. M.: 1979. Further simulations of merging galaxies. *Monthly Notices of the Royal Astronomical Society*, **189**, 831.

WHITMORE, B. C. GILMORE, D. M.: 1991. On the interpretation of the morphology-density relation for galaxies in clusters. *Astrophysical Journal*, **367**, 64.

WHITMORE, B. C., GILMORE, D. M., JONES, C.: 1993. What determines the morphological fractions in clusters of galaxies? *Astrophysical Journal*, **407**, 489.

WYSE, R. F. G.: 1998. Phase-space density constraints on the formation of bulges from discs. *Monthly Notices of the Royal Astronomical Society*, **293**, 429.

ZIEGLER, B. L. BENDER, R.: 1997. The Mg(b)-sigma relation of elliptical galaxies at z of about 0.37. *Monthly Notices of the Royal Astronomical Society*, **291**, 527.

ZIEGLER, B. L., SAGLIA, R. P., BENDER, R., BELLONI, P., GREGGIO, L., SEITZ, S.: 1999. Probing early-type galaxy evolution with the Kormendy relation. *Astronomy and Astrophysics*, **346**, 13.

Danksagung

Ich danke...

an erster Stelle dem Betreuer meiner Arbeit, Dr. Andreas Burkert, für seinen unerschöpflichen Ideenschatz, seine immerwährende Geduld und seine volle Unterstützung. Es war eine reine Freude, mit ihm zusammenzuarbeiten und eine Freude wird es auch in Zukunft noch sein.

Prof. Dr. Immo Appenzeller und Prof. Dr. Hans-Walter Reinhard Rix, die mir die Möglichkeit gaben, am MPIA zu promovieren und sich im besonderen der Belange der Promotionsstudenten am Institut angenommen haben.

Prof. Dr. Immo Appenzeller und Priv. Doz. Dr. Rainer Spurzem für ihre Bereitschaft, diese Arbeit zu begutachten.

Dr. Adrianne Slyz, Fabian Heitsch und Sebastian Jester für die Unterstützung bei der Korrektur dieser Arbeit.

Steffi, Olaf, Markus, Markus, Markus, Michael, Sebastian und Bernd für die motivierenden SpatzBiergänge.

Dr. Ralf Klessen und Dr. Ralph Peter Andersen für das Meer und den Traktor.

den Mitgliedern der Theoriegruppe für interessante wissenschaftliche Diskussionen.

den Mitarbeitern der EDV-Abteilung des Institutes, die meine Arbeit in hervorragender Weise unterstützt haben.

Christa Fürst für diverse Einblicke in die Schönheiten und die Absurditäten des Lebens.

meinem Freund Mathias Weber.

Mein allergrößter Dank gilt meiner Frau Nathalie, meinen Eltern, meinen Schwestern Birgit und Silke, meinem Schwager Christoph, Markus, und meiner Schwiegerfamilie, mit deren Unterstützung ich es schaffen konnte, erfolgreich an meiner Doktorarbeit zu arbeiten und sie zügig zu vollenden.